DESIGN, FORMATION, AND ELECTRICAL PROPERTIES OF BI-SE CONTAINING HETEROSTRUCTURES

by

MARISA A. CHOFFEL

A DISSERTATION

Presented to the Department of Chemistry and Biochemistry and the
Division of Graduate Studies of the University of Oregon
in partial fulfillment of the requirementsfor the degree of
Doctor of Philosophy

December 2021

DISSERTATION APPROVAL PAGE

Student: Marisa A. Choffel

Title: Design, Formation, and Electrical Properties of Bi-Se Containing Heterostructures.

This dissertation has been accepted and approved in partial fulfillment of the requirements for the Doctor of Philosophy degree in the Department of Chemistry and Biochemistry by:

Amanda Cook-Sneathen	Chairperson
David C. Johnson	Advisor
Darren W. Johnson	Core Member
Benjamin J. McMorran	Institutional Representative

and

Krista Chronister	Vice Provost for Graduate Students

Original approval signatures are on file with the University of Oregon Division of Graduate Studies.

Degree awarded December 2021

DISSERTATION ABSTRACT

Marisa A. Choffel

Doctor of Philosophy

Department of Chemistry and Biochemistry

December 2021

Title: Design, Formation, and Electrical Properties of Bi-Se Containing Heterostructures

New materials are essential for continued technological advancements, but synthesizing new materials remains a significant challenge. The modulated elemental reactants synthesis approach provides tunable parameters to design heterostructures. This dissertation focuses on the interplay of these parameters with reaction pathways, which resulted in the synthesis of a new binary (Mn-Se) compound and of Bi_2Se_3 and BiSe containing heterostructures.

The first section of the dissertation focused on how the local composition of the precursor affected the reaction pathways of various systems. A previously unreported kinetic product containing Mn and Se was found depending on the composition of the precursor. Layer thickness was not a contributing factor to the formation. Based on the hypothesis that local composition has the most impact on what nucleates, synthesizing heterostructures containing Bi_2Se_3 were attempted. Substituent-like effects were observed as a result of the competition between the formation of Bi_2Se_3 or BiSe depending on the electrical properties of the neighboring layer. Understanding how the electrical properties and charge transfer affected the formation of the Bi-M-Se heterostructures was vital for the rest of the dissertation.

The remainder of this dissertation focused on investigating the

charge transfer between BiSe and neighboring layers. Charge transfer from the BiSe to the $MoSe_2$ layer, which resulted in the formation of a kinetic 1T-$MoSe_2$ polymorph, was previously observed in $(BiSe)_{0.97}(MoSe_2)$. $(BiSe)_{1+x}(Bi_2Se_3)_{1+y}(BiSe)_{1+x}(MoSe_2)$ was first synthesized to determine the impact of two BiSe layers on the change in $MoSe_2$ polymorph and metallic temperature dependent resistivity was observed. Charge transfer to the Bi_2Se_3 conduction band was observed in $(Bi_2Se_3)_{1+y}(BiSe)_{1+x}(MoSe_2)$, instead of 1T-$MoSe_2$. These heterostructures examined by X-ray photoelectron spectroscopy to probe the BiSe stabilization. An unprecedented difference in the BiSe structure in $[(BiSe)_{1+x}(MoSe_2)_3]$ prompted an investigation on the importance of the local composition during the initial heating. $(BiSe)_{1+x}(MoSe_2)_n$ heterostructures were synthesized to probe the structure-property relationship of one BiSe layer with multiple $MoSe_2$ layers to further probe the charge transfer.

This investigation has opened new avenues of research both in the Bi-Mo-Se ternary phase diagram and in the importance of understanding reaction mechanisms and tunable parameters to better design and control the formation of desired products.

CURRICULUM VITAE

NAME OF AUTHOR: Marisa A. Choffel

GRADUATE AND UNDERGRADUATE SCHOOLS ATTENDED:

University of Oregon, Eugene, OR
The College of William & Mary, Williamsburg, VA

DEGREES AWARDED:

Doctor of Philosophy, Chemistry, 2021, University of Oregon
Bachelor of Science, Chemistry, 2017, The College of William & Mary

AREAS OF SPECIAL INTEREST:

Materials Science
Thin Film Deposition
Process Control

PROFESSIONAL EXPERIENCE:

Research Assistant, D. C. Johnson Research Group, University of Oregon, 2018 - 2021

Research Assistant, M. D. Pluth Research Group, University of Oregon, 2018 – 2018

Research Assistant, M. M. Haley and D. W. Johnson Research Group, University of Oregon, 2017 – 2018

Research Assistant, K. L. Wustholz Research Group, The College of William & Mary, 2015 – 2017

PUBLICATIONS:

Choffel, M. A.; Gannon, R. N.; Göhler, F.; Miller, A. M.; Medlin, D.; Seyller, T.; Johnson, D. C. Synthesis and Electrical Properties of a New Compound $(BiSe)_{0.97}(Bi_2Se_3)_{1.26}(BiSe)_{0.97}(MoSe_2)$ Containing Metallic 1T-$MoSe_2$. *Chem. Mater.* **2021.**

Choffel, M. A.; Kam, T. M.; Johnson, D. C. Substituent effect in the synthesis of heterostructures. *Inorg. Chem.* **2021**.

Choffel, M. A.; Farling, C. G.; Frano, K. A.; Matecki, M. K.; Zheng, Z.; Svoboda, S. A.; Wustholz, K. L. *Studies in Conservation.* **2021.**

Göhler, F.; Choffel, M. A.; Schmidt, C.; Zahn, D. R. T.; Johnson, D. C.; Seyller, T. Influence of Nanoarchitectures on Interlayer Interaction in Layered Bi-Mo-Se Heterostructures. *J. Phys. Chem. C.* **2021**.

Lammel, M.; Geishendorf, K.; Choffel, M. A.; Hamann, D. M.; Johnson, D. C.; Nielsch, K.; Thomas, A. Fast Fourier transform and multi-Gaussian fitting of XRR data to determine the thickness of ALD grown thin films within the initial growth regime. *Appl. Phys, Lett.* **2020**.

Choffel, M. A.; Hamann, D. M.; Joke, J. A.; Cordova, D. L. M.; Johnson, D. C. The Reaction between Mn and Se Layers. *Z. Anorg. Alle. Chem.* **2018**.

ACKNOWLEDGMENTS

I would like to express my sincere gratitude to the many people I have had the privilege of working with the last four years. First and foremost, to my advisor Professor David C. Johnson. Thank you for allowing me to work and grow within your group, for your guidance and advice, and for always pushing me to think critically. I have grown as a scientist under your mentorship. I would like to express my gratitude for my colleagues – Dr. Renae Gannon, Aaron Miller, Mellie Lemon, Hannah Blackwood, Sarah Rich, and Fischer Havel. Your support, encouragement, collaboration, and enthusiasm made this dissertation possible. To the undergraduate researchers I have worked with and mentored – Taryn Kam, Sarah Chu, Dylan Bardgett, Shannon Fender, and Jordan Joke – thank you for your incredible work ethic and your interest. Thank you to the previous DCJ lab members for laying the groundwork for me to build on and always answering my questions, even if we've never met.

Thank you to CAMCOR and the UO machine shop for your knowledge and support, especially during the lab move. You kept our research on track. Special thank you to Steve Wiemholt for always taking the time to answer my questions. Your willingness to share your knowledge and experience has been invaluable.

My research would not have been possible without my national and international collaborators. I have learned a great deal from Fabian Göhler and Professor Thomas Seyller, who provided their expertise in X-ray photoelectron spectroscopy, as well as Dr. Douglas Medlin and Dr. Ping Lu, for their knowledge and experience with microscopy experiments.

I would like to acknowledge funding from the National Science Foundation under grants DMR-1710214 and 1905185. Sandia

National Laboratories was instrumental for HAADF-STEM images. Sandia National Laboratories is a multimission laboratory managed and operated by National Technology and Engineer- ing Solutions of Sandia, LLC, a wholly owned subsidiary of Honeywell International Inc. for the U.S. Department of Energy's National Nuclear Security Administration under contract DE-NA-0003525. This paper describes objective technical results and analysis. Any subjective views or opinions that might be expressed in the paper do not necessarily represent the views of the U.S. Department of Energy or the United States Government.

To my past professors and post-doctoral, graduate, and undergraduate mentors, you have helped shape me into the scientist and the person I am today. I have learned a great deal from you on how to conduct research, ask questions, and mentor.

To my committee members, I appreciate you for always asking the hard questions. I've learned more from those than I ever thought. Thanks to the Department of Chemistry and Faculty for support and guidance.

Finally, I would not be here today without the unconditional love and support from my parents, grandparents, and friends. Thank you for always picking up my calls. You have kept me grounded more times than I can count.

To my parents, for always believing in me.

TABLE OF CONTENTS

Chapter Page

Chapter Page

Chapter Page

LIST OF FIGURES

Figure Page

Figure Page

Figure Page

Figure Page

LIST OF TABLES

Table Page

CHAPTER I

INTRODUCTION

1.0. Authorship Statement

This chapter was written for this work alone with no intention of publishing it elsewhere. I am the primary author and wrote the following with assistance from my advisor David C. Johnson.

1.1. Overview

Transistors sparked a technology revolution, resulting in the rapid advances in technology that society is accustomed to today. The quick increase in processing and display power coupled with the decrease in device size is largely a result of decreasing the size and increasing the arial density of silicon transistors. However, the size of transistors is reaching their physical limits and it is increasingly more difficulty to maintain the rate of advancement predicted by Moore's Law.[1] New materials need to be developed to continue to advance technology.

Low dimensional materials are one option that may enable advances in device functionality and increases in device density. Carbon nanotubes and other 1D materials, graphene and other 2D materials such as transition metal dichalcogenides, and yet to be discovered low dimensional materials have emergent properties that might be used to overcome current bottlenecks. Using low dimensional materials in devices comes with a unique set of benefits and challenges. The benefits include their 2D thickness,[2-4] substrate independence,[5-6] unique electrical properties,[7-10] and the potential to tune properties by incorporating them into heterostructures.[11-14] To better access these benefits, improvements need to be made to control the junctions between materials,[8,14-15] develop new device architectures unique to the specific nanomaterial,[16] and improve the electrical contacts.[17] However,

the most severe limitation for the application of low dimensional materials in manufacturing is the synthesis of the materials themselves over the large wafer areas. The synthesis needs to be compatible with current wafer scale technology and the targeted materials have to maintain their desired properties while next to the layers that encase them in the device.

1.2. Synthesis of New Materials

Attempts to synthesize new nanomaterials with useful properties have historically depended on serendipity for the formation of unique compounds. In the past decade, advances have been made that enable computation to guide the discovery of novel materials, ideally minimizing exploration time by providing reasonable targets for synthesis. The results of synthetic attempts would be used to further guide the theoretical predictions, yielding more accurate predictions.[18] This process should lead to materials that will address the current limitations to technological advances faster than previously possible. However, of the thousands of compounds predicted by programs such as the Materials Genome project, only a fraction have been successfully formed.[19-25] The predicted compounds are not forming due to approximations made in the calculations that result in systematic errors in formation energies and/or due to the limitations in synthetic techniques.

The limitations for traditional, bulk synthesis methods are significant. Little focus is paid to understanding the reaction mechanisms in the synthesis of solid-state reactions, especially compared to molecular chemistry, which hampers synthesizing materials by design. Molecular chemists have a variety of tools to control the reaction pathway, including protection groups,[26] atalysis,[27] substituent effects, local coordination rules, and bond dissociation energies.[28] No general rules can be applied to predict kinetic solids as

transition metals can exist in several oxidation states and can be non-stochiometric as a result of vacancies.[29] This makes predicting the product hard not only from the computational perspective but the experimental perspective as well.

Understanding of traditional solid state synthesis is limited to the key parts of interdiffusion, nucleation, and growth.[30-32] Diffusion limited synthesis methods, like heat 'n' beat, require long reaction times at high temperatures in order to promote the movement of atoms.[33] The long diffusion lengths mean A and B will react to form a stable binary product before C can diffuse to the nucleation site. The binary thermodynamic AB product is in a deep energy well and may not react with C. The long diffusion lengths, high reaction temperatures, and long reaction times often prevent the synthesis of predicted ternary or binary products.[34] Nucleation limited synthesis methods that involve a fluid phase allow for more control over the energy landscape. Fluid phases have higher diffusion rates than solids, and the diffusion rates are often enhanced due to convection effects or stirring. The composition of the flux can be used to change the energy landscape of the reacting system, making products that would be metastable in their binary or ternary phase diagrams energetically favorable.[35] Nucleation of kinetic products are possible but unpredictable due to the lack of understanding of what factors influence the evolution of the intermediates and/or products.[36] Predicting what will form is not possible as little is known about the structure or concentration of the chemical species in solution. The need for a synthesis method with tunable experimental parameters to logically control what nucleates is obvious.

Modulated elemental reactants (MER) is a notable advancement

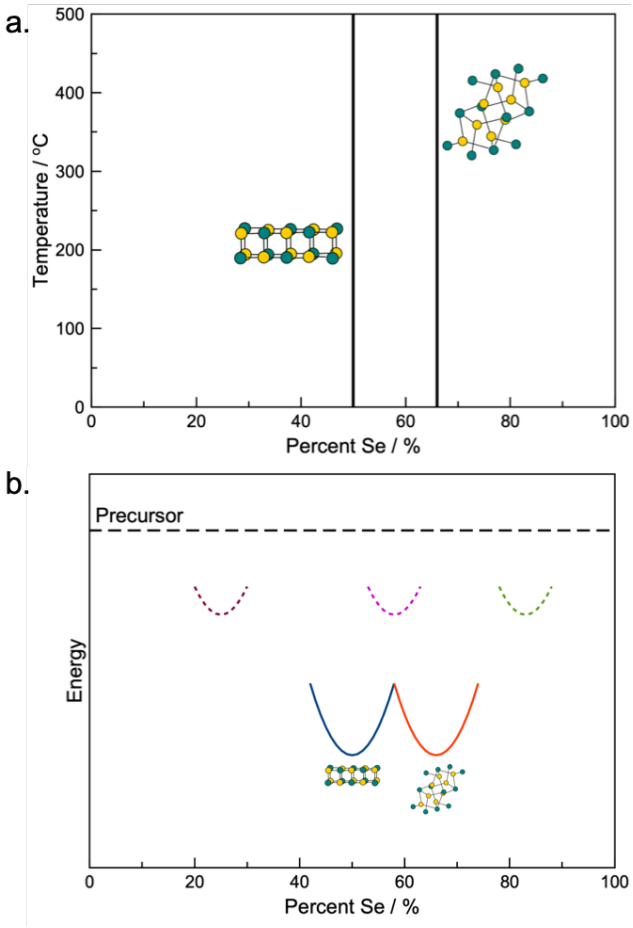

Figure 1.1. (a) An example of a simple binary phase diagram (Mn-Se) with the thermodynamic phases identified and (b) a schematic energy diagram for metastable and thermodynamic products.

in the synthesis of kinetic binary products. Designed precursors are deposited with small diffusion distances to generate an amorphous intermediate. The short diffusion lengths make nucleation the rate limiting step. The compound that forms is the easiest to nucleate, not necessarily the phase that is most thermodynamically stable. The layer thickness affects the diffusion lengths while local composition dictates what nucleates.[37] MER exercises more control over the reaction pathway, intermediates, and final products by adjusting the local composition and layer thickness.[38]

The synthesis of kinetic products using MER is easier when the

phase diagram is relatively simple. For example, the Mn|Se phase diagram (Figure 1a) is one of the simpler systems as there are only two thermodynamic products: rock salt-MnSe and pyrite-$MnSe_2$.[39] The composition space between the thermodynamic products is large, which may allow for the formation of metastable products at higher energies (Figure 1b). The precursor is the highest energy state for the sample. As local composition dictates what nucleates, it is possible to fall into a local free energy minimum that is consistent with the current composition state. The metastable product is stable until more energy is applied to overcome the activation barrier to form a thermodynamic product. In Chapter 3, I describe how I used MER to explore the Mn|Se phase diagram as a function of Se composition and layer thickness to probe the system for kinetic products. When a precursor was deposited with ~80% Se, a previously unreported kinetic product formed at low temperatures. The sample rearranged after annealing at higher temperatures to form the thermodynamic product closest in composition ($MnSe_2$).[40] This is consistent with the prediction based on the energy diagrams as a kinetic product formed but when given enough energy, fell to a deeper, more stable energy well.

The synthesis of kinetic products from a more complex phase diagram like Bi-Se (Figure 2) is unlikely as there are more possible thermodynamic products.[41]Precursors are more likely to fall into the deeper energy well of the thermodynamic products. Formation of a kinetic Bi-Se structure from a precursor that is between 30-60% Se is unlikely as there are several more energetically favorable, thermodynamic Bi-Se structures at these compositions. There is the possibility of forming a kinetic product between 0-30% or 60-100% Se as there is a larger composition difference between the local composition and the closest thermodynamic product, Bi_3Se or Bi_2Se_3, respectively.

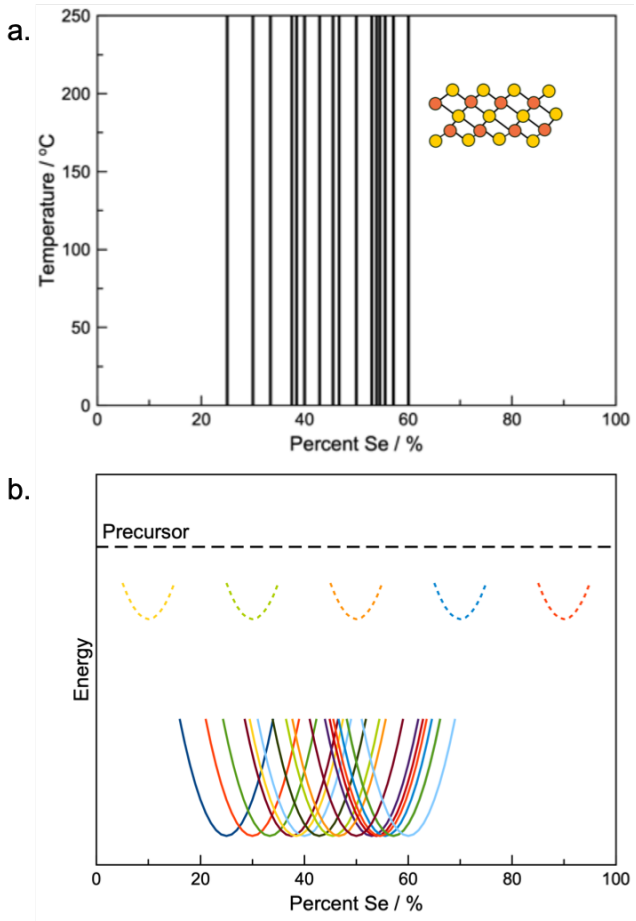

Figure 1.2. (a) An example of a complex binary phase diagram (Bi-Se) with the thermodynamic phases identified and (b) a cartoon energy diagram for metastable and thermodynamic products.

1.3. Multilayer Material Synthesis

As described above, both predicting and synthesizing kinetic binary or ternary products is complicated and unpredictable. The discovery of graphene in 2004[42] ropelled interest in 2D materials, and approaches to physically stack layers to create heterostructures with novel properties were developed. This interest was driven by changes in properties as a result of layer thickness and the immergence of new emergent properties. For example, a transition from an indirect to a direct band gap semiconductor was observed in semiconducting transition metal dichalcogenides when the bulk material is scaled down

to a monolayer.[43] This change resulted in an increase the photoluminescence of the materials.[43-45] Stacks of 2D materials became obvious synthetic targets as predictions were made about their potentially unique properties, and they would be expected to be at least kinetically stable. The ability to stack layers, like Legos, in a precise way to make van der Waals heterostructures has advanced our understanding of interfacial interactions and structure-property relationships. [46-47]A large number of novel phenomena have been reported at the interfaces of the layers including superconductivity,[48] flat band ferromagnetism,[49] and other phenomena.[50-55] The possible combinations of materials to explore new phenomena for possible applications for nanomaterials are limited only by our ability to synthesize them.

Mechanical assembly, or the "Scotch Tape" method, was the synthesis method that propelled this field, enabling researchers to isolate finite thickness layers of materials and determine the thickness of the layers via optical methods.[56] In this process, a piece of tape is adhered to a chunk of material and then peeled off, removing flakes of the material. The tape and flakes combination are then pressed to a surface of choice. When the tape is removed, the bottom layer of the material remains on the substrate.[57] Controlling the flake size and thickness for obtaining finite layers and incorporating them into heterostructures has been a major challenge of current research.[58-60] While improvements to the exfoliation methods have been made in recent years, these methods still rely on sacrificial polymer layers,[61] wet processing,[62] or result in wrinkling and bubbling if too much pressure is applied.[63] The method is further restricted by the need for crystalline products in order to generate the structure, limiting the extended solids to combinations of available products.

Another approach to synthesize heterostructures is to grow them

layer by layer using molecular beam epitaxy (MBE), developed by Arthur and Choi at Bell Laboratories in the 1970s.[64] In MBE, elements are deposited on the surface of a sample, which is held at a specific temperature where surface diffusion is possible to promote nucleation and growth during the deposition. The substrate or previous layer acts as a template for the depositing elements to grow the desired structure. While this synthesis approach is useful for heterostructure synthesis, there are several severe limitations that prevent the scope of possible heterostructures. Epitaxial growth depends on the lattice match with the substrate for the formation of the desired heterostructure as it acts as a template for formation.[65] The limited range of conditions where MBE growth occurs also significantly limits the number of heterostructures that can be made, as it may be possible to grow compound A on B, but not compound B on A. The temperature to promote surface diffusion and nucleation during the deposition also poses a significant issue. High temperatures can affect the probability of incorporation of high vapor pressure elements, resulting in the formation of different stoichiometric phases.[66-67]

MER precursors allow for more control over the energy landscape and suite of experimental parameters than can be used to synthesize targeted heterostructures. Elements are deposited in a $(A|B)_m(C|B)_n$ pattern, where the number of layers of each can vary based on the desired product. The precursor is deposed in a way that mimics the desired nanoarchitecture. Instead of forming an amorphous intermediate, the precursors usually do not completely mix, although of course this depends on the change in free energy (the enthalpy and entropy of mixing) and the temperature.[68] Nucleation can occur during the deposition or at relatively low temperatures and can occur in different layers and different regions simultaneously. Since nucleation does not occur only at the substrate, MER is a non-epitaxial growth

method. Hence, lattice match between the growing constituent and the substrate does not affect the growth of the heterostructure.[69] Other factors can influence formation besides local composition or lattice match.

1.4. Synthesis of Bi-containing Heterostructures

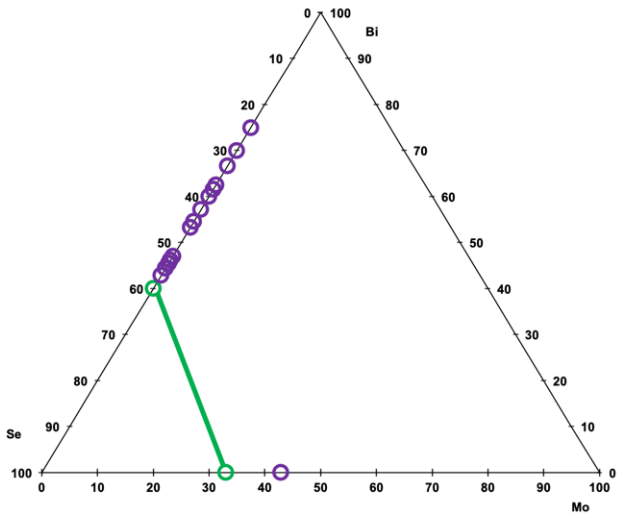

Figure 1.3. Ternary phase diagram for Bi-Mo-Se system with a tie line drawn from Bi_2Se_3 to $MoSe_2$. Thermodynamic binary compounds are marked in purple.

I intended to explore structure-property interactions in Bi_2Se_3-$MoSe_2$ heterostructures to understand the topological properties as a function of layer thickness. Utilizing the control over the local composition and designed precursors, I expected to be able to synthesize heterostructures with compositions consistent along the Bi_2Se_3-$MoSe_2$ tie line (Figure 1.3). Bi_2Se_3 is of interest as it has an unique near-gap electronic structure, which makes for a good thermoelectric materials,[70] and is predicted to be a topological insulators.[71-72] Topological insulators are a type of quantum material with interior insulating states and conducting surface states, which have potential applications for quantum computing. Unfortunately, the bulk conductivity dominates the measurements, making it challenging

to characterize the topological transport properties.[73-74] Bi_2Se_3 has traditionally been subject to extrinsic doping to minimize the influence of the bulk states but high doping concentrations can cause impurity scattering.[75-76] Surface dominated conductance has been observed when TIs are synthesized in thin films, making them an ideal avenue to study the metallic properties.[77] $MoSe_2$ was the ideal partner to start synthesizing Bi_2Se_3-containing heterostructures as it is a large gap semiconductor.[78] Hence, it's conductivity would be very small relative to the surface conductance of the Bi_2Se_3, permitting the exploration of TIs a function of Bi_2Se_3 thickness. My plan was to synthesize other Bi_2Se_3-containing heterostructures with other neighboring layers to explore proximity effect between layers. Transition metal dichalcogenides (TMDs) were used by several research groups as companion constituents to explore the effect of topological states on superconductivity,[79] and magnetism.[80] I intended to contribute to this growing library by synthesizing Bi_2Se_3-$NbSe_2$ heterostructures with different layering sequences to understand the structure-property relationships. However, the initial reports of Bi_2Se_3-containing heterostructure synthesis hinted at a more complicated reaction mechanism that previously anticipated.

Differences in the growth of Bi_2Se_3-TMD heterostructures depending on the TMD sparked my investigation into the effect of the electrical properties of the neighboring layer on the synthesis of Bi-Se containing heterostructures. Researchers reported that a kinetic, rock-salt structured BiSe layer formed at the interface between Bi_2Se_3 and $NbSe_2$ but not Bi_2Se_3 and $MoSe_2$.[81-84] Before I could pursue synthesizing the Bi-Mo-Se heterostructures on the Bi_2Se_3-$MoSe_2$ tie line, I needed to understand the cause of this difference in formation and understand the competition with BiSe-$MoSe_2$ compounds (Figure

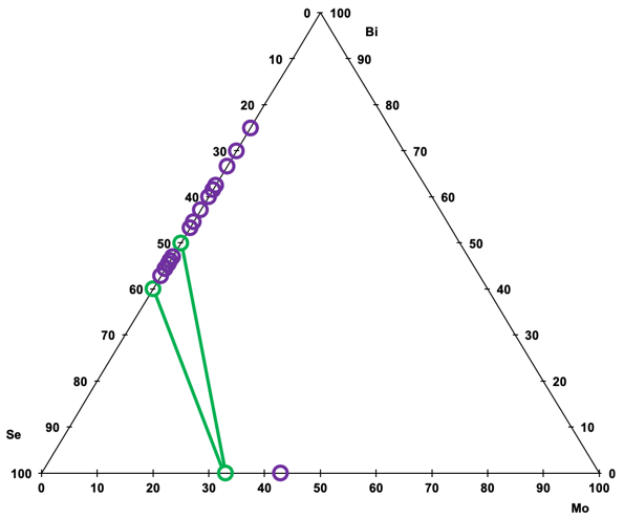

Figure 1.4. Ternary phase diagram for Bi-Mo-Se system with tie lines drawn from Bi_2Se_3 and BiSe to $MoSe_2$. Thermodynamic binary compounds are marked in purple.

1.4). Due to the oxidation state of Bi, the kinetic, rock-salt BiSe structure stabilizes its formation one of two ways: by localizing the charge through the formation of Bi-Bi bonds (Bi^0) or through the electron donation to the neighboring layer (Bi^{3+}).[85-88] Rock-salt BiSe can therefore only form when paired with an electron acceptor.[86-92] In chapter 4, I detail my exploration of the formation of the Bi-Se layer based on the electrical properties of the neighboring layer. I determined precursors with metallic layers would segregate to form $[(BiSe)_{1+\gamma}]_1[(MSe_2)]_1$ and Bi_2Se_3 while precursors with semiconducting layers would form $[(Bi_2Se_3)_{1+\delta}]_1[(MSe_n)]_1$. If there is competition between two polytypes with different electrical properties, adjusting the composition will influence the formation of the final product. Understanding how the electrical properties and composition affected the formation of the Bi-Mo-Se heterostructures was vital to exploring the composition space between the Bi_2Se_3-$MoSe_2$ and BiSe-$MoSe_2$ tie lines.[93]

As the synthesis of Bi_2Se_3-$MoSe_2$ containing heterostructures is

more complicated than originally anticipated, I focused the remainder of my dissertation on preliminary investigations in the composition space between the Bi_2Se_3-$MoSe_2$ and BiSe-$MoSe_2$ tie lines. The kinetic products discussed in this dissertation are marked on the ternary phase diagram for the BiSe-$MoSe_2$-Bi_2Se_3 system and the composition

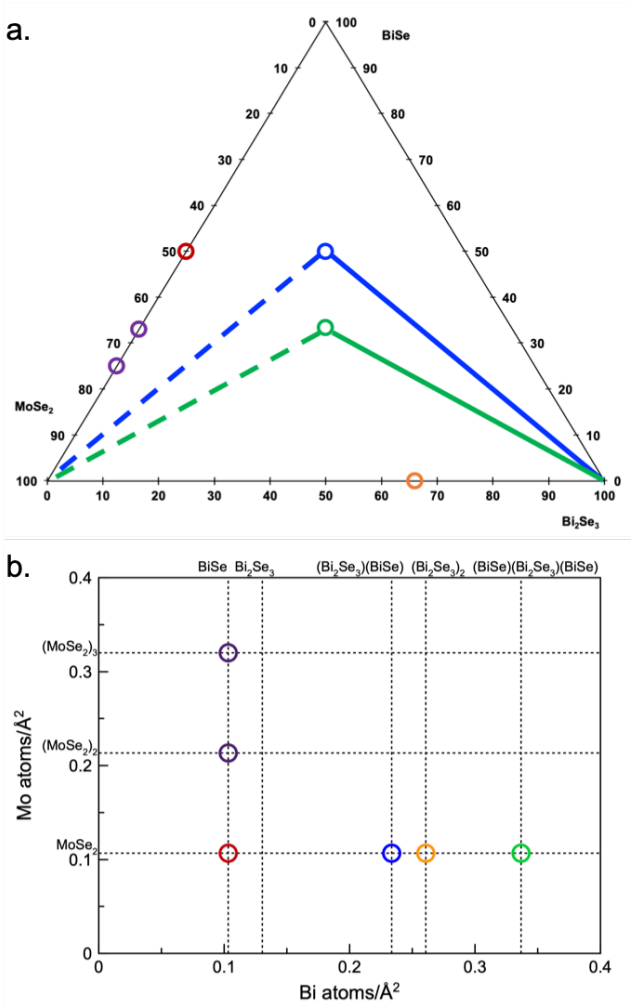

Figure 1.5. (a) Ternary phase diagram for BiSe-$MoSe_2$-Bi_2Se_3 system with the heterostructures reported here in marked with circles. Tie lines are drawn between mixed heterostructures to illustrate other heterostructures that can be synthesized with solid (increasing the Bi_2Se_3 layers) and dashed (increasing the $MoSe_2$ layers) lines. (b) Composition space of the heterostructures based on estimated amounts of Mo and Bi necessary for formation of the heterostructures.

space in terms of Bi and Mo (Figure #). The red dot marks the only previously synthesized BiSe-$MoSe_2$ heterostructure: $(BiSe)_{0.97}(MoSe_2)_1$.[94] Hadland et al. observed that BiSe acted as an electron donor, resulting in ~40% of the $MoSe_2$ was the kinetic 1T metallic polytype. In order to further explore the charge transfer from BiSe to $MoSe_2$, I first synthesized a $(BiSe)_{1+x}(Bi_2Se_3)_{1+y}(BiSe)_{1+x}(MoSe_2)$ (blue dot) heterostructure. Bi_2Se_3 was used as a buffer layer between the BiSe layers as multiple BiSe layers will not form next to each other.[95] An isostructural compound had previously been reported, indicating the $MoSe_2$ containing heterostructure would be possible.[96] There were unexpected competing reaction pathways between the desired structure and $[(Bi_2Se_3)_{1+y}]_2(MoSe_2)$ (orange dot), which indicated their local free energy minima are close in energy. As observed in Figure #b, the compositions for $(BiSe)_{1+x}(Bi_2Se_3)_{1+y}(BiSe)_{1+x}(MoSe_2)$, $[(Bi_2Se_3)_{1+y}]_2(MoSe_2)$, and $(Bi_2Se_3)_{1+y}(BiSe)_{1+x}(MoSe_2)$ are all very close together. Control over the composition of the precursor is vital for the synthesis of the intended product. With two BiSe layers next to the $MoSe_2$ layer, an increased amount of 1T-$MoSe_2$ (~60%) and metallic temperature dependent resistivity was observed.[97]

I then varied the structure to synthesize $(Bi_2Se_3)_{1+y}(BiSe)_{1+x}(MoSe_2)$ (green dot) to further probe the structure-property relationship. Because of the layering of the heterostructure, the BiSe layer transfers its electron to one of two layers in the $(BiSe)_{0.97}(MoSe_2)_1$. Bi_2Se_3 was expected to act as a buffer between the BiSe-$MoSe_2$ pair, meaning the change transfer would occur to one $MoSe_2$ layer. I expected a slight increase in the amount of 1T-$MoSe_2$ in this heterostructure as BiSe would donate its electron to a single layer of $MoSe_2$ instead of two in the $(BiSe)_{0.97}(MoSe_2)_1$. Instead, there was no 1T-$MoSe_2$ observed *via* X-ray photoelectron spectroscopy (XPS). Bi_2Se_3 is a small gap semiconductor and may be able to accept the electrons

from BiSe.[98] Both the nanoarchitecture of this and the previous structure can be varied by increasing the number of layers of Bi_2Se_3 or $MoSe_2$ to further probe the interactions between layers and structure, as illustrated by the tie lines in Figure 1.5a.

In collaboration with Fabian Göhler, these heterostructures were explored via XPS to probe the stabilization of the metastable layers. We determined BiSe stabilized in one of two ways in both heterostructures: transfer an electron to the $MoSe_2$ and/or Bi_2Se_3 layer or localize the charge in the antiphase boundaries. However, simple rigid band gap models may not be adequate to describe these heterostructures.[99]

Three of the heterostructures ($[(BiSe)_{1+x}(MoSe_2)_n]$) probed in the previously discussed paper sparked an interesting discussion of the structure of the BiSe layer. The $(BiSe)_{1+x}(MoSe_2)_n$ family of heterostructures, where n = 1, 2, and 3, were synthesized to probe this structure-property relationship of one BiSe layer with multiple $MoSe_2$ layers before further complicating the structure to follow the dashed tie lines on Figure 1.5a. There was a discrepancy in the previous literature about the BiSe structure when layered with different dichalcogenide neighboring layers. When layered with one layer of either $TiSe_2$ or $NbSe_2$, the BiSe basal plane observed was rectangular. However, when layered with more than one layer, the basal plane appeared to depend on the transition metal. The basal plane for $(BiSe)_{1+x}(TiSe_2)_n$ heterostructures was rectangular but basal plane changed for the $(BiSe)_{1+x}(NbSe_2)_n$ heterostructures to a square.[100-102] Variations in the BiSe structure were never seen in the same heterostructure until I synthesized two samples with similar *c*-axis lattice parameters consistent with $(BiSe)_{1+x}(MoSe_2)_3$ but different BiSe basal planes. The major difference in the samples was the starting compositions, which may have played a role in the formation of different basal planes. The formation reaction of these samples could provide information on how

to best control the synthesis of designed compounds.

Based on the previous exploration, I was able to synthesize the $(BiSe)_{1+x}(MoSe_2)_n$ family of heterostructures, where n = 1, 2, and 3, with rectangular basal planes to further explore the changes in electrical properties as a function of nanoarchitecture. $(BiSe)_{1+x}(MoSe_2)_3$ shows increased resistivity compared to $(BiSe)_{0.97}(MoSe_2)_1$, which may indicate no networks of 1T-$MoSe_2$ have formed as a result of the charge transfer.

1.5. Dissertation Overview

The different chapters of the following dissertation highlight the design, formation, and electrical properties of several different materials. Section I contains Chapters I and II, which consists of an overview of the broad interests in these heterostructures and the methods used in the subsequent chapters to characterize the materials. Chapter II briefly discusses the process control and development of new standard operating procedures for the deposition chamber necessary to increase the yield of on target heterostructures.

Chapter III was published in *Zeitschrift für anorganische und allgemeine Chemie* in 2018. I am the primary author of the manuscript. I assisted with writing/editing the manuscript and collecting/analyzing the diffraction data. Co-authors include Danielle M. Hamann, Jordan A. Joke, Dmitri Leo M. Cordova, and David C. Johnson. Danielle M. Hamann was my mentor on this project and helped analyze the data and edited the manuscript. David C. Johnson is my advisor and edited the manuscript. A previously unreported Mn-Se product was observed.

Chapter IV was published in *Inorganic Chemistry* in 2021, focusing on the substituent effects of Bi-Se precursors when layered with neighboring layers with different electrical properties. I am the primary author of the manuscript. I wrote and edited the manuscript and collected and analyzed the diffraction data. Co-authors include

Taryn M. Kam and David C. Johnson. Taryn M. Kam assisted in collecting and analyzing the diffraction data while David C. Johnson is my advisor and edited the manuscript.

The next section, which includes Chapters V – VIII, focuses on the synthesis of BiSe-Bi_2Se_3-$MoSe_2$ containing heterostructures. Chapter V was published in *Chemistry of Materials* in 2021 on the synthesis and electrical properties of $(BiSe)_{0.97}(Bi_2Se_3)_{1.26}(BiSe)_{0.97}(MoSe_2)$. I am the primary author of this manuscript, made the heterostructures, collected and analyzed the diffraction data, and analyzed the electrical data. The co-authors include Renae N. Gannon, Fabian Göhler, Aaron M. Miller, Douglas L. Medlin, Thomas Seyller, and David C. Johnson. Renae N. Gannon and Douglas L. Medlin collected and analyzed the electron microscopy data and edited the manuscript. Fabian Göhler and Thomas Seyller collected and analyzed the XPS data. Aaron M. Miller collected the electrical measurements. David C. Johnson is my advisor and edited the manuscript. Chapter VI is unpublished work on $(Bi_2Se_3)_{1.26}(BiSe)_{0.97}(MoSe_2)$. I primarily wrote the manuscript with my advisor David C. Johnson, and I collected and analyzed the diffraction and electrical data. Fabian Göhler and Thomas Seyller collected and analyzed the XPS data. Chapter VII was published in *The Journal of Physical Chemistry C* in 2021. I am the second author on the manuscript, synthesized the samples, collected and analyzed the diffraction data, and wrote the accompanying paragraphs in the manuscript. Fabian Göhler is the primary author and wrote a majority of the manuscript. Co-authors include Constance Schmidt, Dietrich R. T. Zahn, David C. Johnson, and Thomas Seyller.

The final section, which includes Chapters VIII - IX, explores the variations observed in the BiSe basal plane depending on composition of the precursor. All of the following chapters contain unpublished work

in collaboration with a variety of collaborators. Chapter VIII explores the change in basal plane structure in a Bi-containing layer a sample targeting the same nanoarchitecture but with different compositions. I primarily wrote the manuscript with my advisor David C. Johnson and collected/analyzed the diffraction. Aaron Miller collected the electrical data. Fabian Göhler and Thomas Seyller collected and analyzed the XPS data. Chapter IX focuses on the $(BiSe)_1(MoSe_2)_n$ family of heterostructures, where n = 1, 2, and 3, with the rectangular basal plane. I primarily wrote the manuscript with my advisor David C. Johnson and collected/analyzed the diffraction and electrical data. STEM images were collected and analyzed by Renae N. Gannon and Ping Lu. Aaron Miller assisted in the collection and analysis of the electrical data.

1.6. Bridge

Chapter I contains an unpublished overview of the dissertation written primarily by myself and edited by my advisor David C. Johnson. The next chapter focuses on the experimental methods used to explore the structure, reaction mechanisms, and properties of the samples discussed within the dissertation.

CHAPTER II

EXPERIMENTAL PROCEDURES

2.0. Authorship Statement

This work was written by me for this work alone with assistance from my advisor David C. Johnson.

2.1. Synthesis of Layered Precursors with Modulated Elemental Reactants

The background description of MER precursors was previously described in detail in Chapter 1 Section 1.3. The precursors are deposited at pressures below 5×10^{-7} torr in a designed way $[(M|Se)_m|(N|Se)_n]$ to mimic the nanoarchitecture of the desired heterostructures. The layer sequence is repeated to make films with a desired total thickness, typically ~30 nm in the samples made in the following chapters. Metals were deposited using an electron beam gun and selenium was deposited using a Knudson effusion cell. The substrate was typically either a Si wafer with a native oxide layer or a fused quartz substrate. Pneumatic shutters were controlled with quartz crystal monitors for the individual elements using an Inficon IC6 Deposition Controller. The deposition controller monitored the rate of the elements and the thickness deposited to close the shutters once the desired amounts of material were deposited. The amount of material desired was inputted as a unit of thickness, however, it is only proportional to the actual thickness. For this reason, it is referred to in the following chapters as a "fake-Angstrom" (fÅ).

2.2. X-ray Fluorescence and Statistical Process Control

As composition and layer thickness are key experimental parameters controlling the nucleation of kinetic heterostructures, measuring the exact amount of material within a precursor is critically important for vapor deposition techniques. Rutherford backscattering, electron probe micro-analysis, particle-induced X-ray emission, X-ray

photoelectron spectroscopy, time-of-flight secondary ion mass spectrometry, and a variety of electron microscopy techniques have all been previously used to measure composition.[1-4] However, there are a number of limitations associated with each, including expense, extensive sample preparation, and sensitivity. Recently it was shown that x-ray fluorescence (XRF) can be used to relate the intensity measured in the experiment to the absolute amounts of each element within the sample quickly, cheaply, and nondestructively.[5] XRF intensities for the heterostructures discussed here in were collected with a Rigaku ZSX Primus-II with a rhodium X-ray tube. The ability to

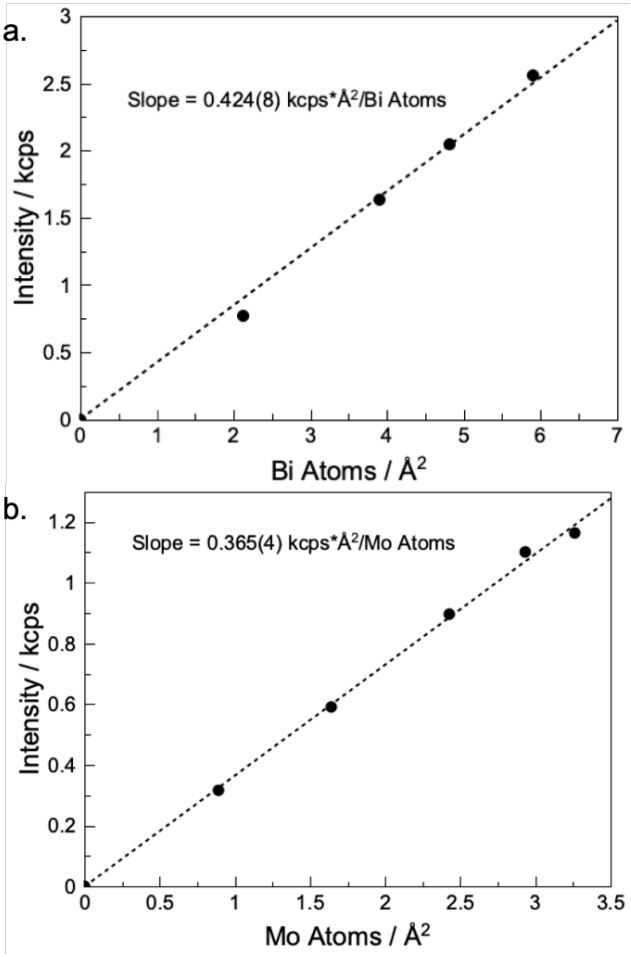

Figure 2.1. Graphs of the XRF intensity vs the number of atoms per unit area for (a) Bi and (b) Mo determined from binary samples.

monitor the amount of each element with XRF is ideal for the synthesis of kinetic products and calibrating depositions.

XRF measurements were taken after every deposition for comparison to the estimated values for the designed heterostructure and process control. The calibration curves (Figure 2.1) were used to determine the amount of material in a sample from the measured XRF intensities for the individual elements.[5] The amounts were then compared with the estimated values for each constituent calculated from of the lattice parameters and unit cells of the bulk constituents (Bi_2Se_3, $MoSe_2$, etc.). The magnitude of the differences between the estimated and measured amounts of each element were used to determine the viability of the formation of the targeted heterostructure. The number of layers of the targeted compound could be calculated from the limiting element. The XRF intensities were also used to correlate the amount of material deposited in the sample with the thickness of each element inputted to the Inficon deposition controller. Dividing the XRF intensity by the total number of fÅ inputted to the deposition controller for each element is referred to as the normalized

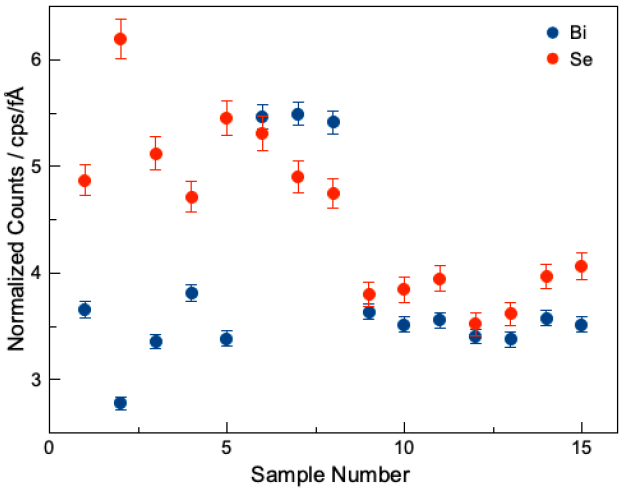

Figure 2.2. Graph of the normalized counts of Bi (blue) and Se (orange) plotted as a function of sample number in a single chamber cycle.

counts (cps/fÅ). The normalized counts for each element were used to monitor the consistency of the deposition.

Large fluctuations in the normalized counts of many elements were observed once the measured amounts of material were correlated with the thickness provided to the deposition controller. Variations as large as 21% and 17% were noted for Bi and Se, respectively (see figure 2.2). In the first few samples, it was noted that when less Bi was deposited on the sample, more Se than expected was deposited. These large variations required me and other group members to make quite a few samples before obtaining a precursor that had close to the targeted amounts of each element. Decreasing the variation would dramatically increase yield of precursors that had the targeted amounts of each element.

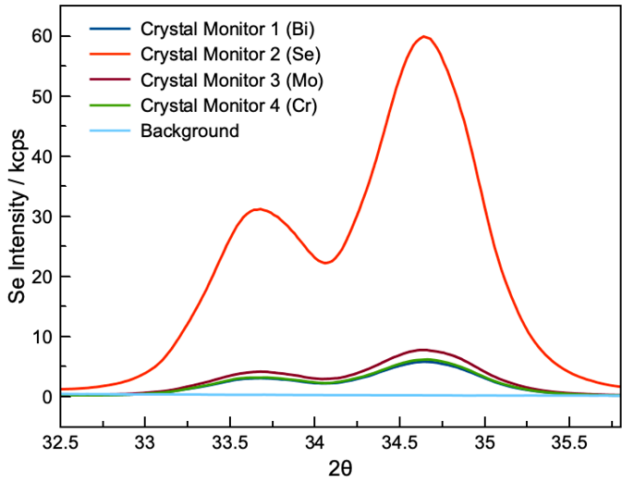

Figure 2.3. XRF Se intensities measured on the quartz crystals monitoring four different elements.

I proposed that the cause of the variation in normalized counts resulted from a variation in Se partial pressure in the chamber as the chamber temperature changes during the deposition of sequential precursors. If true, then varying amounts of Se would be depositing on all of the quartz crystal monitors depending on the partial pressure,

leading the deposition controller to believe more of the metal was deposited than actually was. The Se atmosphere would also account for more Se deposited in the samples than expected. To test this hypothesis, I measured the Se amounts of material on the quartz crystal monitors (Figure 2.3). As Se was deposited on Crystal Monitor 2, a large intensity is expected. If there was not a Se atmosphere, then the Se intensity should be consistent with the background on the other three crystals. The significant Se intensity observed on Crystal Monitors 1, 3, and 4, where Bi, Mo, and Cr were deposited, respectively, were evidence of significant cross talk between the Se and the other elements.

In order to decrease the deposition errors, I proposed a "bake-out" where the chamber was heated to promote Se vaporization off the walls of the chamber. The Se should condense in places that would not heat up during a normal deposition, such as the cryo cold head and the top walls of the chamber. Two high melting sources (Mo, 2623 ^{o}C) were placed in two of the e-beam guns and a getter source (Ti)[6] was placed in the final e-beam gun. We proposed the two Mo sources would act as heat sources in the chamber prompting the Se to vaporize and react with the Ti or condense on the colder parts of the chamber. The Se cell remained in its home position but not heated, and its thermocouples were used to monitor the temperature of the deposition chamber.

Information on the temperature, pressure, e-beam gun powers, and rates were collected as a function of time during the "bake-out" to monitor for the presence of a Se atmosphere (Figure 2.4). We observed a steady increase in the temperature of the Se cell throughout the experiment. After depositing for ~ 30 minutes, a small rate of 0.01 Å/s was observed on Crystal Monitor 2. As the Se cell was not turned on, the measured rate on Crystal Monitor 2 resulted from the increasing Se partial pressure as the chamber temperature increased. Between 30-

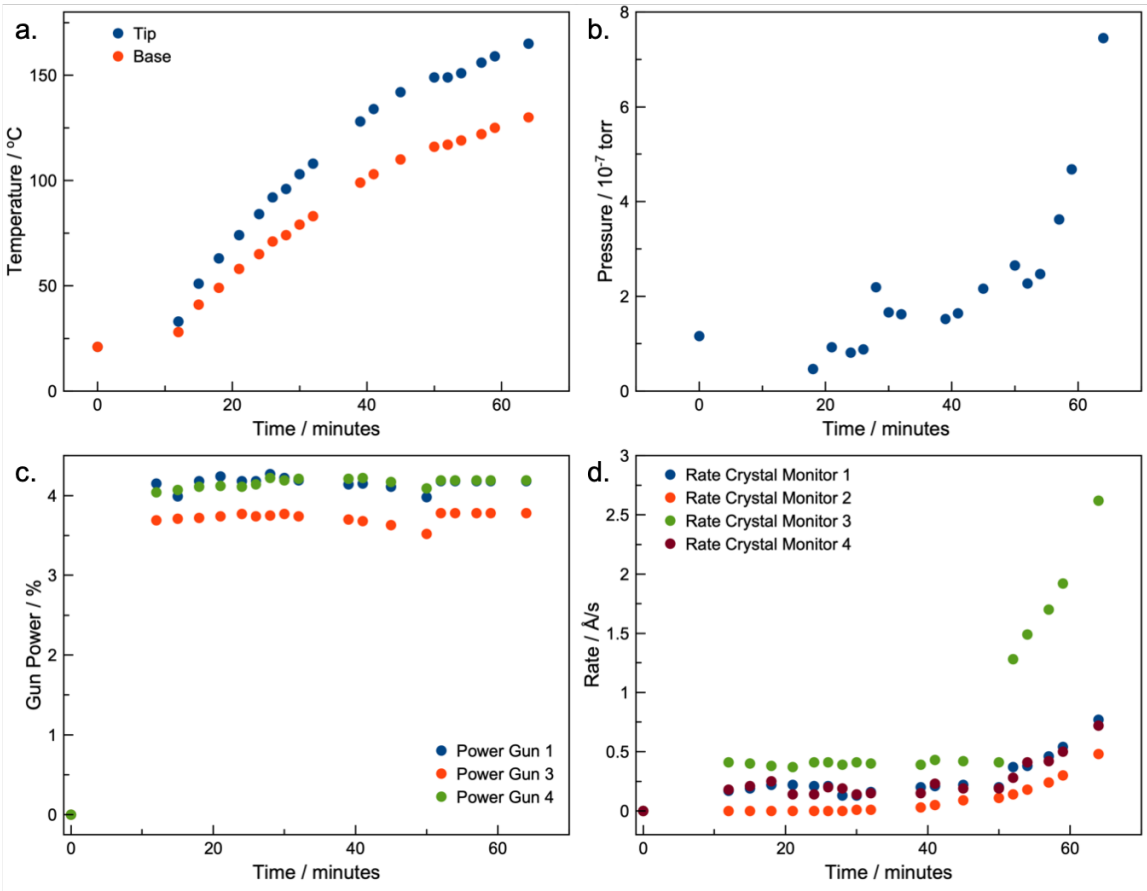

Figure 2.4. (a) Temperature, (b) Pressure, (c) e-beam gun power, and (d) rate collected during the "bake-out"

50 minutes, significant changes to the pressure, rates, and gun powers indicated an increase in the Se partial pressure. The pressure increased by 46% and the rate of Crystal Monitor 2 continued to increase. The powers of the three e-beam guns, which were controlled by the computer to maintain a constant rate, decreased between 3-7% while their rates stayed the same.Using less power to maintain the same rate indicated that the Se was also depositing on the quartz crystal monitors of the other metals. Approximately 52 minutes into the experiment, the e-beam gun powers were removed from computer control and set to a constant power to maintain deposition. The pressure and the rates observed on all of the quartz crystal monitors continued to increase as the system heated.

Based on this experiment there are three major indicators that a Se atmosphere is present in the deposition chamber:

1) increases in pressure

2) increases in rate on quartz crystals above sources that are not being heated

3) decreases in power when maintaining a set rate

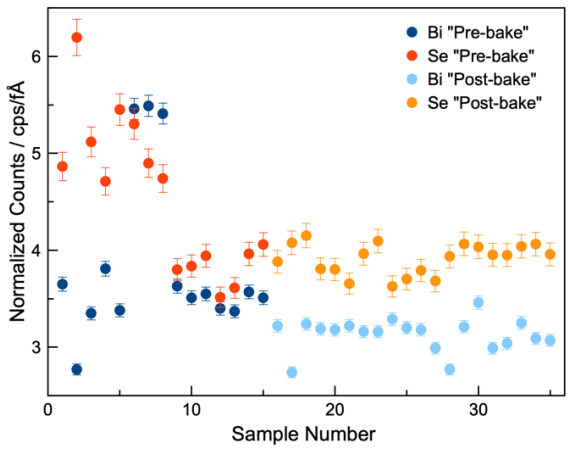

Figure 2.5. Graph of the normalized counts of Bi (blue) and Se (orange) plotted as a function of sample number pre- and post-bake-out for comparison.

Figure 2.5 reports the normalized counts for Bi and Se recorded for two chamber cycles: one pre-bake-out and one post-bake-out. There is a distinct difference in the pre- and post-bake-out normalized counts for both elements. Before implementing the bake-out, the variation in the normalized counts for Bi and Se were 21% and 17%, respectively. After implementing the bake-out, the variation in the normalized counts for Bi and Se reduced to 5% and 4%, respectively. This drastic reduction in deposition error for these two elements indicates that changes in the Se partial pressure in the chamber was a major source of error. Frequently heating the deposition chamber can reduce the background Se partial pressure, minimizing the variation in the amount of each element deposited. This greatly increases the number of prepared

precursors where the amount of each element is within several percent of the targeted values.

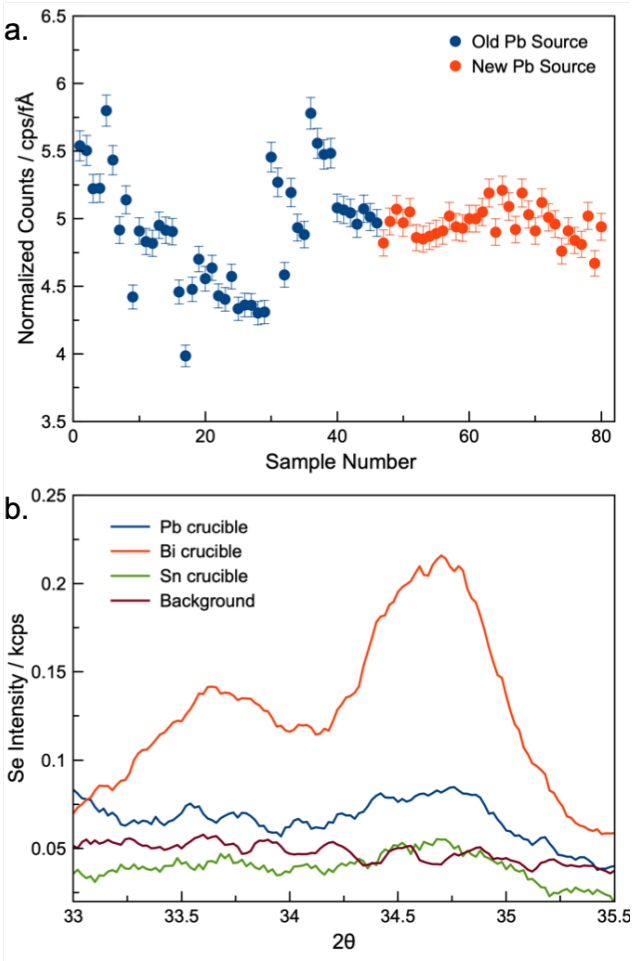

Figure 2.6. (a) Pb normalized counts distinguished by chamber cycle and (b) Se XRF intensity for three different crucibles.

The Se further complicated the deposition error as the Se condensed on and reacted with several of the sources (Figure 2.6). Linear decreases were observed in the Pb normalized counts that continued even after the chamber was baked out (Figure 2.6a). The normalized counts would fluctuate in the middle of a chamber cycle, resulting in a variation of ~11% in the amount of Pb deposited relative to the targeted value. We hypothesized that the Se atmosphere may react with the sources themselves and react to form a M_xSe_y source.

Using XRF, we determined there were Se impurities in low deposition temperature sources such as Sn, Bi, and Pb, which may have resulted in the uncontrollable and unpredictable linear decrease (Figure 2.6b). When a new Pb sources were used for the last two chamber cycles, the variation in the normalized counts was reduced to ~4%. New sources for the low melting point elements are necessary at the beginning of every chamber cycle in order to maintain a consistent deposition.

2.3. Structural Characterization Techniques

X-ray reflectivity (XRR) and specular and in-plane X-ray diffraction (XRD) are ideal techniques to monitor interdiffusion and nucleation and determine lattice parameters for MER precursors. In general, XRD depends on an incident X-ray of some wavelength (λ) diffracting off of planes of atoms some distance (d) apart at some incident angle (θ). This is the basis of Bragg's Law: $n\lambda = 2d \sin(\theta)$.[7] Different geometries are used to access various information. XRR and specular XRD were collected using a θ/2θ coupled geometry to probe the surface of the film and determine the total thickness, repeat thickness, smoothness, and number of layers. XRR is information collected at low angles resulting from reflection and refraction of the beam off of the top and bottom of the film. Total thickness was calculated using modified Braggs law and the spacing between the Kiessig fringes.[8] Repeating thicknesses was determined by the spacing of the Bragg reflections in the XRD patterns. Evenly spaced reflections indicated the Bragg maxima belonged to a single family of reflections (00*l*). Consistency between the experimental and estimated *c*-axis lattice parameters are a good indication that the designed heterostructure has formed. XRR and specular XRD were collected on a Bruker D8 Discover diffractometer using Cu-K_α radiation. Grazing incidence XRD was collected several randomly oriented samples and resulted in mixed reflections. Grazing incidence in-plane XRD was

collected to probe the ab plane of atoms and provides information about the *a*- and *b*-axis lattice parameters. Based on this, we can determine the individual constituents in the heterostructure. Grazing incidence and grazing incidence in-plane XRD information was collected using a Rigaku SmartLab with a Cu source.

High-Angle Annular Dark Field-Scanning Transmission Electron Microscopy (HAADF-STEM) and Energy Dispersive X-ray Spectroscopy (EDS) were used to probe the local composition and structure of the heterostructures to confirm the hypotheses made based on the diffraction data. Before measurements can be taken, a small cross-section of the film is milled as a representative piece of the sample. For HAADF-STEM images, an electron is then accelerated through the sample and moved across the entire cross section. The electrons scatter across the surface from the nucleus of the atom and are collected by the detector. Because the scattering is atom dependent, the intensity of the images depends on the atomic number, where atoms with high atomic appear the brightest.[9] EDS is similar to XRF in that and electron beam, instead of an x-ray, excites a core shell electron from the atom and the unique atomic structure of each atom allows for the distinction of atoms. It is useful for determining the position of the atoms within the heterostructure and observing reactions at the bottom and top of the sample.[10]

2.4. Electrical Characterization Techniques

X-ray photoelectron spectroscopy (XPS) measurements were performed by a collaborator, Fabian Göhler, to probe the binding energies of the elements. XPS is a surface sensitive technique that depends on the photoelectric effect to identify the elements within a material and their chemical states. A focused x-ray of some known wavelength (λ) hits the surface of the sample prompting electrons to emit. The electrons' kinetic energy is measured and can be used to

determine the energy of binding of the measured electron. The peaks on the spectrum, therefore, correspond to a specific electron shell and can be used as a fingerprint technique.[11-12] XPS was used to determine the oxidation states of Bi, Mo, and Se in the Bi-Mo-Se heterostructures described here in.

Hall and resistivity measurements were performed on a custom-built system. A closed cycle He crysostat was used to modulate the temperature between 30-300 K. Measurements were made on samples deposited on quartz, shadowed to form a van der Pauw cross,[13] using a LABVIEW program to collect and control the temperature, voltage, current, and magnetic field.

2.5. Bridge

Chapter II focused on the general overview of the synthesis and characterization methods used within this dissertation to make the discussed heterostructures and explore their formation and properties. Significant attention was paid to the process control of the synthesis method, which revolutionized how we make samples using the described method. This chapter contains unpublished work written by myself and edited my advisor. The next chapter utilized this synthesis method to explore the formation of binary compounds and probe for kinetic products.

CHAPTER III

THE REACTION BETWEEN MN AND SE LAYERS

3.0. Authorship Statement

Chapter III was published in *Zeitschrift für anorganische und allgemeine Chemie* in 2018. Co-authors include Danielle M. Hamann, who acted as my mentor on the project, Jordan A. Joke, who performed several preliminary experiments, and Dmitri Leo M. Cordova. David C. Johnson is my adviser and I am the primary author of the manuscript.

3.1. Introduction

In general, the formation of crystalline solids from the elements or via the reaction between compounds is not well understood.[1–3] While there is a consensus that interdiffusion, nucleation, and growth are key parts of the formation process, there is little understanding of how these fundamental reaction steps can be controlled with experimental parameters. This knowledge is crucial for planning a directed synthesis.[4] A promising approach to investigate the formation mechanism of crystalline solids is based on using precursors containing alternating layers of the elements.[5] An advantage of this approach, called modulated elemental reactants [6] or nanoalloying [7] is the ability to form a homogenous, amorphous intermediate.[8] Synthetically accessible metastable compounds need to be more stable than an amorphous intermediate of the same composition.[9] Fortunately, the composition of amorphous intermediates can be systematically controlled to influence which compounds nucleate first.[10–12] This has enabled the synthesis of a number of metastable compounds.[13]

The Mn-Se system has been the subject of multiple recent investigations using epitaxial growth techniques[14–16] and solution phase synthesis approaches,[14,15,17–21] which were driven by the desire

to make discrete magnetic layers, magnetic nanoparticles, or diluted magnetic semiconductors.[22–24] Only two thermodynamically stable compounds are known in the Mn-Se system. Both can be prepared using traditional high temperature reactions of the elements.[25,26] The monoselenide, α-MnSe, has a sodium chloride crystal structure and the diselenide, $MnSe_2$, has a cubic pyrite structure. In both compounds Mn is octahedrally coordinated by Se. In α-MnSe, Se is octahedrally coordinated by Mn. In $MnSe_2$, there are discrete Se_2 dimers, and the Se is tetrahedrally coordinated by one Se atom and three Mn atoms. These structures are closely related. Replacing the Se dimers in the pyrite by Se atoms at the center of mass of the Se dimers results in the rock salt structure. In addition to the two thermodynamically stable compounds, two metastable MnSe polymorphs (β-MnSe and γ-MnSe) have been reported to form as nanocrystals from solutions.[27,28]

The purpose of the present investigation is to study the formation mechanisms of MnSe and $MnSe_2$ from multilayered Mn-Se precursors where the ratio of the elements and the total amount of elements per repeating layer were varied to determine parameters required to form amorphous reaction intermediates and to discover if any metastable compounds nucleate at low reaction temperatures. A number of films with different ratios of Mn and Se were prepared with two bilayer thicknesses. Alternating layers of Mn and Se were deposited to obtain the four target compositions and different bilayer thicknesses. The bilayers were repeated multiple times to increase the sample volume. The evolution of the films as a function of temperature was followed using X-ray diffraction. The sequence of phase formation changed with both composition and bilayer thickness. MnSe formed from films that were close to a one to one ratio of Se and Mn during the deposition. For compositions containing ~60% Se, an amorphous intermediate formed and the first compound crystalized depended on bilayer thickness.

MnSe formed first in the film with thin bilayers while a mixture of $MnSe_2$ and MnSe formed in the film with thicker bilayers. Both the thin and thicker bilayer films with a 1:2 ratio of Mn to Se were amorphous as deposited and the first crystalline compound formed was $MnSe_2$ from both precursors. Both of the films with initial compositions of ~80% Se formed a new metastable compound whose diffraction pattern was consistent with a monoclinic unit cell. These results show that amorphous intermediates can be formed from precursors with thin bilayer thicknesses and that both the composition and the bilayer thickness influence which compound nucleates first.

3.2. Experimental

The precursors were synthesized using a vacuum depositions chamber operating at pressures below 5×10^{-7} Torr. Manganese was deposited using an electron beam gun and selenium was deposited using a Knudson effusion cell. All films were deposited on silicon wafers with a native oxide layer. Deposition was controlled using quartz crystal microbalances (QCM) to monitor the rate of deposition and the amount of material deposited in each layer. Different amounts of manganese and selenium were deposited for each precursor in order to target four different compositions. For each of the compositions investigated, precursors with two different bilayer thicknesses were prepared. Twenty-four bilayers were deposited in each precursor.

The samples were annealed at each temperature for 30 minutes on a hot plate in a nitrogen atmosphere with an oxygen pressure of less than 1 ppm. The initial annealing temperature was 50°C and the annealing temperatures were increased in steps of 50°C. X-ray reflectivity, X-ray fluorescence and grazing incidence x-ray diffraction scans were collected after each annealing step. X-ray reflectivity was collected using a Burker D8 Discover diffractometer using Cu-Kα radiation. Grazing incidence x-ray diffraction (XRD) scans were

collected on a Rigaku SmartLab with a Cu source. X-ray fluorescence data was collected on a Rigaku ZSX Primus-II with a rhodium X-ray tube.

Calibration samples containing Mn and Se were annealed in a selenium atmosphere, forcing the formation of pure $MnSe_2$ films as confirmed by diffraction scans. The X-ray fluorescence intensity of both Mn and Se were measured. Since the proportionality factor between Se intensity and the number of Se atoms per unit area was known from an earlier study,[29] we could calculate the number of Se atoms per unit area in each sample. The number of manganese atoms/ unit area in each sample was calculated from this using the stoichiometric ratio between manganese and selenium. The linear relationship between XRF intensity and atoms per unit area for both Mn and Se were used to determine the composition of the films in this study.

3.3. Results and Discussion

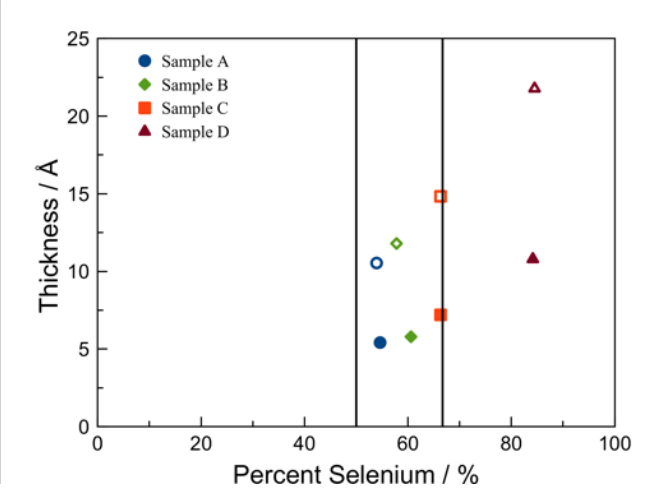

Figure 3.1. Summary of the composition and thickness of the prepared precursors.

A number of precursor films were prepared with systematic changes in composition and layer thickness to probe how the reaction mechanism varies as a function of these experimental parameters. One

set of precursors was prepared where the bilayer Mn|Se thicknesses were on the order of that require to form a single unit cell of MnSe or $MnSe_2$. Four films (A1-D1) were made with compositions shown in Figure 3.1. A second set of four precursors (A2-D2) was prepared with bilayer thicknesses approximately twice that of the precursors A1-D1 with similar compositions (see Figure 3.1). X-ray reflectivity scans of the as deposited samples contained only a few Kiessig fringes. While there were enough Kiessig fringes to determine the film thickness, the termination of fringes at 2.5 to 6.5 degrees indicates a surface roughness of ~ 20 Å calculated using the approach of Parratt.[30]

The grazing incidence diffraction patterns of the as deposited precursors are shown in Figure 3.2. The diffraction patterns of the two samples with a starting composition of ~ 54 % selenium, A1 and A2, indicated that both crystalized α-MnSe during the deposition. Distinct reflections at 32.9 and 47.2 degrees from the (200) and (220) reflections and a weak reflection at 58.7 degrees from the (222) reflection are apparent in the scans. The vertical dashed lines in Figure 3.2 indicate the locations of these reflections for α-MnSe. In addition to the α-MnSe reflections, there is a broad maximum centered at ~55 degrees with a sharp maximum at 54 degrees that are assigned to a surface component, as these features are not apparent in specular diffraction scans. We suspect that this feature is due to a surface oxide from the magnitude of the intensity of the oxygen signal in the XRF data. This surface component is present in all of the as deposited samples. The rest of the samples, all more Se rich than A1 and A2, have much broader and weaker maxima in the as deposited scans, suggesting that they may be amorphous as deposited. The broad maximum at ~32 degrees shifts to a lower angle as the samples become more Se rich.

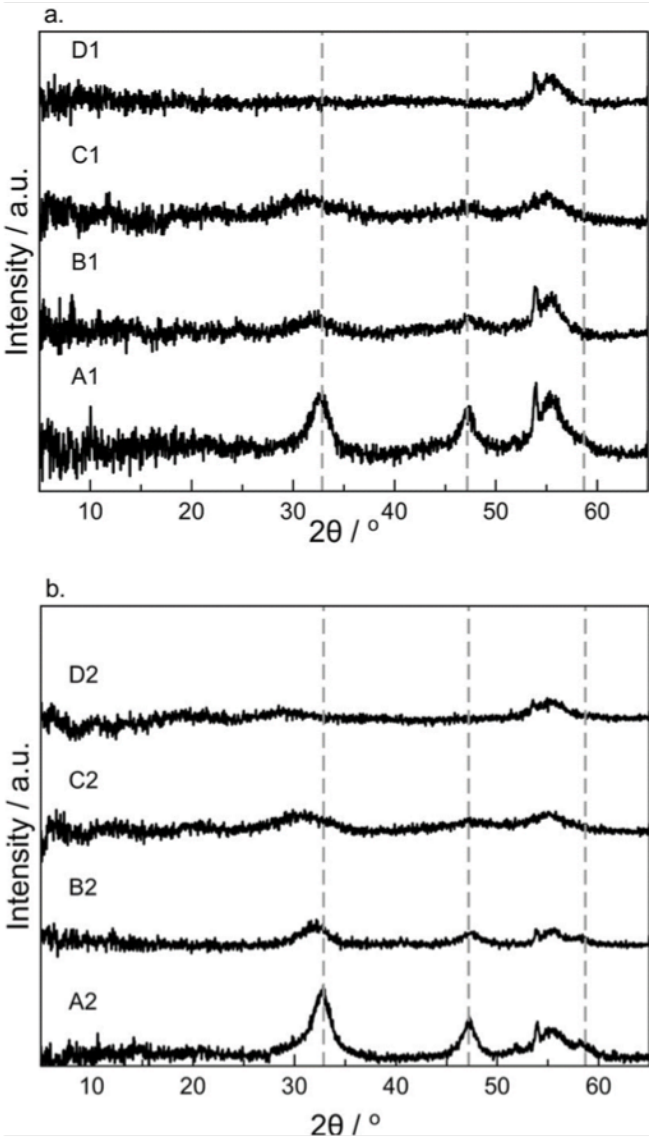

Figure 3.2. Grazing incidence diffraction scans of the eight precursors before any annealing (a. films A1-D1 and b. films A2-D2). The dashed vertical lines at 32.9, 47.2, and 58.7° mark the locations of the (200), (220), and (222) reflections of the α-MnSe.

Even for the B samples this maximum is at an angle lower than that expected for the (200) reflection of α-MnSe.

All of the samples were annealed at sequentially higher temperatures to follow the evolution of the films. Diffraction patterns and x-ray fluorescence (XRF) data were obtained after each annealing

temperature. The XRF data for samples A1 and A2 showed that the initial films were 54% Se and 46% Mn. The Se content of the films decreased due to sublimation of Se between 100 and 250°C. The composition of the films remained approximately constant between 250 and 400°C, slightly Mn rich relative to the stoichiometry of MnSe. This

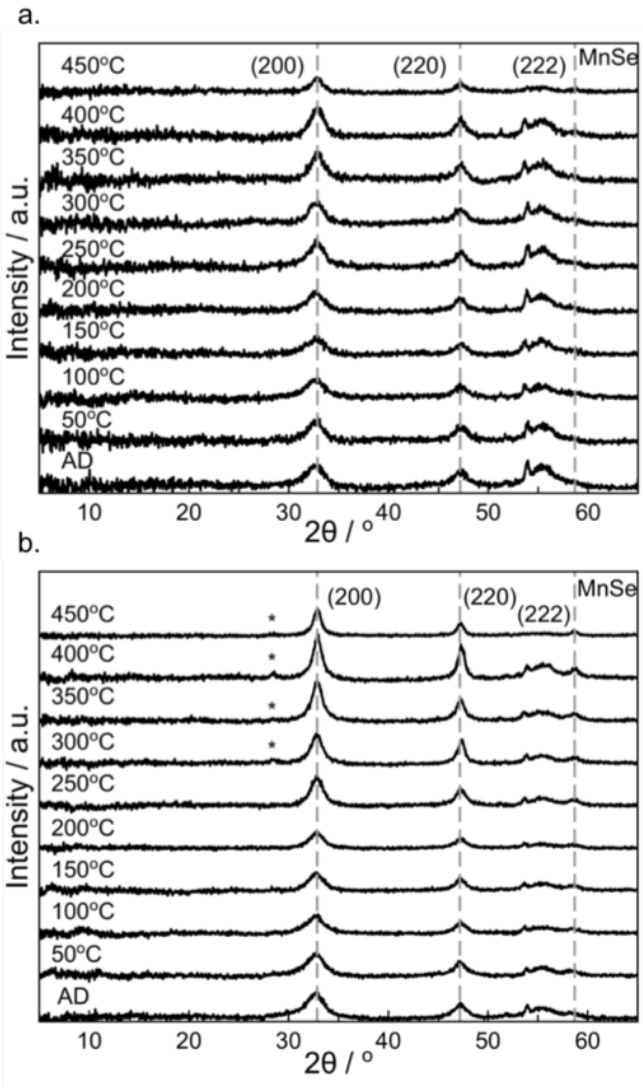

Figure 3.3. Grazing incidence diffraction scans collected for samples A1(a) and A2(b) as a function of annealing temperature. The (111) reflection of α-MnSe has been marked by an asterisk.

difference is presumably due to the presence of a Mn oxide on the surface of the samples. Both samples showed increasing oxygen content and decreased Se content after annealing at 450°C. Figure 3.3 contains the diffraction patterns collected during the annealing study for samples A1 and A2. For both the A1 and A2 sample, the reflections of MnSe in the as deposited films sharpen and increase in intensity as the annealing temperature is increased. In sample A2, the weak (111) reflection of MnSe becomes visible after annealing at 300°C, reflecting the increasing crystallinity of the samples. There is a decrease in the intensity of the Bragg reflections at 450°C, which is correlated with an increase in the oxygen fluorescence signal and decrease in Se fluorescence as measured by XRF. This annealing data confirms that the as deposited films of both thicknesses formed MnSe on deposit, even though the films contained extra Se. The lattice parameter of the MnSe in both samples (5.44(1) Å) is independent of annealing temperature and in agreement with the 5.45 Å cubic unit cell reported in the literature.[31] This data suggests that it will be difficult to obtain amorphous films with compositions near a 1 to 1 ratio of Mn to Se using modulated precursors.

Samples B1 and B2, which were approximately 60% Se and 40% Mn as deposited, evolved differently due to their different bilayer thicknesses. Figure 3.4 contains the grazing incidence diffraction scans collected from these samples after each annealing temperature. In sample B1, which is slightly more Se rich than sample B2, the broad diffraction maxima present in the as deposited film change, becoming consistent with the formation of MnSe after annealing at 150° C. Sample B2, which has thicker bilayers and is slightly more Mn rich than sample B1, forms a mixture of $MnSe_2$ and MnSe during this annealing step. This may be a consequence of a non-uniform composition in sample B2 due to the thicker bilayers. The $MnSe_2$ lattice

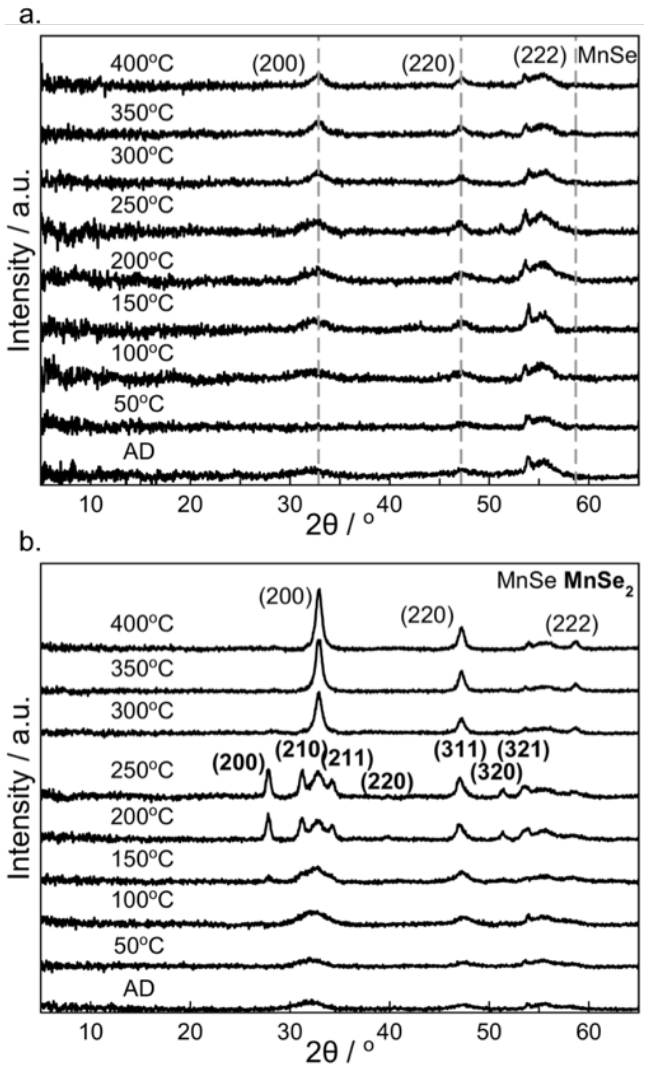

Figure 3.4. Grazing incidence diffraction scans of samples B1 (a) and B2 (b) as a function of annealing temperature.

parameters determined from the diffraction scans for sample B2 are smaller (6.40(1) Å) than the literature value of c = 6.417 Å.[26] During the higher temperature anneals, sample B1 behaves similarly to sample A1. The rate of Se loss decreases during the 250 and 400°C anneals, with its composition becoming Mn rich relative to MnSe, presumably due to a surface oxide. The MnSe reflections become sharper and more intense as annealing temperature is increased. During the 200 and 250°C annealing of sample B2, the reflections of $MnSe_2$ sharpen and grow in

intensity. There is Se loss during the 300°C annealing of sample B2, and the diffraction pattern after this anneal shows a significant increase in the intensity of MnSe reflections. Only reflections for MnSe are visible in the diffraction patterns obtained after the 350°C anneal. The sample after annealing at 400°C has a composition of 52% Mn and48% Se, with the excess Mn again due to the existence of a surface oxide.

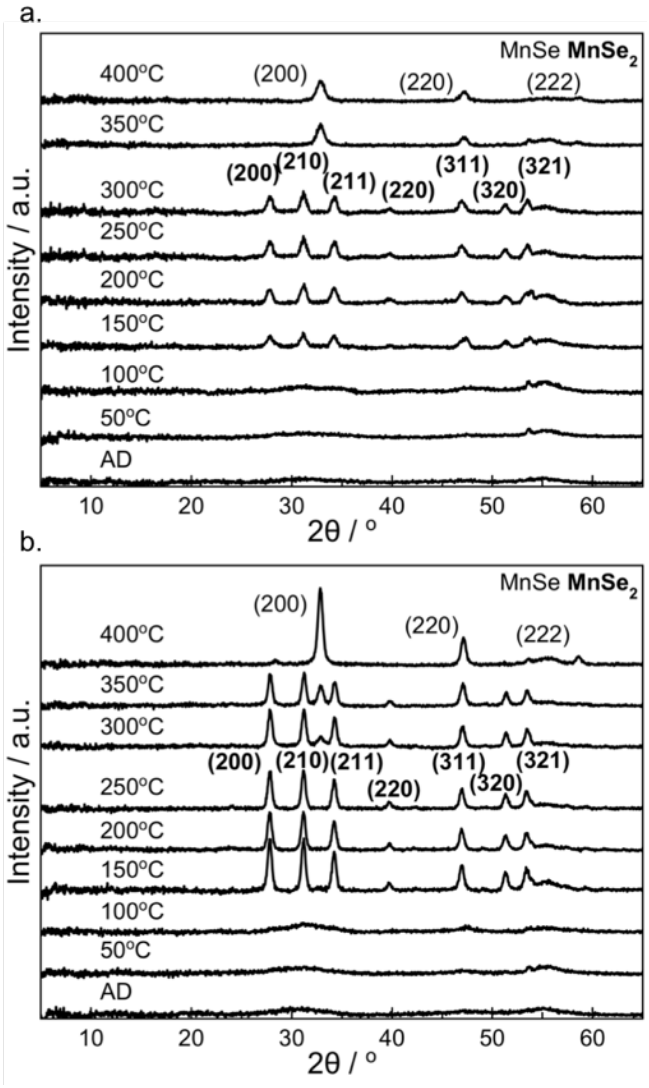

Figure 3.5. Grazing incidence diffraction scans collected from samples C1 (a) and C2 (b) as a function of annealing temperature.

Precursors C1 and C2 behaved similarly as a function of annealing temperature. They were both amorphous and had compositions close to stoichiometry of $MnSe_2$ as deposited. As shown in Figure 3.5, both samples formed $MnSe_2$ after annealing at 150°C. The $MnSe_2$ lattice parameter 6.41(1) Å, determined from the diffraction patterns of both samples, matches the literature value of 6.417 Å.[26] To decrease the loss of Se from sublimation, sample C2 was covered with a silicon wafer while C1 was not. As a consequence, sample C1 loses Se at a much faster rate as a function of annealing temperature than sample C2 and reflections for MnSe are visible at a much lower annealing temperature. The ratio of Mn to Se in sample C2 remained near a 1 to 2 ratio until 350°C. After annealing at 400°C, the ratio of Mn to Se changed, becoming 1 to 1.1. After this annealing temperature MnSe was the dominant compound in the diffraction pattern.

Precursors D1 and D2 surprised us, forming a compound not found on the equilibrium phase diagram during the annealing study. The as deposited precursors were both greater than 80% selenium and the equilibrium phase diagram indicates they should evolve to form a mixture of $MnSe_2$ and Se. Both samples were amorphous as deposited and did not change during the 50 and 100°C annealing as shown in Figure 3.6. Both samples form a previously unreported compound on annealing at 150°C, and all the reflections in both samples can be indexed to a small monoclinic unit cell with lattice parameters a = 4.942(2) Å, b = 4.32(3) Å, c = 3.779(1) Å, and β = 90.13(3)°. The relative intensities of the reflections, however, are different in the two scans, suggesting that there may be different amounts of preferred orientation or there may be different relative occupancies of crystallographic sites in the two samples. The composition of the D1 sample is close to a 1 to 2 ratio of Mn to Se as a result of significant Se loss during annealing at

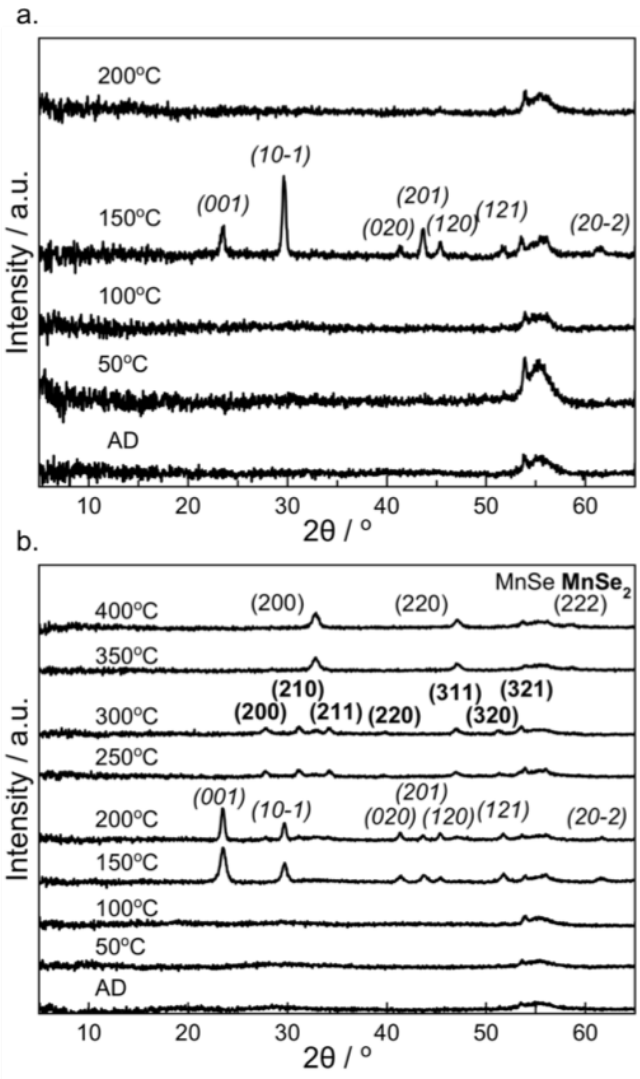

Figure 3.6. Grazing incidence diffraction scans of samples D1 (a) and D2 (b) as a function of annealing temperature

150°C. This suggests that the composition of the new compound is likely to be near a 1 to 2 ratio of Mn to Se. The composition of the D2 sample did not change significantly on annealing at 150°C, perhaps as a consequence of it being much thicker than sample D1. After annealing at 200°C, the diffraction pattern of sample D2 has small reflections consistent with the formation of $MnSe_2$ and the reflections for the new compound have sharpened. After annealing at 200°C, the diffraction pattern of sample D1 is very different, without any sharp

reflections. The XRF data indicates that sample D1 lost a significant amount of Se at this annealing temperature, with a final composition close to 1 to 1 between Mn and Se. At 250°C, the diffraction pattern for sample D2 contains reflections consistent with a film of $MnSe_2$ and the composition from the XRF data is consistent with this. At higher annealing temperatures, sample D2 behaves similar to sample C2, losing Se and forming MnSe.

There are several differences between the samples with thinner bilayers (A1-D1) and those with thicker bilayers (A2-D2). The samples with thinner bilayers all lose Se at a faster rate than the samples with thicker bilayers. Since samples A1-D1 are all much thinner in total thickness than A2-D2, this suggests that Se loss is limited by diffusion of Se to the surface. The samples with thinner bilayers also end up being more Mn rich (and Se poor) relative to the samples with thicker bilayers. We believe that this is due to the Mn containing oxide forming on surface of the samples. Since the samples with thinner bilayers are also thinner in total thickness, this oxide consumes a larger fraction of the total Mn in the film.

Previous investigations using modulated elemental reactants indicated that there is a critical bilayer thickness, with precursors layered below the critical thickness forming amorphous intermediates and those layered above the critical thickness nucleating binary compounds at the interface between elemental layers.[31] The results of the annealing studies as a function of composition and bilayer thickness of the Mn-Se samples suggest that the critical bilayer thickness in this system is a function of composition. Both the thicker and the thinner samples closest in composition to the stoichiometry of MnSe (A1 and A2) formed MnSe during the deposition. The samples with ~ 60% Se, B1 and B2, were x-ray amorphous but evolved differently. We suspect that at this composition sample B1 was below

the critical thickness while sample B2 was above the critical thickness. All of the samples with a lower Mn to Se ratio formed amorphous intermediates. The thicker and thinner bilayer samples (C1 and C2, D1 and D2) nucleated the same first compound.

3.4. Conclusions

This study showed that it is possible to form amorphous Mn-Se intermediates from modulated elemental reactants if they are more than 60% Se. The critical bilayer thickness at this composition is on the order of 1 nm. Films that were more Mn rich formed MnSe during deposition. Films that were more Se rich formed amorphous intermediates and no difference in the evolution of the films were observed for bilayer thicknesses less than ~ 2 nm. In the most Se rich films investigated, a new metastable compound was discovered. The diffraction pattern can be indexed to a monoclinic unit cell with lattice parameters of a = 4.942(2) Å, b = 4.32(3) Å, c = 3.779(1) Å, and β = 90.13(3)°.

3.5. Bridge

Chapter III focused on Mn and Se containing heterostructures to probe the formation of binary precursors depending on the local composition and layer thickness, which are two tunable parameters in Modulated Elemental Reactants. Local composition had the greatest impact on the formation of the final product(s) and a previously unreported kinetic binary compound was found. This chapter was previously published with co-authors in *Zeitschrift für anorganische und allgemeine Chemie* in 2018. I made all of the samples and collected and analyzed the diffraction data. The co-authors include Danielle M. Hamann, who was my mentor on this project and helped analyze the data and edited the manuscript, Jordan A. Joke, who performed several preliminary experiments to test the viability of the project, Dmitri Leo

M. Cordova, and David C. Johnson, who was my advisor and edited the manuscript. Understanding how layer thickness and local composition affected nucleation of the final product was imperative for the formation of heterostructures discussed in the next chapters.

CHAPTER IV

SUBSTITUENT EFFECTS IN THE SYNTHESIS OF HETEROSTRUCTURES

4.0. Authorship Statement

Chapter IV was published in *Inorganic Chemistry* in 2021. I am the primary author of the manuscript while Taryn Mieko Kam collected several annealing studies and David C. Johnson acted as my adviser and helped to edit the manuscript.

4.1. Introduction

The synthesis of heterostructures, compounds containing the intergrowth of two distinct structures, has become increasingly important. A large number of novel phenomena have been predicted and discovered in heterostructures, including superconductivity,[1] topological states,[2] and other phenomena.[3-13] While most of these ground-breaking discoveries were initially performed on mechanically assembled samples via "scotch tape synthesis," the ability to prepare larger area samples as thin films on a variety of substrates is needed for applications and for fundamental investigations.[14]

Heterostructures are thought to form by the heterogenous nucleation of one layer off of the other, both in van der Waals epitaxial growth and in other synthesis approaches. Clearly the structure of an existing layer will have a significant impact on the structure of the subsequent layer that forms.[15-17] In addition to lattice matching, the electronic properties of an existing layer could also have a significant "substituent effect" on the identity of the next layer that forms. Substituent effects, where functional groups in one part of a molecule impact the rate of reactivity or orientation of an addition reaction in another region of the molecule due to electron donation or withdrawal, are well known in molecular chemistry.[18-19] They are an important tool

used by molecular chemists to design reaction sequences to form targeted compounds. To our knowledge, no one has reported "substituent-like" electronic effects impacting the reaction pathway or the final product in the synthesis of compounds with extended inorganic structures.

Recently very different structures formed when attempting to grow Bi_2Se_3 on $MoSe_2$ substrates vs $NbSe_2$ substrates *via* van der Waals epitaxy.[20-23] Growth of Bi_2Se_3 on $MoSe_2$ was straightforwardly accomplished by adjusting the Bi and Se deposition rates and substrate temperature.[20-22] Attempts to grow Bi_2Se_3 layers directly on $NbSe_2$ surfaces by similarly tuning the Bi and Se deposition rates and substrate temperature however, failed. Instead, the unexpected and unavoidable growth of an interfacial layer of BiSe on the $NbSe_2$ was observed. Subsequent growth resulted in Bi_2Se_3 layers growing on top of the BiSe interfacial layer.[23] Since both $MoSe_2$ and $NbSe_2$ are structurally similar transition metal dichalcogenides, this difference is surprising. Both dichalcogenides consist of strongly bonded Se-M-Se trilayers with lone pairs facing outward. It was suggested that the growth of the interfacial rock salt structured BiSe layer alleviated the ~20% lattice mismatch between Bi_2Se_3 and $NbSe_2$.[23] However, the lattice mismatch between Bi_2Se_3 and $MoSe_2$ is larger (~24%), suggesting other factors cause this striking difference in products formed.

We speculated that the difference in the electrical properties of $MoSe_2$ and $NbSe_2$ was the cause of the different growth behaviors. 2H-$MoSe_2$ is a semiconductor while all polymorphs of $NbSe_2$ are metallic. To test this hypothesis, we investigated the growth of Bi_2Se_3 and Bi_2Se_3 containing heterostructures, varying the electronic properties of the second constituent. We used a non-epitaxial growth technique, modulated elemental reactants (MER) to minimize the impact of lattice mismatch on the products formed. We found that the reaction pathway

and final products indeed depend on whether the second constituent is a metal ($TiSe_2$, VSe_2) or a semiconductor (PbSe, 2H-$MoSe_2$). When M = Ti or V, the samples formed $[(BiSe)_{1+\gamma}]_1[(MSe_2)]_1$ with the excess Bi and Se segregating to the top of the film forming Bi_2Se_3. The precursors with Bi|Se layers alternating with Pb|Se layers formed metastable products during deposition, which transform into $[(PbSe)_{1+x}]_1[Bi_2Se_3]_1$ at relatively low annealing temperatures. When Bi|Se bilayers are deposited sequentially with Mo|Se bilayers, the composition of the precursor dictates the formation of the product. Stochiometric amounts of Se in the precursors result in the formation of a mix of $[(Bi_2Se_3)_{1+\delta}]_1[(MoSe_2)]_1$ and $[(BiSe)_{1+\gamma}]_1[(MoSe_2)]_1$. Excess Se in the precursor results in the formation of just $[(Bi_2Se_3)_{1+\delta}]_1[(MoSe_2)]_1$. The $MoSe_2$ in $[(BiSe)_{1+\gamma}]_1[(MoSe_2)]_1$ is a mix of semiconducting 2H and metallic 1T polymorphs.[24] The $MoSe_2$ layered with Bi_2Se_3 is only the semiconducting 2H polymorph.[25] These results suggest that "substituent-like" electronic effects exist in the synthesis of extended solids, impacting the reaction pathway.

4.2. Experimental

Precursors were prepared using a custom vapor deposition chamber, where ultra-thin layers of atoms were deposited in a designed sequence $(Bi|Se)_2|M|Se$) to mimic the architecture of the targeted Bi_2Se_3-MSe_x products. Bismuth, lead, titanium, vanadium, and molybdenum were deposited using an electron beam gun while selenium was deposited using a Knudson effusion cell. The deposition rates were controlled using quartz crystal monitors. The amount of each element deposited in each layer was controlled by opening shutters for the time required to deposit the targeted amounts. The precursors were deposited on an unheated Si (100) wafer with a native oxide layer. The $(Bi|Se)_2$ sequence was deposited such that it contained the number of atoms required to form a Bi_2Se_3 quintuple layer. The

M|Se layers contained the required number of atoms to form either a (100) orientated bilayer of PbSe or the number of atoms required to form a single Se-M-Se trilayer of the targeted transition metal dichalcogenide (TMD). The targeted atoms / $Å^2$ for each constituent were calculated using the lattice parameters of the bulk crystalline structures.

The amounts of each element actually deposited were determined using x-ray fluorescence (XRF).[26] XRF intensities were collected for each element for the as-deposited samples on a Rigaku ZSX Primus II wavelength-dispersive X-ray fluorescence spectrometer with a Rh x-ray source. The proportionality constants converting intensity to atoms/$Å^2$ were determined by synthesizing films of the most Se rich thermodynamic products for each metal and using the previously determined proportionality constant for Se.

X-ray scattering data was collected using several different geometries. X-ray reflectivity (XRR) data was used to determine the total film thickness and film roughness from the Kiessig fringes. Specular and grazing incident in-plane x-ray diffraction (XRD) was used to determine the extent of crystallinity, the repeating layer thicknesses, and the lattice parameters of reaction intermediates and compounds formed. The XRR and specular XRD information was obtained using Cu Kα radiation on a Bruker D8 DISCOVER diffractometer. Grazing incidence in-plane XRD was collected on a Rigaku Smartlab diffractometer with Cu Kα radiation.

Annealing studies were performed to follow the evolution of the precursors as they self-assembled into the final product(s). The precursors were annealed starting at 100°C in a nitrogen glovebox with an oxygen pressure of less than 1 ppm. The same piece of each precursor was annealed at each temperature, which was increased by 50°C for each subsequent anneal. Diffraction data was collected after annealing at each temperature.

4.3. Results

MER is a non-epitaxial growth technique where the amount of each element and the sequence of layers are controlled to create a layered precursor with a designed nanoarchitecture.[27] The thickness of the elemental layers determines the diffusion lengths in the precursors. Since diffusion lengths can be reduced to less than a nanometer, nucleation typically becomes the rate limiting step in forming a crystalline solid.[28] What nucleates typically is controlled by local composition, enabling in the formation of kinetic products either during the deposition or during subsequent annealing.[29] For more complex precursors containing two or more regions with different local compositions, metastable products structurally related to the nanoarchitecture of the precursor often form.[29-30] The ability to monitor interdiffusion *via* XRR, composition using XRF, and nucleation at the

Table 4.1. A summary of the composition and thickness information of the precursors.

	Atoms / Å² per layer			Number of Layers Deposited	Repeating Thickness (Å)	Total Sample Thickness (Å)
Sample	**Bi**	**M**	**Se**			
Bi_2Se_3 quintuple layer	0.130		0.201			
Bi|Se Sample A	0.128(1)		0.185(7)	64	9.40(2)	603.7(3)
Bi|Se Sample B	0.108(1)		0.195(8)	32	8.56(1)	273.8(2)
$(PbSe)_1(Bi_2Se_3)_1$	0.130	0.107	0.31			
Pb|Se|Bi|Se Sample	0.143(1)	0.108(1)	0.29(1)	20	16.48(2)	329.6(2)
$(Bi_2Se_3)_1(TiSe_2)_1$	0.130	0.093	0.39			
Ti|Se|Bi|Se Sample	0.140(1)	0.093(2)	0.36(1)	20	14.80(2)	289(1)
$(Bi_2Se_3)_1(VSe_2)_1$	0.130	0.103	0.41			
V|Se|Bi|Se Sample	0.136(1)	0.097(1)	0.42(2)	20	16.28(2)	320(1)
$(Bi_2Se_3)_1(MoSe_2)_1$	0.130	0.107	0.41			
Mo|Se|Bi|Se Sample A	0.135(1)	0.103(1)	0.455(5)	19	17.64(5)	334.2(2)
Mo|Se|Bi|Se Sample B	0.133(1)	0.104(1)	0.42(4)	19	16.46(2)	316(1)

multiple interfaces in a precursor *via* XRD makes these designed precursors ideal to monitor reaction pathways.[31]

Table 4.1 summarizes the sequence of layers deposited, the amount deposited in each sequence, the thickness of the repeating sequence of layers, the number of repeating sequences deposited, and the total thickness of the precursor for each of the precursors in this study. It also contains the estimated number of atoms of each element required in each precursor. The estimated lattice parameters of the targeted heterostructures were determined by simply adding the *c*-axis lattice parameters of the constituent layers. The amount of each element in the precursors are all within 10% of the targeted values. The thickness of the repeating sequence of layers for the precursors are all consistent with the measured amounts of the deposited elements and close to the estimated *c*-axis lattice parameters for the targeted heterostructures. The composition and structural data collected on the as-deposited precursors indicate that they all have the intended nanoarchitectures and local compositions expected for the targeted Bi_2Se_3 containing compounds.

We first examined the evolution of diffraction patterns from the two Bi|Se samples, both as-deposited and after annealing at different temperatures. Since both samples were very similar, here we discuss the data collected on Bi|Se sample A. The data for Bi|Se sample B can be found in the Appendix A. The as-deposited specular XRD pattern (Figure 4.1) does not contain a diffraction maximum resulting from the sequential deposition of the elements, indicating that mixing of the elements occurred during deposition. The specular pattern did contain four broad reflections at higher angles. The first three reflections are evenly spaced and index to a family of reflections that suggest a lattice parameter that is an integer multiple of 15.67(1) Å. There is also a broad

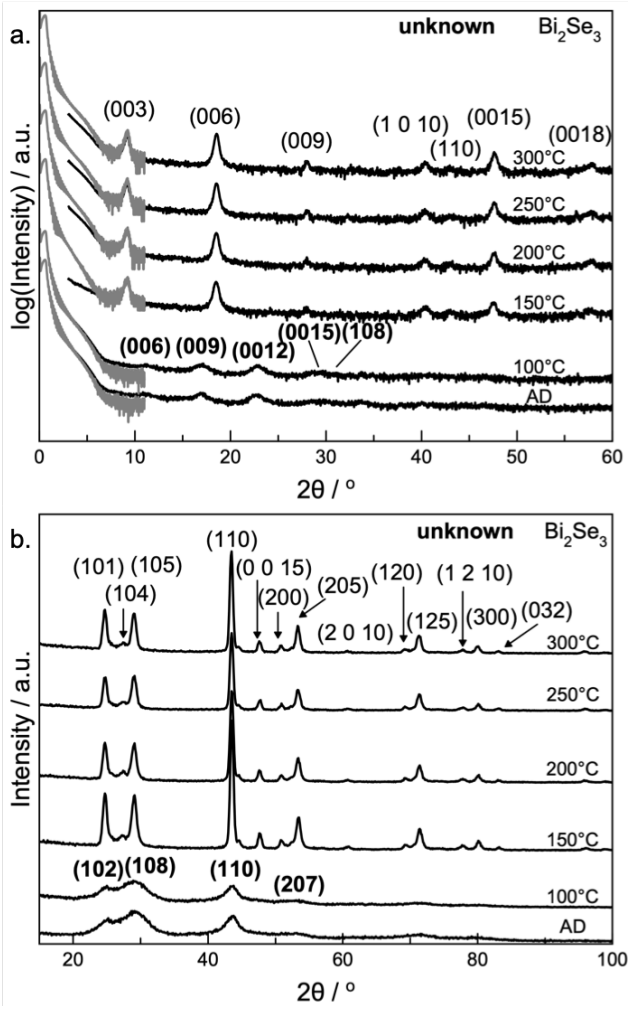

Figure 4.1. (a) XRR (gray) and specular (black) x-ray diffraction and (b) in-plane x-ray diffraction patterns on Bi|Se sample A collected after annealing at the temperatures indicated. The font of the indices matches the identified phase.

maximum at ~29.16(8)° 2θ that is observed in the in-plane XRD pattern, suggesting that the product is not crystallographically aligned with the substrate. The as-deposited in-plane XRD pattern contains three additional broad reflections. The known bismuth selenides with hexagonal unit cells all have two common reflections: an intense reflection at ~43° 2θ that is indexed as a (110) reflection and an intense reflection at ~30° 2θ, which is indexed as an (10*l*) reflection.[32-35] Assuming that the 43.55(8)° 2θ reflection in the in-plane XRD pattern

is the (110) reflection, we can index all of the observed reflections in the specular and in-plane XRD patterns using lattice parameters of a = 4.13(1) Å and c = 47.07(1) Å. These lattice parameters fall within the range of lattice parameters for known hexagonal Bi_nSe_m compounds (4.1355(5) Å ≤ a ≤ 4.332(6) Å, 22.8 Å ≤ c ≤ 97.100 Å), but do not match any of those previously reported.[32-35]

The evolution of structure was followed by collecting specular and in-plane XRD patterns after annealing at each temperature (Figure 4.1). The diffraction patterns at 100°C are very similar to the as-deposited patterns, with no change in intensity or peak shape of the reflections. After annealing at 150°C, however, all of the reflections found in the as-deposited patterns are absent and a set of new reflections are present. The new reflections can be indexed as (*hkl*) reflections from a hexagonal unit cell yielding an *a*-axis lattice parameter of 4.12(1) Å and a *c*-axis lattice parameter of 28.68(1) Å. These are within the range of values previously reported for bulk Bi_2Se_3 (4.115 Å ≤ a ≤ 4.151 Å and 28.25 Å ≤ c ≤ 29.0 Å).[36-38] The crystalline layers are not perfectly aligned to the substrate as mixed (*hkl*) reflections are observed in both patterns. The reflections in the diffraction patterns do not change in intensity or peak position after annealing at higher temperatures, indicating that the formed Bi_2Se_3 is stable at these temperatures. This is consistent with the known Bi-Se phase diagram.[39]

Diffraction patterns collected on the Pb|Se|Bi|Se precursor as a function of temperature are shown in Figure 4.2. The as-deposited precursor does not contain a Bragg maximum from the deposition sequence of alternating Pb|Se and Bi|Se layers, indicating that enough mixing occurred during the deposition to eliminate periodic electron density gradients. Both the specular and in-plane diffraction patterns contain broad reflections at ~24.64(1)°, 29.23(5)°, and 42.23(1)° 2θ. These reflections can be indexed as reflections associated with a cubic

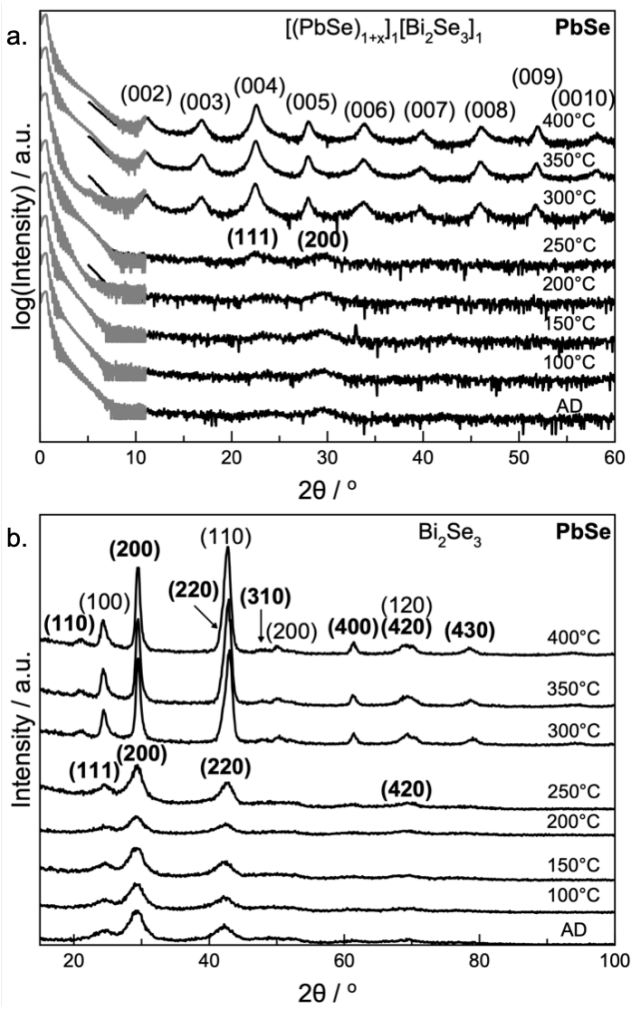

Figure 4.2. (a) XRR (gray) and specular (black) x-ray diffraction and (b) in-plane x-ray diffraction as a function of temperature on the Pb|Se|Bi|Se precursor.

unit cell with an *a*-axis lattice parameter of 6.073(1) Å. This is within the range reported for PbSe (6.03(1) - 6.128(1) Å),[40-41] suggesting that the precursor is segregating during the deposition forming domains of rock salt structured PbSe, perhaps with some Bi substitutions and associated vacancies. No additional reflections appear and the intensities of the as-deposited reflections do not change significantly as the sample is annealed at or below 250°C. After annealing at 300°C, a set of evenly spaced reflections appear in the specular diffraction pattern and new reflections are observed in the in-plane diffraction

pattern. The *c*-axis lattice parameter determined by the (00*l*) reflections in the specular pattern is 15.853(2) Å, which is slightly larger than the sum of the *c*-axis lattice parameters of PbSe and a single quintuple layer of Bi_2Se_3 (15.63 Å). The reflections in the in-plane XRD pattern can be indexed as (*hk*0) reflections from both a cubic and a hexagonal unit cell. The *a*-axis lattice parameters for the cubic phase (a = 6.041(4) Å) is within the range reported for PbSe (6.03(1) - 6.128(1) Å),[40-41] The *a*-axis lattice parameters for the hexagonal phase (a = 4.199(3) Å) is close to those reported for Bi_2Se_3 (4.115 Å ≤ a ≤ 4.178(1) Å).[36,42] The diffraction patterns of the sample do not change after annealing at 350 and 400°C. The lattice parameters and stability at these temperatures is consistent with the formation of $[(PbSe)_{1+x}]_1[Bi_2Se_3]_1$, which is a member of the naturally occurring homologous series made from the building blocks PbSe and Bi_2Se_3. This compound reported as $(PbSe)_5(Bi_2Se_3)_3$ or $Pb_5Bi_6Se_{14}$ due to the formation of an in-plane supercell when grown from a melt.[43] We see no evidence for the formation of this in-plane supercell. This may be a result of extensive turbostratic disorder as observed for PbSe-dichalcogenide misfit layer compounds prepared from designed precursors.[44-46]

Diffraction patterns collected on the Ti|Se|Bi|Se precursor as a function of temperature are shown in Figure 4.3. Unlike the Bi|Se and Pb|Se|Bi|Se precursors, the first Bragg reflection from the artificial layering of the elements is observed, indicating that complete mixing of the layers has not occurred. The thickness of the repeating Ti|Se|Bi|Se layers (14.80(2) Å) is slightly smaller than the estimated *c*-axis lattice parameter of the targeted $[(Bi_2Se_3)_{1+\delta}]_1[(TiSe_2)]_1$ heterostructure (15.52 Å), as the amounts of Ti and Se deposited were below the targeted values. Broad reflections are observed at 14.70(1)° and 29.65(1)° 2θ in

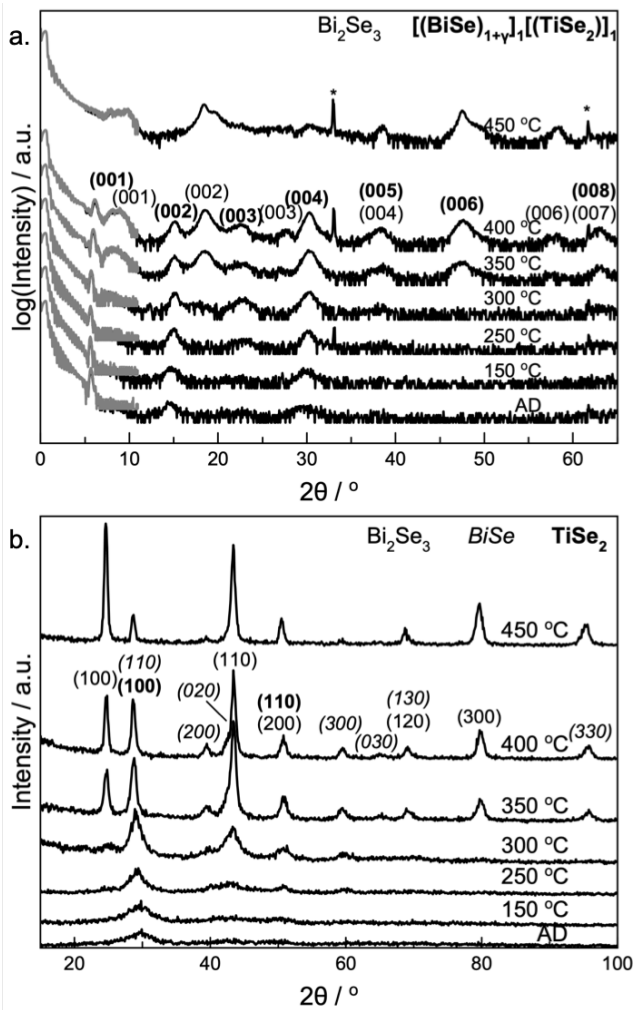

Figure 4.3. (a) XRR (gray) and specular (black) x-ray diffraction and (b) in-plane x-ray diffraction as a function of temperature on the Ti|Se|Bi|Se precursor. The asterisk marks on the sharp reflections at ~31° and 62° 2θ are from the Si substrate.

the specular XRD pattern that can be indexed as (00*l*) reflections, yielding a *c*-axis lattice parameter that is a multiple of 6.019(1) Å. There are several broad and weak reflections in the in-plane XRD pattern are consistent with (*hk*0) reflections from BiSe and $TiSe_2$ observed from $[(BiSe)_{1+\gamma}]_1[(TiSe_2)]_1$.[47] Annealed to 150°C, the intensity of the reflection from the Ti|Se|Bi|Se modulation in the precursor decreases, while the intensity of reflections from the crystalline phases increase in both diffraction patterns. After annealing at 250°C, additional reflections are

visible in the specular and in-plane XRD patterns consistent with the growth of $[(BiSe)_{1+\gamma}]_1[(TiSe_2)]_1$. The specular reflections are consistent with a single family of (00*l*) reflections with a *c*-axis lattice parameter of 11.75(2) Å. The reflections in the in-plane XRD pattern can be indexed as (*hk*0) reflections of both a hexagonal and a rectangular basal plane yielding lattice parameters of a_{hex} = 3.60(5) Å, a_{rect} = 4.45(1) Å, and b_{rect} = 4.19(1) Å which are consistent with the presence of $TiSe_2$ and BiSe, respectively. These lattice parameters suggest that the misfit layer compound $[(BiSe)_{1+\gamma}]_1[(TiSe_2)]_1$ has formed (c = 11.81(2) Å, a_{hex} = 3.580(3) Å, a_{rect} = 4.564(2) Å, and b_{rect} = 4.246(1) Å).[47]

The reflections in the specular and in-plane XRD patterns from $[(BiSe)_{1+\gamma}]_1[(TiSe_2)]_1$ increase in intensity after annealing at 300°C, but new broad and weak reflections in the both patterns that suggest that small grains of Bi_2Se_3 are now present. After the 350°C annealing, the reflection from the Ti|Se|Bi|Se modulation is now consistent with the higher order reflections from $[(BiSe)_{1+\gamma}]_1[(TiSe_2)]_1$. A second family of (*00l*) reflections is clearly present at this temperature. The *c*-axis lattice parameters from these two families of reflections are 11.77(1) Å and 9.61(1) Å, indicating the presence of both $[(BiSe)_{1+\gamma}]_1[(TiSe_2)]_1$ and Bi_2Se_3.[47-48] New reflections also appear in the in-plane diffraction pattern and the intensity of existing reflections increase as their line widths decrease significantly. The reflections can be indexed as (*hk*0) reflections of two hexagonal unit cells and a third phase with a rectangular basal plane that are consistent with Bi_2Se_3, $TiSe_2$, and BiSe. After annealing at 400°C, the reflections from $[(BiSe)_{1+\delta}]_1[(TiSe_2)]_1$ and Bi_2Se_3 in the specular pattern become sharper and more intense, yielding *c*-axis lattice parameters of 11.793(5) Å and 9.569 (5) Å. The lattice parameters determined from the (*hk*0) reflections in the in-plane pattern (a_{hex} =4.166(5) Å, a_{hex} = 3.59(1)Å, a_{rect} = 4.583(2) Å, and b_{rect} = 4.245(2) Å) are also consistent with those reported for Bi_2Se_3 (4.115 Å

≤ a ≤ 4.178(1) Å)[36,42] and $[(BiSe)_{1+\gamma}]_1[(TiSe_2)]_1$.[47] After annealing at 450°C, the reflections broaden in the specular pattern and reflections from BiSe become weaker in the in-plane diffraction pattern as $[(BiSe)_{1+\gamma}]_1[(TiSe_2)]_1$ begins to decompose to the thermodynamic compounds. The diffraction data collected while annealing suggests that the sample segregates to form the misfit compound $[(BiSe)_{1+\gamma}]_1[(TiSe_2)]_1$ and Bi_2Se_3. There is no evidence of the formation of $[(Bi_2Se_3)_{1+\delta}]_1[(TiSe_2)]_1$ at any temperature.

Diffraction patterns collected on the V|Se|Bi|Se precursor as a function of temperature are shown in Figure 4.4. Similar to the Ti|Se|Bi|Se precursor, the V|Se|Bi|Se precursor exhibits an initial layering reflection at low angles as a result of the artificial layering and additional broad reflections in the specular and in-plane diffraction patterns. The d-spacing of layering reflection (16.28(2) Å) is slightly larger than the estimated *c*-axis lattice parameter for $[(Bi_2Se_3)_{1+\delta}]_1[(VSe_2)]_1$ (15.61 Å). The broad reflections in the specular XRD pattern at ~14.48(1)° and 29.06(1)° 2θ can be indexed as members of the same family of reflections. The interplane spacing is consistent with the formation of a compound with a unit cell that is a multiple of 6.13(2) Å. The in-plane diffraction pattern contains a very broad reflection at ~30° 2θ, where the (100) reflection from VSe_2 would be expected.

The V|Se|Bi|Se sample evolved through several intermediate structures defined by three distinct temperature ranges. In the lowest temperature regime, T≦150°C, the reflections observed in the as-deposited specular XRD pattern are present and their intensity increases as annealing temperature increases. After annealing at 100°C, there is a slight increase in intensity of the reflection at ~30° 2θ in the in-plane diffraction pattern. After annealing at 150°C, two

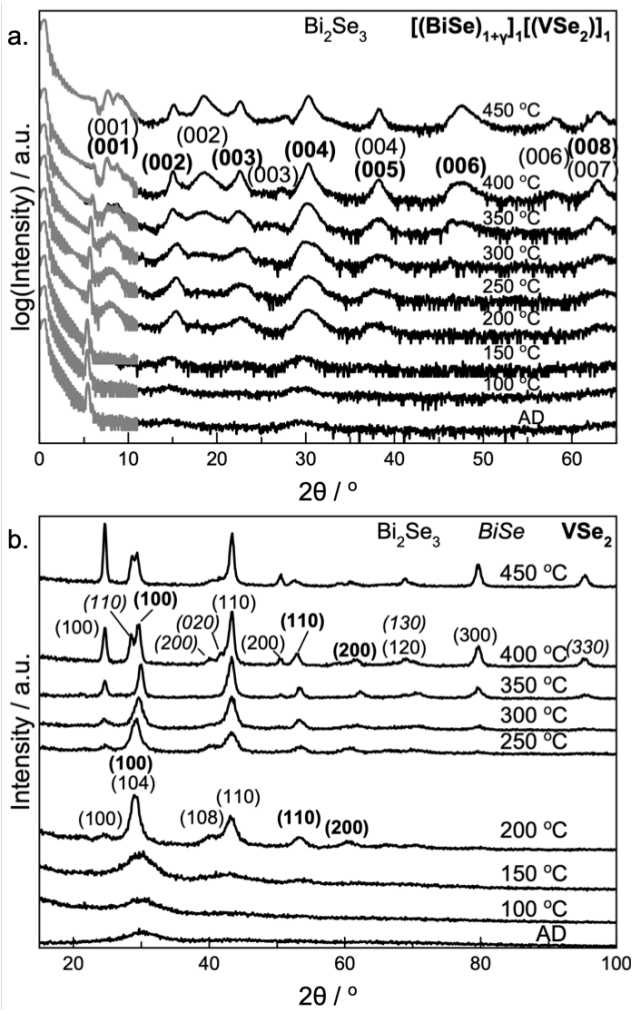

Figure 4.4. (a) XRR (gray) and specular (black) x-ray diffraction and (b) in-plane XRD as a function of temperature on the V|Se|Bi|Se precursor.

additional weak and broad reflections appear close to the expected angles for VSe_2 and Bi_2Se_3 reflections.

The second temperature regime begins after annealing at 200°C. The intensity of the Bragg reflection from the artificial layering decreases and shifts to higher angle, indicating that the layer thickness has decreased. XRF data reveals that the sample lost 15% of its Se content during this anneal. New broad reflections appear in the specular and in-plane XRD patterns. The specular XRD pattern contains five, broad reflections consistent with a period of ~11.7 Å. Shoulders in the higher angle reflections suggest that two phases with

similar *c*-axis lattice parameters (11.53(2) Å and 11.95(3) Å) are present. These values are much less than that expected for $[(Bi_2Se_3)_{1+\delta}]_1[(VSe_2)]_1$ (*c* ~15.61 Å) and bracket the reported c-axis lattice parameter of $[(BiSe)_{1+\gamma}]_1[(VSe_2)]_1$ (*c* = 11.78(1) Å).[49] Most of the new reflections that appear in the in-plane scan can be indexed as (*hk*0) reflections of two hexagonal unit cells with *a*-axis lattice parameters of 4.20(1) Å and 3.48(7) Å. The large errors are due to the large line widths. These lattice parameters are larger than expected for Bi_2Se_3 (4.115 Å ≤ *a* ≤ 4.178(1) Å)[36,42] and VSe_2 (*a* = 3.43(1) Å),[40] respectively. The remaining reflections at ~29.20° and ~39.90° 2θ can be indexed as the (104) and (108) reflections of Bi_2Se_3. After annealing at 250°C, the (104) and (108) reflections decrease in intensity and after annealing at 300°C they are no longer observed. A new reflection grows in at a higher angle than the ~29.20° 2θ reflection during the 250 and 300°C anneals, consistent with the (100) reflection of VSe_2.

The third temperature regime begins after annealing at 350°C, where the Bragg maxima from the artificial layering of the precursor significantly decreases in intensity, the sample loses Se, and the thermodynamically stable products expected from the phase diagram ($[(BiSe)_{1+\gamma}]_1[(VSe_2)]_1$ and Bi_2Se_3) form. The reflections in the specular XRD pattern can be indexed to two different phases: a phase with a *c*-axis lattice parameter of 11.7(1) Å and a second phase with a *c*-axis lattice parameter of 10.0(4) Å. The in-plane reflections after annealing to 350°C can all be indexed as (*hk*0) reflections of two hexagonal unit cells. The reflections for these two compounds become more defined after annealing at higher temperatures. The reflection from the initial layering of the elements in the specular XRD pattern is absent after annealing at 400°C. The reflections in the specular XRD pattern can be indexed yielding *c*-axis lattice parameters of 11.772(4) Å and 9.568(4) Å. The first phase is consistent with $[(BiSe)_{1+\gamma}]_1[(VSe_2)]_1$ (*c* = 11.78(1)

Å).[49] The second phase is consistent with Bi_2Se_3.[48] The in-plane reflections after annealing at 400°C can be indexed as (*hk*0) reflections of two hexagonal unit cells and a third phase with a rectangular basal plane. The hexagonal phases have *a*-axis lattice parameters of 4.165(8) Å and 3.465(6) Å, which are consistent with the reported *a*-axis lattice parameters for Bi_2Se_3 (4.115 Å ≤ *a* ≤ 4.178(1) Å)[36,42] and VSe_2 (a = 3.43(1) Å),[40] respectively. The reflections from the rectangular basal plane yield lattice parameters of *a* = 4.56(4) Å and *b* = 4.30(4) Å, which are consistent with the lattice parameters reported previously for $[(BiSe)_{1+\gamma}]_1[(MSe_2)]_1$ heterostructures.[24,50] The sample consists of a combination of $[(BiSe)_{1+\gamma}]_1[(VSe_2)]_1$ and Bi_2Se_3 after annealing at 400°C.

We find no evidence for the formation of the targeted $[(Bi_2Se_3)_{1+\delta}]_1[(TiSe_2)]_1$ or $[(Bi_2Se_3)_{1+\delta}]_1[(VSe_2)]_1$ heterostructures at any temperature. This is despite the precursors having the composition and nanoarchitecture that should favor their formation *via* a near diffusionless transition. The nucleation of $TiSe_2$ and VSe_2 during the deposition may permit charge transfer from nuclei of BiSe to the TMD layer, promoting the nucleation of BiSe over Bi_2Se_3.

Since $MoSe_2$ forms both a semiconducting 2H polymorph and a metallic 1T polymorph, we explored the reaction pathway of two different Mo|Se|Bi|Se precursors. Diffraction patterns collected as a function of temperature on Mo|Se|Bi|Se precursor A, which contains excess Se, are shown in Figure 4.5. The as-deposited XRR and specular XRD patterns contain Bragg reflections from the artificial layering of the elements, similar to the other M|Se|Bi|Se precursors. The reflections observed yield a layering thickness of 17.63(5) Å, which is larger than the estimated *c*-axis lattice parameter of the targeted $[(Bi_2Se_3)_{1+\delta}]_1[(MoSe_2)]_1$ heterostructure (16.06 Å) due to the extra Se. There is also a single broad reflection observed in the in-plane XRD

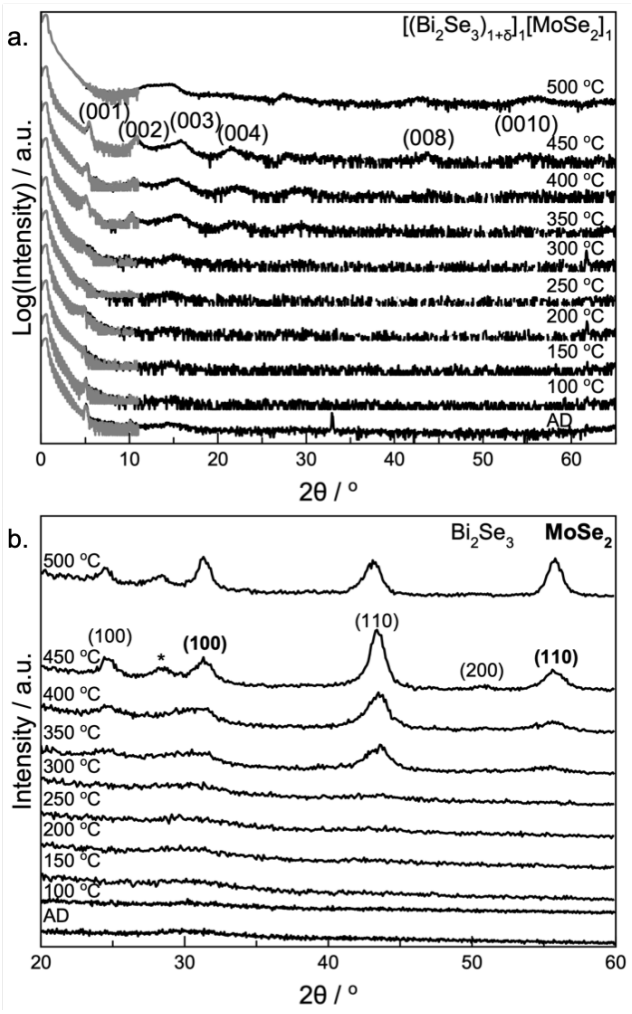

Figure 4.5. (a) XRR (gray) and specular (black) x-ray diffraction and (b) in-plane x-ray diffraction as a function of temperature on Mo|Se|Bi|Se Precursor A. The asterisk marks an unidentified reflection.

pattern at ~30° 2θ. No major changes occur in either pattern after annealing at 100°C. After annealing at 150°C, the first order reflection from the modulation of the elements shifts to lower 2θ and the second order reflection (~10° 2θ) is no longer observed, suggesting mixing of the elements. There is also a decrease in the number of Kiessig fringes in the XRR pattern, indicating an increase in roughness. Minimal changes are observed in the specular and in-plane XRD patterns after annealing at 200°C. After the 250°C anneal, the first order artificial layering reflection is very broad and the broad reflection at ~14° 2θ has decreased in intensity. There is no change in the in-plane XRD pattern. Both patterns remain the same after annealing at 300°C. After

annealing at 350°C, the number of reflections observed in the specular and in-plane XRD patterns increases dramatically and XRF indicates the sample lost 7% of its Se. Five broad reflections are observed in the specular XRD pattern. The first three reflections are consistent with a single family of reflections with a c-axis lattice parameter of 17.12(5) Å, which is larger than estimated for a $[(Bi_2Se_3)_{1+\delta}]_1[(MoSe_2)]_1$ heterostructure. The two reflections observed above 20° 2θ are not consistent with the first three reflections, but can be indexed as the (003) and (004) reflections of a repeating unit with a *c*-axis lattice parameter of 12.13(6) Å. The broad linewidths of the reflections indicate the coherent domain sizes are small. Four broad reflections are observed in the in-plane pattern, which are consistent with two hexagonal unit cells, one with an *a*-axis lattice parameter of 4.16(2) Å and another with an *a*-axis lattice parameter of 3.32(1) Å. These are close with those reported for Bi_2Se_3 (4.115 Å ≤ a ≤ 4.178(1) Å)[36,42] and $MoSe_2$ (a = 3.32(1) Å),[24] respectively. After annealing at 400° C, the sample's composition is within error of the estimated amounts required for a $[(Bi_2Se_3)_{1+\delta}]_1[(MoSe_2)]_1$ heterostructure. The first three reflections in the specular XRD pattern shift slightly to higher angles resulting in a smaller *c*-axis lattice parameter (17.08(5) Å). The reflections above 20° shift to lower angles, changing the *c*-axis lattice parameter to 12.2(2) Å. No changes are observed in the in-plane XRD pattern. After annealing at 450°C, all of the observed now narrower reflections in the specular pattern can be indexed as members of the same family of reflections with a *c*-axis lattice parameter of 16.56(6) Å. This *c*-axis lattice parameter is consistent with the estimated *c*-axis lattice parameter for a $[(Bi_2Se_3)_{1+\delta}]_1[(MoSe_2)]_1$ heterostructure (16.06 Å). The reduced line widths indicate larger crystalline domains. The reflections in the in-plane pattern are also narrower and more intense at this temperature. The *a*-axis lattice parameters (4.16(1) Å and 3.30(1) Å) change minimally compared to the previous temperature and are consistent with Bi_2Se_3[36,42] and $MoSe_2$,[24] respectively. The reflection observed at ~28° 2θ is not consistent with either hexagonal unit cell. After annealing to 500°C, several reflections are lost, the line widths increase, and the intensity decreases in the specular pattern. The intensity of the reflections consistent with Bi_2Se_3 in the in-plane pattern

decreases at this temperature. The changes in both patterns indicate the sample decomposes due to loss of material.

Unlike the previously discussed Ti|Se|Bi|Se and V|Se|Bi|Se precursors, Mo|Se|Bi|Se precursor A with excess Se forms the desired $[(Bi_2Se_3)_{1+\delta}]_1[(MoSe_2)]_1$ heterostructure via a convoluted reaction pathway. The large line widths of the (00*l*) reflections suggests the structure contains many stacking defects, similar to the diffraction data shown earlier for $[(PbSe)_{1+x}]_1[Bi_2Se_3]_1$.

Mo|Se|Bi|Se precursor B, which is closer to the stoichiometry of the targeted $[(Bi_2Se_3)_{1+\delta}]_1[(MoSe_2)]_1$ compound forms a not very well crystallized mixture of $[(Bi_2Se_3)_{1+\delta}]_1[(MoSe_2)]_1$ and $[(BiSe)_{1+\gamma}]_1[(MoSe_2)]_1$ after annealing at 500°C. A detailed analysis of the changes in the diffraction patterns of this sample as a function of annealing temperature is provided in Appendix A. The evolution is similar to precursor A, however once $[(BiSe)_{1+\gamma}]_1[(MoSe_2)]_1$ forms it never reacts with the remaining Bi and Se to form $[(Bi_2Se_3)_{1+\delta}]_1[(MoSe_2)]_1$.

4.4. Discussion

The differences in the growth mechanisms of the Bi|Se containing heterostructures indicates the electronic structure of the constituent layers impacts the reaction pathway of the precursors and the identity of the compounds formed. Similar to the directing groups in molecular chemistry, the electronic properties of the neighboring M|Se layer dictate whether the Bi|Se layer forms Bi_2Se_3 or BiSe. When a precursor with just Bi|Se layers having a 2:3 ratio of Bi:Se are annealed, Bi_2Se_3 forms. Precursors containing the identical Bi|Se bilayer form heterostructures containing BiSe when the M|Se layer forms a metal ($TiSe_2$, VSe_2, 1T-$MoSe_2$). Heterostructures form containing the targeted Bi_2Se_3 layer only when the M|Se layer forms a semiconductor (PbSe or 2H-$MoSe_2$). The BiSe containing heterostructures are more stable than the targeted Bi_2Se_3 containing heterostructures due to charge transfer from the BiSe to the

dichalcogenide which result in strong ionic interactions between the BiSe and dichalcogenide layers.[24,47,49-50] If the bismuth atoms can reduce the transition metal, BiSe will form. If not, Bi_2Se_3 will form.

The local composition of Mo|Se|Bi|Se precursors controls whether $[(BiSe)_{1+\gamma}]_1[(MoSe_2)]_1$ or $[(Bi_2Se_3)_{1+\delta}]_1[(MoSe_2)]_1$ form. Both compounds are local free energy minima in the energy landscape and are close in composition. $[(Bi_2Se_3)_{1+\delta}]_1[(MoSe_2)]_1$ forms from Mo|Se|Bi|Se precursors when they contain the stoichiometric amount of Bi and Mo and excess Se. Presumably the excess amounts of Se in Mo|Se|Bi|Se reduces the amount of charge transfer from Bi to Mo, resulting in the nucleation and growth of 2H-$MoSe_2$, which is the only polymorph observed in the XPS of $[(Bi_2Se_3)_{1+\delta}]_n[(MoSe_2)]_1$ compounds.[25] Mixtures of $[(BiSe)_{1+\gamma}]_1[(MoSe_2)]_1$ and $[(Bi_2Se_3)_{1+\delta}]_1[(MoSe_2)]_1$ form if there is not sufficient excess Se. $[(BiSe)_{1+\gamma}]_1[(MoSe_2)]_1$ contains both 2H and 1T as measured in the XPS.[24]

Our results may explain the van der Waals epitaxy results when growth of Bi_2Se_3 layers were attempted on dichalcogenides. Bi_2Se_3 layers can be grown on semiconducting 2H-$MoSe_2$ using MBE[20-22] because the depositing Bi atoms cannot donate electrons to the $MoSe_2$ substrate. Bi_2Se_3 layers cannot be grown directly on metallic $NbSe_2$ using MBE[23] because the depositing Bi atoms donate electrons to the $NbSe_2$ substrate, enabling BiSe to form at the interface. The ability to donate charge depends on the electronic structure of the adjacent layer. Lattice matching is a less important parameter.

4.5. Conclusions

The self-assembly of Bi_2Se_3 layers from ternary M|Se|Bi|Se precursors depends strongly on the "substituent-like" effects of the neighboring M|Se layer. Bi|Se and Pb|Se|Bi|Se precursors respectively crystallized Bi_2Se_3 and $[(PbSe)_{1+x}]_1[Bi_2Se_3]_1$ through similar

reaction pathways, as neither sample contains a layer than can accept electrons. Ti|Se|Bi|Se and V|Se|Bi|Se precursors both formed a mixture of $[(BiSe)_{1+\gamma}]_1[(MSe_2)]_1$ and Bi_2Se_3, as the TMD layer acts as an electron acceptor, resulting in strong ionic interactions between the BiSe and TMD layers. Varying the composition of Mo|Se|Bi|Se precursor controls whether $[(BiSe)_{1+\gamma}]_1[(MoSe_2)]_1$ or $[(Bi_2Se_3)_{1+\delta}]_1[(MoSe_2)]_1$ form and the polymorph(s) of $MoSe_2$ that are present. Our results indicate the electronic properties of neighboring layers play a significant role in the synthesis of heterostructures, analogous to the role electron withdrawing and donating groups play in the reaction rates and formation of products in molecular chemistry. Understanding these interactions and their effect on the reaction pathway is vital for the design and synthesis of novel compounds for future applications.

4.6. Bridge

Chapter IV was previously published with co-authors in *Inorganic Chemistry* in 2021, where we determined that there are substituent-like effects in heterostructures that can impact their nucleation and growth. The electronic properties of the neighboring layer in a precursor impacted the formation of the final product in Bi and Se containing heterostructures. This may be another tunable parameter by which to control the formation of various products. I made the samples, collected and analyzed the diffraction data, and wrote the manuscript. My co-authors on this paper were Taryn M. Kam, who assisted in collecting and analyzing the diffraction data, and David C. Johnson, who was my advisor and edited the manuscript. The charge transfer observed in this paper prompted an exploration of the charge transfer from kinetic BiSe to $MoSe_2$, where Bi_2Se_3 acted as a buffer layer in the heterostructure.

CHAPTER V

SYNTHESIS AND ELECTRICAL PROPTERITES OF A NEW COMPOUND $(BISE)_{0.97}(BI_2SE_3)_{1.26}(BISE)_{0.97}(MOSE_2)$ CONTAINING METALLIC 1T-$MOSE_2$

5.0. Authorship Statement

Chapter V was published in *Chemistry of Materials* in 2021. Co-authors include Renae N. Gannon and Douglas L. Medlin, who collected and analyzed the HAADF-STEM data, Fabian Göhler and Thomas Seyller, who collected and analyzed the XPS data, and Aaron Miller, who collected and analyzed the electrical data. David C. Johnson is my adviser, and I am the primary author of the manuscript.

5.1. Introduction

Group 6 semiconducting transition metal dichalcogenides have been the subject of extensive research over the last several decades due to their potential applications in catalysis,[1-3] photovoltaics,[4] supercapacitors,[5] and rechargeable battery systems.[6] The structure of these MX_2 compounds (where M = Mo, W and X = S, Se) consists of a hexagonal layer of metal atoms sandwiched between two hexagonal chalcogen layers.[7-8] Depending on the stacking of these trilayers, several polymorphs are possible, with the semiconducting 2H polymorph being the most common with ABA BAB stacking. This stacking results in trigonal prismatic coordination of the metal.[9-10] The recent discovery that the Group 6 compounds transition from an indirect- to a direct- band gap semiconductor when the bulk material is scaled down to a monolayer has created significant excitement as one of the first examples of an emergent property in a monolayer.[11-13] The transition from an indirect to a direct band gap semiconductor, which increases absorption and photoluminescence, has great promise for applications in optical devices.[12,14-16]

Ternary and higher order compounds containing the Group 6 X-M-X trilayers can also have ABC stacking of the layers, resulting in octahedral coordination of the metal and metallic conductivity.[3,17-20] These structural and electronic changes were first discovered in the alkali intercalation of the Group 6 compounds.[18,21-22] The ability to vary the intercalant, change carrier concentration by varying the amount of intercalate, and the discovery of superconductivity in these compounds resulted in a surge of activity.[18,23-24] Haering and coworkers recognized the potential of these compounds as battery cathodes, leading to the first commercialized lithium ion batteries.[25] More recently, there has been surge in publications on single and few layer 1T-MX_2 compounds due to improved catalytic properties for hydrogen evolution[2-3] and reduced contact resistances in 1T-2H-1T source-channel-drain field effect transistors.[19,26]

The high mobility and the volatility of alkali metal intercalants creates challenges in their synthesis and in subsequent processing steps when adjacent to other compounds.[27] An alternative way to create 1T-MX_2 layers is the presence of an adjacent strong electron donating layer. MSe layers, where M = Sb, Bi or a rare earth metal, have been reported to donate charge to neighboring dichalcogenide layers in misfit layered compounds.[28] These MSe layers have much lower vapor pressures than typical intercalants and are much less likely to diffuse. A recent paper on $(BiSe)_{0.97}(MoSe_2)$ reported a 40/60 ratio of 1T/2H polymorph in the $MoSe_2$ layer, with a significant reduction in electrical resistivity relative to 2H $MoSe_2$.[29] To increase the fraction of 1T-MX_2, more charge donation is required. However, $[(BiSe)_{1+x}]_n(MoSe_2)$ compounds cannot be made, as multiple layers of BiSe are not stable next to each other.[30]

In this paper we report the synthesis, structure, and properties of $(BiSe)_{1+x}(Bi_2Se_3)_{1+y}(BiSe)_{1+x}(MoSe_2)$, probing how increasing the ratio

of BiSe/$MoSe_2$ layers affects the percentages of 2H and 1T polymorphs in the $MoSe_2$ layer. $(BiSe)_{1+x}(Bi_2Se_3)_{1+y}(BiSe)_{1+x}(MoSe_2)$ was targeted as isostructural compounds have previously been reported.[31] The synthesis of the desired heterostructure is nontrivial, as it is only kinetically stable and avoiding the formation of $[(Bi_2Se_3)_{1+y}]_2(MoSe_2)$ requires excess Bi and Se in the precursor. The $(BiSe)_{1+x}(Bi_2Se_3)_{1+y}(BiSe)_{1+x}(MoSe_2)$ formed crystallographically aligned with respect to the substrate, but this is due to the morphology of the precursor, not epitaxial growth. The extensive turbostratic disorder between the constituent layers indicates that epitaxial growth does not dominate the self-assembly of the precursor into the heterostructure. High-angle annular dark field scanning transmission electron microscopy (HAADF-STEM) images confirms the layered nature of $(BiSe)_{1+x}(Bi_2Se_3)_{1+y}(BiSe)_{1+x}(MoSe_2)$ and indicates that two different polymorphs of $MoSe_2$ are present. X-ray photoelectron spectroscopy (XPS) data also indicates that 1T-$MoSe_2$ is present in increased quantities relative to $(BiSe)_{0.97}(MoSe_2)$. Resistivity measurements of $(BiSe)_{1+x}(Bi_2Se_3)_{1+y}(BiSe)_{1+x}(MoSe_2)$ show it is metallic, which are consistent with the increased amount of 1T-$MoSe_2$ in the heterostructure. The Hall data is more complicated due to the heterogeneous mix of phases in the structures resulting in a change in carrier type as temperature is varied.

5.2. Experimental

Precursors targeting $(BiSe)_{1+x}(Bi_2Se_3)_{1+y}(BiSe)_{1+x}(MoSe_2)$ were synthesized *via* physical vapor deposition of the elements at pressures below 5×10^{-7} torr, using the repeating sequence Mo|Se|Bi|Se|(Bi|Se|Bi|Se)|Bi|Se. Bismuth and molybdenum were deposited using an electron beam gun and selenium was deposited using a Knudson effusion cell. A Si (100) wafer with a native oxide layer and fused quartz were used as substrates. The bulk crystalline

structures of the individual constituents were used calculate the desired amount of material in each layer such that each Mo|Se layer had the number of atoms required to form a single Se-Mo-Se trilayer of $MoSe_2$, each Bi|Se layer had the number or atoms required to form a bilayer of a rock salt structured BiSe and each (Bi|Se|Bi|Se) had the number or atoms required to form a quintuple Se-Bi-Se-Bi-Se layer of Bi_2Se_3. A previously published calibration method[32] was used to optimize the deposition parameters. X-ray fluorescence (XRF) intensities were collected with a Rigaku ZSX Primus-II with a rhodium X-ray tube to determine the amount of each metal deposited. The proportionality constant between XRF intensity and amount of Mo and Bi the film was determined by preparing samples of $MoSe_2$ and Bi_2Se_3 and using the Se proportionality constant previously reported.[32]

X-ray reflectivity (XRR) and specular x-ray diffraction (XRD) data was collected on a Bruker D8 Discover diffractometer using Cu-$K\alpha$ radiation. Grazing incidence in-plane XRD information was collected using a Rigaku SmartLab with a Cu source.

Precursors were annealed at targeted temperatures for 15 minutes in a glove box with a nitrogen atmosphere where O_2 pressure was below 0.5 ppm to promote their self-assembly into the crystalline products.

A cross-section of the sample was prepared with a FEI Helios Nanolab 600i DualBeam Scanning Electron Microscope (SEM)/Focused Ion Beam (FI) using standard lift-out methods.[33] A protective layer of Sharpie carbon and FIB deposited carbon was applied to the surface. High Angle Annual Dark Field-Scanning Transmission Electron Microscope (HAADF-STEM) images of the cross-section were collected on a probe-corrected Thermo Fisher Scientific Themis Z STEM at 300 keV.

X-ray photoelectron spectroscopy (XPS) measurements were carried out at room temperature at a pressure of less than 3×10^{-10} mbar using Al-Kα radiation from a SPECS XR-50M X-ray source with SPECS Focus 500 crystal monochromator, and a SPECS Phoibos 150 MCD-9 hemispherical analyzer equipped with a nine channeltron detector. Cleaving of samples prior to XPS measurements was done by mounting the sample between two steel plates using a combination of low-degassing EPO TEK H72 and H22 epoxy resins. Breaking of the top plate under the flow of dry nitrogen in the load lock of the UHV system exposes the buried interfaces of the film. Spectral analysis was carried out by fitting the high-resolution core level spectra with multiple Voigt-profiles. Lorentzian lifetimes widths used in the fits were determined beforehand on commercially available single crystals as well as MER-grown binary samples.

Temperature dependent resistivity measurements were collected on the samples between 24 and 298 K using the van der Pauw method on a home-built system.

5.3. Results and Discussion

Six precursors were deposited as we attempted to prepare $(BiSe)_{1+x}(Bi_2Se_3)_{1+y}(BiSe)_{1+x}(MoSe_2)$. The amounts of each element required to form 11 and 10 layers of a $(BiSe)_{1+x}(Bi_2Se_3)_{1+y}(BiSe)_{1+x}(MoSe_2)$ heterostructure were estimated using the lattice parameters and structures of the binary constituents and/or structurally related compounds (Table 5.1). The compositions, total thickness, and repeating layer thickness of each precursor are summarized in Table 5.1. The fluctuation of the measured amounts for the precursors around the targeted values reflects the reproducibility of the deposition but is valuable as our initial target value is only an estimate. Compositions for each precursor were determined from the

Table 5.1. Amounts of material and repeating thicknesses for samples targeting the $(BiSe)_{1+x}(Bi_2Se_3)_{1+y}(BiSe)_{1+x}(MoSe_2)$ nanoarchitecture.

Sample	Atoms / Å^2 per layer in precursor before annealing			Total Thickness (Å)	Number of Layers Deposited	Number of Layers Crystallized	Repeating Thickness (Å)
	Bi	Mo	Se				
Sample 1	3.88(8)	1.15(2)	6.5(3)	309.7(9)	11	10	28.37(2)
Sample 2	3.53(7)	1.37(3)	6.6(3)	308.7(5)	11	10	27.69(2)
Sample 3	3.19(6)	1.21(2)	7.6(4)	312.9(8)	11	10	28.49(2)
Sample 4	3.41(7)	0.90(2)	7.0(3)	291.2(7)	11	10	27.28(2)
Sample 5	3.46(7)	1.22(2)	7.0(3)	302.7(4)	11	-	27.78(2)
Sample 6	3.54(7)	1.15(2)	7.1(4)	315.0(8)	11	-	27.89(2)
(BiSe) (Bi_2Se_3) (BiSe) ($MoSe_2$)	3.71	1.18	6.8		11		28.06
	3.37	1.07	6.2		10		
(Bi_2Se_3)$_2$ ($MoSe_2$)	2.87	1.18	6.8		11		25.56
	2.61	1.07	6.2		10		

XRF intensities of each element for the total film and the previously described calibration method.[31] The precursors were closer in composition to the stoichiometry of $(BiSe)_{1+x}(Bi_2Se_3)_{1+y}(BiSe)_{1+x}(MoSe_2)$ than to the composition estimated for 11 or 10 layers of $[(Bi_2Se_3)_{1+y}]_2(MoSe_2)$, a potentially competing local free energy minima. The XRR patterns of all of the precursors contained a first order Bragg reflection from the sequence of deposited layers, indicating that the elements in the precursor did not completely mix during the deposition. The thicknesses of all of the repeating sequence of elemental layers were close to the estimated *c*-axis lattice parameter for the $(BiSe)_{1+x}(Bi_2Se_3)_{1+y}(BiSe)_{1+x}(MoSe_2)$ heterostructure (28.06 Å) determined by adding the *c*-axis lattice parameters of the constituents. The amounts of each element deposited in the repeating sequence Mo|Se|Bi|Se|(Bi|Se|Bi|Se)|Bi|Se suggests that forming 10 or 11 layers of $(BiSe)_{1+x}(Bi_2Se_3)_{1+y}(BiSe)_{1+x}(MoSe_2)$ would involve the smallest diffusion distances for the elements.

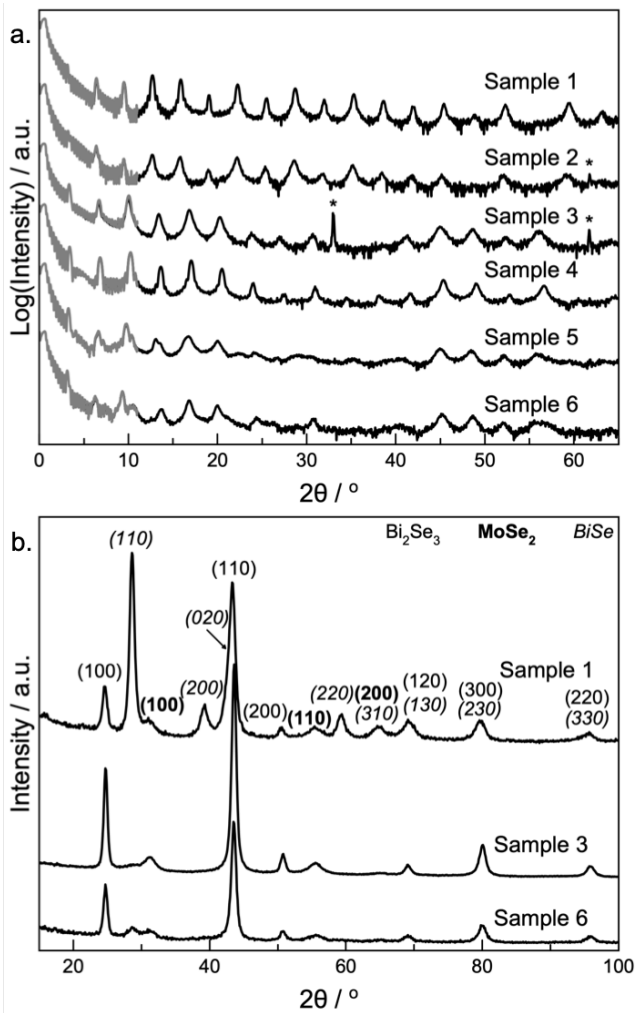

Figure 5.1. (a) XRR (gray) and specular x-ray diffraction and (b) representative in-plane x-ray diffraction patterns of the samples after annealing to 350°C. Asterisks in (a) mark the reflections that result from the Si substrate. The reflections for the different components are marked in (b) in varying fonts consistent with the labels in the top right corner.

All of the samples were annealed to 350°C to quickly evaluate what compounds self-assembled from the precursors and the resulting specular and in-plane diffraction patterns are shown in Figure 5.1. The reflections observed in the specular diffraction patterns of samples 1 and 2 index to single families of (00*l*) reflections with *c*-axis lattice parameters of 27.97(1) Å and 27.79(2) Å, respectively. Both are close to the estimated *c*-axis lattice parameter of

$(BiSe)_{1+x}(Bi_2Se_3)_{1+y}(BiSe)_{1+x}(MoSe_2)$ (28.06 Å). The in-plane reflections can be indexed as (*hk*0) reflections for three different constituents: two hexagonal unit cells and a unit cell with a rectangular basal plane. The calculated lattice parameters ($a_{hex,1}$ = 4.170(3) Å, $a_{hex,2}$ = 3.311(4) Å, a_{rect} = 4.600(1) Å and b_{rect} = 4.238(1) Å) are consistent with those expected for Bi_2Se_3 (a = 4.178(1) Å), $MoSe_2$ (a = 3.32(1) Å), and BiSe (a = 4.61(1) Å and b = 4.26(1) Å), respectively.[29,31] This diffraction data indicates that $(BiSe)_{1+x}(Bi_2Se_3)_{1+y}(BiSe)_{1+x}(MoSe_2)$ formed from these precursors. Surprisingly, samples 3 and 4 formed $[(Bi_2Se_3)_{1+y}]_2(MoSe_2)$ instead of the targeted compound $(BiSe)_{1+x}(Bi_2Se_3)_{1+y}(BiSe)_{1+x}(MoSe_2)$ whose composition they were closest to. The evenly spaced reflections in the specular x-ray diffraction yield *c*-axis lattice parameters of 26.38(1) Å and 25.96(1) Å, respectively, which are close to the estimated *c*-axis lattice parameter for $[(Bi_2Se_3)_{1+y}]_2(MoSe_2)$ (25.56 Å). The in-plane maxima can be indexed as (*hk*0) reflections to two different hexagonal unit cells with *a*-axis lattice parameters of 4.154(2) Å and 3.309(5) Å, which are close to those expected for Bi_2Se_3 and $MoSe_2$, respectively.[29,31] Intensity at ~28.6° 2θ suggests that a small amount of BiSe may have formed. The specular diffraction scans for samples 5 and 6 have sharp reflections at low angles and broader diffraction maxima at high angles, suggesting that the samples have not fully self-assembled at this temperature. The high angle reflections yield *c*-axis lattice parameters of 26.32(1) Å and 26.27(1) Å for samples 5 and 6, respectively, which is close to the estimated *c*-axis lattice parameter of $(Bi_2Se_3)_{1+y}]_2[(MoSe_2)$. The reflections observed in the in-plane pattern of sample 6 can be indexed to two different hexagonal unit cells. The lattice parameters calculated from the peak positions (a_{hex} = 4.158(3) Å, a_{hex} = 3.304(7) Å,) are consistent with those expected for Bi_2Se_3 and $MoSe_2$. Higher intensity at ~28.6° 2θ suggests that more BiSe is present in this sample than found in sample 3. The different products formed

shows how sensitive the reaction pathway is to the composition and structure of the precursors.

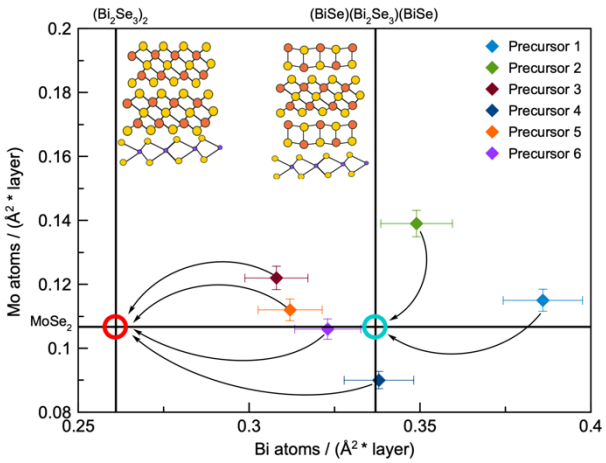

Figure 5.2. Amounts of Bi and Mo in the samples compared to the estimated amounts to form $[(Bi_2Se_3)_{1+y}]_2(MoSe_2)$ (red circle) and $(BiSe)_{1+x}(Bi_2Se_3)_{1+y}(BiSe)_{1+x}(MoSe_2)$ (blue circle).

In conventional high temperature solid state synthesis, the composition of the starting mixture determines the product or ratio of products that form. In reactions of layered precursors, the local compositions and nanoarchitecture become important parameters as they control what nucleates and the diffusion lengths required for growth. Due to reactions with the substrate and/or oxidation at the surface, it is common to form one or more fewer unit cells of the intended heterostructure than the number of layers deposited.[34] We observed this in the precursors studied here, as the Laue oscillations around the (002) reflections in samples 1-4 indicate that 10 unit cells formed from the 11 repeating sequences deposited. Figure 5.2 graphs the amounts of Mo and Bi in each of the samples, normalized to the 10 unit cells that crystalized, and arrows are used to indicate whether they formed $(BiSe)_{1+x}(Bi_2Se_3)_{1+y}(BiSe)_{1+x}(MoSe_2)$ or $[(Bi_2Se_3)_{1+y}]_2(MoSe_2)$. Samples 1 and 2 have enough Bi and Mo to make the ten layers of $(BiSe)_{1+x}(Bi_2Se_3)_{1+y}(BiSe)_{1+x}(MoSe_2)$ that formed. Samples 3-6 are all deficient in one element compared to

$(BiSe)_{1+x}(Bi_2Se_3)_{1+y}(BiSe)_{1+x}(MoSe_2)$. Instead of forming 9 unit cells of $(BiSe)_{1+x}(Bi_2Se_3)_{1+y}(BiSe)_{1+x}(MoSe_2)$, they instead evolve into $[(Bi_2Se_3)_{1+y}]_2(MoSe_2)$. We speculate that the significant excess of Se (5-13%) relative to the amounts of Bi and Mo in these precursors may have promoted the formation of Bi_2Se_3 rather than BiSe by Le Chatelier's principle. Since Laue oscillations are observed in samples 1-4, long range diffusion is required to transport the excess amounts of Bi and Mo out of the coherent crystalline domains. The excess Se probably acts as a flux. Samples with excess Mo relative to the compound formed have broader diffraction maxima, which we speculate is due to $MoSe_2$ inclusions, which reduces the size of coherent domains. Excess Bi has been observed to form Bi_2Se_3 on the top of the sample in other Bi containing heterostructures,[30,35] suggesting that it is more mobile than excess Mo. Our results indicate that the local free energy minima in the energy landscape for $(BiSe)_{1+x}(Bi_2Se_3)_{1+y}(BiSe)_{1+x}(MoSe_2)$ and $[(Bi_2Se_3)_{1+y}]_2[(MoSe_2)]$ are close in energy.

Specular and in-plane XRD scans were collected on sample 1 as a function of annealing temperature to determine the optimal formation conditions for $(BiSe)_{1+x}(Bi_2Se_3)_{1+y}(BiSe)_{1+x}(MoSe_2)$ (Figure 5.3). The specular XRD pattern of the as-deposited precursor contains reflections from two different sources. The sharp first order Bragg reflection results from the composition modulation of the precursor from the deposited sequence of elemental layers. The broader diffraction maxima at higher angles result from small crystalline domains that nucleated and grew during the deposition process. The broad diffraction maxima can all be indexed to a single family of (00*l*) reflections with a *c*-axis lattice parameter of 28.0(1) Å. This value is close to the estimated *c*-axis lattice parameter for $(BiSe)_{1+x}(Bi_2Se_3)_{1+y}(BiSe)_{1+x}(MoSe_2)$ (28.06 Å). Evidence for

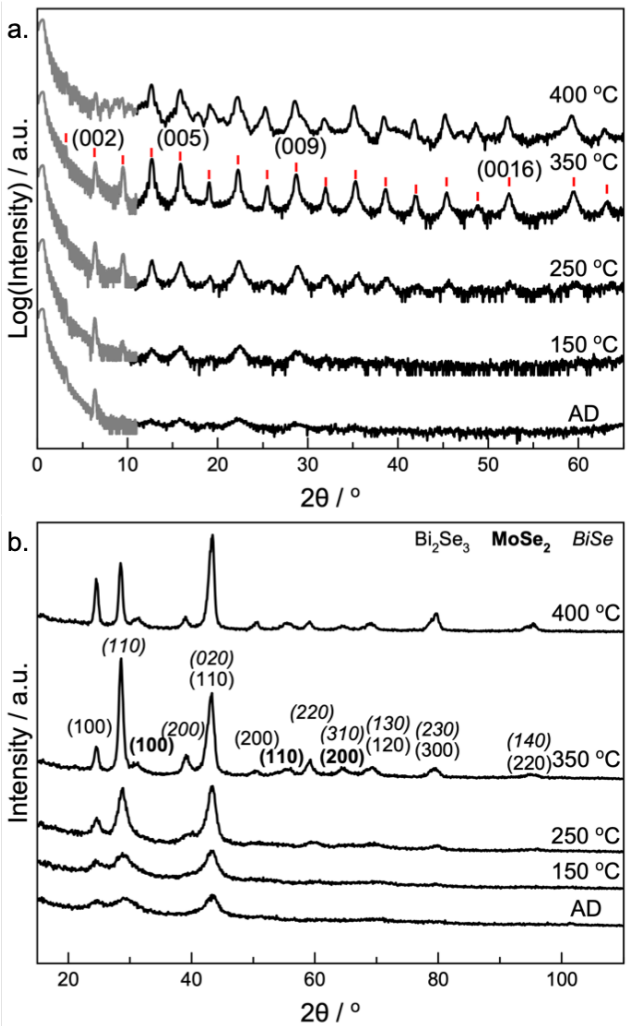

Figure 5.3. (a) XRR (gray) and specular XRD (black) patterns and (b) in-plane XRD patterns of Sample 1 as a function of temperature. The red lines indicate the 2θ values for reflections calculated using the *c*-axis lattice parameter of the structure (27.97(1) Å). Indices are indicated above some reflections.

crystallization during deposition is also found in the in-plane XRD pattern. The broad reflections are consistent with the (100) and (110) reflections for Bi_2Se_3 and the (110) and (020) reflections for BiSe.[31] After annealing at 150°C, there are slight increases in intensity of the existing reflections in both the specular and in-plane XRD patterns, but no new reflections are observed. The XRR pattern has fewer Kiessig fringes, suggesting that there is an increase in the roughness of the film as atoms diffuse. After annealing at 250°C, the intensity of reflections in

the specular and in-plane XRD patterns increase, linewidths decrease and additional reflections are visible in both patterns. Even more reflections appear after annealing at 350°C and the existing reflections in both patterns increase in intensity and decrease in linewidth. The XRR pattern indicates that the film smoothness increased during annealing at 350°C. Laue oscillations are now apparent between low angle Bragg reflections, indicating the sample is 10 repeating layers thick. The total thickness of the sample based on the Kiessig fringes in the XRR pattern is 306.9(3) Å. Based on the *c*-axis lattice parameter and the number of layers indicated from the Laue oscillations, the thickness of the crystalline BiSe-Bi_2Se_3-BiSe-$MoSe_2$ repeating structure is ~279.7 Å. The difference, ~27 Å, is approximately the thickness of 3 quintuple layers of Bi_2Se_3, which is observed in the STEM images discussed next. The lattice parameters calculated from both patterns remain consistent with the formation of $(BiSe)_{1+x}(Bi_2Se_3)_{1+y}(BiSe)_{1+x}(MoSe_2)$ at this temperature. The (00*l*) reflections in the specular XRD pattern lose intensity, broaden, and new reflections appear after annealing at 400°C, indicating that $(BiSe)_{1+x}(Bi_2Se_3)_{1+y}(BiSe)_{1+x}(MoSe_2)$ is decomposing. The in-plane reflections of BiSe decrease in the intensity, suggesting that the decomposition of this layer is responsible for the deterioration of the heterostructure. The annealing study indicates that $(BiSe)_{1+x}(Bi_2Se_3)_{1+y}(BiSe)_{1+x}(MoSe_2)$ begins to self-assemble during the deposition and the self-assembly is completed and excess Bi and Se diffuse to the top of the film after annealing at 350°C.

A HAADF-STEM image from a cross section of sample 1 annealed at 350°C is contained in Figure 5.4. The 10 repeating units of $(BiSe)_{0.97}(Bi_2Se_3)_{1.26}(BiSe)_{0.97}(MoSe_2)$, containing a quintuple layer of Bi_2Se_3, a bilayer of BiSe, a trilayer of $MoSe_2$, and a bilayer of BiSe are

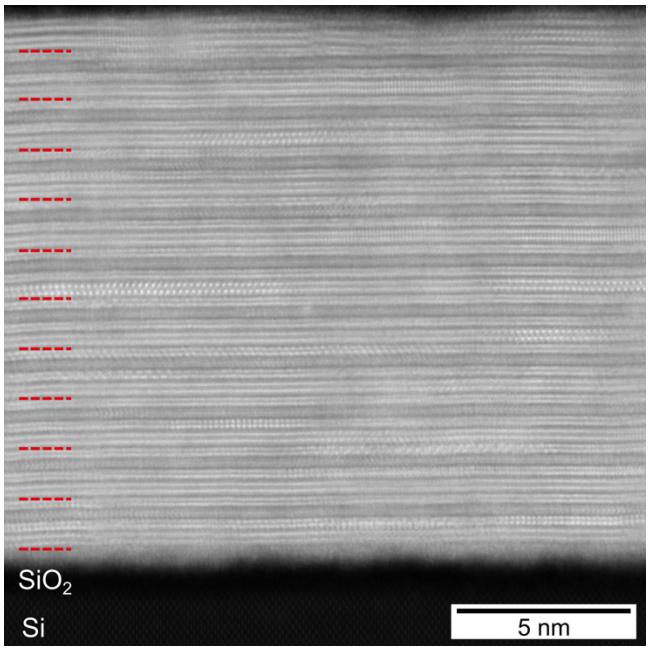

Figure 5.4. Representative HAADF-STEM image of the $(BiSe)_{0.97}(Bi_2Se_3)_{1.26}(BiSe)_{0.97}(MoSe_2)$ heterostructure annealed to 350°C on a Si substrate with its native SiO_2 surface layer. The 10 repeating sequences of layers resulting in Laue oscillations are indicated on the left with red dashed lines.

clearly visible. The 10 unit cells agree with the number determined from the Laue oscillations in the XRD pattern. There is a thin amorphous region present on the bottom of the film and two extra Bi_2Se_3 layers are present on the top of the sample. Similar diffusion of excess Bi and Se to the top of a sample forming Bi_2Se_3 layers was previously reported in other bismuth containing heterostructures.[30,35] The first crystalline layer in the heterostructure above the substrate is Bi_2Se_3, which is surprising since a Mo|Se layer was first in the deposition sequence. The energy dispersive x-ray spectroscopy (EDS) map shows that the bottom of the film contains an amorphous mixture including Mo, Se, Si and O (Figure B.1). The intensity of Se on the bottom of the film is less than that of the Se intensity in $MoSe_2$ layers, suggesting that at least some of the Mo may react with the SiO_2 coated Si surface during deposition or annealing. Grain boundaries within layers and varying

orientations within and between layers are present for all constituents, suggesting multiple nucleation sites. The resulting turbostratic disorder is commonly found in samples prepared from modulated precursors. [36-38]

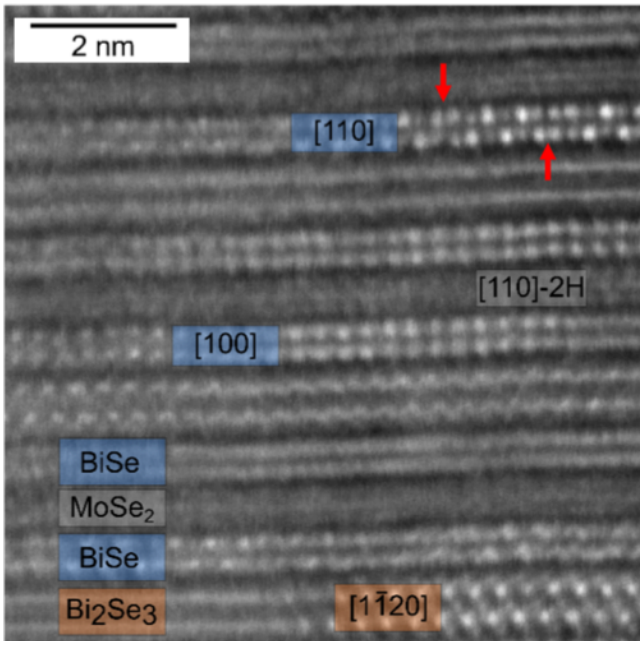

Figure 5.5. HAADF-STEM image of the $(BiSe)_{0.97}(Bi_2Se_3)_{1.26}(BiSe)_{0.97}(MoSe_2)$ heterostructure with zone axes labeled for each constituent. Antiphase boundaries are observed in regions of the film containing BiSe orientated along the [110] zone axis and marked with red arrows.

A higher magnification HAADF-STEM image is shown in Figure 5.5 which clearly shows the atomically abrupt interfaces between the structurally different layers. Different layers having different zone axis orientations are observed, with the orientations changing both within and between layers. A single quintuple layer containing a Se-Bi-Se-Bi-Se stacking sequence is observed when the Bi_2Se_3 layer is oriented along a <11$\bar{2}$0> zone axis. Antiphase boundaries are clearly visible in BiSe layers when they are oriented along a <110> zone axis. The different orientations are thought to result from different nucleation sites both in the same and in different layers, resulting in the extensive rotational disorder observed.

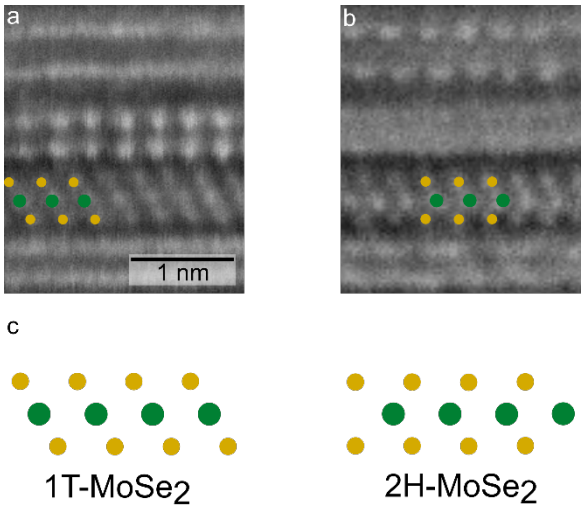

Figure 5.6. HAADF-STEM images which show a region of a) 1T-$MoSe_2$ and b) 2H-$MoSe_2$. The schematics below the images show the expected [110] zone axis images for 1T-$MoSe_2$ and 2H-$MoSe_2$ [Mo (green) and Se (yellow)].

While not both contained in the image in Figure 5.5, we identified regions in the sample where small domains of the two different polytypes of $MoSe_2$ could be identified when they are orientated down a <110> zone axis. The diagonal slashes shown in Figure 5.6a are consistent with an octahedrally coordinated 1T-$MoSe_2$ polymorph and the chevrons in Figure 5.6b are consistent with a trigonal prismatic coordinated 2H-$MoSe_2$ structure. That only small local regions are observable with these zone axis orientations reflects the small size of the $MoSe_2$ grains. XPS of the Mo 3d, Se 3d, and Bi 5d core levels was collected on cleaved films to gain information about the electronic states found in $(BiSe)_{0.97}(Bi_2Se_3)_{1.26}(BiSe)_{0.97}(MoSe_2)$, and representative spectra are shown in Figure 7. Spectral analysis of the Mo 3d core level spectrum (Figure 5.7a) reveals contributions from two different components, with Mo $3d_{5/2}$ binding energies of 228.25 ± 0.05 eV and 228.93 ± 0.05 eV. An additional broad component centered at 229.47 ±

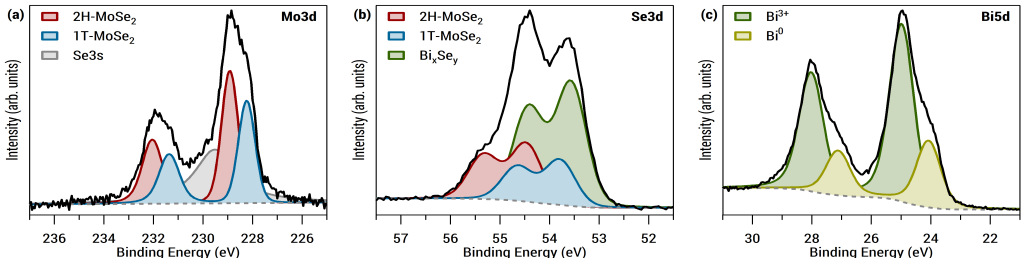

Figure 5.7. XPS analysis of the (a) Mo 3d, (b) Se 3d, and (c) Bi 5d core levels. Experimental data is shown as a solid black line, while the different components of the spectral analysis are in color.

0.11 eV is required to account for the signal from an overlapping Se 3s core level. The Mo 3d binding energies are consistent with those reported previously for 1T- and 2H-$MoSe_2$, both in $(BiSe)_{0.97}(MoSe_2)$ (228.3 ± 0.1 eV and 228.9 ± 0.1 eV) and the individual polymorphs,[2,29,39] consistent with the observations in the HAADF-STEM images. The percentage of each polytype can be estimated from the relative intensities of the different $MoSe_2$ components in the spectrum. The amount of 1T-polymorph is found to be between 40 and 60%, which is higher than that observed in $(BiSe)_{0.97}(MoSe_2)$.[29] Se is expected to be in a Se^{2-} oxidation state regardless of whether it is found in the $MoSe_2$ polymorphs or the bismuth constituents.[40] Previous reports show that the Se 3d core levels of 1T- and 2H-$MoSe_2$ are found at slightly different binding energies, and that the chemical shift between them is similar to that observed in the Mo 3d spectrum.[2] Any difference in binding energy for Se in Bi_2Se_3 and BiSe is too small to be distinguished. Our fit of the Se $3d_{5/2}$ spectrum is shown in Figure 5.7b, and the Se $3d_{5/2}$ binding energies (54.47 ± 0.05 eV for 2H-$MoSe_2$, 53.79 ± 0.05 eV for 1T-$MoSe_2$, and 53.57 ± 0.05 eV for Se bound to Bi) are consistent with those previously reported.[29] Two components are required to fit the Bi 5d spectrum (Figure 5.7c) as evident by the asymmetry of both the $5d_{3/2}$ and $5d_{5/2}$ lines towards lower binding energies. The position of the higher binding energy line (24.99 ± 0.05 eV) is consistent with Bi^{3+},

slightly larger than that observed in bulk Bi_2Se_3 (24.75 eV) and close to values reported for Bi atoms in BiSe (24.93-25.00 eV). The component at lower binding energy (24.13 ± 0.12 eV) has previously been assigned as Bi^0, due to Bi atoms at antiphase boundaries involved in Bi-Bi bonds between adjacent atoms (23.4-24.3 eV).[29,41] From the relative intensity of the two components, we can estimate that approximately 30-50% of the Bi atoms in the BiSe layers are involved in Bi-Bi bonds at antiphase boundaries. The percentage of Bi involved in Bi-Bi bonds at antiphase boundaries in $(BiSe)_{0.97}(Bi_2Se_3)_{1.26}(BiSe)_{0.97}(MoSe_2)$ is similar to the $(BiSe)_{0.97}(MoSe_2)$ heterostructure,[29] however there are two BiSe layers for each $MoSe_2$ layer in $(BiSe)_{0.97}(Bi_2Se_3)_{1.26}(BiSe)_{0.97}(MoSe_2)$ while there is only one per $MoSe_2$ layer in $(BiSe)_{0.97}(MoSe_2)$. Therefore, more charge donation to $MoSe_2$ occurs in $(BiSe)_{0.97}(Bi_2Se_3)_{1.26}(BiSe)_{0.97}(MoSe_2)$, increasing the percentage of 1T-$MoSe_2$. This interpretation is supported by density functional theory and crystal orbital Hamilton population calculations, which show that both charge donation to adjacent layers and antiphase boundary formation stabilize the BiSe rock salt structure by acting as "sinks" for excess electrons.[39] Charge donation from the BiSe layers to $MoSe_2$ layers stabilizes the octahedral 1T polymorph instead of the thermodynamic trigonal prismatic 2H polymorph.[19-20,29]

In-plane electrical resistivity data for several $(BiSe)_{0.97}(Bi_2Se_3)_{1.26}(BiSe)_{0.97}(MoSe_2)$ samples are shown in Figure 5.8 along with the resistivity reported for $(BiSe)_{0.97}(MoSe_2)$. The two compounds have strikingly different temperature dependencies. The resistivity of $(BiSe)_{0.97}(MoSe_2)$ exponentially increases as the temperature is decreased, indicating an activated conduction mechanism typical for a semiconductor.[29] Since 2H-$MoSe_2$ is semiconducting in the bulk,[42] the amount of metallic 1T-$MoSe_2$[18-20] is not enough to create a continuous conducting network. In contrast, the room temperature resistivities of the

$(BiSe)_{0.97}(Bi_2Se_3)_{1.26}(BiSe)_{0.97}(MoSe_2)$ samples are all very similar to each other, ~17(2) μΩm, with a near linear decrease in resistivity as the temperature decreases, indicating that this compound is metallic. We suspect that the metallic conductivity results from a continuous network of1T-$MoSe_2$ across the sample, consistent with the significantly higher percentage of 1T-$MoSe_2$ determined from our XPS data. While 1T-$MoSe_2$ is reported to be metallic,[18-20] we were unable to find resistivity data as a function of temperature for 1T-$MoSe_2$ reported in the literature. We used alkali metal intercalates of MoS_2, in which the MoS_2 has the 1T polymorph due to electron donation from the alkali metals, as a comparison instead. These compounds have room temperature resistivities ranging from 25 to 50 μΩm,[17] approximately twice the resistivity measured here for $(BiSe)_{0.97}(Bi_2Se_3)_{1.26}(BiSe)_{0.97}(MoSe_2)$, where the $MoSe_2$ sample is only ~ 20% of the volume of the unit cell.

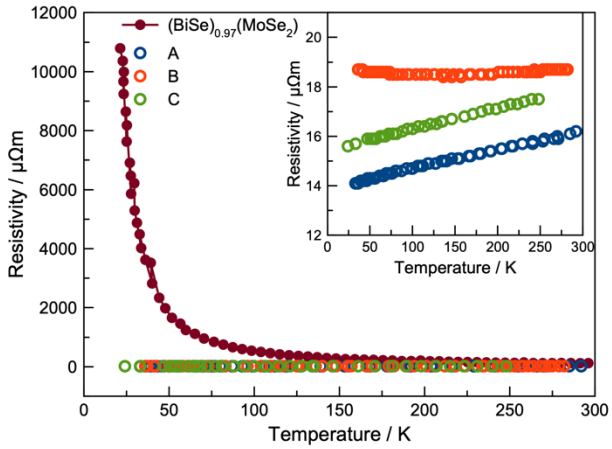

Figure 5.8. Temperature-dependent resistivity data of three $(BiSe)_{0.97}(Bi_2Se_3)_{1.26}(BiSe)_{0.97}(MoSe_2)$ samples (A, B, and C) from precursor 1 are plotted as a function of temperature for comparison with the $(BiSe)_{0.97}(MoSe_2)$ heterostructures. The inset figure graphs the data for the $(BiSe)_{0.97}(Bi_2Se_3)_{1.26}(BiSe)_{0.97}(MoSe_2)$ samples on an expanded scale.

In-plane Hall data was collected on $(BiSe)_{0.97}(Bi_2Se_3)_{1.26}(BiSe)_{0.97}(MoSe_2)$ to obtain more information about

its electrical behavior. The Hall data is compared to a structurally similar $(BiSe)_{0.97}(Bi_2Se_3)_{1.26}(BiSe)_{0.97}(TiSe_2)$ in Figure 5.9, as Hall data was not reported for $(BiSe)_{0.97}(MoSe_2)$.[29,31] The Hall coefficient is negative for $(BiSe)_{0.97}(Bi_2Se_3)_{1.26}(BiSe)_{0.97}(TiSe_2)$ across the temperature range, indicating electrons are the majority carrier.[31] Charge transfer of electrons from BiSe to $TiSe_2$ was suggested as the source of the carriers, with the electrons in the $TiSe_2$ layers dominating the conductivity.[31] The Hall coefficient of $(BiSe)_{0.97}(Bi_2Se_3)_{1.26}(BiSe)_{0.97}(MoSe_2)$ is also negative at room temperature, but changes sign as temperature is decreased below 235 K. Interpreting the Hall and conductivity data for $(BiSe)_{0.97}(Bi_2Se_3)_{1.26}(BiSe)_{0.97}(MoSe_2)$ is complicated, since we know from the XPS data that this compound contains a heterogeneous mix of 2H- and 1T-$MoSe_2$. Based on prior reports that 1T-$MoSe_2$ is metallic and 2H-$MoSe_2$ is semiconducting, the current is likely concentrated in the portion of the sample that is the 1T polymorph, which forms a low resistivity percolation pathway through the film. The small value of the Hall coefficient is consistent with the metallic behavior observed in the temperature dependence of the resistivity data. Since the sign of the Hall coefficient changes with temperature, the small magnitude of the Hall coefficient may also be a consequence of the electrons in the 1T-$MoSe_2$ layer competing with holes in the two BiSe layers in the unit cell.

The structural data, electrical transport data and XPS results are consistent with the BiSe layers donating charge to the $MoSe_2$ layers in $(BiSe)_{0.97}(Bi_2Se_3)_{1.26}(BiSe)_{0.97}(MoSe_2)$. The XPS data shows that the amount of 1T-$MoSe_2$ relative to 2H-$MoSe_2$ is larger than that observed in $(BiSe)_{0.97}(MoSe_2)$, and the resistivity of $(BiSe)_{0.97}(Bi_2Se_3)_{1.26}(BiSe)_{0.97}(MoSe_2)$ is lower than that of $(BiSe)_{0.97}(MoSe_2)$.[29,31] However, our understanding of how the properties

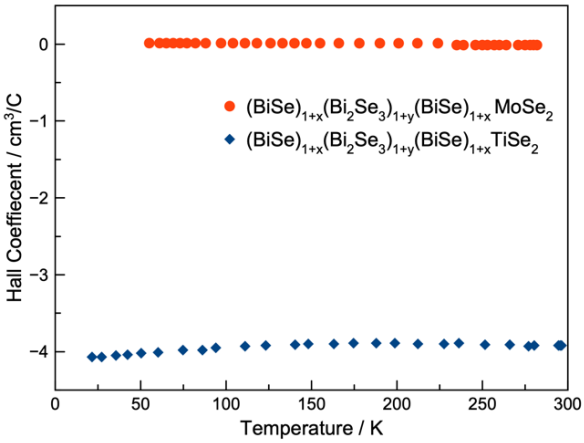

Figure 5.9: Temperature-dependent Hall data plotted as a function of temperature for $(BiSe)_{0.97}(Bi_2Se_3)_{1.26}(BiSe)_{0.97}(MoSe_2)$. Data for the structurally similar $(BiSe)_{0.97}(Bi_2Se_3)_{1.26}(BiSe)_{0.97}(TiSe_2)$ heterostructures is provided for comparison.

of monolayers change as a result of being adjacent to different substrates and constituents is limited. The Hall data indicates that at least two bands are contributing to the electrical conductivity. We have no data that indicates whether this contribution comes from the BiSe or the Bi_2Se_3 layers. Preparing homologous compounds with thicker Bi_2Se_3 (m) or $MoSe_2$ (n) layers, $(BiSe)_{0.97}[(Bi_2Se_3)_{1.26}]_m(BiSe)_{0.97}(MoSe_2)_n$, and correlating the electrical properties and the resulting percentage of 1T and 2H polymorphs of $MoSe_2$ with the values of *m* and/or *n* might enable us to better understand the interaction between constituent layers.

5.4. Conclusions

The new metastable heterostructure $(BiSe)_{0.97}(Bi_2Se_3)_{1.26}(BiSe)_{0.97}(MoSe_2)$ was prepared by self-assembly from designed precursors. Excess Bi was required to obtain $(BiSe)_{0.97}(Bi_2Se_3)_{1.26}(BiSe)_{0.97}(MoSe_2)$, which diffused during growth to form a cap of Bi_2Se_3. The *c*-axis and in-plane lattice parameters are consistent with the formation of $(BiSe)_{0.97}(Bi_2Se_3)_{1.26}(BiSe)_{0.97}(MoSe_2)$.

The HAADF-STEM imaging indicates that two different polymorphs of $MoSe_2$ form as small domains and that the BiSe layers contained antiphase boundaries. The XPS Bi 5d spectra contain intensity from two oxidation states of Bi, which is consistent with Bi^0 in Bi-Bi bonds at the antiphase boundaries of BiSe and Bi^{3+} in the Bi-Se bonds in Bi_2Se_3 and BiSe. Two oxidation states of Mo were also observed in the XPS Mo 3d spectra, consistent with the presence of both 2H- and 1T-$MoSe_2$. According to XPS, about 40- 60% of the $MoSe_2$ in the heterostructure was of the 1T polytype. The low resistivity values at room temperature and the metallic temperature dependence are consistent with the formation of a continuous network of 1T-$MoSe_2$. The heterogeneous mix of $MoSe_2$ polytypes complicates the interpretation of the Hall data. The low magnitude is consistent with the metallic behavior observed in the resistivity. The change in the carrier type as a function of temperature indicates that carriers in more than one band contribute to the conductivity. The thermal stability and metallic resistivity of $(BiSe)_{0.97}(Bi_2Se_3)_{1.26}(BiSe)_{0.97}(MoSe_2)$ might make it useful as an ohmic contact for devices containing $MoSe_2$ layers.

5.5. Bridge

Chapter V focused on the formation and electrical properties of a new compound $(BiSe)_{0.97}(Bi_2Se_3)_{1.26}(BiSe)_{0.97}(MoSe_2)$ containing kinetic 1T-$MoSe_2$. Due to the unexpected competing reaction pathways between the desired structure, control over the composition of the precursor was vital. A significant increase in the amount of 1T-$MoSe_2$ and metallic temperature dependent resistivity was observed in the sample. This chapter was previously published in *Chemistry of Materials* in 2021 with several co-authors, including Renae N. Gannon, Fabian Göhler, Aaron M. Miller, Douglas L. Medlin, Thomas Seyller, and David C. Johnson. I made the samples, collected and analyzed the diffraction data, analyzed the electrical date, and primarily wrote the

manuscript. Renae N. Gannon and Douglas L. Medlin collected and analyzed the electron microscopy data and edited the manuscript. Fabian Göhler and Thomas Seyller collected and analyzed the XPS data. Aaron M. Miller collected the electrical measurements. David C. Johnson was my advisor and edited the manuscript. Based on this study, we changed the nanoarchitecture of the heterostructure to further probe the charge transfer of the BiSe layer in the next chapter.

CHAPTER VI

EXPLORATION OF CHARGE TRANSFER TO NEIGHBORING LAYERS IN A NEW COMPOUND: $(BI_2SE_3)_{1.25}(BISE)_{0.97}(MOSE_2)$

6.0. Authorship Statement

This chapter was primarily written by me for the purposes of publication. David C Johnson is my advisor and edited the manuscript. Fabian Göhler and Thomas Seyller collected and analyzed the XPS data.

6.1. Introduction

Stacking 2D materials like Legos to form van der Waals heterostructures, an approach that has been used by many research groups since the discovery of graphene, has increased interest in 2D materials and resulted in the discovery of new emergent properties.[1-3] The ability to systematically change constituents, layer thicknesses, layer order and rotational orientation of layers in Van der Waals heterostructures has led to an increased understanding of interfacial interactions and the relationship between the structure and properties.[4-6] Synthesizing heterostructures with traditional synthetic approaches remains a challenge, however, as most heterostructures are only kinetically stable. Vapor phase growth techniques have been tuned to grow 2D materials on specific substrates, including other 2D materials. However, it is typically not possible to grow both A on B and B on A. Additional complications result from the high vapor pressure of chalcogenides and the interaction between constituents which can impact which phase nucleates at an interface.[7]

The Bi-Mo-Se ternary phase diagram illustrates these challenges and it has been of particular interest due to the emergent properties of $MoSe_2$ and the topological properties of Bi_2Se_3. $MoSe_2$ is a group 6 semiconducting transition metal dichalcogenide with trigonal prismatic

coordination and a large band gap that transitions from an indirect to a direct band gap as the bulk structure is scaled down to a single monolayer.[6,8-9] A kinetic polytype with octahedral coordination and metallic properties was first discovered from alkali intercalation.[10-12] Subsequent reports shown that 1T-$MoSe_2$ can also be synthesized in heterostructrures when the other constituent layers are strong electron donors. One such strong electron donating layer is rock salt structured BiSe, which is not present in the binary Bi-Se phase diagram.[13] Computational studies have proposed that the BiSe rock salt structure can be stabilized by either electron donation to a neighboring layer or localizing the electrons in Bi-Bi antiphase boundaries.[14] Bi_2Se_3 is a small band gap semiconductor which is commercially used as a thermoelectric material due to its high performance.[15] It is also a topological insulator.[16-17] There are a several other binary Bi-Se compounds, which structurally consist of layers of Bi_2Se_3 intergrown with Bi layers. A number of kinetically stable Bi-Mo-Se ternary heterostructures have been synthesized. $(BiSe)_{0.97}(MoSe_2)$ has previously been reported and ~40% of the $MoSe_2$ was found in the kinetic, metallic 1T polytype as a result of charge transfer from the BiSe layer to the neighboring $MoSe_2$ layer.[13] $(BiSe)_{0.97}(Bi_2Se_3)_{1.26}(BiSe)_{0.97}(MoSe_2)$ has been prepared, and it the percentage of 1T-$MoSe_2$ was reported to be larger than in $(BiSe)_{0.97}(MoSe_2)$. Bi_2Se_3-$MoSe_2$ heterostructures have been synthesized *via* molecular beam epitaxy to explore possible applications of the topological properties of Bi_2Se_3 in devices.[18-20] A recent publication highlighted the competition between the formation of Bi_2Se_3 and BiSe adjacent to dichalcogenides, which is impacted by the ability of the dichalcogenide to accept charge from the adjacent Bi-Se layer.[21]

This paper reports the synthesis, structure, and properties of $(Bi_2Se_3)_{1+y}(BiSe)_{1+x}(MoSe_2)$ to probe the competition between charge

transfer of the BiSe layer to $MoSe_2$ and Bi_2Se_3 and formation of Bi-Bi antiphase boundaries. $(Bi_2Se_3)_{1+y}(BiSe)_{1+x}(MoSe_2)$ formed crystalgraphically aligned with respect to the substrate from precursors that cover a large composition gradient around the estimated amounts. The nanoarchitecture of the precursor appears to be the key factor in forming this compound. We were quite surprised that X-ray photoelectron spectroscopy (XPS) data indicates that no 1T-$MoSe_2$ and that only ~30% of the Bi in the BiSe layer are in Bi-Bi bonds at antiphase boundaries. A shift in the binding energies of the Bi^{3+} indicate the electron is incorporated into the Bi_2Se_3 conduction band. The room temperature resistivity of $(Bi_2Se_3)_{1+y}(BiSe)_{1+x}(MoSe_2)$ is between those reported for $(BiSe)_{0.97}(MoSe_2)$ and $(BiSe)_{0.97}(Bi_2Se_3)_{1.26}(BiSe)_{0.97}(MoSe_2)$, despite the lack of 1T-$MoSe_2$. Room temperature Hall data indicates that the major carriers are electrons, and the lower carrier concentration than calculated based on the number of Bi^{3+} atoms in the BiSe layer suggests carriers are activated. Variable temperature measurements are needed to better understand the conduction in this new compound.

6.2. Experimental

Operating at pressures below 5×10^{-7} Torr, precursors were deposited in a Mo|Se|Bi|Se|Bi|Se sequence to mimic the nanoarchitecture of the $(Bi_2Se_3)_{1+y}(BiSe)_{1+x}(MoSe_2)$ crystalline product on a on a silicon wafer with a native oxide layer and fused quartz. Bismuth and molybdenum were deposited using an electron beam gun while selenium was deposited using a Knudson effusion cell. Specifics of the synthesis method have been previously described.[13,23-24] The precursors were subjected to annealing steps starting at 150°C for 15 minutes, which were increased by 50°C for each subsequent step. The samples were annealed in a N_2 atmosphere where the O_2 pressure was below 0.5 ppm.

The experimental amounts of material were measured using a Rigaku ZSX Primus-II with a rhodium X-ray tube and a previously published calibration method.[24] The target amounts of Bi, Mo, and Se were determined based on the number of atoms in the bulk unit cell or previously reported structures, which were normalized for the area of the basal plane. Determining the amount of material within the precursor and each subsequent annealing step with a proportionality constant has been previously discussed at length.[18,22,25]

Structural data was determined by X-ray reflectivity (XRR) and several X-ray diffraction (XRD) techniques. XRR and specular XRD data was collected on a Bruker D8 Discover diffractometer using Cu-*K*α radiation. The total thickness and layer thickness were determined based on the spacing of the Kiessig fringes and Bragg reflections, respectively. Grazing incidence in-plane XRD information was collected using a Rigaku SmartLab with a Cu source, which was used to determine the sequence of constituent formation and *a*- and *b*-axis lattice parameters.

Annealed samples were prepared for XPS measurements by cleaving the samples to expose the inner layers of the film. Cleaving was done by by mounting the sample in between two steel plates using a combination of low-degassing EPO TEK H72 and H22 epoxy resins and using dry nitrogen to break the top plate off of the sample in a load lock of the UHV system. Using Al-Kα radiation from a SPECS XR-50M X-ray source with SPECS Focus 500 crystal monochromator, and a SPECS Phoibos 150 MCD-9 hemispherical analyzer equipped with a nine channeltron detector, the XPS measurements were performed at room temperature and pressures less than 3×10^{-10} mbar. The resulting spectra were fit with multiple Voigt-profiles.

Room temperature resistivity and hall measurements were

collected on a custom-built system using the van der Pauw method.

6.3. Results and Discussion

Table 6.1. Amounts of Material, repeating thickness, and total thickness for precursors targeting a $[(Bi_2Se_3)_{1+\delta}]_1[(BiSe)_{1+\gamma}]_1[(MoSe_2)]_1$ nanoarchitecture.

Sample	Atoms of each element / Å^2			Number of constituent layers or unit cells based on M			Repeating Sequence Thickness (Å)	Total Thickness (Å)
	Bi	Mo	Se	BiSe + Bi_2Se_3 M = Bi	$MoSe_2$ M = Mo	unit cells M = Se		
Target	3.22	1.50	7.28	14	14	14	22.06	308.8
Sample 1	3.04(1)	1.60(8)	7.0(4)	13.0	15.0	13.6	22.02(5)	307.0(3)
Sample 2	3.45(1)	1.50(7)	7.3(4)	14.8	14.1	14.1	22.36(9)	327.1(8)

Two precursors were deposited to determine if it is possible to make a $[(Bi_2Se_3)_{1+\delta}]_1[(BiSe)_{1+\gamma}]_1[(MoSe_2)]_1$ heterostructure. A sequence of Mo|Se|Bi|Se|Bi|Se elemental layers was deposited 14 times in each precursor. The estimated amounts of each element required in each constituent layer to form each structurally unique layer in the heterostructure were calculated using the lattice parameters and structures of the binary constituent compounds and/or structurally related layers in other reported heterostructures. The amount of Mo and Se in each Mo|Se bilayer was intended to be that required to form a single $MoSe_2$ layer while one Bi|Se bilayer targeted BiSe and the other targeted Bi_2Se_3. Table 6.1 summarizes their measured composition, repeat thicknesses and total thicknesses of the as-deposited precursors. Sample 1 has enough Mo to make 15 $MoSe_2$ trilayers, enough Bi to make 13 repeats of $[(Bi_2Se_3)_{1+\delta}]_1[(BiSe)_{1+\gamma}$, and enough Se to make 13.6 unit cells of $[(Bi_2Se_3)_{1+\delta}]_1[(BiSe)_{1+\gamma}]_1[(MoSe_2)]_1$. Sample 2 has enough Mo to make 14 layers of $MoSe_2$, almost enough Bi to make 15 repeats of $[(Bi_2Se_3)_{1+\delta}]_1[(BiSe)_{1+\gamma}$ and enough Se to make the targeted 14 unit cells of $[(Bi_2Se_3)_{1+\delta}]_1[(BiSe)_{1+\gamma}]_1[(MoSe_2)]_1$. The repeating thicknesses of the precursors determined from the first order Bragg

reflection observed in the XRR resulting from the sequence of deposited layers are reasonable considering the number of deposited atoms in and both are very close to the estimated *c*-axis lattice parameter for the $[(Bi_2Se_3)_{1+\delta}]_1[(BiSe)_{1+\gamma}]_1[(MoSe_2)]_1$ heterostructure calculated by summing the *c*-axis lattice parameters of the constituent layers. This as-deposited data indicates that while both precursors have the approximate nanoarchitecture and composition in each layer to form the targeted heterostructure, significant rearrangement needs to occur. Precursor 1 can only form 13 unit cells of the heterostructure and excess Mo needs to diffuse away from the growth front. Precursor 2 can form 14 unit cells, but excess Bi needs to diffuse away from the growth front.

Specular and in-plane XRD collected on sample 1 as a function of annealing temperature to determine the sequence of phase formation is shown in Figure 6.1. The specular XRD pattern of the as deposited precursor contains sharp Bragg reflections resulting from the composition modulation of the precursor due to the deposited sequence of elemental layers. There are also two very broad and low intensity reflections between 10-20^o 2θ, which indicate that very small crystallites formed during the deposition. This is corroborated by the broad and low intensity reflections found in the in-plane diffraction patterns. After annealing at 200^o C, the broad reflections observed in both of the as deposited patterns increase in intensity and no new reflections are observed. After annealing at 300^o C new broad reflections appear and can be indexed as 00*l* reflections, yielding a *c*-axis lattice parameter of 22.4(1) Å. New reflections are also observed in the in-plane pattern and the previously existing reflections have higher intensities and decreased line widths. After annealing at 450 ^{o}C, additional, evenly spaced specular reflections are present and index to a single family of (00*l*) reflections with a *c*-axis lattice parameter of 22.387(6) Å, which is

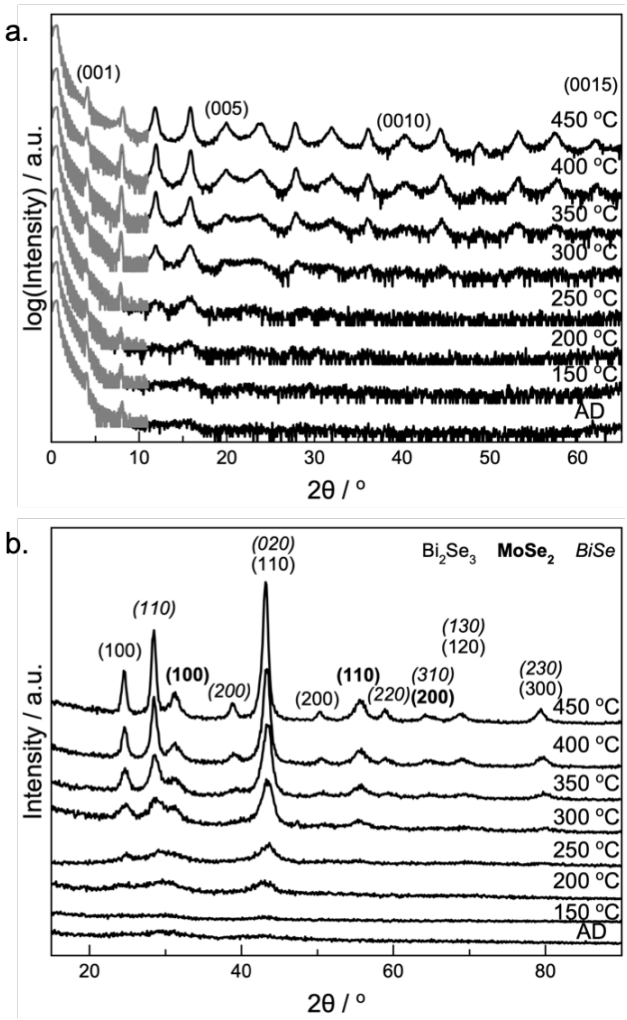

Figure 6.1. (a) Specular and (b) grazing incidence in-plane XRD patterns for the $[(Bi_2Se_3)_{1+\delta}]_1[(BiSe)_{1+\gamma}]_1[(MoSe_2)]_1$ sample 1 as a function of temperature.

slightly larger than the estimated *c*-axis lattice parameter of the targeted heterostructure based on the sum of the *c*-axis lattice parameters of the constituents (22.06 Å). The reflections in the in-plane XRD pattern can be indexed as (*hk*0) reflections for three different constituents: two hexagonal unit cells and a phase with a rectangular basal plane. The hexagonal unit cells have *a*-axis lattice parameters of 4.188(4) Å and 3.304(4) Å, which are consistent with those previously reported for Bi_2Se_3 and $MoSe_2$, respectively.[13,26] The rectangular basal plane with an *a*-axis lattice parameter of 4.639(2) Å and a *b*-axis lattice

parameter of 4.248(2) Å is consistent with those previously reported for BiSe.[13,26] The diffraction data suggests that annealing to 450 °C is necessary to self-assemble a $(Bi_2Se_3)_{1+y}(BiSe)_{1+x}(MoSe_2)$ heterostructure from the precursor. The diffraction data does not rule out possible small $MoSe_2$ inclusions as a result of the excess Mo and Se in the precursor.

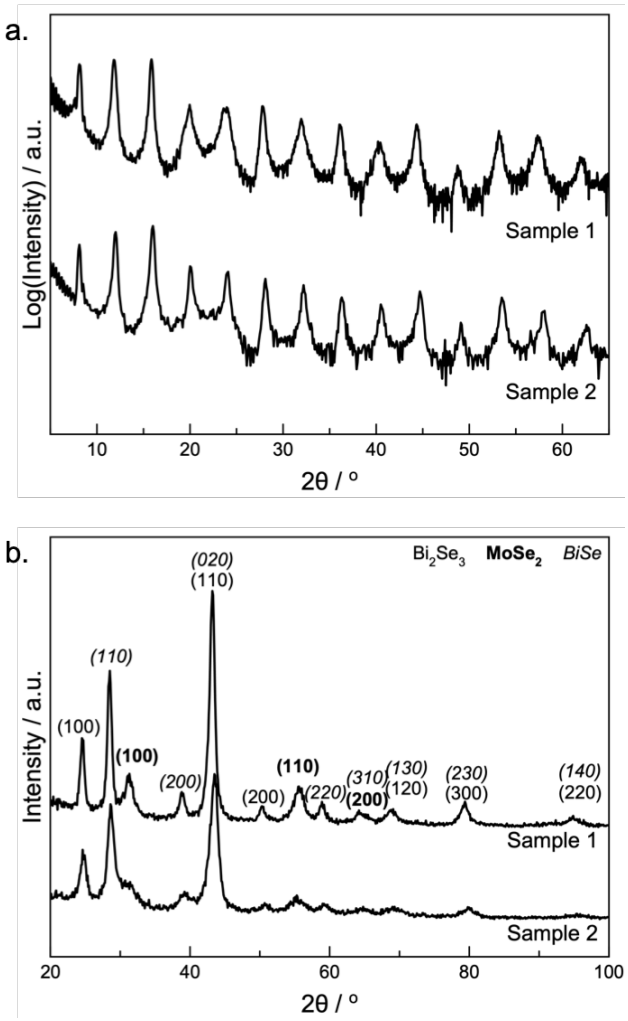

Figure 6.2. (a) Specular and (b) in-plane XRD patterns for samples 1 annealed at 450°C and for sample 2 annealed at 350°C.

Sample 2 was annealed to explore the impact of excess Bi on the self-assembly of the precursors and it had partially decomposed after it was annealed at 450°C. However, annealing sample 2 at 350°C resulted in specular and in-plane diffraction patterns that were very

similar to those collected on Sample 1 after it was annealed at 450 °C (Figure 6.2). The positions of the maxima are consistent between the two samples in both specular and in-plane diffraction patterns, indicating the two samples formed the same phase. This is evident from their similar *c*-axis lattice parameters of 22.387(6) Å and 22.393(4) Å for samples 1 and 2, respectively. The in-plane reflections in sample 2 can be indexed as belonging to two different hexagonal unit cells and one with a rectangular basal plane. The reflections observed in sample 2 yield *a*-axis lattice parameters of 4.159(5) Å and 3.322(9) Å for the two hexagonal unit cells and an *a*-axis lattice parameter of 4.600(4) Å and a *b*-axis lattice parameter of 4.222(3) Å for the rectangular basal plane. These in-plane lattice parameters are consistent with those of sample 1 and with the literature values previously reported for Bi_2Se_3 (a = 4.178(1) Å),[26] $MoSe_2$ (3.32(1) Å),[13] and BiSe (a = 4.61(1) Å and b = 4.26(1) Å) layers in similar heterostructures.[13]

The specular reflections in sample 1 are broader than those in sample 2, likely due to the excess amounts of Mo in the precursor that may react to form $MoSe_2$ inclusions in the structure. The differences in the initial compositions also impacts the annealing conditions, as sample 1 had to be annealed at 450 °C to obtain the targeted structure while the narrowest reflections are observed after annealing sample 2 at 350 °C and decomposition is observed at 400 °C. This data indicates that$[(Bi_2Se_3)_{1+\delta}]_1[(BiSe)_{1+\gamma}]_1[(MoSe_2)]_1$ forms from precursors with a range of initial compositions if they also have similar nanoarchitectures.

X-ray photoelectron spectroscopy (XPS) of the Mo 3d, Se 3d, and Bi 5d core levels was obtained to determine the oxidation states of the metals (Figure 6.3). The data collected at the Mo $3d_{5/2}$ binding energy can be fit using a doublet at 228.79 ± 0.05 eV and an additional component at 229.58 ± 0.12 eV to account for the signal from the Se 3s

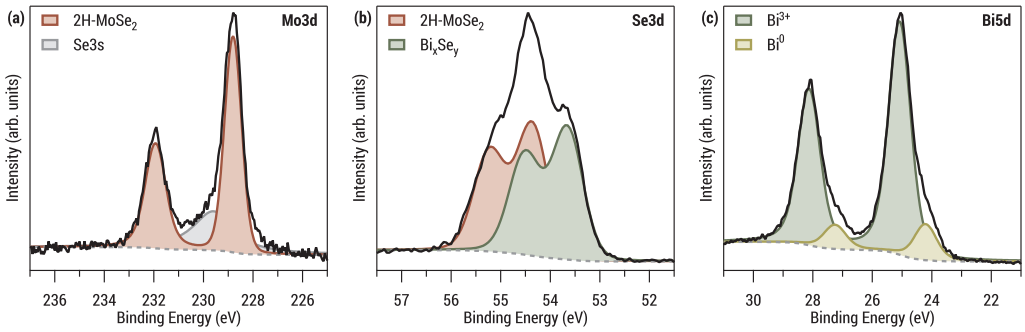

Figure 6.3. XPS analysis of a) Mo 3d, (b) Se 3d, and (c) Bi 5d core levels for $(Bi_2Se_3)_{1.26}(BiSe)_{0.97}(MoSe_2)$.

core level, which overlaps the Mo 3d spectrum. This Mo 3d binding energy is consistent with that reported previously for 2H-$MoSe_2$.[13,18,27-28] No evidence for 1T-$MoSe_2$ is found in the data. This result is surprising since 40% of the $MoSe_2$ in $(BiSe)_{0.97}(MoSe_2)$ and ~60% of the $MoSe_2$ in $(BiSe)_{0.97}(Bi_2Se_3)_{1.26}(BiSe)_{0.97}(MoSe_2)$ was reported to be 1T-$MoSe_2$,[13,18] presumably because the BiSe layers donate electrons to the $MoSe_2$ layers. The spectral analysis of the Se 3d core level contains two different binding energies, at 53.65 ± 0.05 eV and 54.36 ± 0.06 eV, which are consistent with Se bound to Bi and 2H-$MoSe_2$, (Figure 6.3b). Since 1T- and 2H-$MoSe_2$ have different Se 3d core level binging energies, this data is also consistent with there being no 1T-$MoSe_2$ in the sample.[13,18,27] Two components are required to fit the asymmetry of the Bi $5d_{3/2}$ and $5d_{5/2}$ lines at 25.05 ± 0.05 eV and 24.17 ± 0.05 eV. The higher binding energy is larger than expected for bulk Bi_2Se_3 but is consistent with the Bi^{3+} oxidation state observed previously in $(BiSe)_{0.97}(Bi_2Se_3)_{1.26}(BiSe)_{0.97}(MoSe_2)$.[18] The lower binding energy is consistent with previous reports for Bi^0 often observed in Bi-Bi bonds at antiphase boundaries.[13,29] The difference in the areas of the two components indicates that ~30% of the Bi in the BiSe layer are in Bi-Bi bonds.[30] The amount of antiphase boundaries formed is consistent with those previously measured for $(BiSe)_{0.97}(MoSe_2)$.[13,30] The XPS data

suggests that the BiSe layer forms a considerable number of Bi-Bi bonds rather than transferring enough charge to form 1T-$MoSe_2$.[14] As the binding energies consistent with 2H-$MoSe_2$ are within the error for the bulk values, it is unlikely any charge transfer occurred to this layer. The shifts to higher binding energies in the Bi and Se peaks relative to the bulk for Bi_2Se_3 may result from charge transfer from the BiSe.[30-31] This is consistent with previous reports, which determined that charge donation to the Bi_2Se_3 layer is favored over charge donation to the Mo|Se precursor layer.[30]

Table 6.2. Room temperature transport properties for $(Bi_2Se_3)_{1.25}(BiSe)_{0.97}(MoSe_2)$ with $(BiSe)_{0.97}(MoSe_2)$ and $(BiSe)_{0.97}(Bi_2Se_3)_{1.26}(BiSe)_{0.97}(MoSe_2)$ for comparison.

	Room Temperature		
Sample	Resistivity (μΩm)	Hall coefficient (cm^3/C)	Carrier Concentration (cm^{-3})
$(Bi_2Se_3)_{1.25}(BiSe)_{0.97}(MoSe_2)$	60(2)	-0.18(1)	$3.6(3) \times 10^{19}$
$(BiSe)_{0.97}(MoSe_2)$	121(4)	-0.036(2)	$3.6(2) \times 10^{20}$
$(BiSe)_{0.97}(Bi_2Se_3)_{1.26}(BiSe)_{0.97}(MoSe_2)$	18.1(6)	-0.012(1)	$5.4(3) \times 10^{20}$

Room temperature transport properties for $(Bi_2Se_3)_{1.25}(BiSe)_{0.97}(MoSe_2)$ are reported in Table 6.2 along with those for $(BiSe)_{0.97}(MoSe_2)$ and $(BiSe)_{0.97}(Bi_2Se_3)_{1.26}(BiSe)_{0.97}(MoSe_2)$. The room temperature resistivity of $(Bi_2Se_3)_{1.25}(BiSe)_{0.97}(MoSe_2)$ is in between those reported for $(BiSe)_{0.97}(MoSe_2)$ and $(BiSe)_{0.97}(Bi_2Se_3)_{1.26}(BiSe)_{0.97}(MoSe_2)$. The lower resistivity of $(BiSe)_{0.97}(Bi_2Se_3)_{1.26}(BiSe)_{0.97}(MoSe_2)$ relative to $(BiSe)_{0.97}(MoSe_2)$ correlates with the increased amount of 1T-$MoSe_2$ in $(BiSe)_{0.97}(Bi_2Se_3)_{1.26}(BiSe)_{0.97}(MoSe_2$ determined from XPS measurements, which is reasonable since bulk 1T $MoSe_2$ is metallic.[13,18,30] Since $(Bi_2Se_3)_{1.25}(BiSe)_{0.97}(MoSe_2)$ has no 1T-$MoSe_2$ and bulk 2H-$MoSe_2$ is semiconducting, we expected a higher resistivity than $(BiSe)_{0.97}(MoSe_2)$ and $(BiSe)_{0.97}(Bi_2Se_3)_{1.26}(BiSe)_{0.97}(MoSe_2)$. However, the

resistivity is between these two compounds with a resistivity of 60(2) μΩm. The resistivity is higher than the room temperature resistivities reported for epitaxially grown Bi_2Se_3 thin films (4-6 μΩm).[32]

The room temperature Hall coefficients for all three measurements are negative, indicating electrons are the major carrier type in the heterostructures. The magnitude of the Hall coefficient of $(Bi_2Se_3)_{1.25}(BiSe)_{0.97}(MoSe_2)$ is significantly higher than the other two heterostructures, which suggests a significantly lower carrier concentration. However, calculating carrier concentrations and average resistivity values for either $(BiSe)_{0.97}(MoSe_2)$ or $(BiSe)_{0.97}(Bi_2Se_3)_{1.26}(BiSe)_{0.97}(MoSe_2)$ may not be valid as these samples are composites containing a mixture of 1T and 2H-$MoSe_2$. Since 1T-$MoSe_2$ is metallic[10,33-34] and 2H-$MoSe_2$ is semiconducting[35] with a much higher resistivity, the current will be concentrated in the 1T regions when these layers are parallel with one another and the direction of current. The charge donation from BiSe occurs mainly to the metallic 1T part of the heterostructure instead of modulation doping the 2H-$MoSe_2$. In $(Bi_2Se_3)_{1.25}(BiSe)_{0.97}(MoSe_2)$, the XPS data suggests that charge transfer from the BiSe layer to the Bi_2Se_3 layer. We calculate that between 4.4(2) x 10^{22} electrons/cm^{-3} would be donated from BiSe to Bi_2Se_3 based on the amount of Bi^{3+} in the BiSe layer determined from XPS.[30] The estimated carrier concentration is several orders of magnitude larger than the experimental carrier concentration, indicating charge may be lost at defects within the sample, such as grain boundaries. High angle annular dark field scanning transmission electron microscopy images may provide insight into other possible defects. Assuming that all of these electrons need to be activated to conduct, we calculate a gap of 0.183(2) eV between the trap states and the Bi_2Se_3 conduction band. The calculated band gap is approximately half of the reported for bulk Bi_2Se_3 (0.3 eV).[36]

6.4. Conclusions

Probing the Bi-Mo-Se phase diagram for possible kinetic products with MER provides information about the reaction between elements and the interfacial interactions between layers. The $(Bi_2Se_3)_{1.25}(BiSe)_{0.97}(MoSe_2)$ formed from precursors that covered a large composition gradient, indicating that the energy well of the heterostructure is large. The BiSe layer was expected to stabilize via charge donation to the $MoSe_2$ layer or form antiphase boundaries. Instead, shifts in the XPS measured binding energies indicate that the BiSe layer stabilized its structure by donating charge to the Bi_2Se_3 layer or formed Bi-Bi bonds. Surprisingly, the room temperature resistivity was between those reported for $(BiSe)_{0.97}(MoSe_2)$ and $(BiSe)_{0.97}(Bi_2Se_3)_{1.26}(BiSe)_{0.97}(MoSe_2)$, despite the lack of 1T-$MoSe_2$. The room temperature Hall indicates that the major carriers are electrons, consistent with the charge transfer from BiSe to a neighboring layer. However, the experimental carrier concentration is lower than estimated based on the number of charge donating Bi atoms in the BiSe layer.

Lingering questions remain about this heterostructure. High angle annular dark field scanning tunneling electron microscopy images would provide insight into the stacking and layers of the heterostructure as well as probe for differences in structure of the constituents. Variable temperature measurements are necessary to understand the conduction in this compound.

6.5. Bridge

Chapter VI contains unpublished, co-authored work on the changes in structure and properties in a $(Bi_2Se_3)_{1.26}(BiSe)_{0.97}(MoSe_2)$ heterostructure. I made the precursors, analyzed the structural and electrical data, and primarily wrote the manuscript. Fabian Göhler and Thomas Seyller collected and analyzed the XPS data. David C. Johnson

was my advisor and edited the manuscript. Surprisingly, we determined there was another avenue for the BiSe layer to form besides the formation of Bi-Bi bonds or charge donation to the $MoSe_2$ layer. Instead, charge transfer occurs to the Bi_2Se_3 layer. To probe the stabilization of the BiSe layer through charge transfer, I collaborated with Fabian Göhler and Thomas Seyller to explore these previously discussed heterostructures with XPS.

CHAPTER VII

INFLUENCE OF NANOARCHITECTURES ON INTERLAYER INTERACTIONS IN LAYERED BI-MO-SE HETEROSTRUCTURES

7.0. Authorship Statement

Chapter VII was published in the *Journal of Physical Chemistry C* in 2021 in collaboration with Fabian Göhler, Constance Schmidt, Dietrich R. T. Zahn, David C. Johnson, and Thomas Seyller. Fabian Göhler is the first author of the publication. I synthesized and characterized the samples hear in and wrote the accompanying paragraphs. David C. Johnson is my advisor and edited the manuscript.

7.1. Introduction

A current hot topic in materials science is the stacking of quasi-two-dimensional (2D) layers into so-called van der Waals heterostructures.[1,2] Usually, this is done by either manual stacking of individual exfoliated layers[3] or sequential layer-by- layer growth via chemical or physical vapor deposition.[4] Both approaches have their limitations, however. Manual stacking is limited to bulk compounds that can be cleaved, so this approach cannot be used to prepare heterostructures containing metastable 2D sheets[4] or 2D layers of compounds with three-dimensional (3D) structures. Layer-by-layer growth is restricted, to constituents with compatible growth conditions for each individual layer, and this places a limit on the achievable complexity.[5] An alternative approach to synthesize a large number of layered heterostructures is the self-assembly of modulated, amorphous precursors by annealing at elevated temperatures.[6] By controlling the local composition and nanostructure of the precursors, one can dictate a reaction pathway toward a thin film with a desired layering sequence

of the constituent layers[7] if the product is at least kinetically stable in the local minimum of the free energy landscape.[8,9]

While the binary compound Bi_2Se_3 is thermodynamically stable, rock-salt-structured BiSe has so far only been stabilized in misfit layer chalcogenides[10] and their rotational disordered derivatives.[11] As reported previously, charge transfer from BiSe into $MoSe_2$ in the heterostructure $(BiSe)_{0.97}MoSe_2$ resulted in the coexistence of the stable, semiconducting 2H-phase and the metastable, metallic 1T-phase of $MoSe_2$.[12] Specifically targeting the synthesis of either polytype is of great interest for applications in devices based on two-dimensional semi- conductors, since it is possible to fabricate contacts between 1T- and 2H-MoX_2 that show significantly lower contact resistance compared with metal/2H-MoX_2 contacts and thus enhance device performance.[13,14]

To be able to control the incorporation of such metastable phases into new heterostructures, one needs to first understand how individual layers interact in different local environments. A series of heterostructures can be created by systematically changing the composition, structure, or thickness of individual building blocks. This allows a controlled investigation of interlayer interactions that occur in these compounds and also allows one to probe their effect on the stability of the constituents. X-ray photoelectron spectroscopy (XPS) is a versatile tool to investigate such interactions and determine the different electronic states of the elements in the hetero- structures. For example, the 1T- and 2H-polytypes of $MoSe_2$ can be distinguished due to the different binding energies of their respective Mo 3d and Se 3d core levels, where those of the metallic phase are found at lower binding energies than for the semiconducting phase.[15-17] Additionally, XPS has been widely used on a variety of layered structures to get insight into phenomena such as charge transfer,[18,19] changes in structure,[20] or

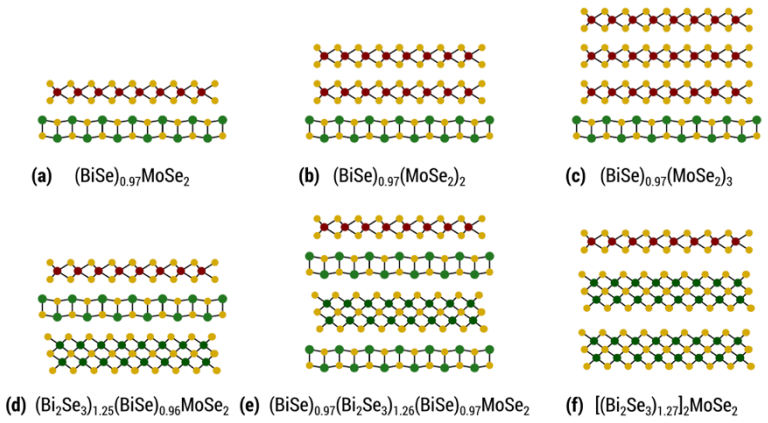

Figure 7.1. Schematic depiction of the various heterostructures investigated showing the structures of the individual building blocks. The samples were prepared as thin films consisting of the repeating stacking of these building blocks up to a total film thickness of about 30-50 nm via the modulated elemental reactants synthesis approach.

layer intermixing.[21] In this study, we compared two binary ($MoSe_2$, Bi_2Se_3) and six ternary Bi–Mo–Se compounds with different structural repeat units as shown in Figure 7.1: $(BiSe)_{0.97}(MoSe_2)_n$ with n = 1–3, $(Bi_2Se_3)_{1.25}(BiSe)_{0.97}MoSe_2$, $(BiSe)_{0.97}(Bi_2Se_3)_{1.26}(BiSe)_{0.97}MoSe_2$, and $[(Bi_2Se_3)_{1.27}]_2MoSe_2$. Using a combination of XPS and Raman spectroscopy, we were able to show the impact of the nanoarchitecture on the electronic and structural properties of the individual heterostructures.

7.2. Experimental

Elemental layers of Bi, Mo, and Se were deposited by means of physical vapor deposition in a high vacuum chamber at less than 1×10^{-6} Torr, with the repeat sequence mimicking the nanoarchitecture of the desired product. Opening and closing of the pneumatic shutters above the different elemental sources was controlled via a LabVIEW program, while evaporation rates were monitored using quartz crystal microbalances. Using a combination of X-ray fluorescence (XRF) and X-ray diffraction (XRD), the amount of material in the individual

elemental layers was calibrated,[22] so that a bilayer of Mo and Se yields a monolayer of $MoSe_2$ upon crystallization. Depending on composition, a bilayer of elemental Bi and Se may form either BiSe or Bi_2Se_3. Upon annealing on a hot plate in an inert N_2 atmosphere with less than 1 ppm of oxygen, the precursors self-assembled into the desired crystalline products. As was described in detail by Hadland et al.[12,23] for binary $MoSe_2$ and $(BiSe)_{0.97}MoSe_2$, the precursors were annealed at increasing temperatures to find the optimal annealing conditions for crystallization. The quality of the films was investigated using X-ray reflectivity, XRF, specular XRD, and in-plane XRD.

Prior to the XPS measurements, the thin film samples had to be cleaved to have a surface area free of oxides and other contaminants. This was achieved by attaching two steel plates to the back and front of the sample using low-degassing epoxy adhesives and subsequent breaking of the top plate in the load lock chamber of the vacuum system under a flow of dry nitrogen. Electrical contacts between the sample and sample holder were made using a silver-filled, conductive EPO-TEK H22 epoxy on the edges of the samples, while an insulating EPO-TEK H72 epoxy was used on the sample plane to avoid disturbance of the spectra by electrons emitted from the silver particles. In each experiment, both the upper and lower cleavage planes can be investigated. The cleaving process may also be repeated to reveal interfaces buried deeper in the film. The XPS system consisted of a SPECS XR 50M X-ray source equipped with a SPECS FOCUS 500 crystal monochromator providing Al Kα radiation and a SPECS PHOIBOS 150 MCD-9 hemispherical analyzer with a nine channeltron detector. The operating pressure of the system was below 3×10^{-10} mbar.

Raman spectroscopy was carried out in ambient conditions using a LabRam HR800 Raman system and a 2400 grooves per mm grating. The excitation wavelength was 514.7 nm.

7.3. Results and Discussion

7.3.1. Synthesis and Structure

Binary samples of $MoSe_2$ and Bi_2Se_3 as well as the various ternary Bi–Mo–Se heterostructures shown in Figure 7.1 were prepared from designed amorphous precursors *via* the modulated elemental reactants (MER) synthesis approach.[30] The precursors for the six targeted structures shown in Figure 7.1 were deposited on Si(100) substrates with a native SiO_2 layer, with a targeted total film thickness between 30 and 50 nm. They were annealed to form the targeted heterostructures and characterized via specular and in-plane X-ray diffraction (XRD) scans (Figure 7.2). The specular patterns exhibit evenly spaced reflections that are consistent with a single family of (00l) reflections, indicating that the samples are crystallographically aligned to the substrate and are single phase. The *c*-axis lattice parameter was determined for each of the samples (Table 7.1) and is consistent with the estimated *c*-axis lattice parameters determined from the sum of literature values of the respective constituent layers (*c*-Bi_2Se_3 ~9.5 Å, *c*-BiSe ~6 Å, and *c*-$MoSe_2$ ~6.56 Å).[12,23,27,31] The grazing incidence in-plane patterns of these samples confirmed that they are crystallographically aligned with the substrate, as all of the observed Bragg maxima can be indexed as (*hk*0) reflections from the constituent layers. The lattice parameters determined from the indexed reflections are summarized in Table 7.1. The in-plane lattice parameters of $MoSe_2$ in all of the compounds are similar and within the range reported for the a-axis lattice parameter of bulk $MoSe_2$.[28,29] The in-plane lattice parameters of Bi_2Se_3 in the hetero structures containing it are all slightly above the range reported for bulk Bi_2Se_3 ($4.115 \leq a \leq 4.151$ Å)

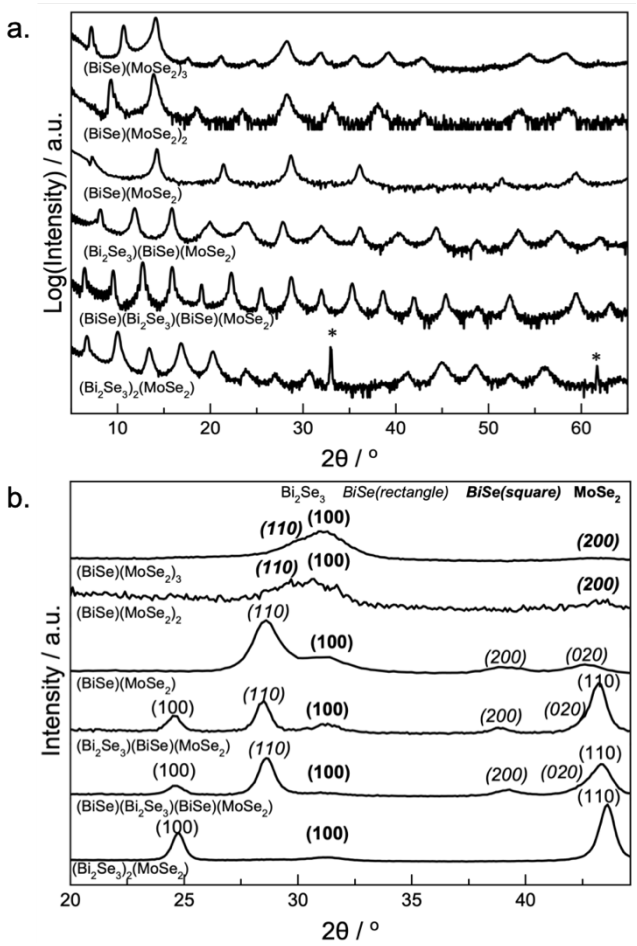

Figure 7.2. (a) Specular and (b) in-plane X-ray diffraction patterns of the annealed Bi-Mo-Se samples. The sharp reflections marked with an asterisk are consistent with the Si substrate.

with $[(Bi_2Se_3)_{1.27}]_2MoSe_2$ closest to the bulk values.[24,25] The a-axis lattice parameters reported for the three Bi_2Se_3-containing compounds are, however, consistent with the reported *a*-axis lattice parameters when the thickness of Bi_2Se_3 is reduced to a few monolayers.[32] Surprisingly, the in-plane lattice parameters of BiSe change considerably in the compounds investigated. In $(BiSe)_{0.97}MoSe_2$, $(Bi_2Se_3)_{1.25}(BiSe)_{0.97}MoSe_2$, and $(BiSe)_{0.97}(Bi_2Se_3)_{1.26}(BiSe)_{0.97}MoSe_2$, the BiSe reflections indicate a rectangular in-plane unit cell, consistent with the presence of nonperiodic antiphase boundaries occurring perpendicular to the *a*-axis. The randomly located longer Bi−Bi bond

Table 7.1. Experimental Lattice Parameters of the Annealed Bi-Mo-Se Heterostructures.

Lattice parameters (Å)						
	estimated c axis (Å)	c-axis lattice parameter	Bi_2Se_3 a	BiSe a	BiSe b	$MoSe_2$ a
Range of reported values			4.115 - 4.151	4.45(2)-4.571(1)	4.23(2)-4.247(1)	3.289 – 3.32
References			24, 25	26, 27	26, 27	28, 29
$(BiSe)_{0.97}(MoSe_2)_3$	25.68	25.013(2)		4.22(2)	4.22(2)	3.316(9)
$(BiSe)_{0.97}(MoSe_2)_2$	19.12	18.670(8)				
$(BiSe)_{0.97}(MoSe_2)_1$	12.56	12.45(2)		4.61(1)	4.26(1)	3.32(1)
$(Bi_2Se_3)_{1.25}(BiSe)_{0.97}(MoSe_2)$	22.06	22.376(6)	4.17(1)	4.685(3)	4.202(1)	3.303(6)
$(BiSe)_{0.97}(Bi_2Se_3)_{1.26}(BiSe)_{0.97}(MoSe_2)$	28.06	27.9777(9)	4.170(3)	4.600(1)	4.238(1)	3.311(4)
$[(Bi_2Se_3)_{1.27}]_2(MoSe_2)$	25.56	26.38(1)	4.154(2)			3.309(5)

distance averages with the shorter Bi−Se bond distances to yield a larger *a*-axis lattice parameter relative to the *b*-axis, which contains only Bi−Se bonds. This was previously observed in a number of heterostructures containing BiSe alternating with single dichalcogenide layers.[12,26,27] The in-plane diffraction patterns of the $(BiSe)_{0.97}(MoSe_2)_2$ and $(BiSe)_{0.97}(MoSe_2)_3$ samples, however, indicate a square unit cell that is 10% smaller than in the other samples. This was observed previously in $BiSe_{1+\delta}(NbSe_2)_n$, where the square unit cell for samples with n greater than 1 was correlated with the lack of antiphase boundaries in these samples.[26] The additional layers of $NbSe_2$ were thought to be efficient charge-accepting layers promoting the formation of Bi^{3+} via charge transfer over the formation of Bi^0 via antiphase boundaries. The decrease in antiphase boundaries and resulting increase in charge transfer stabilizing the rock-salt structure has been computationally observed.[33] The a-axis lattice parameter determined for the square unit cell is consistent with that previously reported (a = 4.24(1) Å).[26] To summarize, the specular and in-plane diffraction data as well as X-ray fluorescence (XRF) data (see Table C.1) used to determine the amount of each element in the films are consistent with the targeted nanoarchitectures as shown in Figure 7.1.

7.3.2. Results of X-ray Photoelectron and Raman Spectroscopy

After the structural characterization, XPS measurements were conducted on freshly cleaved samples of the different heterostructures. To interpret the raw data, a peak deconvolution procedure had to be applied to identify the different states contributing to the spectra. This was first performed on bulk-like binary samples of 2H-$MoSe_2$ and Bi_2Se_3 prepared via the MER synthesis.

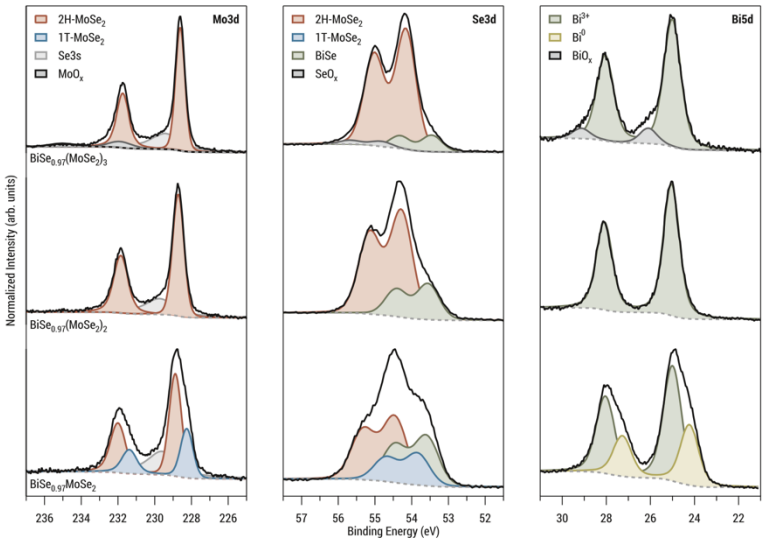

Figure 7.3. Representative XPS core-level spectra of $(BiSe)_{0.97}(MoSe_2)_n$ with n = 1 (bottom row),[12] 2 (middle row), and 3 (top row) along with the respective spectral analysis. The formation of 1T-$MoSe_2$, as well as the presence of the Bi^0 state, is only observed for n = 1. For n = 3, additional components are necessary to account for the presence of oxides.

Using a doublet of Voigt profiles, the observed binding energies for 2H-$MoSe_2$ are 228.80 eV for Mo $3d_{5/2}$ and 54.33 eV for Se $3d_{5/2}$. The Lorentzian lifetime widths of the two spin–orbit split components of the Mo 3d core level are 0.09 and 0.39 eV, respectively, due to a Coster–Kronig broadening of the $3d_{3/2}$ state.[34] The Gaussian peak width is 0.54 eV. An additional component around 229.5 eV is necessary to account for the interfering Se 3s core level. For the Se 3d

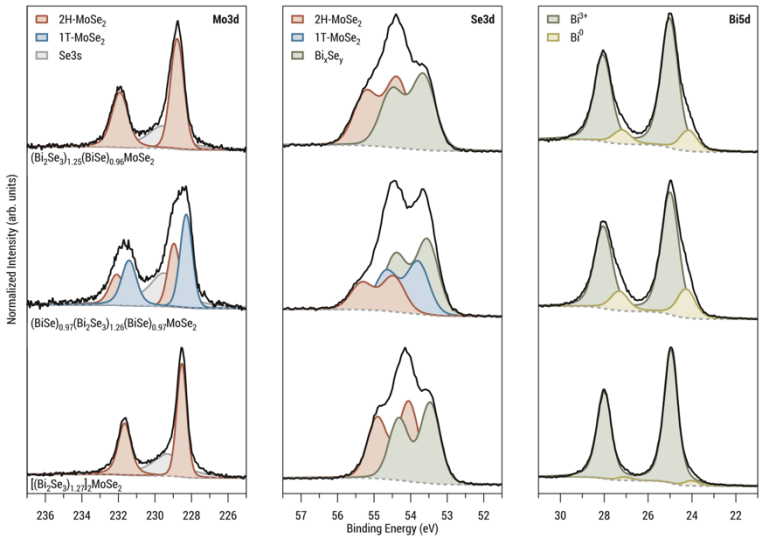

Figure 7.4. Representative XPS core-level spectra of $[(Bi_2Se_3)_{1.27}]_2(MoSe_2)$ (bottom row), $(BiSe)_{0.97}(Bi_2Se_3)_{1.26}(BiSe)_{0.97}MoSe_2$ (middle row), and $(Bi_2Se_3)_{1.25}(BiSe)_{0.97}MoSe_2$ (top row) along with the respective spectral analysis. While the formation of 1T-$MoSe_2$ is only observed in samples with two layers of BiSe in the repeat unit, all samples show the presence of the Bi^0 state.

core level, the lifetime width was experimentally determined to be 0.1 eV and the Gaussian peak width was 0.52 eV.

Bi_2Se_3 has a binding energy of 53.39 eV for Se $3d_{5/2}$ with a Gaussian width of 0.61 eV. For the electronic state of the bismuth atoms, we focused our analysis on the Bi 5d core level because even though the intensity of the Bi 4f is much higher, it overlaps with the Se 3p core level. Here, the Bi^{3+} oxidation state of Bi_2Se_3 is found at 24.74 eV with a lifetime width of 0.33 eV and a Gaussian width of 0.38 eV, which is in good agreement with measurements taken on a single-crystalline bulk sample. The peak shape of the Bi 5d core level of binary Bi_2Se_3 is slightly asymmetric, probably due to atomic vacancies or excess selenium causing a semimetallic rather than semiconducting behavior.[35] Since rock-salt-structured BiSe is not stable as a bulk compound,[33] it was not possible to synthesize and investigate a single-phase binary sample of BiSe.

Table 7.2. Results of the Analysis of the Mo 3d Core-Level Spectra.[a]

Sample	2H-$MoSe_2$ binding energy	1T-$MoSe_2$ binding energy	Fraction of 2H-$MoSe_2$ (%)	Mo 3d Gaussian width	Se 3s binding energy
2H-$MoSe_2$ (bulk-like)	228.80 ± 0.05		0	0.54	229.50 ± 0.10
Bi_2Se_3 (bulk-like)			-	-	229.73 ± 0.05
$(BiSe)_{0.97}(MoSe_2)_1$	228.91 ± 0.05	228.33 ± 0.05	25-36	0.75	229.78 ± 0.16
$(BiSe)_{0.97}(MoSe_2)_2$	228.65 ± 0.07		0	0.61	229.57 ± 0.16
$(BiSe)_{0.97}(MoSe_2)_3$	228.61 ± 0.07		0	0.55	229.43 ± 0.15
$(Bi_2Se_3)_{1.25}(BiSe)_{0.97}$ $(MoSe_2)$	228.79 ± 0.05		0	0.80	229.58 ± 0.12
$(BiSe)_{0.97}(Bi_2Se_3)_{1.26}$ $(BiSe)_{0.97}(MoSe_2)$	228.93 ± 0.05	228.25 ± 0.05	41-60	0.75	229.47 ± 0.11
$[(Bi_2Se_3)_{1.27}]_2(MoSe_2)$	228.52 ± 0.05		0	0.60	229.30 ± 0.05

[a]Mo $3d_{5/2}$ binding energies and Gaussian peak widths are averaged over all measurements for a certain sample type and given in eV. For the amount of 1T-$MoSe_2$, the observed minimum and maximum concentrations are given for each sample type. For binary Bi_2Se_3, only the Se 3s peak is observed in this region.

Table 7.3. Results of the Analysis of the Bi 5d Core-Level Spectra.[a]

Sample	Bi^{3+} binding energy	Bi^0 binding energy	Bi 5d Gaussian width	Fraction of Bi^0 (total), %	Fraction of Bi^0 (per BiSe), %
Bi_2Se_3 (bulk-like)	24.75 ± 0.05		0.38	0	
$(BiSe)_{0.97}(MoSe_2)_1$	24.99 ± 0.05	24.27 ± 0.09	0.79	34-42	34-42
$(BiSe)_{0.97}(MoSe_2)_2$	25.01 ± 0.05		0.67	0	0
$(BiSe)_{0.97}(MoSe_2)_3$	25.01 ± 0.05		0.73	0	0
$(Bi_2Se_3)_{1.25}(BiSe)_{0.97}$ $(MoSe_2)$	25.05 ± 0.05	24.17 ± 0.05	0.72	12-15	28-25
$(BiSe)_{0.97}(Bi_2Se_3)_{1.26}$ $(BiSe)_{0.97}(MoSe_2)$	24.99 ± 0.05	24.13 ± 0.12	0.77	19-30	32-49
$[(Bi_2Se_3)_{1.27}]_2(MoSe_2)$	24.755± 0.05	24.00 ± 0.05	0.55	4-7	

[a]Bi $3d_{5/2}$ binding energies and Gaussian peak widths are averaged over all measurements for a certain sample type and given in eV. The intensity if the Bi^0 state is given as a fraction of the total peak area as well as normalized to a single BiSe layer, assuming that all of the Bi atoms in Bi_2Se_3 are in the Bi^{3+} state.

Table 7.4. Results of the Analysis of the Se 3d Core-Level Spectra as a Superposition of One Component for Se Atoms Bound to Bi in BiSe and/or Bi_2Se_3 and Two Components for Se Bound in 2H- and 1T-$MoSe_2$, respectively.[a]

Sample	Bi_xSe_y binding energy	2H-$MoSe_2$ binding energy	1T-$MoSe_2$ binding energy	Se 3d Gaussian width
2H-$MoSe_2$ (bulk-like)		54.33 ± 0.05		0.52
Bi_2Se_3 (bulk-like)	53.39 ± 0.05			0.61
$(BiSe)_{0.97}(MoSe_2)_1$	53.62 ± 0.05	54.47 ± 0.05	53.89 ± 0.06	0.70
$(BiSe)_{0.97}(MoSe_2)_2$	53.50 ± 0.06	54.20 ± 0.07		0.62
$(BiSe)_{0.97}(MoSe_2)_3$	53.45 ± 0.05	54.16 ± 0.05		0.60
$(Bi_2Se_3)_{1.25}(BiSe)_{0.97}(MoSe_2)$	53.65 ± 0.05	54.36 ± 0.06		0.71
$(BiSe)_{0.97}(Bi_2Se_3)_{1.26}(BiSe)_{0.97}(MoSe_2)$	53.57 ± 0.05	54.47 ± 0.05	53.79 ± 0.05	0.67
$[(Bi_2Se_3)_{1.27}]_2(MoSe_2)$	53.46 ± 0.05	54.04 ± 0.05		0.59

[a]Se $3d_{5/2}$ binding energies and Gaussian peak widths are averaged over all measurements for a certain sample type and given in eV.

The results obtained from the binary samples were used to constrain the possible parameters when fitting the spectra of the heterostructures (Figures 7.3 and 7.4). As such, core hole lifetime widths, spin−orbit splitting, and branching ratios of the respective peak doublets were kept constant at the values determined from the binary compounds during the routine. Important fit parameters from the peak analysis of the Mo 3d, Bi 5d, and Se 3d core levels for the six different heterostructures are summarized in Tables 7.2−4, respectively. All values are either averaged over multiple (usually 2−4) measurements for each sample type or given as a range of values when appropriate. The average elemental composition of the measured surface area was derived from XPS peak intensities and can be found in Table C.1.

Figure 7.3 shows representative Mo 3d, Se 3d, and Bi 5d spectra of $BiSe_{0.97}(MoSe_2)_n$ samples with an increasing thickness of the dichalcogenide block in the repeat unit from n = 1 to 3. As reported previously,[12] the samples with n = 1 show two different states in the Mo 3d spectrum, which can be assigned to 2H-$MoSe_2$ at 228.91 eV and

1T-$MoSe_2$ at 228.33 eV. Three components are found in the Se 3d spectrum, one corresponding to Se bound in BiSe at 53.62 eV and one each for 2H-$MoSe_2$ and 1T-$MoSe_2$ at 54.47 and 53.89 eV, respectively. In the fit of the Se 3d core level, the chemical shift and intensity ratio of the two $MoSe_2$ components were constrained to the values observed in the Mo 3d spectrum. Two states are observed in the Bi 5d spectrum at 24.99 and 24.27 eV, respectively. The higher energy line is assigned to bismuth atoms in the regular rock-salt bonding of the BiSe layers, which should be in a Bi^{3+} state. The lower energy line is linked to a local distortion of the crystal structure, where Bi–Bi bonding is observed at so-called antiphase boundaries.[26] The bismuth atoms at an antiphase boundary can be viewed as being in a Bi^0 state. By comparing the intensity of the respective components to the total peak area, the percentage of 1T-$MoSe_2$ in the $MoSe_2$ layers as well as the amount of Bi atoms at antiphase boundaries in BiSe can be quantified.

By increasing the number of $MoSe_2$ layers to n = 2 or 3 (middle and top rows in Figure 7.3), only a single phase of $MoSe_2$ can be observed, with a binding energy that is slightly smaller than in the bulk. In the Bi 5d spectrum, only the Bi^{3+} state is observed, which implies that there is no formation of antiphase boundaries in BiSe in these samples, in excellent agreement with the in-plane diffraction data. This is similar to observations made in $BiSe_{1+\delta}(NbSe_2)_n$, where the number of antiphase boundaries decreased drastically with increased thickness of the $NbSe_2$ block in the repeat unit.[26,33] The sample with n = 3 shows a slight oxidation of the investigated surface area, as indicated by additional components at higher binding energies in the spectra. As expected, the intensity of the component assigned to selenium atoms bound in BiSe decreases with increasing n, from an average of 27% of the total peak area for n = 1, over 21% for n = 2, down to 12% for n = 3.

Figure 7.4 shows representative spectra of the samples containing Bi_2Se_3 along with or instead of BiSe. Peak analysis was carried out in the same manner as described above for the $BiSe_{0.97}(MoSe_2)_n$ series of samples. Only samples with two bilayers of BiSe in the repeat unit are observed to feature both phases of $MoSe_2$, while the $MoSe_2$ layers in $(Bi_2Se_3)_{1.25}(BiSe)_{0.97}MoSe_2$ and $[(Bi_2Se_3)_{1.27}]_2MoSe_2$ are single phase. The selenium atoms are expected to be in a Se^{2-} state regardless of whether they are bound in Bi_2Se_3 or BiSe.[33] Hence, only a single component was used in the spectral analysis to describe the whole block. As should be expected, with an increased thickness of the Bi_xSe_y block, the intensity of the component assigned to selenium atoms bound to bismuth in the Se 3d spectrum is much higher than in $BiSe_{0.97}(MoSe_2)_n$, at around 52% on average. All samples show the presence of the Bi^{3+} as well as the Bi^0 state in the Bi 5d spectrum, where the intensity of the Bi^0 state ranges from up to 30% in $(BiSe)_{0.97}(Bi_2Se_3)_{1.26}(BiSe)_{0.97}MoSe_2$ down to ≤7% in $[(Bi_2Se_3)_{1.27}]_2MoSe_2$.

The presence of the Bi^0 state in a sample containing only Bi_2Se_3 layers is unexpected. Since its intensity is very small, it is reasonable to assume that it is due to defects in the layered structure or inclusions of elemental Bi. Under the assumption that the Bi^0 state is only due to the presence of antiphase boundaries in the BiSe layers in $(Bi_2Se_3)_{1.25}(BiSe)_{0.97}MoSe_2$ and $(BiSe)_{0.97}(Bi_2Se_3)_{1.26}(BiSe)_{0.97}MoSe_2$, the fraction of atoms in the Bi^0 state per BiSe bilayer can be calculated. This is done by comparison of the in-plane unit cell area of BiSe and Bi_2Se_3 and relating this to the overall composition of the sample. Using the in-plane lattice parameters of BiSe and Bi_2Se_3 discussed earlier, 43% of all Bi atoms are bound in BiSe in $(Bi_2Se_3)_{1.25}(BiSe)_{0.97}MoSe_2$and 60% in $(BiSe)_{0.97}(Bi_2Se_3)_{1.26}(BiSe)_{0.97}MoSe_2$. Consequently, roughly a third of all bismuth atoms in BiSe are at an antiphase boundary in

$(Bi_2Se_3)_{1.25}(BiSe)_{0.97}MoSe_2$, while it is 32–49% in $(BiSe)_{0.97}(Bi_2Se_3)_{1.26}(BiSe)_{0.97}MoSe_2$. As can be seen from the last column in Table 7.3, these values are similar to those observed in $BiSe_{0.97}MoSe_2$.

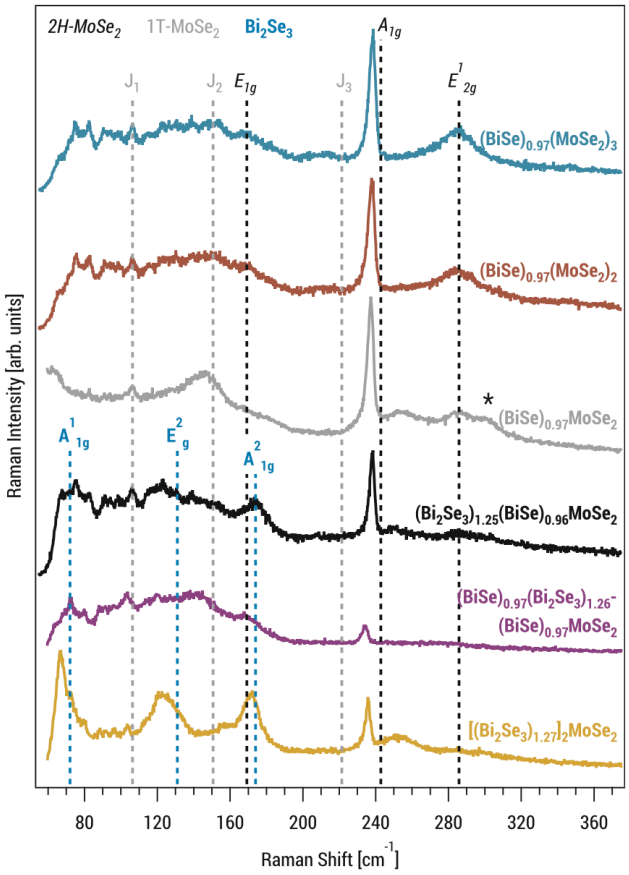

Figure 7.5. Representative Raman spectra of various Bi-Mo-Se heterostructures. Spectra are offset for clarity. The positions of the modes expected for (few-layer) 2H- and 1T-$MoSe_2$ and Bi_2Se_3, according to the literature,[36-38] are indicated by vertical lines. The signal marked with an asterisk stems from the silicon substrates.

In those samples that have both polytypes of $MoSe_2$, assigning the different components in the Mo 3d core-level spectra to 2H- and 1T-$MoSe_2$ is straightforward. However, as can be seen in Table 7.2, the binding energy of the Mo 3d core level is in between the values expected for either phase for $BiSe_{0.97}(MoSe_2)_2$, $BiSe_{0.97}(MoSe_2)_3$, and

$[(Bi_2Se_3)_{1.27}]_2MoSe_2$. Thus, Raman spectroscopy measurements were carried out on all samples to aid the interpretation of the XPS data. The resulting spectra are shown in Figure 7.5, along with vertical lines indicating the position of the Raman modes observed in few-layer, binary 2H-$MoSe_2$, 1T-$MoSe_2$, and Bi_2Se_3.[36-38] The prominent A_{1g} mode of 2H-$MoSe_2$ is present in all samples but found at lower wavenumbers in the heterostructures, as is expected when decreasing the layer thickness down to a monolayer.[39] An apparent shift of the A^1_{1g} and E^2_g modes of Bi_2Se_3 is also observed in $[(Bi_2Se_3)_{1+\delta}MoSe_2$.

While it appears that the spectrum for $BiSe_{0.97}MoSe_2$ features the expected J_1 and J_2 modes of 1T-$MoSe_2$, peak identification is not straightforward in the other samples, as there is a signal around 106 cm^{-1} even in the single-phase samples. Since the Raman spectrum of rock-salt BiSe was not known before, measurements were carried out on $BiSe_{1.00}TiSe_2$ and $BiSe_{1.11}NbSe_2$ samples as well. Apparently, there are a multitude of Raman modes in the range 60−180 cm^{-1} linked to rock-salt BiSe that are interfering with the expected modes of 1T-$MoSe_2$ and Bi_2Se_3 (see Figures C.1 and C.2). Thus, understanding the impact of antiphase boundary formation and different neighboring transition metal dichalcogenide (TMDC) layers on the Raman modes of BiSe should be a focus of further experimental and theoretical investigations.

In conclusion, we can correctly assign the single-phase samples to be of the 2H-polytype. Unfortunately, though, due to an overlap with the BiSe modes, identification of 1T-$MoSe_2$ appears to be not definitely possible using Raman spectroscopy in these samples.

7.3.3. Stabilization of 1T-$MoSe_2$ via Electron Transfer

It was hypothesized that the 1T-phase of $MoSe_2$ is stabilized via electron donation from BiSe in $BiSe_{0.97}MoSe_2$.[12] Occupied antibonding

states near the Fermi level in BiSe, which also explain why it is unstable in the bulk, make it an effective electron donor.[33] Due to the trivalent character of Bi, BiSe has one electron per formula unit to donate to the neighboring layer. However, as discussed above, the formation of Bi–Bi bonds at antiphase boundaries leads to a charge localization, reducing the number of available electrons.[33]

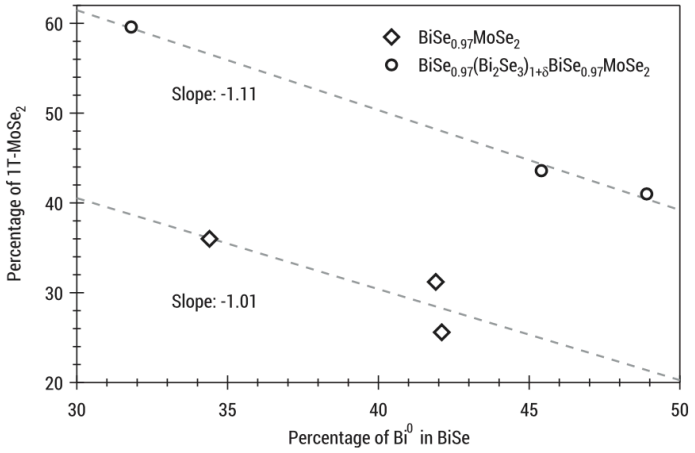

Figure 7.6. Correlation between the amount of 1T-$MoSe_2$ and the intensity of the Bi^0 state in the BiSe layers in $(BiSe)_{0.97}(MoSe_2)$ and $(BiSe)_{0.97}(Bi_2Se_3)_{1.26}(BiSe)_{0.97}(MoSe_2)$. Each data point represents the surface area measured after independent cleaving attempts. The data set for both sample types appear to follow a linear trend with a similar slope.

Therefore, an increased number of antiphase boundaries in the BiSe layers should lead to a reduced amount of 1T-$MoSe_2$ in the heterostructures. Since the number of antiphase boundaries apparently varies throughout the film, this hypothesis can be tested by plotting the percentage of 1T-$MoSe_2$ in the Mo 3d core level over the intensity of the Bi^0 state per BiSe bilayer, as can be seen in Figure 7.6. Each data point represents a different surface area, measured after an individual cleaving attempt, for the two sample types $BiSe_{0.97}MoSe_2$ and $(BiSe)_{0.97}[(Bi_2Se_3)_{1.26}(BiSe)_{0.97}MoSe_2$. Overall, the yield of 1T-$MoSe_2$ is higher in the samples with two layers of BiSe per repeat unit, as there

are more electrons available for donation into $MoSe_2$. The two data sets appear to show a linear dependence with a similar slope, where an increased number of antiphase boundaries reduces the amount of 1T-$MoSe_2$ by up to 20%. By doing a naive linear extrapolation of our data sets, one could expect a yield of around 70% 1T-$MoSe_2$ in $BiSe_{0.97}MoSe_2$ and 95% in $(BiSe)_{0.97}(Bi_2Se_3)_{1.26}(BiSe)_{0.97}MoSe_2$ at zero antiphase boundaries, which in the latter case would be close to a single-phase film. An effective way toward higher doping efficiency could be the replacement of Bi_2Se_3 in this heterostructure with a layer that suppresses antiphase boundary formation in BiSe.[33]

Since Bi_2Se_3 has no electrons available for donation, it was expected that there would be no formation of 1T-$MoSe_2$ in $[(Bi_2Se_3)_{1.27}]_2MoSe_2$. This is indeed observed experimentally as Raman spectroscopy clearly identifies the films to be solely composed of the semiconducting 2H-$MoSe_2$. The hetero- structures are not without interlayer interactions though, as the binding energies of the XPS core-level spectra corresponding to the constituent layers are shifted from their respective bulk positions. For the $MoSe_2$ layers, the Mo 3d as well as Se 3d core levels are shifted by about 0.3 eV toward lower binding energies. In a rigid band model, this can be explained by electron extraction out of the $MoSe_2$ layers, which lowers the Fermi level from inside the band gap to the top of the valence band. Since XPS binding energies are measured with respect to the Fermi level, this leads to the observed shift toward lower binding energies. In contrast, the Bi 5d and Se 3d core levels of Bi_2Se_3 are shifted toward higher binding energies by 0.20 and 0.07 eV, respectively. As Bi_2Se_3 is a small gap semiconductor with a band gap of about 0.3 eV,[35] this shift can be explained by the population of empty Bi 5p and Se 5p states above the band gap,[40] even though the observed shifts deviate slightly from a rigid

band model. Apparently, the Bi_2Se_3 layers act as an electron acceptor in the heterostructure.

This may also explain why no formation of 1T-$MoSe_2$ is observed in the $(Bi_2Se_3)_{1.26}(BiSe)_{0.97}MoSe_2$ heterostructures that contain one layer of Bi_2Se_3 and one layer of BiSe in the repeat unit. As shown above, the number of antiphase boundaries formed in the rock-salt BiSe layers in these samples is of the same order as in $(BiSe)_{0.97}MoSe_2$ and $(BiSe)_{0.97}(Bi_2Se_3)_{1.26}(BiSe)_{0.97}MoSe_2$, which is why additional electrons should be available to facilitate the formation of the metallic polytype during growth. However, only 2H-$MoSe_2$ is observed experimentally, and the binding energies are within error of the bulk-like binary samples. The binding energies of the Bi 5d and Se 3d core levels of the Bi_xSe_y block are found to be about 0.3 eV higher than those of bulk Bi_2Se_3, implying that additional charges were accepted by Bi_2Se_3. It appears that the energetic cost of storing additional electrons in the Bi_2Se_3 layer is smaller than the energy required to form the metastable 1T- polytype of $MoSe_2$.

The amount of charge that a single Bi_2Se_3 layer can accept has to be limited, since the formation of high percentages of 1T-$MoSe_2$ is observed in $(BiSe)_{0.97}(Bi_2Se_3)_{1.26}(BiSe)_{0.97}MoSe_2$. Looking at the observed binding energies for Bi_xSe_y, a shift of approximately 0.2 eV toward higher binding energies is observed in these samples as well. This suggests that the available electrons from BiSe are not only stored in 1T- $MoSe_2$ and at antiphase boundaries but to some extent also in Bi_2Se_3. Replacing the Bi_2Se_3 layer in these heterostructures with another layer that does not accept electrons could be another straightforward way to increase the yield of 1T-$MoSe_2$. Potential candidates could be layers that readily donate electrons themselves, such as PbSe or SnSe.[41]

7.3.4. Charge Distribution in $BiSe_{0.97}(MoSe_2)_n$

Our model of charge transfer from BiSe into the other layers has so far been successful in explaining the observations in four of the six heterostructures. However, the samples containing a single layer of rock-salt BiSe and two or three layers of $MoSe_2$ do not appear to fit within this framework. As the Raman spectra clearly show, both of these heterostructures contain 2H-$MoSe_2$. According to the XPS core-level spectra, the $MoSe_2$ layers are single phase and there are no antiphase boundaries in BiSe. The two known mechanisms to stabilize rock-salt BiSe are charge localization via antiphase boundary formation and electron donation into the neighboring TMD layers.[33] Since no Bi^0 states-that are characteristic for antiphase boundary formation-are observed in either sample type, the electrons have to be accepted into the $MoSe_2$ layers. A reduction in antiphase boundary formation was also observed in $BiSe_{1+\delta}(NbSe_2)_n$ with increasing n, as the available charges from BiSe could be distributed over multiple $NbSe_2$ layers.[26]

If the electrons from BiSe are taken up by the $MoSe_2$ layers, an increase in binding energy would be expected in a rigid band model for the Mo 3d and Se 3d core levels of $MoSe_2$, as additional states above the Fermi level have to be populated. The opposite is observed experimentally, with the binding energies compared to n = 1 being about 260 meV smaller for n = 2 and 300 meV smaller for n = 3. As discussed above, such a shift to lower binding energies would imply a loss of electrons within a rigid band model, which causes the Fermi energy to move away from the band gap toward the valence band maximum.

Since both constituent layers-BiSe and $MoSe_2$-cannot be electron donors, the assumption of a simple rigid band shift in the $MoSe_2$ layers

is probably not valid. The band structures of TMDs are known to undergo some drastic changes when approaching the monolayer limit,[42] with $MoSe_2$ changing from an indirect to a direct band gap when it is a monolayer. Only subtle differences are observed when comparing bi- and trilayer samples, with a major change in band alignment only occurring for a single layer.[43] According to the angle-resolved photo-electron spectroscopy (ARPES) measurements by Zhang et al.,[43] the position of the valence band maximum (VBM) is 1.53 eV below the Fermi level in monolayer $MoSe_2$. This energy difference decreases down to 1.17 eV for a bilayer, 1.09 eV for a trilayer, and 0.98 eV for eight layers of $MoSe_2$. Under the assumption that the core-level binding energies shift by the same amount as the VBM, we would expect to observe a 360 meV shift toward lower binding energies when going from n = 1 to 2 and a 440 meV shift when going from n = 1 to 3, before taking into account any changes that are due to band filling because of electron transfer from BiSe. Zhang et al.[43] also showed that the Fermi level shifts by 130 meV when populating the conduction band minimum with electrons in monolayer $MoSe_2$ (460 meV for eight layers). As discussed above, this shift should be observable as an increase in binding energy for the core-level spectra. A shift in the same order of magnitude is also observed when comparing the binding energies of bulk-like $MoSe_2$ and $BiSe_{0.97}MoSe_2$, suggesting that there is also some charge transfer into the regions with the semiconducting phase of $MoSe_2$ in this heterostructure.

Thus, the core-level shifts we observe experimentally for the $MoSe_2$ layers in $BiSe_{0.97}(MoSe_2)_n$ can be explained by a combination of a small increase in binding energy due to the population of the conduction band states and a larger decrease in binding energy due to a change in band structure with increased layer thickness. Mapping the band structure of the different heterostructures using ARPES

would be an ideal tool to test this hypothesis experimentally. Unfortunately though, conventional ARPES measurements are not possible on these kinds of samples due to the extensive rotational disorder that is inherent to samples prepared using modulated elemental reactants.

7.4. Conclusions

To summarize, we were able to investigate interlayer interactions in metastable, layered heterostructures built up from different stacking orders of BiSe, Bi_2Se_3, and $MoSe_2$. Charge transfer between the layers plays an important role in determining the crystal structure and electronic structure of the different sample types. The rock-salt-structured BiSe bilayers in the heterostructures are stabilized by electron transfer into the neighboring $MoSe_2$ and/or Bi_2Se_3 and localization of electrons in Bi^0 at antiphase boundaries. If charges can be distributed over multiple $MoSe_2$ layers, antiphase boundary formation is suppressed. The formation of the metallic 1T-polytype of $MoSe_2$ is only observed in $(BiSe)_{0.97}MoSe_2$and $(BiSe)_{0.97}(Bi_2Se_3)_{1.26}(BiSe)_{0.97}MoSe_2$and is facilitated via electron transfer from BiSe. In these samples, a decrease in antiphase boundary formation can drastically increase the yield of 1T-$MoSe_2$ in the heterostructures. Simple rigid band models may not be sufficient to describe interlayer interactions in such heterostructures, as the band structure of the individual layers changes depending on the thickness of the building block.

7.5. Bridge

Chapter VII probed the formed heterostructures using XPS to understand the stabilization of the kinetic BiSe layer and was previously published in *The Journal of Physical Chemistry C* in 2021. Fabian Göhler is the primary author, collected the XPS of these

samples, and wrote a majority of the manuscript. Thomas Seyller was his advisor and edited the manuscript. I am the second author on the manuscript, synthesized the samples, collected and analyzed the diffraction data, and wrote the accompanying paragraphs in the manuscript. David C. Johnson was my advisor and edited the manuscript. Constance Schmidt collected Raman spectroscopy on the samples with her advisor, Dietrich R. T. Zahn. They both edited the manuscript. The chapter further probes the interfacial interactions between layers in heterostructures that stabilized the formation of the constituents. In synthesizing the samples for this paper, I discovered a change in the structure of the BiSe layer, prompting an exploration of local composition impacts on structure of the constituents.

CHAPTER VIII

COMPOSITION DEPENDENT BASAL PLANE STRUCTURES OF BISE IN $(BISE)_{1+\delta}(MOSE_2)_3$ HETEROSTRUCTURES

8.0. Authorship Statement

This chapter was prepared for future publication. I am the primary author. David C. Johnson acted as my advisor and edited the paper. Other co-authors include Renae N. Gannon, Fabian Göhler, Aaron M. Miller, Douglas L. Medlin, Ping Lu, and Thomas Seyller.

8.1. Introduction

The following study probes the changes in the BiSe basal plane structure as a function of precursor composition. Three precursors were deposited with varying the amounts of material around that needed for 12 layers of $(BiSe)_{(1+x)}(MoSe_2)_3$. We expected the precursors with less amounts of material to form fewer layers of the heterostructure. While this did happen, and unexpected change in the BiSe basal plane was observed. In a precursor that had the amounts of material necessary to make the desired heterostructure, the BiSe basal plane proceeded through a square basal plane to form a rectangular basal plane in the crystalline superlattice. In the precursors that had less material, the BiSe basal plane remained square in the crystalline superlattice. Small changes in the *c*-axis lattice parameter were also reported depending on the basal plane of the BiSe structure. The Laue oscillations of the off-composition sample were also unexpected as they indicated more layers crystallized than were possible based on the amounts of material and high angle annular dark field scanning transmission electron microscopy images for the sample. We concluded that interference from the excess layers of $MoSe_2$ resulted in the increased number of Laue oscillations in the specular diffraction

patterns. This study has interesting implications for the formation of designed heterostructures.

8.2. Experimental

Precursors were synthesized by depositing a repeating sequence of elemental layers, (Bi|Se) + 3(Mo|Se), to mimic the composition along the *c*-axis of the targeted $(BiSe)_{1+x}(MoSe_2)_3$ compound. The deposition parameters for the Bi|Se layer were adjusted to yield a layer containing the correct number of atoms to form a bilayer of a rock salt structured BiSe. The deposition parameters for the Mo|Se layers were adjusted to yield a layer containing the correct number of atoms to form a single Se-Mo-Se trilayer of $MoSe_2$. The number of atoms / $Å^2$ for Bi, Mo, and Se actually deposited for each precursor was determined a previously published XRF calibration method.[1] X-ray fluorescence (XRF) intensities were collected for each precursor and subsequent annealing step with a Rigaku ZSX Primus-II with a rhodium X-ray tube. The precursors were annealed at increasing temperatures for 15 minutes in a glove box with a nitrogen atmosphere where O_2 pressure was below 0.5 ppm.

Structural data was collected on each precursor and after each annealing temperature using a Bruker D8 Discover diffractometer using Cu-$K\alpha$ radiation for the low angle and specular XRD and a Rigaku SmartLab with a Cu source for the in-plane XRD. Total thickness was determined based on the spacing of the Kiessig fringes in the low angle. Repeat layer thickness and *c*-axis lattice parameter were determined from the spacing of the Bragg reflections which *a*- and *b*-axis lattice parameters were determined from the in-plane Bragg reflections.

HAADF-STEM measurements were taken on cross-sections of the films, which were prepared with a FEI Helios NanoLab 600i DualBeam FIB-SEM using standard lift-out procedures. The images were collected

using either a probe-corrected Thermo Fisher Scientific Themis Z STEM at 300 keV or a FEI Titan G2 80–200 scanning transmission electron microscope (STEM) with a Cs probe corrector and ChemiSTEM technology (X-FEG and SuperX EDS with four windowless silicon drift detectors) operated at 200 kV.

XPS measurements were performed on a using Al-Kα radiation from a SPECS XR-50M X-ray source with SPECS Focus 500 crystal monochromator, and a SPECS. The samples were cleaved prior to measurements by mounting the sample in between two steel plates using a combination of low-degassing EPO TEK H72 and H22 epoxy resins. The samples were cleaved to expose the buried interfaces under the flow of dry nitrogen in a load lock of the UHV system. The measurements were performed at pressure of less than 3×10^{-10} mbar at room temperature. The analysis was performed on the core level spectra by fitting them with multiple Voigt-profiles.

8.3. Results and Discussion

Table 8.1. Amounts of Material and Lattice Parameters for $(BiSe)_{(1+x)}(MoSe_2)_3$ precursors.

	Total Atoms / Å^2			Number of layers based on Bi, Mo or Se			Repeating Thickness (Å)	Total Film Thickness
Sample	Bi	Mo	Se	BiSe	$MoSe_2$	$(BiSe)(MoSe_2)_3$ based on Se		
Target	1.24	3.84	8.9	12	36	12	25.68	308.16
Sample 1	1.25(3)	3.88(4)	9.0(3)	12.1	36.3	12.1	27.38(2)	324.7(5)
Sample 2	1.06(3)	3.52(4)	9.3(3)	10.3	33.0	12.5	27.63(2)	327.2(3)
Sample 3	0.97(3)	3.65(4)	9.1(3)	9.4	34.2	12.3	26.39(2)	320.6(5)

Precursors were deposited in a repeating sequence to mimic the formation of $(BiSe)_{(1+x)}(MoSe_2)_3$ and the amounts of each element and the structure of the as deposited precursors are reported in Table 8.1.

The amount of each metal deposited in sample 1 are very close to the amount required to form 12 layers of $(BiSe)_{1+x}(MoSe_2)_3$ and there is a slight excess of Se. Therefore, we expected this precursor to form the expected heterostructure *via* a near diffusionless reaction pathway and the excess Se should evaporate upon annealing. Samples 2 and 3 both have a significant excess of Se and do not have enough of either Bi and Mo to form 12 layers of the desired heterostructure. The amount of Bi is the rate limiting reagent in both samples. Significant diffusion is

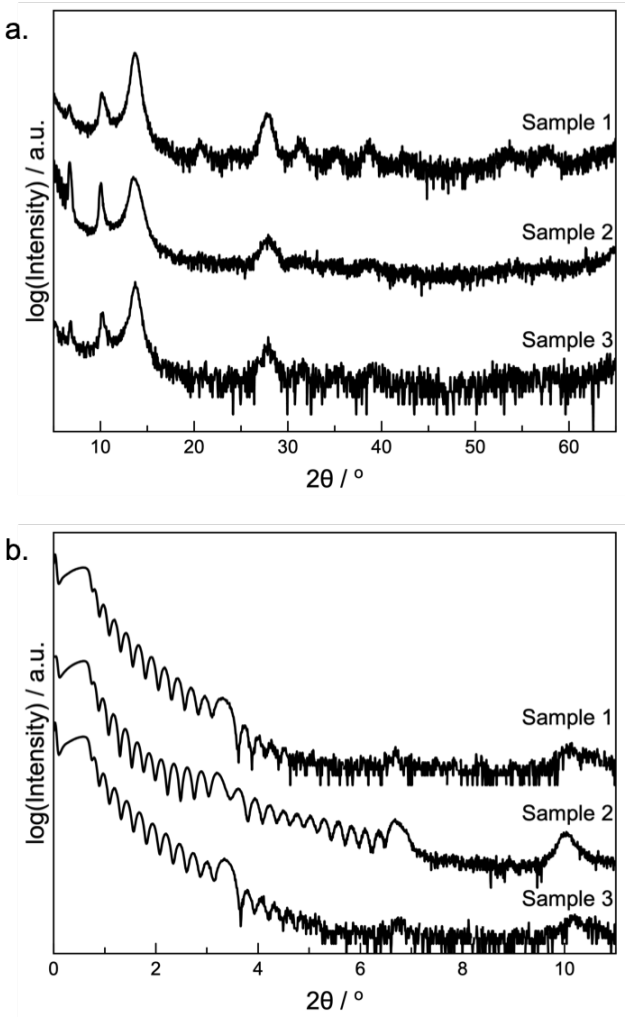

Figure 8.1. (a) XRR and (b) specular x-ray diffraction patterns of the as deposited samples.

necessary for the formation of the targeted repeating structure. The excess amounts of Se in relation to the amounts of Bi and Mo may act as a flux to promote movement of atoms between layers.

XRR and specular XRD scans of each of the as deposited precursors are shown in Figure 8.1. Kiessig fringes and Bragg reflections at low angles in the XRR scans from the sequence of deposited layers are observed, indicating that the elemental layers did not completely intermix during the deposition. The thickness of the repeating sequence of layers was calculated from the Bragg reflections and are shown in Table 8.1. The layer thicknesses are all larger than the estimated *c*-axis lattice parameter of the targeted heterostructure determined by adding the *c*-axis lattice parameters of the constituent layers (25.68 Å). The measured thicknesses are consistent with the number of atoms deposited in each repeating sequence determined using XRF, with the low amounts of Bi and Mo in precursors 2 and 3 compensated by the excess Se deposited. The initial layering reflections indicate the precursors have a composition modulation similar to the desired heterostructure, although the local compositions in samples 2 and 3 deviate from the targeted values. Total thicknesses determined from the spacing of the Kiessig fringes (Table 8.1) are within 1% of the repeating thickness multiplied by the number of layers deposited. The high angle specular diffraction patterns of all of the samples contain broad diffraction maxima consistent with an (00*l*) family of reflections and the calculated c-axis lattice parameters are all close to that expected for the targeted hetereostructure (Figure 8.1a). The widths and intensities of the reflections provide some insight into the extent of crystallization during the deposition. The narrow width of the (002) reflection for all three samples is consistent with 12 deposited layers scattering coherently. The high intensity of the (002) reflection for all three samples indicates that the entire diffraction area contributes to

the scattering. The (004) and (008) reflections in each sample, which result from crystalline domains of the forming heterostructures, are considerably weaker in intensity and broader than the 002 reflection in each scan. The widths of these reflections in samples 1 and 3 are similar and indicate that small domains, three unit cells thick, are participating in the coherent scattering. The larger linewidths of these reflections in sample 2 indicate that approximately two unit cells are participating in the coherent scattering. The lower intensities of the (004) and (008) reflections indicate that only a small percentage of the sample area is scattering. The higher intensity of these reflections in sample 1 indicating that more coherent domains are present.

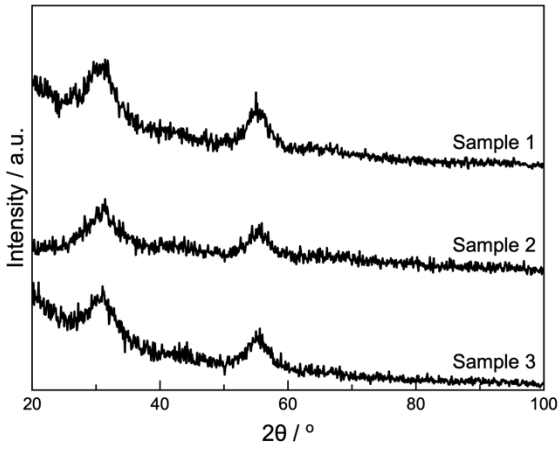

Figure 8.2. In-plane x-ray diffraction patterns of the as deposited samples.

In-plane diffraction patterns were collected on the as deposited samples to further probe the extent of nucleation and growth during the deposition (Figure 8.2). The in-plane diffraction patterns all contain two broad reflections at angles consistent with the (100) and (110) reflections of $MoSe_2$. The formation of $MoSe_2$ in the as deposited precursor is consistent with the previously published $(BiSe)_{0.97}(MoSe_2)$ and binary $MoSe_2$, as $MoSe_2$ by itself forms small grains during

deposition.[2-3] There may be a very broad reflection between the $MoSe_2$ reflections, indicating that smaller domains of BiSe may also be present in samples 1-3.

The XRF, XRR and XRD data enable us to describe the structure of the as deposited precursors. They all consist of 12 elementally modulated layers with the period of the modulation approximately that of the targeted heterostructure. The composition of the layers in the precursors, however, deviate from that of the targeted heterostructure. The XRD data indicates that small domains with a structure close to that of the targeted heterostructures have formed during the deposition in all of the samples. The domains are 2-3 unit cells in thickness containing laterally small $MoSe_2$ domains separated by even smaller domains of BiSe. The size and number of these domains are both larger for the sample that was closest in composition to the targeted heterostructure. The following paragraphs describe the evolution of these precursors as a function of annealing temperature and time. The results of these investigations provide insight as to how to influence the solid state reaction path in the energy landscape using local composition and nanoarchitecture to control the order in which the constituent layers crystalize.

XRR and specular XRD scans were collected on sample 1 after annealing at the indicated temperatures to determine the sequence of phase formation and determine the optimal annealing temperatures for a sample with close to the desired local composition (Figure 8.3). The specular XRD pattern of the as deposited precursor contains Bragg reflections that result from two different sources in the sample. The sharp first order Bragg reflection results from the composition modulation of the precursor due to the deposited sequence of elemental layers. The repeating thickness determined from this reflection

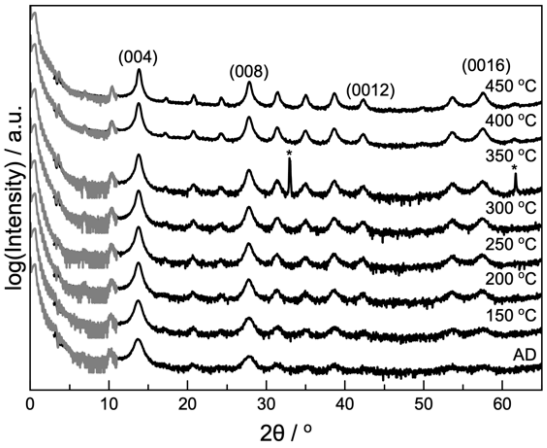

Figure 8.3. XRR (gray) and specular XRD (black) patterns for sample 1 as a function of temperature. Reflections consistent with the Si substrate are marked with an asterisk.

(27.38(2) Å) is higher than expected for $(BiSe)_{1+x}(MoSe_2)_3$ (25.68 Å). The broader diffraction maxima at higher angles result from small crystalline domains that nucleated and grew during the deposition process. The broad diffraction maxima can all be index to a single family of (00*l*) reflections with a repeating thickness of 25.69(2) Å. This thickness is smaller than the modulation thickness and consistent with the estimated *c*-axis lattice parameter for $(BiSe)_{1+x}(MoSe_2)_3$. The high angle reflections in the specular diffraction pattern increase in intensity and line widths decrease as annealing temperature is increased, indicating that the expected $(BiSe)_{1+x}(MoSe_2)_3$ heterostructure is self-assembling. After annealing at 300 °C, the position of the first order reflection and its line width become consistent with the reflections at higher angles, indicating that the sample has lost the modulated layering from the deposition and consists almost entirely of the targeted heterostructure. After annealing at 450°C the single family of (00*l*) reflections yield a *c*-axis lattice parameter of 25.651(3) Å, which is consistent with the estimated *c*-axis lattice parameter of

$(BiSe)_{1+x}(MoSe_2)_3$ (25.68 Å). Sight changes in the amounts of material are noted based on the XRF as the amounts of both Bi and Se decreased. Loss of Se at high temperatures is expected due to vaporization. The loss of Bi at high temperatures was unexpected but results from vapor transport during the annealing process to the sample cover. The amounts of material indicate that there is enough material to form ~11 layers of the desired heterostructure.

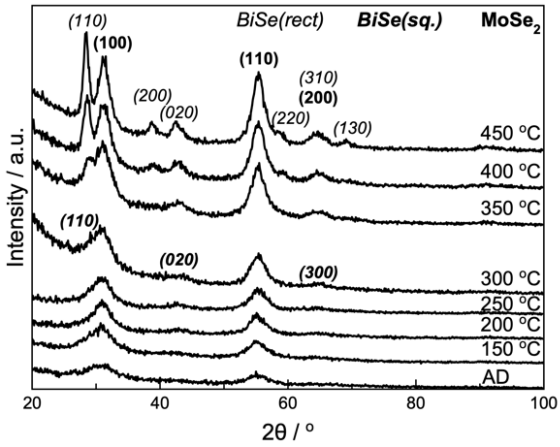

Figure 8.4. Grazing incidence in-plane XRD for sample 1 as a function of temperature.

The evolution of the in-plane diffraction pattern, shown in Figure 8.4, provides information about the sequence of constituent layer formation. The in-plane XRD pattern contains broad reflections observed at 30.1° and 55.0° 2θ, which are consistent with the (100) and (110) reflections $MoSe_2$[4] and a broad reflection consistent with BiSe.[5] The reflections from $MoSe_2$ in the as deposited precursor increase in intensity and decrease in line width as annealing temperature is increased. The reflections consistent with the BiSe phase are consistent with a square basal plane after annealing at 300 °C. The reflections consistent with BiSe shift to lower angles after annealing at 350 °C,

resulting in the reflection at ~29° 2θ. After annealing at 400 °C, another reflection is observed at ~39° 2θ, indicating the basal plane of BiSe is changing. After annealing at 450 °C, the reflections in the in-plane pattern can be indexed to (*hk*0) reflections of two different unit cells: a hexagonal unit cell and a rectangular basal plane. The hexagonal unit cell has an *a*-axis lattice parameter of 3.323(5) Å, which is consistent with $MoSe_2$ (3.32(1) Å).[2] The rectangular basal plane has an *a*-axis lattice parameter of 4.598(7) Å and a *b*-axis lattice parameter of 4.256(4) Å, consistent with the BiSe constituent (a = 4.61(1) Å and b = 4.26(1) Å) found in $(BiSe)_{0.97}(MoSe_2)$.[2] Similar rectangular basal plane lattice parameters for a BiSe layer were also reported for $(BiSe)_1(TiSe_2)_n$[6] compounds and $(BiSe)(NbSe_2)_1$.[7] Small grains of $MoSe_2$ form during the deposition and grow as the sample is annealed while the BiSe layer evolves through a square basal plane at low temperatures to form the final rectangular structure.

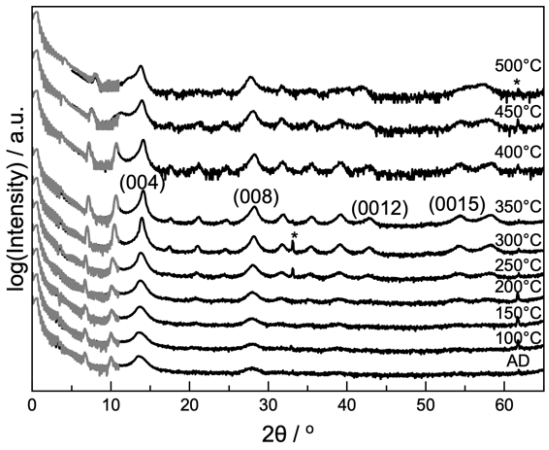

Figure 8.5. XRR (gray) and specular XRD (black) patterns for sample 2 as a function of temperature.

XRR and specular XRD scans were collected on samples 2 (Figure 8.5) after annealing at the indicated temperatures to compare the

reaction pathway to that of sample 1. As in Sample 1, the sharp diffraction maxima at low angles result from the elemental modulation in the precursor and to (00*l*) reflections while the broad reflections result from small crystalline grains of a heterostructure, which index to (00*l*) reflections with a repeating thickness of 25.7(1) Å. The high angle reflections increase in intensity and decrease in line width as the precursor was annealed at higher temperatures. After annealing at 250 ^{o}C, the reflections that result from the initial layering shift to higher angles and their widths broaden slightly. The XRR pattern has fewer Kiessig fringes, suggesting that there is an increase in the roughness of the film. After annealing at 300°C, the reflections at lower angles and high angles can all be indexed as a single family of (*00l*) reflections, yielding a *c*-axis lattice parameter of (25.396(3) Å). This is smaller than the *c*-axis lattice parameter found for $(BiSe)_{1+x}(MoSe_2)_3$ (25.68 Å) in sample 1. Laue oscillations are observed between the (003) and (004) reflections at this temperature, indicating most of the sample contains an integral number of unit cells, discussed in depth below. After annealing at 350°C, there is an increased asymmetry between the (003) and (004) reflections and the Laue interference pattern is no longer present, indicating that the sample contains regions with different film thicknesses. The reflections decrease in intensity, indicating decomposition at 450 and 500°C, which is surprising compared to sample 1.

The in-plane XRD patterns were collected on samples 2 (Figure 8.6) as a function of temperature. The broad reflections consistent with reflections from a hexagonal unit cell ($MoSe_2$) in the as deposited grow in intensity and sharpen as the annealing temperature increases. This suggests the domains increase in size and the amount of crystalline $MoSe_2$ increases with annealing. After annealing at 250 ^{o}C, the broad reflection at ~43^{o} 2θ, which is not consistent with the hexagonal unit

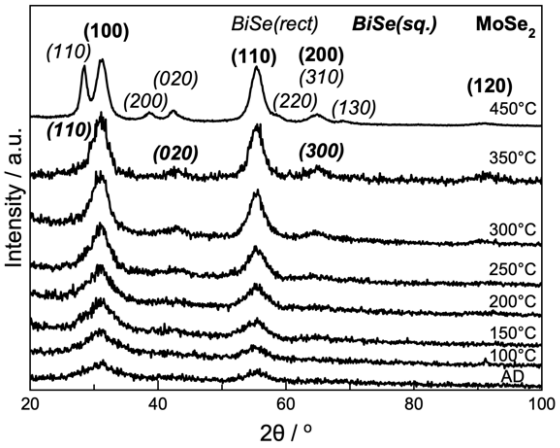

Figure 8.6. Grazing incidence in-plane XRD patterns for the sample 2 as a function of temperature.

cell, grows in intensity. After annealing at 300°C, the reflections in the in-plane pattern can be indexed as (*hk*0) reflections for two different constituents: a hexagonal unit cell and a phase with a square basal plane. The reflections can be indexed to a hexagonal unit cell consistent with $MoSe_2$ [2] (a = 3.316(9) Å) and a compound with a square basal plane with an *a*-axis lattice parameter of 4.22(2). A similar BiSe structure was reported in the $(BiSe)_{1+x}(NbSe_2)_n$ heterostructures, where n > 1.[5] After annealing at 350°C, there is no change in the in-plane pattern though indications of degradation are observed in the specular pattern. After annealing to 450°C, there is a change in the basal plane of the BiSe constituent from square to rectangular as there are shifts in the existing reflections to lower angles. However, the specular pattern exhibits signs of sample degradation at this temperature. A similar annealing study was performed on sample 3 and reported in the SI. Similar to sample 1, sample 2 forms a rectangular basal plane structure at high temperatures for the BiSe layer through a square basal plane intermediate. However, the superlattice has started to decompose before the rectangular BiSe forms in the superlattice, indicating that

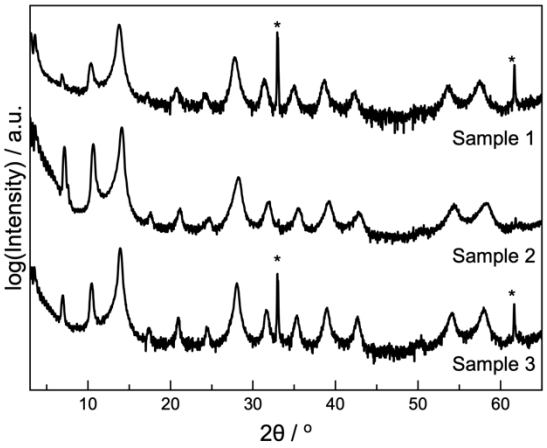

Figure 8.7. Specular XRD patterns for each of the samples after the precursors were annealed at 350 °C.

the square basal plane may also be a stable structure.

The precursors were annealed to 350 °C to evaluate what forms and their resulting specular XRD patterns are shown in Figure 8.7. Quite surprisingly, all of the specular diffraction patterns contained evenly spaced Bragg maxima that could be indexed as (00*l*) reflections, indicating that they each crystallize a single phase heterostructure with *c*-axis lattice parameters that were close each other [25.62(1), 25.396(3) Å, and 25.451(2) Å for samples 1-3, respectively]. The smaller *c*-axis lattice parameters for samples 2 and 3 relative to what formed in sample 1 suggests that their constituent structures may be different. This is supported by the different relative intensities of the (00*l*) reflections, particularly those between 5 and 20° 2θ. The smaller *c*-axis lattice parameters for the superlattice may indicate that the *c*-axis lattice parameter of the BiSe constituent is smaller than previously reported. While samples 2 and 3 are forming the same heterostructure with similar c-axis lattice parameters to sample 1, there is a distinct difference in the basal plane structure of the BiSe constituent.

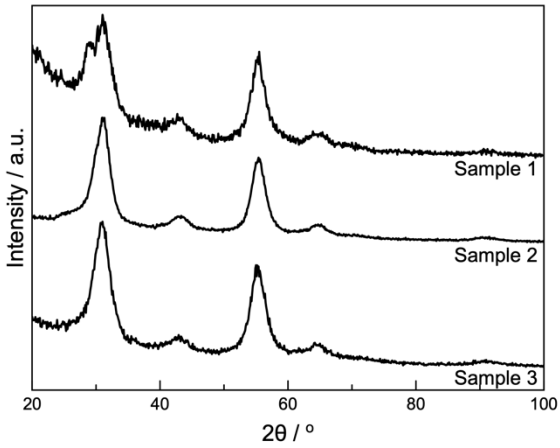

Figure 8.8. In-plane XRD patterns for the $(BiSe)_{1+x}(MoSe_2)_3$ samples annealed to 350 °C.

In-plane XRD patterns were collected on samples 1-3 to probe for differences in structure and the patterns are shown in Figure 8.8. While the reflections consistent with the BiSe layer in sample 1 formed as a rectangular basal plane, the reflections observed for the BiSe layer in samples 2 and 3 indicate a square basal plane formed at this temperature. The change from a rectangular to a square basal plane results in a 9% change in area for the BiSe structure. The formation of two different basal plane structures of a BiSe layer with different TMD layers has been previously reported. When BiSe was layered with increasing layers of $NbSe_2$, a rectangular basal plane was only observed when n = 1[7] while a square structure was reported for samples were n = 2 and 3.[5] The formation of the two different basal planes in BiSe in samples forming the same heterostructure is unprecedented.

An expanded view of the specular XRD patterns for samples 2 and 3 (Figure 8.9) contains small oscillations between the Bragg maxima due to the finite number of unit cells present in each sample. No oscillations are observed in sample 1, therefore the total thickness

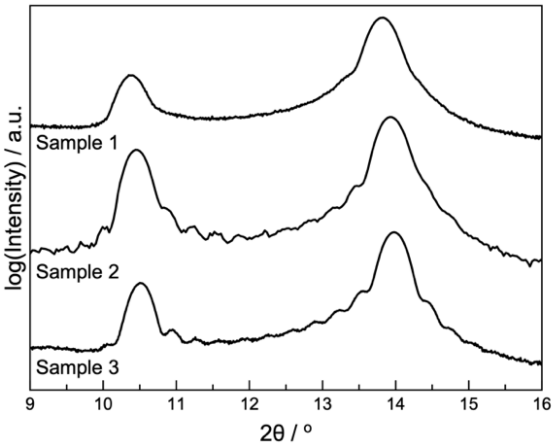

Figure 8.9. Specular XRD patterns for each of the samples after the precursors were annealed at their optimal annealing conditions focused on the 7-18° 2θ range for the presence of Laue oscillations.

of the crystalline sample can be estimated based on the *c*-axis lattice parameter and number of layers possible based on the XRF amounts of material (282.16(5) Å). The XRF data taken after annealing indicates that if 11 layers of $Bi_{1-x}Se$ contain all of the Bi, then the stoichiometry of this layer is Bi_1Se_1. Laue oscillations are observed in samples 2 and 3, from which we can determine the finite number of crystalline layers in the sample. For sample 2, there are 10 minima which indicates that the sample contains 11 unit cells of the heterostructure formed. The XRF data taken after annealing indicates that if 11 layers of $Bi_{1-x}Se$ contain all of the Bi, then the stoichiometry of this layer is $Bi_{0.74}Se$. There is enough Mo to form 33 layers of $MoSe_2$, or 11 repeating units containing three layers of $MoSe_2$. There is enough Se to form 11 layers of a $(Bi_{0.74}Se)_{1+x}(MoSe_2)_3$. For sample 3, there are 10 minima which indicates that the sample contains 11 unit cells of the heterostructure formed. The XRF data taken after annealing indicates that if 11 layers of $Bi_{1-x}Se$ contain all of the Bi, then the stoichiometry of this layer is $Bi_{0.57}Se$. There is enough Mo to form 34 layers of MoSe2, or 11 repeating

units containing three layers of $MoSe_2$ plus a layer of excess $MoSe_2$. There is enough Se to form 12 layers of a $(Bi_{0.57}Se)_{1+x}(MoSe_2)_3$. These calculations assume complete layers are formed, however there may be interference from the excess amounts of material within the sample.

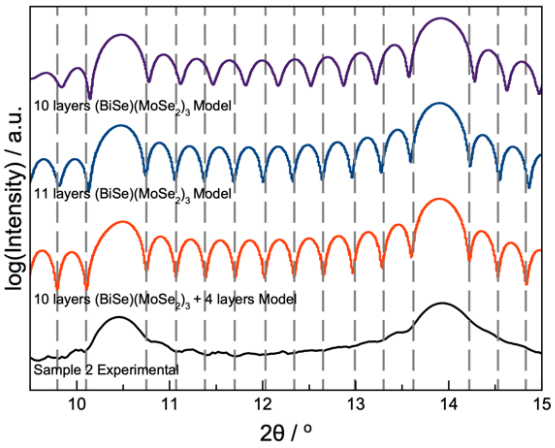

Figure 8.10. Specular XRD pattern focused on the 7-18° 2θ shows good agreement between the experimental pattern for sample 2 (black) and the calculated patterns (orange, blue, and purple).

In order to account for any interference from the excess amounts of material in the samples, we attempted to model the Laue interference patterns as seen in Figure 8.10. Based on the specular pattern, we expected to see 11 layers of $(Bi_{1-x}Se)_{1+x}(MoSe_2)_3$. There is good agreement between the number and position of the minima in the model and the experimental pattern. The amounts of material are consistent with 11 layers of $(Bi_{0.74}Se)_{1+x}(MoSe_2)_3$. However, if we take the Bi as the limiting reagent, the sample would form 10 perfect $(BiSe)_{1+x}(MoSe_2)_3$ layers. Modeling 10 layers is inconsistent with our specular pattern as there is one less minima for the Laue oscillations between the Bragg reflections. Modelling 10 perfect layers with 4 layers of excess $MoSe_2$ to maintain the total thickness, however, results in a model that is consistent with the number of fringes in the experimental pattern with minima at

consistent 2θ values. We have not seen published modeling of Laue oscillations that considers extra layers above or below a finite number of unit cells. This modeling indicates that four $MoSe_2$ layers under 10 unit cells of the sample results in oscillations that match the experimental pattern and also that expected for 11 unit cells. This may result because of the structural similarity of the added four layers of $MoSe_2$ to the unit cell of the heterostructure, which contains four layers – three $MoSe_2$ and one BiSe – that results in a *c*-axis lattice parameter that is equal to that of four $MoSe_2$ layers.

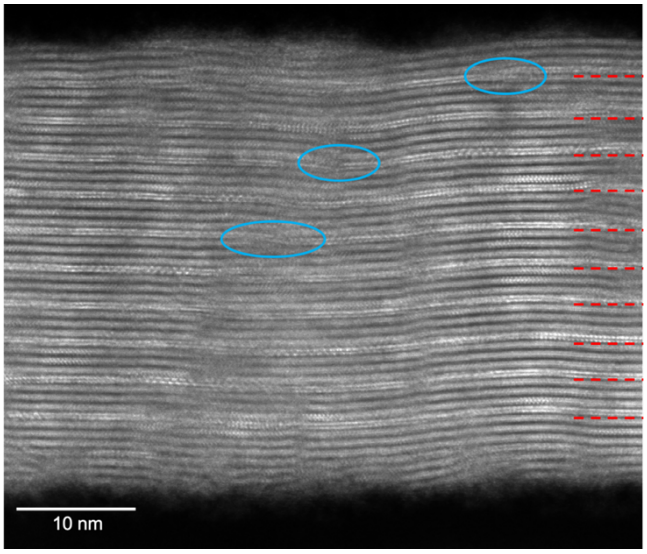

Figure 8.11. Representative HAADF-STEM image of sample 1 annealed to its optimal annealing temperature on a Si substrate with a native oxide layer. 10 repeating units are observed and are indicated with red dashes. Several step defects are observed in the layers and are marked with blue circles.

A representative HAADF-STEM image from a cross section of sample 1 is contained in Figure 8.11 in order to determine the number of repeating units, confirm stacking, and probe for defects. 10 repeating units of $(BiSe)_{(1+x)}(MoSe_2)_3$, containing a bilayer of BiSe and three trilayers of $MoSe_2$ are visible. There are seven additional layers of

crystalline planes observed at the bottom of the sample that appear to be a mix of $MoSe_2$ and BiSe from changes in contrast and areas aligned along zone axes. Identifying the amount of each constituent structure in each layer is not possible due to the density of defects observed at the bottom of the sample and the turbostractic disorder, which is common in samples prepared from modulated precursors.[8-10] The first full layer identified at the surface of the sample is a layer of $MoSe_2$, which was unexpected, considering the deposition ended by depositing the Bi|Se precursor. The lack of a BiSe layer on the top of the sample, however, is consistent with the loss of Bi and Se upon annealing to the optimal annealing temperature. There are small beads of material occasionally above the first full layer that may contain additional Mo, Bi and Se. The image of this sample is also unexpectedly complicated by several step defects between the BiSe layer and the surrounding $MoSe_2$ layers, circled in blue, and possible inclusions. The step defects may result from offsets in the initial $MoSe_2$ nucleation and growth

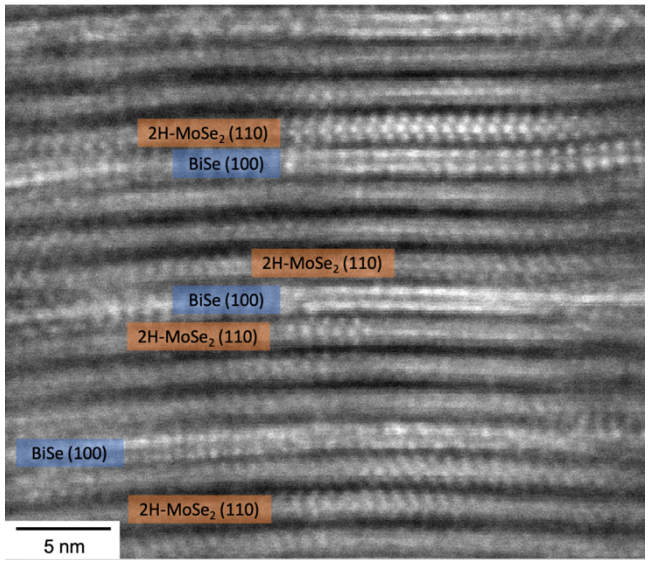

Figure 8.12. HAADF-STEM image of $(BiSe)_{(1+x)}(MoSe_2)_3$ with the zone axes labeled.

during the deposition, which occurs throughout the sample, not only from the substrate.[11] The more complicated areas in the HAADF STEM image may result from a step defect occurring in the middle of the sample. This may be particularly true for the complicated seven layers containing both BiSe and $MoSe_2$ at the bottom of the film.

A higher magnification HAADF-STEM image of $(BiSe)_{(1+x)}(MoSe_2)_3$ is shown in Figure 8.12. This image contains atomically abrupt interfaces between each layer of material. The various zone axes observed in the sample are marked in Figure 8.12. The different zone axes observed within a layer are a result nucleation occurring throughout the sample during deposition. The different zone axes observed in the image reflect the turbostratic disorder found in the sample. The chevrons observed in the Mo|Se layers along the <110> zone axis are consistent with the trigonal prismatic coordination of the 2H-$MoSe_2$ polytype. No octahedrally coordinated 1T-$MoSe_2$ is observed in the images collected. BiSe is only observed along the <100> zone axis and since Bi-Bi dimers occurring at antiphase boundaries are only observed along the <110> zone axis, we cannot comment on their existence within the sample.

A representative HAADF-STEM image from a cross section of sample 2 is contained in Figure 8.13 to confirm the number of repeating units, confirm the stacking, and probe for defects. 10 repeating units of $(BiSe)_{(1+x)}(MoSe_2)_3$, containing a bilayer of BiSe and three trilayers of $MoSe_2$ are visible. Identification of the repeating units was harder for this sample than sample 1 possibly due to increased BiSe/$MoSe_2$ inclusions or offsets. However, the bottom of sample 2 is similar to that of sample 1, where seven additional layers of crystalline planes are observed that may be a mix of $MoSe_2$ and BiSe. There are no significant changes in contrast or visible zone axes, which may result from the

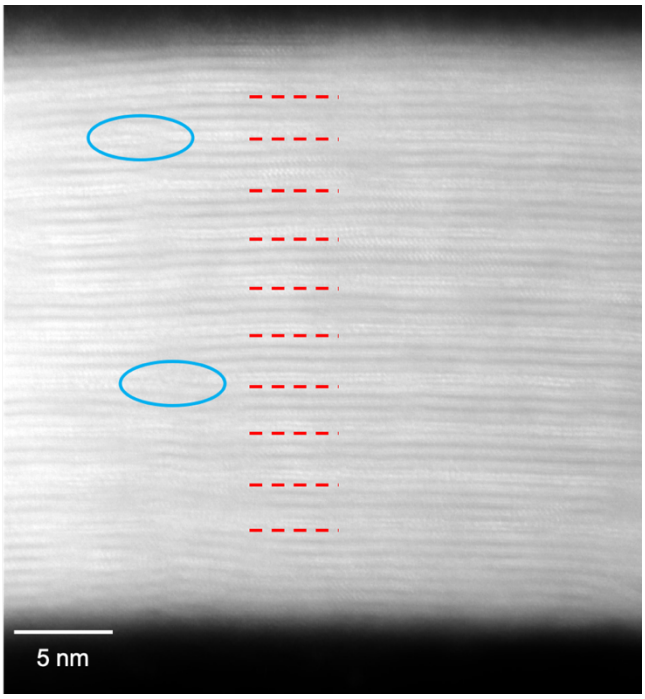

Figure 8.13. Representative HAADF-STEM image of sample 2 annealed to its optimal annealing temperature on a Si substrate with a native oxide layer. 10 repeating units are observed and are indicated with red dashes. Several step defects are observed in the layers and are marked with blue circles.

offset or the turbostractic disorder, making it hard to identify the layers. The first full layer identified at the surface of the sample is $MoSe_2$, consistent with that observed in sample 1 and inconsistent with the deposition order. Based on the amounts of material, not enough Bi was deposited in each layer to make the desired BiSe layer. Therefore, the formation of a partial layer on top would be consistent with the amount of material available in the layer. Bi atoms deposited on the top of the sample may move into the sample to fill in the vacancies left in the other layers. Similarly, to sample 1, we cannot identify everything in the beads of material on the surface of the sample so they may contain additional Mo, Bi and Se. There are several step defects noted in the film. The defects may result from the offsets in the initial $MoSe_2$ nucleation and growth during the deposition and the similarities in the.

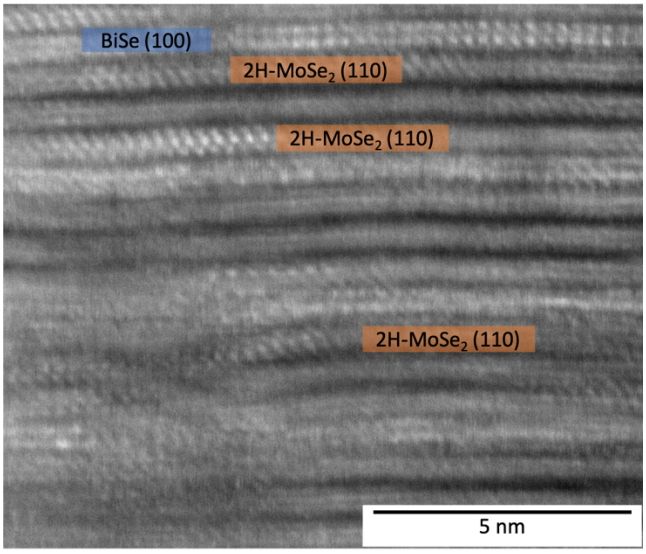

Figure 8.14. HAADF-STEM image of sample 2 with the zone axes labeled.

c-axis lattice parameters of the individual constituents

A higher magnification HAADF-STEM image of $(Bi_{0.74}Se)_{1+x}(MoSe_2)_3$ is shown in Figure 8.14. This image clearly shows the atomically abrupt interfaces between most of the layers of material, but these interfaces become hasty around the step defect observed. The various zone axes observed in the sample are marked in Figure 8.13, where various zone axes are observed within and between layers as a result of the turbostratic disorder. As with sample 1, the only zone axes observed are consistent with the <110> zone axis of 2H-$MoSe_2$ and the <100> zone axis of BiSe. No zone axes consistent with 1T-$MoSe_2$ or the <110> zone axis of BiSe are observed in the sample. We are unable to comment on the existence of 1T-$MoSe_2$ or the Bi-Bi bonds that occur at antiphase boundaries in the BiSe layer in this sample.

8.4. Conclusions

To summarize, two different basal plane structures of BiSe formed in crystalline superlattices that both formed $(BiSe)_{(1+x)}(MoSe_2)_3$ from designed precursors. The precursors started to nucleate small

grains of the desired heterostructure during the deposition despite three different compositions. Slight changes in the *c*-axis lattice parameter are consistent with the changes in the basal plane structure. More in-depth investigations into the structure and electrical properties of these two different structures are underway but their formation could provide more information about the formation of heterostructures.

8.5. Bridge

Chapter VIII explored the impact of the local composition on the structure of the constituents focused on the change in the basal plane observed in the kinetic BiSe structure for heterostructures with the same nanoarchitecture. This study provided further insight into the roles of nucleation and diffusion in samples that impact the final product. This work is unpublished, co-authored material where I made the samples, analyzed the diffraction and electrical data, and wrote the manuscript. Co-authors include Renae Gannon, Douglas L. Medlin, Ping Lu, Fabian Göhler, Aaron A. Miller, Thomas Seyller, and David C. Johnson. Renae Gannon, Douglas L. Medlin, and Ping Lu collected and analyzed the electron microscopy data. Fabian Göhler and Thomas Seyller collected and analyzed the XPS data. Aaron A. Miller collected and analyzed the electrical data. David C. Johnson was my advisor and edited the manuscript. Understanding two possible structures of the BiSe layer allowed for the exploration of a single structure as the nanoarchitecture changed.

CHAPTER IX

EFFECT OF CHARGE TRANSFER ON THE FORMATION OF 1T-$MoSe_2$ IN $(BiSe)_{1+\delta}(MoSe_2)_N$ HETEROSTRUCTURES

8.0. Authorship Statement

I am the primary author of this chapter and worked with several co-authors, including Renae N. Gannon, Fabian Göhler, Aaron M. Miller, Ping Lu, Thomas Seyller, and David C. Johnson, for the collection and analysis of the data.

9.1. Introduction

Interest in 2D layers of transition metal dichalcogenides (TMDs) has increased since the discovery of graphene.[1] Group 6 TMDs have been of particular interest for their layer thickness dependent band gap [2-4] and various applications. [5-9] Two polytypes are possible, which result in a structure and property change. The thermodynamic structure is a trigonal prismatic coordination with ABA BAB stacking and is a semiconductor (2H). [10-11] The kinetic structure is octahedrally coordinated (ABC stacking) with metallic conductivity (1T). [12-15]

The kinetic polytype of group 6 TMDs has been the subject of significant scientific interest, both in how to synthesize it and its possible applications. The kinetic structure was first discovered through alkaili intercalation into group 6 semiconducting compounds. [13,16-17] The 1T-MX_2, where M = Mo, W and X = S, Se, have been used as battery cathodes in lithium ion batteries,[18] catalyses for hydrogen evolution,[6-7] and in field-effect transistors.[14,19] It was recently shown that the presence of a strong electron donor would result in the formation of the kinetic 1T structure. One such strong electron donor is the kinetic BiSe structure that is predicted to stabilize its structure through charge donation to neighboring layers or the formation of Bi-Bi bonds. Recent reports of $(BiSe)_{0.97}(MoSe_2)$ and

$(BiSe)_{0.97}(Bi_2Se)_{1.26}(BiSe)_{0.97}(MoSe_2)$ heterostructures have seen increases in the amount of 1T-$MoSe_2$ as the number of BiSe layers increased.[20-21]

To understand the changes in charge donation as a result of the changes in structure, a family of $(BiSe)_{(1+x)}(MoSe_2)_n$ precursors, where n = 1, 2, and 3, were deposited using modulated elemental reactants. The heterostructures formed crystalgraphically aligned to the substrate from designed precursors. No 1T-$MoSe_2$ was observed in the high angle annular dark field scanning transmission electron microscopy (HAADF-STEM) images due to the turbostractic disorder of the sample. X-ray photoelectron spectroscopy measurements observed ~30% of the $MoSe_2$ layers are in the 1T polytype in $(BiSe)_{0.97}(MoSe_2)_1$. Measurements are still needed for the $(BiSe)_{(1+x)}(MoSe_2)_2$ and $(BiSe)_{(1+x)}(MoSe_2)_3$ heterostructures to determine if 1T-$MoSe_2$ forms in these heterostructures. While temperature dependent electrical measurements are still necessary for $(BiSe)_{(1+x)}(MoSe_2)_2$, differences are apparent in $(BiSe)_{0.97}(MoSe_2)_1$ and $(BiSe)_{0.97}(MoSe_2)_3$. $(BiSe)_{0.97}(MoSe_2)_1$ has a lower resistivity as a result of networks of metallic 1T-$MoSe_2$. The resistivity of $(BiSe)_{0.97}(MoSe_2)_3$ is higher indicating semiconducting behavior without the metallic networks. The carrier concentration decreases as the temperature decreases, although the carrier concentration is several orders of magnitude less than estimated based on the amount of Bi within the sample. More information is necessary to account for this discrepancy.

9.2. Experimental

Using a custom vacuum deposition chamber, precursors were synthesized using modulated elemental reactants at pressures below 5×10^{-7} Torr. Elements were deposited in a $(Mo \mid Se)_n \mid (Bi \mid Se)_m$ pattern, where n is the number of desired $MoSe_2$ layers and m is the number of desired BiSe layers in the film, using computer controlled shutters to

alternate the deposition and monitor the layer thickness. Bismuth and molybdenum were deposited using an electron beam gun. Selenium was deposited using a Knudson effusion cell. Elements were deposited on a silicon wafer with a native oxide layer for structural measurements and quartz for electrical measurements. An annealing study was performed on the $(BiSe)(MoSe_2)_3$ precursor starting at 150 °C for 15 minutes and temperatures were increased by 100 °C to determine how increasing the number of $MoSe_2$ layers affects the optimal annealing conditions.

The X-ray fluorescence (XRF) intensities were measured using a Rigaku ZSX Primus-II with a rhodium X-ray tube and a previously published calibration method.[22] Proportionality constants were determined between the amount of material and XRF intensities as previously described[21-23] and used to determine the amount of Bi, Mo, and Se within the samples.

Structural information was determined through X-ray reflectivity (XRR) and specular and in-plane X-ray diffraction (XRD). The total thickness and layer thickness were determined based on the spacing of the Kiessig fringes and Bragg reflections, respectively, and the data was collected on a Bruker D8 Discover diffractometer using Cu-$K\alpha$ radiation. The sequence of constituent formation and *a*- and *b*-axis lattice parameters were determined from the in-plane XRD reflections, which were collected using a Rigaku SmartLab with a Cu source.

Samples were prepared for HAADF-STEM measurements by first making a cross-section of the film with a FEI Helios NanoLab 600i DualBeam FIB-SEM using standard lift-out procedures. The images were collected using a FEI Titan G2 80–200 scanning transmission electron microscope (STEM) with a Cs probe corrector and ChemiSTEM technology (X-FEG and SuperX EDS with four windowless silicon drift

detectors) operated at 200 kV.

Temperature dependent resistivity and hall measurements were collected on a custom-built system using the van der Pauw method between 30 – 298 K.

9.3. Results and Discussion

Table 9.1. Amounts of Material and Lattice Parameters for $(BiSe)_{(1+x)}(MoSe_2)_n$ precursors.

		Total Atoms / Å^2			Number of layers or unit cells based on M				
Sample	n	Bi	Mo	Se	BiSe M = Bi	$MoSe_2$ M = Mo	unit cells M = Se	Repeating Sequence Thickness (Å)	Total Thickness (Å)
Target	1	2.45	2.52	7.7	24	24	24	~12.56	
Sample 1a	1	2.47(7)	2.53(6)	7.8(3)	24.2(9)	23.9(6)	23.5(9)	12.34(3)	312.6(3)
Target	2	1.63	3.35	8.3	16	32	16	~19.12	
Sample 2a	2	1.69(6)	3.13(6)	8.1(3)	16.6(7)	29.5(6)	15.6(6)	18.76(1)	306.6(6)
Target	3	1.22	3.77	8.8	12	36	12	~25.68	
Sample 3a	3	1.25(5)	3.82(7)	9.0(3)	12.3(6)	36.5(7)	12.8(5)	25.63(9)	324.7(5)

Precursors were synthesized by depositing a repeating sequence of elemental layers, (Bi|Se) + n(Mo|Se), to mimic the composition along the *c*-axis of the targeted $(BiSe)_{1+x}(MoSe_2)_n$ compounds, where n = 1, 2, and 3. The targeted amounts of each element in the precursors were calculated based on the lattice parameters and structures of the binary bulk constituents or structurally related layers in other reported heterostructures. The total number of atoms / Å^2 for Bi, Mo, and Se was determined using a previously published calibration XRF method and are reported in Table 9.1.[22] The number of layers or unit cells

possible based on each individual element were determined by dividing the experimentally determined total amount of each element by the estimated amounts necessary for one layer. Comparing the amount of each element in the precursors with the estimated targets shows that samples 1a and 3a are within a monolayer of the targeted amounts, while sample 2a is ~ three monolayers of $MoSe_2$ short of the target value. Mo is the rate limiting reagent for Sample 2a so only 14 layers of $(BiSe)_{1+x}(MoSe_2)_2$ can form and significant interdiffusion between layers will be required.

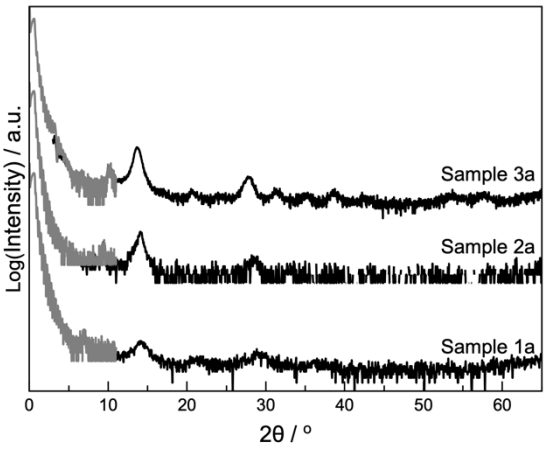

Figure 9.1. XRR (gray) and specular (black) XRD patterns for the as deposited precursors.

XRR and specular XRD patterns for the as deposited precursors were taken to ascertain the nanoarchitecture of the precursors (Figure 9.1). Bragg reflections from the sequence of deposited layers were observed in XRR scans of the as-deposited precursors, indicating that the elemental layers did not completely mix during the deposition. The thickness of the repeating sequence of layers was calculated from these reflections (Table 9.1). The repeating thicknesses for samples 1a and 3a were consistent with estimated *c*-axis lattice parameters determined by adding the *c*-axis lattice parameters of the constituent layers. The

repeating thickness for sample 2a is smaller than the estimated *c*-axis lattice parameter, which is consistent with the deficiency of material deposited relative to the targets. Broad reflections above 10° 2θ in all three precursors indicate that nucleation of small grains of the superlattice occurs during the deposition. Total thicknesses of the precursors were determined based on the spacing of the Kiessig fringes at low angles (Table 9.1) and are consistent with the amount of material within the samples. The XRF and XRR data indicates that the composition and thickness of the repeating sequence of elemental

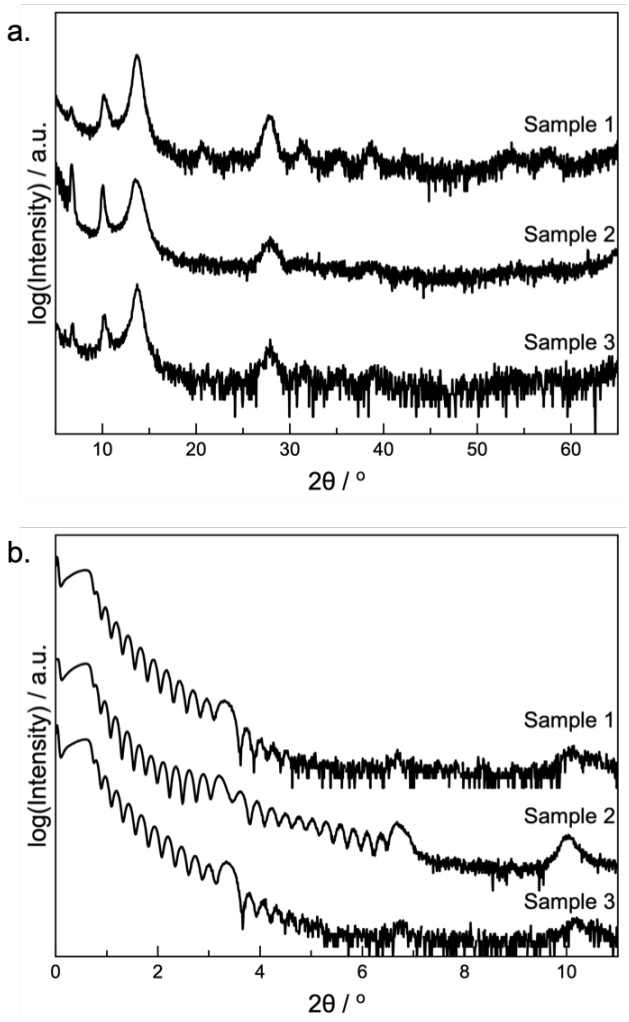

Figure 9.2. (a) XRR (gray) and specular (black) XRD patterns and (b) grazing incidence in-plane XRD patterns for the sample 3a as a function of temperature.

layers in the as deposited precursors for each sample are close enough to that expected for the targeted heterostructures for an exploration of their formation and properties.

Specular and in-plane XRD scans (Figure 9.2) were collected on sample 3a after annealing at the indicated temperatures to follow the formation of the heterostructure and determine the optimal annealing temperatures. The specular XRD pattern of the as deposited precursor contains Bragg reflections that result from two different sources in the sample. The first is a sharp first order Bragg reflection resulting from the composition modulation of the precursor due to the deposited sequence of elemental layers. The repeating thickness determined from the sharp first order Bragg reflection is higher than expected for $(BiSe)_{1+x}(MoSe_2)_3$ (25.68 Å). The second are broader diffraction maxima at higher angles that result from small crystalline domains with *c*-axis lattice parameters close to the modulation lengths that nucleated and grew during the deposition process. The broad diffraction maxima can all be index to a single family of (00*l*) reflections with a repeating thickness of 25.69(2) Å. The repeating thickness is consistent with both the estimated *c*-axis lattice parameter for $(BiSe)_{1+x}(MoSe_2)_3$ and the modulation length in the low angle. Evidence for crystallization during deposition is also found in the in-plane XRD pattern in the broad reflections observed at 30.1° and 55.0° 2θ, which are consistent with the (100) and (110) reflections $MoSe_2$,[24] and a broad, low intensity reflection at around ~43° 2θ, indicative of BiSe.[20] Increases in intensity and decreases in line width are observed after annealing at 150 and 250 °C. Significant differences are observed in the in-plane reflections after annealing at 350 °C. The reflection at ~43° 2θ has grown in intensity and a new reflection is observed at ~28° 2θ, indicating larger BiSe grains are growing. The specular reflections continue to increase in intensity and decrease in line width. After annealing to 450 °C, all of

the reflections in the the specular pattern index to a single family of (00*l*) reflections, yielding a *c*-axis lattice parameter of 25.651(3) Å. This *c*-axis lattice parameter is consistent with the estimated a *c*-axis lattice parameter for $(BiSe)_{1+x}(MoSe_2)_3$ (25.68 Å). The in-plane reflections can be indexed to (*hk*0) reflections consistent with a hexagonal unit cell and a rectangular basal plane. The hexagonal unit cell yields an *a*-axis lattice parameter of 3.322(7) Å while the rectangular basal plane yields an *a*-axis lattice parameter of 4.614(9) Å and a *b*-axis lattice parameter

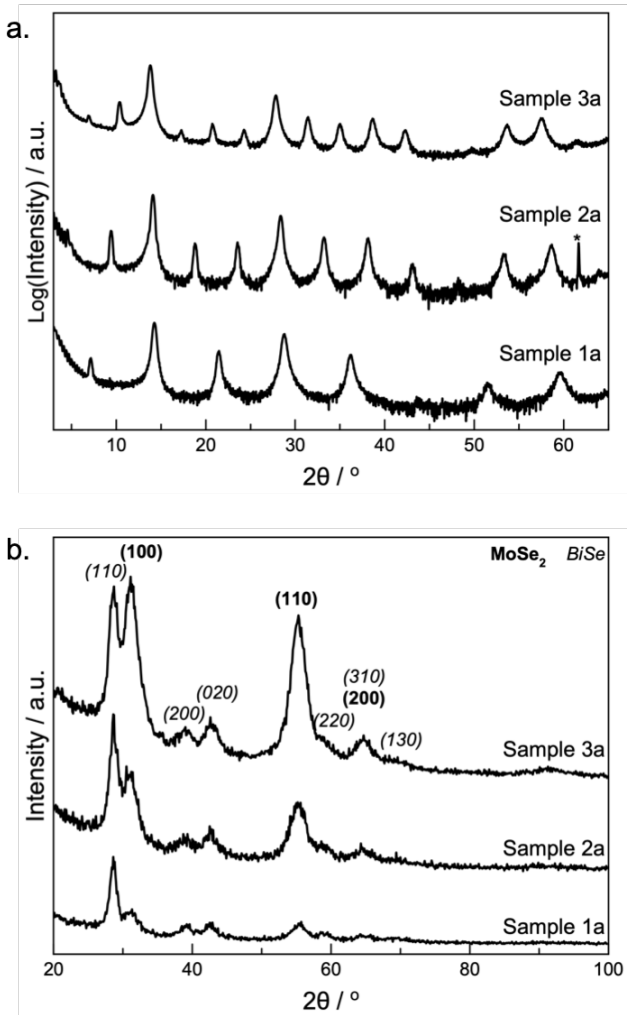

Figure 9.3. (a) Specular and (b) in-plane XRD patterns for the $(BiSe)_{1+x}(MoSe_2)_n$ precursors annealed to their optimal annealing temperatures.

of 4.236(6) Å.These are consistent with those previously reported for the $(BiSe)_{0.97}(MoSe_2)_1$.[20] There is no evidence in either pattern of Bi_2Se_3 impurities. The optimal annealing conditions for the heterostructure were 450 °C for 15 minutes, which is higher than expected based on $(BiSe)_{0.97}(MoSe_2)$.[20] The higher annealing temperature likely resulted from the increased layers of $MoSe_2$, as bulk $MoSe_2$ requires high temperatures and long reaction times to nucleate.[24]

Representative specular and grazing incidence in-plane XRD patterns were collected for the samples after annealing to their optimal annealing temperatures (Figure 9.3). All maxima are evenly spaced and index to single families of (00*l*) reflections, indicating a strong crystallographic alignment to the substrate. The *c*-axis lattice parameter for the n = 1 sample agrees with that previously reported for $(BiSe)_{0.97}(MoSe_2)$. The *c*-axis lattice parameter for each heterostructure increases by 6.62(9) Å as n increases, which is slightly larger than expected based on the previously reported *c*-axis lattice parameter of 2H-$MoSe_2$ (6.460(1) Å).[25] The crystallographic alignment of the layers with the substrate is corroborated by the in-plane patterns where all the maxima can be indexed as (*hk*0) reflections. All of the samples formed a hexagonal unit cell ($MoSe_2$) and a rectangular basal plane (BiSe), which is consistent with the previously published $(BiSe)_{0.97}(MoSe_2)$ sample.[20] The lattice parameters for each sample can be found in Table 9.2.

Table 9.2. Lattice parameters for the $(BiSe)_{1+x}(MoSe_2)_n$ samples after annealing.

		Lattice Constants (Å)				
Sample	n	*c*	*a*-BiSe	*b*-BiSe	*a*-$MoSe_2$	Misfit param.
Target	1	~12.56	4.61(1)	4.23(2)	3.288(2)	
Sample 1a	1	12.416(8)	4.602(5)	4.249(3)	3.32(1)	0.98
Target	2	~19.12	4.61(1)	4.23(2)	3.288(2)	
Sample 2a	2	18.876(1)	4.604(7)	4.235(5)	3.325(8)	0.98
Target	3	~25.68	4.61(1)	4.23(2)	3.288(2)	
Sample 3a	3	25.651(3)	4.614(9)	4.236(6)	3.322(7)	0.98

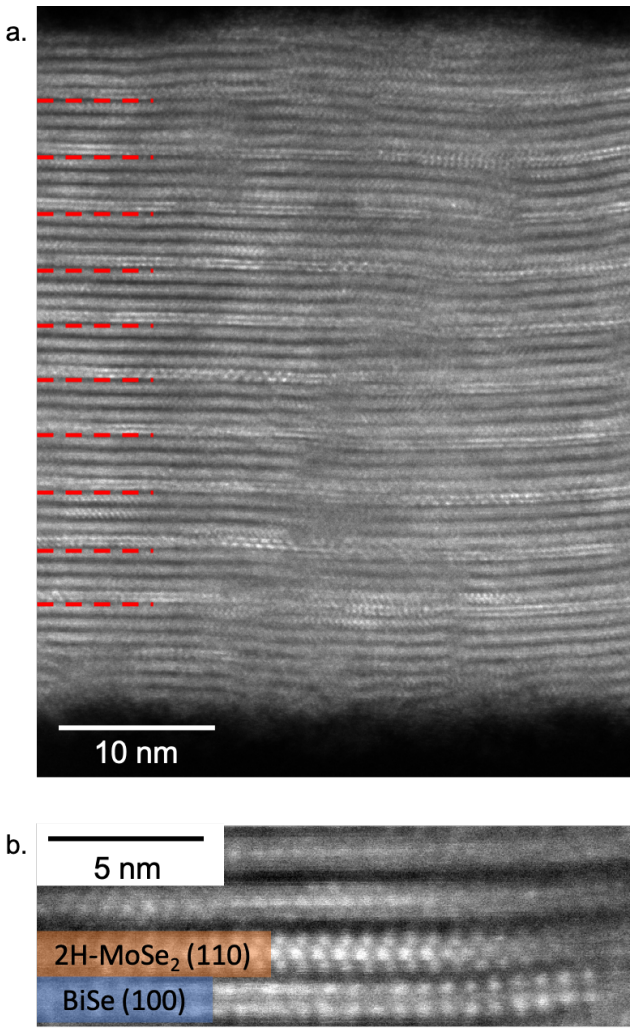

Figure 9.4. Representative HAADF-STEM image of the (a) full and (b) one layer of sample 3a. The red dashed lines indicate the different repeating units. The zone axes observed are marked.

HAADF-STEM images from a cross section of the $(BiSe)_{0.98}(MoSe_2)_3$ heterostructure formed by annealing Sample 3a were collected to determine the ordering of the constituent layers and the number of layers. A representative image of the entire film is shown in Figure 9.4a. A majority of the sample contains ten repeating units of a bilayer of BiSe and three trilayers of $MoSe_2$, with excess crystalline layers on the bottom of the sample. This is surprising based on the XRF and XRD patterns as the sample had enough material to make twelve

layers of the $(BiSe)_{1+x}(MoSe_2)_3$ heterostructure. The first layer at the top of the sample is $MoSe_2$, which is unexpected given the layering sequence of the deposition. There are crystalline deposits on the top of the sample that may contain the Bi and Se (plus O) from the deposited BiSe precursor layer. The bottom seven layers of the film may contain BiSe-$MoSe_2$ inclusions but due to the turbostractic disorder, which is common in samples prepared from modulated precursors, we are not able to identify the layers.[26-28] A representative image of one of the repeating units is shown in Figure 9.4b. There are abrupt interfaces between the layers of each constituent. Two zone axes are observed: the <100> of BiSe and the <110> of 2H-$MoSe_2$. No zone axes consistent with 1T-$MoSe_2$ or the <110> of BiSe are observed within the sample but this may be due to the turbostractive disorder. Further investigation via XPS is necessary to determine the extent of each $MoSe_2$ polymorph within the sample and the amount of Bi-Bi bonds that occur at antiphase boundaries.

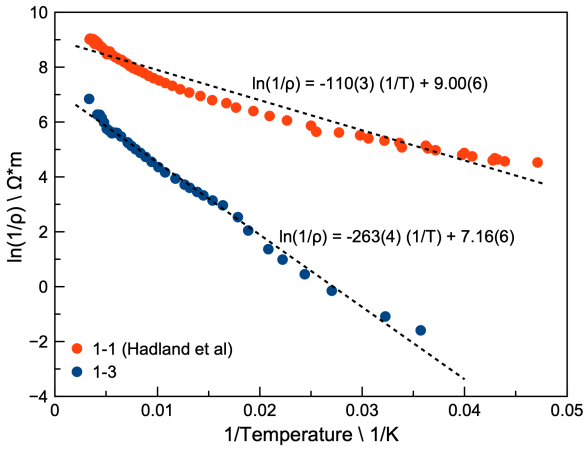

Figure 9.5. Temperature-dependent resistivity data plotted as [ln(1/ρ)] versus (1/T) for the $(BiSe)_{1+x}(MoSe_2)_n$ heterostructures.

To understand how the resistivity changes as the number of $MoSe_2$ layers increases, resistivity as a function of temperature was

collected (Figure 9.5). The temperature dependence of the resistivity of $(BiSe)_{0.98}(MoSe_2)_1$ is challenging to interpret, because the $MoSe_2$ layer consists of domains of both 1T and 2H polytype. Since the resistivity suggests an activated conductivity, the conducting 1T domains must not form a continuous pathway, and the activation energy(s) may represent a hopping energy between these conducting domains. The low temperature data fits to a band gap of 0.0146(3) eV while the high temperature data indicates a band gap of 0.0430(9) eV. This is smaller than that reported for bulk 2H-$MoSe_2$ (1.28-1.45 eV)[29] and for few layer 2H-$MoSe_2$ (~0.2 eV).[30] The temperature dependence of $(BiSe)_{0.98}(MoSe_2)_2$ has yet to be measured. The resistivity of $(BiSe)_{0.98}(MoSe_2)_3$ is significantly higher than that of $(BiSe)_{0.98}(MoSe_2)_1$, reflecting the lack of 1T-$MoSe_2$ indicated by both XPS data and HAADF-STEM images. A band gap extracted from the temperature dependence of the resistivity of $(BiSe)_{0.98}(MoSe_2)_3$ is 0.045(8) eV, suggesting the charge transfer creates an impurity band below the conduction band.

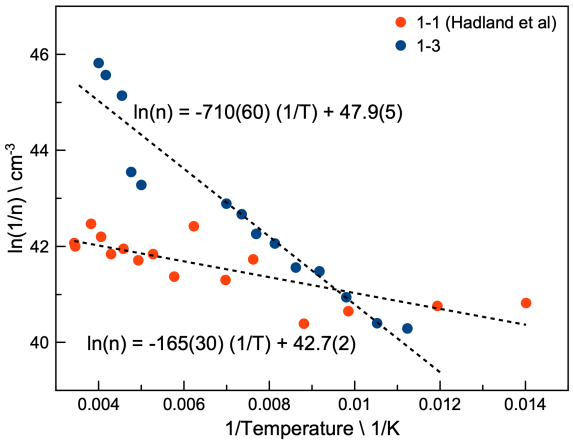

Figure 9.6. Temperature-dependent carrier concentration [ln(1/n)] plotted as a function of temperature (1/T) for the $(BiSe)_{1+x}(MoSe_2)_n$ heterostructures assuming a single band model.

Additional data about the conductivity of these samples were

obtained by measuring Hall coefficients as a function of temperature. Figure 9.6 graphs the carrier concentration [ln(1/n)] as a function of inverse temperature (1/T), from which activation energy can be extracted assuming a single band model. A single band model is probably not accurate for the $(BiSe)_{0.98}(MoSe_2)_1$ heterostructure since it is a composite with two different polymorphs of $MoSe_2$. We have not yet measured the temperature dependence of the Hall coefficient for $(BiSe)_{0.98}(MoSe_2)_2$. The carrier concentration of $(BiSe)_{0.98}(MoSe_2)_3$ decreases as the temperature decreases, indicative of a semiconductor. This yields an intrinsic number of carriers in this sample of 7(3) x 10^{20} cm^{-3}, which is several orders of magnitude lower that the carrier concentration assumes that each Bi atom donates one electron to $MoSe_2$ (4.9(3) x 10^{22} cm^{-3}). Additional data is necessary to formulate a rational explanation for the observed behavior.

9.4. Conclusions

The $(BiSe)_{(1+x)}(MoSe_2)_n$ family of precursors, where n = 1, 2, and 3, were synthesized to probe charge donation from BiSe to increasing layers of $MoSe_2$. The heterostructures formed crystallgraphically aligned to the substrate with differences in their *c*-axis lattice parameters consistent with the size of a $MoSe_2$ trilayer and a BiSe bilayer with a rectangular basal plane. XPS measurements on the $(BiSe)_{0.97}(MoSe_2)_2$ and $(BiSe)_{0.97}(MoSe_2)_3$ are necessary to determine how much, if any, 1T-$MoSe_2$ formed as no 1T-$MoSe_2$ was observed in the HAADF-STEM images due to the turbostratic disorder. 1T-$MoSe_2$ was observed in the XPS measurements of $(BiSe)_{0.97}(MoSe_2)_1$, which account for the lower resistivity compared to $(BiSe)_{0.97}(MoSe_2)_3$. The carrier concentration of $(BiSe)_{0.97}(MoSe_2)_3$ when assuming a single band model is several magnitudes lower than the estimated number of carriers. More information is needed to fully understand the conduction of these samples.

9.5. Bridge

Chapter IX focused on how changing the nanoarchitecture of the heterostructure impacts the electrical properties of BiSe-$MoSe_2$ containing heterostructures where the basal plane is rectangular. This is unpublished and ongoing work. I made the samples, analyzed the diffraction and electrical data, and wrote the manuscript. Fabian Göhler and Thomas Seyller collected and analyzed the XPS data. David C. Johnson was my advisor and edited the manuscript. The final chapter will provide a summary of my work and provide an outlook for future projects, focused on exploring structure/property relationships and understanding of how solids react.

CHAPTER X

CONCLUSIONS, SUMMARY, AND FUTURE OUTLOOK

Silicon transistors have reached the fundamental limits of their applications. The development of new materials is necessary as demands for rapid improvements in our technology continue to rise. The emergent properties and the ability to tune the interfacial interactions between layers in heterostructures are two major reasons they have been considered for implementation in devices. However, synthesis was and remains a significant limitation to our ability to synthesize new predicted products and/or heterostructures, both in research and in manufacturing.

Modulated elemental reactants synthesis method allows for the synthesis of single-phase structures and heterostructures. In this method, there are two tunable parameters, local composition and layer thickness, by which to control the formation of the final product. This dissertation has emphasized the importance of the local composition of the heterostructure in the formation of the final products, both in single phase structures (Mn-Se) and heterostructures (Bi-Mo-Se). The control over the local compositions would not be possible without the ability to measure the amounts of material within the sample using X-ray fluorescence. With this method, we are able to not only measure the amount of material within our sample but better control the amounts deposited in our precursor and route out sources of error in our deposition process.

While local composition is important in synthesis of designed heterostructures, other factors may influence the formation of the final product. This was apparent in the attempts to synthesize Bi_2Se_3-MSe_2 heterostructures. Precursors layered with metallic layers segregated to

form $[(BiSe)_{1+\gamma}]_1[(MSe_2)]_1$ and Bi_2Se_3. Precursors with semiconducting layers formed $[(Bi_2Se_3)_{1+\delta}]_1[(MSe_n)]_1$. The influence of the electronic properties of the neighboring layer and charge transfer were reminiscent of the substituent effects observed in organic chemistry and are another tunable parameter to influence the formation of heterostructures.

The remainder of this dissertation focused on the preliminary investigations in the composition space between the Bi_2Se_3-$MoSe_2$ and BiSe-$MoSe_2$ tie lines in the Bi-Mo-Se ternary phase diagram. The heterostructures described herein were of interest to probe the charge transfer and formation of Bi-Bi bonds in BiSe. Local composition largely influenced the formation of products that were close in composition. While competition was expected between the charge transfer and the formation of Bi-Bi bonds, there was unexpected competition between which layer the charge would donate to in heterostructures containing both Bi_2Se_3 and $MoSe_2$. The charge transfer affected the conduction in of the heterostructures in a variety of ways. BiSe-$MoSe_2$ containing heterostructures were of interest for the charge transfer to multiple layers of $MoSe_2$ and the composition dependence of the BiSe basal plane structure.

This dissertation is a starting point for synthesizing heterostructures in the Bi-Mo-Se ternary phase diagram. In the future, the nanoarchitectures described herein can be varied by increasing the number of layers of Bi_2Se_3 or $MoSe_2$. The heterostructures would further probe the interactions between layers and structure and the influence of charge transfer and local composition on formation.

Novel heterostructures were synthesized with the modulated elemental reactants synthesis method. The projects proposed a new parameter that may influence the synthesis of designed

heterostructures while reinforcing the importance of local composition. Increased understanding of the importance of parameters the effect diffusion, nucleation, and growth improve our ability to synthesize new compounds and/or heterostructures for future use in devices.

APPENDIX A

SUPPORTING INFORMATION FOR CHAPTER IV

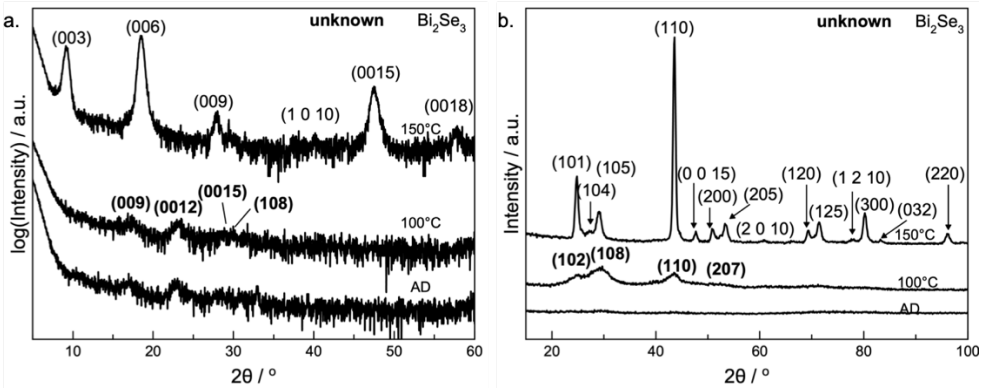

Figure A.1. (a) Specular and (b) in-plane diffraction patterns on Bi|Se Sample B collected as a function of annealing temperature.

Diffraction patterns were collected on Bi|Se Sample B as a function of annealing temperature and are shown in Figure S1. This precursor follows the same reaction pathway as Bi|Se Sample A. Sample B forms the same unknown hexagonal intermediate at low temperatures. The reflections in the as-deposited and after annealing at 100 °C patterns are consistent with those observed for the Bi|Se Sample A. The positions of the reflections shift and their intensity increases after annealing to 150 °C. These reflections can be indexed as (*hkl*) reflections from a hexagonal unit cell yielding an *a*-axis lattice parameter of 4.154(2) Å and a *c*-axis lattice parameter of 28.702(7) Å, which are consistent with Bi_2Se_3.[1] The sample forms the expected thermodynamic compound at low temperatures, with similar evolution as Sample A.

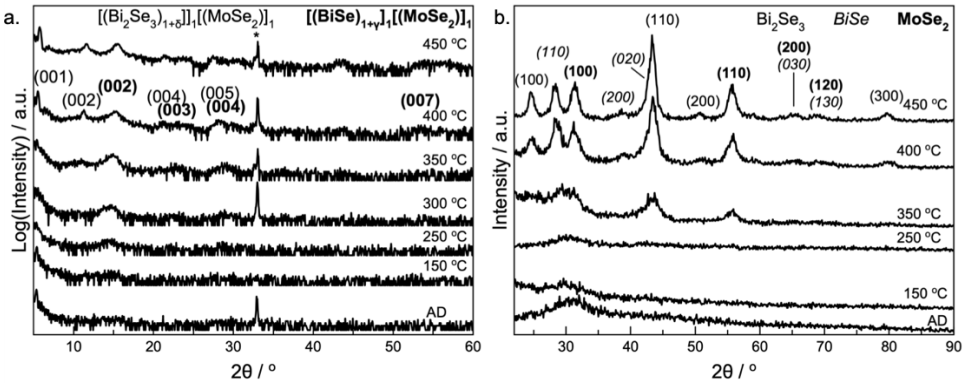

Figure A.2. (a) Specular and (b) in-plane diffraction patterns on Bi|Se Sample B collected as a function of annealing temperature. The sharp reflection at ~33° 2θ is consistent with the Si substrate.

Diffraction patterns were collected on Mo|Se|Bi|Se Sample B as a function of annealing temperature and are shown in Figure 5. Mo|Se|Bi|Se Sample B follows a similar evolution as Mo|Se|Bi|Se Sample A. An artificial layering reflection is observed at low 2θ with a d-spacing of 16.46 (2) Å, which is consistent with the estimated *c*-axis lattice parameter of $[(Bi_2Se_3)_{1+\delta}]_1[(MoSe_2)]_1$ (16.06 Å). The specular pattern of the precursor also exhibits a broad reflection at 15.60(1)° 2θ that is not related to the initial layering reflection. There is a single broad and weak reflection at 31.10(1)° 2θ in the in-plane pattern that is consistent with the (100) reflection of $MoSe_2$. As the sample was annealed at 100, 150, 200, and 250 °C. the intensity of the initial layering reflection decreases and reflection at ~15° 2θ increases in the specular pattern. There are too few reflections in either the specular or the in-plane patterns to unambiguously index or identify any phases after any of these annealing steps. After annealing at 350 °C, new reflections are observed in the specular and in-plane patterns. After annealing to 400 °C, the reflections in both patterns grow in intensity. The reflections in the specular pattern can be indexed to two families of (00*l*) reflections with *c*-axis lattice parameters of 16.07(3) Å and 12.02(2) Å. These are consistent with *c*-axis lattice parameters estimated for $[(Bi_2Se_3)_{1+\delta}]_1[(MoSe_2)]_1$ and reported for $[(BiSe)_{1+\gamma}]_1[(MoSe_2)]_1$ (12.45(2) Å),[2] respectively. The reflections in the in-plane pattern can be indexed as (*hk0*) reflections of two different hexagonal unit

cells with *a*-axis lattice parameters of 4.16(1) Å and 3.299(8) Å, and a third phase with a rectangular basal plane with lattice parameters of a = 4.635(7) Å and b = 4.230(4) Å. These lattice parameters are consistent with those reported for Bi_2Se_3 for Bi_2Se_3 (a = 4.1355(5) Å),[1] $MoSe_2$ (a = 3.32(1) Å),[2] and BiSe (a = 4.61(1) Å and b = 4.26(1) Å),[2] respectively. The sample decomposes after annealing to 450 °C due to loss of Se. The sample forms a mixture not very well crystalized $[(Bi_2Se_3)_{1+\delta}]_1[(MoSe_2)]_1$ and $[(BiSe)_{1+\gamma}]_1[(MoSe_2)]_1$ at low temperatures. The formation of the desired $[(Bi_2Se_3)_{1+\delta}]_1[(MoSe_2)]_1$ heterostructure depends on the composition of the precursor. Sufficient Se is necessary in order to prevent the formation of 1T-$MoSe_2$, as seen in the annealing study of Mo|Se|Bi|Se Sample A.

APPENDIX B

SUPPORTING INFORMATION FOR CHAPTER V

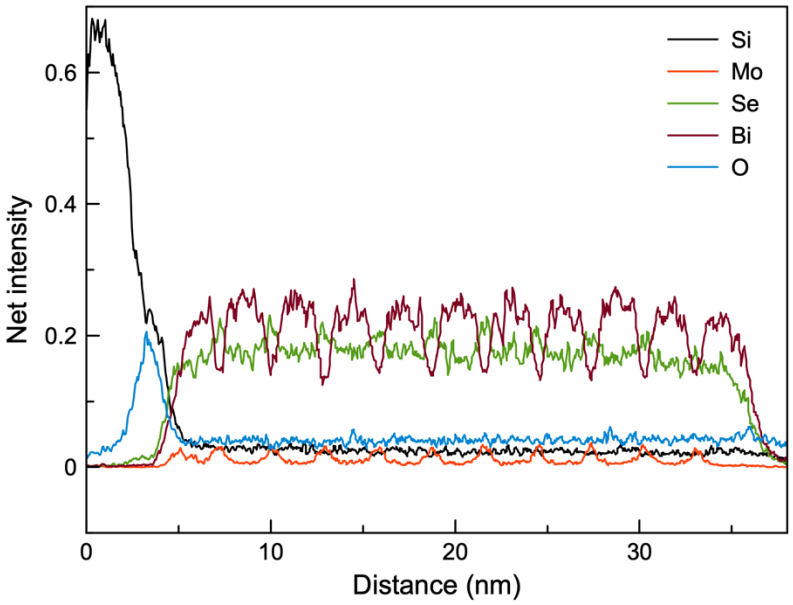

Figure B.1. Electron dispersive x-ray spectroscopy (EDS) line profile from substrate to surface of $(BiSe)_{0.97}(Bi_2Se_3)_{1.26}(BiSe)_{0.97}(MoSe_2)$.

APPENDIX C

SUPPORTING INFORMATION FOR CHAPTER VII

Table C.1. Total number of atoms per A^2 and average chemical composition (in at.%) of the six different compounds as measured via X-ray fluorescence (XRF) and X-ray photoelectron spectroscopy (XPS). XRF data was not available for $(BiSe)_{0.97}MoSe_2$. The composition is measured over the whole film thickness in XRF. In XPS, the collected signal originates from a few layers at the surface, and thus only provides the composition of the topmost layers at the exposed interface after cleaving of the film. Consequently, the sample compositions derived from XRF and XPS differ, but general trends when comparing different sample types are consistent for both methods.

	Atoms / A^2 XRF			**Percent Composition (%) XRF**			**Percent Composition (%) XPS**		
Precursor	**Bi**	**Mo**	**Se**	**Bi**	**Mo**	**Se**	**Bi**	**Mo**	**Se**
$(BiSe)_{0.97}(MoSe_2)_3$	1.07(5)	3.6(2)	8.6(4)	8	27	65	8	34	58
$(BiSe)_{0.97}(MoSe_2)_2$	1.41(7)	3.1(2)	8.3(4)	11	24	65	15	33	52
$(BiSe)_{0.97}(MoSe_2)_1$							27	20	53
$(Bi_2Se_3)_{1.25}(BiSe)_{0.97}(MoSe_2)_1$	3.1(2)	1.61(8)	6.6(3)	27	14	58	40	19	41
$(BiSe)_{0.97}(Bi_2Se_3)_{1.26}(BiSe)_{0.97}(MoSe_2)_1$	3.9(2)	1.15(6)	6.4(3)	34	10	56	47	11	42
$[(Bi_2Se_3)_{1.27}]_2(MoSe_2)_1$	3.1(2)	1.19(6)	6.8(3)	28	11	61	37	14	49

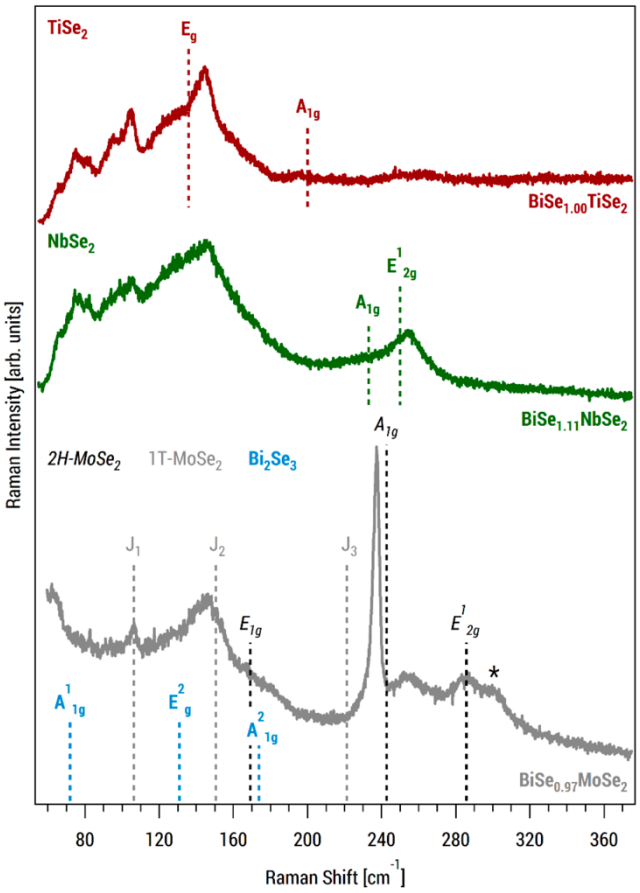

Figure C.1. Raman spectra of BiSe1.00TiSe2 and BiSe1.11NbSe2 in comparison to BiSe0.97MoSe2. The expected positions of the Raman modes of bulk or few-layer TiSe2 [1], NbSe2 [2], 2H- MoSe2 [3], 1T-MoSe2 [4] and Bi2Se3 [5] are indicated by vertical lines. The energy range between 60 – 180 cm^{-1} features a number of signals that can be attributed to rock-salt BiSe. The different intensities and peak shapes observed for these modes, when comparing BiSe1.00TiSe2 and BiSe1.11NbSe2, is likely due to a variation in antiphase boundary formation in these heterostructures, and/or an effect of interactions with different TMDC layers.

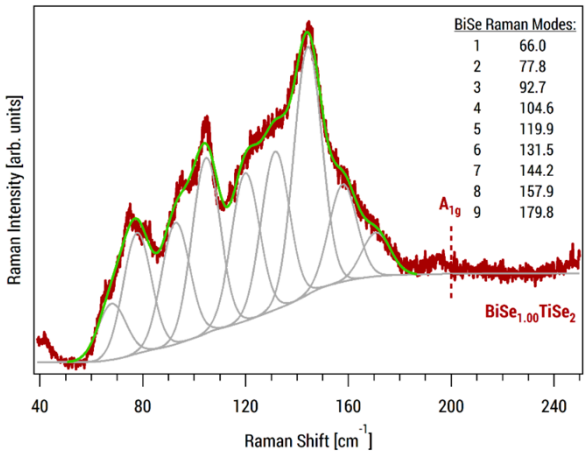

Figure C.2. Fit of the BiSe region of the Raman spectrum of $BiSe_{1.00}TiSe_2$ with multiple Gaussians of identical peak shape. At least nine different modes are necessary to adequately fit the spectrum. Assigning the components to individual vibrational modes requires further theoretical work. The small signal around 195 cm^{-1} corresponds to the A_{1g} mode of $TiSe_2$.

REFERENCES CITED

Chapter I

(1) Moore, G. E. Cramming more components into integrated circuits. *Electronics*. **1965**, *38*, 8.

(2) Kaul, A. B. Two-dimensional layered materials: Structure, properties, and prospects for device applications. *J. Mater. Res*. **2014**, *29*, 348–361

(3) Butler. S. Z.; Hollen, S. M.; Cao, L.; Cui, Y.; Gupta, J. A.; Gutierrez, H. R.; Heinz, T. F.; Hong, S. S.; Huang, J.; Ismach, A. F.; Johnston-Halperin, E.; Kuno, M.; Plashnitsa, V. V.; Robinson, R. D.; Ruoff, R. S.; Salahuddin, S.; Shan, J.; Shi, L.; Spencer, M. G.; Terrones, M.; Windl, W.; Goldberger, J. E. Progress, challenges, and opportunities in two-dimensional materials beyond graphene. *ACS Nano.* **2013**, *7*, 2898–2926.

(4) Lemme, M. C.; Li, L.-J.; Palacios, T.; Schwierz, F. Two-dimensional materials for electronic applications. *MRS Bull*. **2014**, *39*, 711–718.

(5) Arnold, M. S.; Green, A. A.; Hulvat, J. F.; Stupp, S. I.; Hersam, M. C. Sorting carbon nanotubes by electronic structure using density differentiation. *Nat. Nanotechnol*. **2006**, *1*, 60–65.

(6) Liu, J.; Hersam, M. Recent developments in carbon nanotube sorting and selective growth. *MRS Bull*. **2010**, *35*, 315–321

(7) Ganatra, R.; Zhang, Q. Few-layer MoS_2: A promising layered semiconductor. *ACS Nano*. **2014**, *8*, 4074–4099.

(8) Tulevski, G. S.; Franklin, A. D.; Frank, D.; Lobez, J. M.; Park, H.; Afzali, A.; Han, S. -J.; Hannon, J. B.; Haensch, W. Toward high-performance digital logic technology with carbon nanotubes. *ACS Nano.* **2014**, *8*, 8730–8745.

(9) Schwierz, F. Graphene transistors. *Nat. Nanotechnol*. **2010**, *5*, 487–496.

(10) Reddy, D.; Register, L. F.; Carpenter, G. D.; Banerjee, S. K. Graphene field-effect transistors. *J. Phys. D Appl. Phys*. **2011**, *44*, 313001.

(11) Roy, T.; Tosun, M.; Kang, J. S.; Sachid, A. B.; Desai, S. B.; Hettick, M.; Hu, C. C.; Javey, A. Field-effect transistors built from all two-dimensional material components. *ACS Nano.* **2014**, *8*, 6259–6264.

(12) Das, S.; Gulotty, R.; Sumant, A. V.; Roelofs, A. All two dimensional, flexible, transparent, and thinnest thin film transistor. *Nano Lett.* **2014**, *14*, 2861–2866.

(13) Avsar, A.; Vera-Marun, I. J.; Tan, J. Y.; Watanabe, K.; Taniguchi, T.; Castro Neto, A. H.; Ozyilmaz, B. Air-stable transport in graphene-contacted, fully encapsulated ultrathin black phosphorus-based field effect transistors. *ACS Nano*, **2015**, *9*, 4138–4145.

(14) Park, S.; Pitner, G.; Giri, G.; Koo, J. H.; Park, J.; Kim, K.; Wang, H.; Sinclair, R.; Wong, H. -S. P.; Bao, Z. Large-area assembly of densely aligned single-walled carbon nanotubes using solution shearing and their application to field-effect transistors. *Adv. Mater.* **2015**, *27*, 2656–2662.

(15) Cao, Q.; Han, S. -J.; Tulevski, G. S.; Zhu, Y.; Lu, D. D.; Haensch, W. Arrays of single-walled carbon nanotubes with full surface coverage for high-performance electronics. *Nat. Nanotechnol.* **2013**, *8*, 180–186.

(16) Franklin, A. D. Nanomaterials in transistors: From high-performance to thin-film applications. *Science*, **2015**, *349*, 704.

(17) Franklin, A. D.; Farmer, D. B.; Haensch, W. Defining and overcoming the contact resistance challenge in scaled carbon nanotube transistors. *ACS Nano,* **2014***, 8*, 7333–7339.

(18) Kovnir, K. Predictive Synthesis. *Chem. Mater.* **2021**, *33*, 13, 4835–4841.

(19) Gautier, R.; Zhang, X.; Hu, L.; Yu, L.; Lin, Y.; Sunde, T. O. L.; Chon, D.; Poeppelmeier, K. R.; Zunger, A. Prediction and accelerated laboratory discovery of previously unknown 18-electron ABX compounds. *Nat. Chem.* **2015**, *7*, 308−316.

(20) Alberi, K. The 2019 materials by design roadmap. *J. Phys. D: Appl. Phys.* **2019**, *52*, 013001.

(21) Oliynyk, A. O.; Mar, A. Discovery of Intermetallic Compounds from Traditional to Machine-Learning Approaches. *Acc. Chem. Res.* **2018**, *51*, 59−68.

(22) Walters, L. N.; Zhang, C.; Dravid, V. P.; Poeppelmeier, K. P.; Rondinelli, J. M. First-Principles Hydrothermal Synthesis Design to Optimize Conditions and Increase the Yield of Quaternary Heteroanionic Oxychalcogenides. *Chem. Mater.* **2021**, *33*, 2726−2741.

(23) Wustrow, A.; Huang, G.; McDermott, M. J.; O'Nolan, D.; Liu, C. H.; Tran, G. T.; McBride, B. C.; Dwaraknath, S. S.; Chapman, K. W.; Billinge, S. J. L.; Persson, K. A.; Thornton, K.; Neilson, J. R. Lowering Ternary Oxide Synthesis Temperatures by Solid-State Cometathesis Reactions. *Chem. Mater.* **2021**, *33*, 3692−3701.

(24) Yan, F.; Zhang, X.; Yu, Y. G.; Yu, L.; Nagaraja, A.; Mason, T. O.; Zunger, A. Design and discovery of a novel half-Heusler transparent hole conductor made of all-metallic heavy elements. *Nat. Commun.* **2015**, *6*, 7308.

(25) Narayan, A.; Bhutani, A.; Rubeck, S.; Eckson, J. N.; Shoemaker, D. P.; Wagner, L. K. Computational and experimental investigation for new transition metal selenides and sulfides: The importance of experimental verification for stability. *Phys. Rev. B.* **2016**, *94*, 045105.

(26) Jarowicki, K.; Kocienski, P. Protecting groups. *J. Chem. Soc., Perkin Trans.* **1998**, *1*, 4005–4037.

(27) Campbell, C. T. The Degree of Rate Control: A Powerful Tool for Catalysis Research. *ACS Catal.* **2017**, *7*, 2770−2779.

(28) Ingold, C. Structure and mechanism in organic chemistry. **1969**, ISBN 0801404991 9780801404993.

(29) DiSalvo, F. J. Solid state chemistry. *Solid State Commun.* **1997**, *102*, 79–85.

(30) Kraschinski, S.; Herzog, S.; Bensch, W. Low temperature synthesis of chromium tellurides using superlattice reactants: crystallization of layered $CrTe_3$ at 100°C and the decomposition into Cr_2Te_3. *Solid State Sci.* **2002**, *4*, 1237–1243.

(31) Herzog, S.; Kraschinski, S.; Bensch, W. The Reactivity of Cr-Te Superlattice Reactants and of Co-deposited Cr-Te Films: Studies with in-situ X-ray Diffractometry. *Z. Anorg. Allg. Chem.* **2003**, *629*, 1825–1832.

(32) Behrens, M.; Kiebach, R.; Bensch, W.; Haüssler, D.; Jäger, W. The reaction mechanism of a complex intercalation system In situ X-ray diffraction studies of the chemical and electrochemical lithium intercalation in Cr_4TiSe_8 *Inorg. Chem.* **2006**, *45 (6)*, 2704– 2712.

(33) Göselea, U.; Tu, K. N. "Critical thickness" of amorphous phase formation in binary diffusion couples *J. Appl. Phys.* **1989**, *66*, 2619-2626.

(34) West, A. *Solid State Chemistry and its Applications*, John Wiley & Sons, Ltd, New York City, **1984**.

(35) Venna, S. R.; Jasinski, J. B.; Carreon, M. A. structural evolution of zeolitic imidazolate framework. *J. Am. Chem. Soc.*, **2010**, 132, 18030–18033.

(36) Kanatzidis, M. G.; Pöttgen, R.; Jeitschko, W. The Metal Flux: A Preparative Tool for the Exploration of Intermetallic Compounds. *Angew. Chemie Int. Ed.*, **2005**, *44*, 6996–7023.

(37) Noh, M.; Johnson, C. D.; Hornbostel, M. D.; Thiel, J.; Johnson, D. C. Control of Reaction Pathway and the Nanostructure of Final Products through the Design of Modulated Elemental Reactants. *Chem. Mater.* **1996**, *8*, 1625-1635

(38) Williams, J. R.; Johnson, M.; Johnson, D. C. Composition Dependence of the Nucleation Energy of Iron Antimonides from Modulated Elemental Reactants. *J. Am. Chem. Soc.* **2001**, *123*, 1645-1649.

(39) Lasocka, M. Mn-Se (Manganese-Selenium). Binary Alloy Phase Diagrams, II Ed., Ed. T.B. Massalski. **1990**, *3*. 2598-2602.

(40) Choffel, M. A.; Hamann, D. M.; Joke, J. A.; Cordova, D. L. M.; Johnson, D. C. The Reaction Between Mn and Se. *Z. Anorg. Allg. Chem.* **2018**, *644*, 1875–1880.

(41) Okamoto, H. The Bi-Se (Bismuth-Selenium) System. *J. Phase Equilib.* **1994**, *15*, 195-201.

(42) Novoselov, K. S.; Geim, A. K.; Morozov, S. V.; Jiang, D.; Zhang, Y.; Dubonos, S. V.; Grigorieva, I. V.; Firsov, A. A. Electric Field Effect in Atomically Thin Carbon Films. *Science.* **2004**, *306*, 666–669.

(43) Tongay, S.; Zhou, J.; Ataca, C.; Lo, K.; Matthews, T. S.; Li, J.; Grossman, J. C.; Wu, J. Thermally driven crossover from indirect toward direct bandgap in 2D semiconductors: $MoSe_2$ versus MoS_2. *Nano Lett.* **2012**, *12*, 5576−5580.

(44) Splendiani, A.; Sun, L.; Zhang, Y.; Li, T.; Kim, T.; Chim, C.-Y.; Galli, G.; Wang, F. Emerging Photoluminescence in Monolayer MoS_2. *Nano Lett.* **2010**, *10*, 1271–1275.

(45) Yu, Z. G.; Yakosen, B. I.; Zhang, Y.-W. Realizing Indirect-to-Direct Band Gap Transition in Few-Layer Two Dimensional MX_2 (M = Mo, W; S = S, Se). *ACS Appl. Energy Mater.* **2018**, *1*, 4115−4121.

(46) Gaim, A. K.; Grigorieva, I. V. Van der Waals heterostructures. *Nature*, **2013**, *499*, 419.

(47) Serlin, M.; Tschirhart, C. L.; Polshyn, H.; Zhang, Y.; Zhu, J.; Watanabe, K.; Taniguchi, T.; Balents, L.; Young, A. F. Intrinsic quantized anomalous Hall effect in a moiré heterostructure. *Science*, **2020**, *367*, 900–903.

(48) Cao, Y.; Fatemi, V.; Fang, S.; Watanabe, K.; Taniguchi, T.; Kaxiras, E.; Jarillo-Herrero, P. Unconventional superconductivity in magic-angle graphene superlattices. *Nature*. **2018**, *556*, 43-50.

(49) Sharpe, A. L.; Fox, E. J.; Barnard, A. W.; Finney, J.; Watanabe, K.; Taniguchi, T.; Kastner, M. A.; Goldhaber-Gordon, D. Emergent ferromagnetism near three-quarters filling in twisted bilayer graphene. *Science*, **2019**, 365, 605–608.

(50) Dean, C. R.; Wang, L.; Maher, P.; Forsythe, C.; Ghahari, F.; Gao, Y.; Katoch, J.; Ishigami, M.; moon, P.; Koshino, M.; Taniguchi, T.; Wantanabe, K.; Shepard, K. L.; Hone, J.; Kim, P. Hofstadter's butterfly and the fractal quantum Hall effect in moiré superlattices. *Nature*, **2013**, *497*, 598–602.

(51) Hunt, B.; Sanchez-Yamagishi, J. D.; Young, A. F.; Yankowitz, M.; LeRoy, B. J.; Watanabe, K.; Taniguchi, T.; Moon, P.; Koshino, M.; Jarillo-Herrero, P.; Ashoori, R. C. Massive Dirac Fermions and Hofstadter Butterfly in a van der Waals Heterostructure. *Science*, **2013**, *340*, 1427–1430.

(52) Jin, C.; Regan, E. C.; Yan, A.; Iqbal Bakti Utama, M.; Wang, D.; Zhao, S.; Qin, Y.; Yang, S.; Zheng, Z.; Shi, S.; Watanabe, K.; Taniguchi, T.; Tongay, S.; Zettl, A.; Wang, F. Observation of moiré excitons in WSe_2/WS_2 heterostructure superlattices. *Nature*, **2019**, *567*, 76–80.

(53) Tran, K.; Moody, G.; Wu, F.; Lu, X.; Choi, J.; Kim, K.; Rai, A.; Sanchez, D. A.; Quan, J.; Singh, A.; Embley, J.; Zepeda, A.; Campbell, M.; Autry, T.; Taniguchi, T.; Watanabe, K.; Lu, N.; Banerjee, S. K.; Silverman, K. L.; Kim, S.; Tutuc, E.; Yang, L.; MacDonald, A. H.; Li, X. Evidence for moire excitons in van der Waals heterostructures. *Nature*, **2019**, *567*, 71–75.

(54) Cao, Y.; Fatemi, V.; Demir, A.; Fang, S.; Tomarken, S. L.; Luo, J. Y.; Sanchez-Yamagishi, J. D.; Watanabe, K.; Taniguchi, T.; Kaxiras, E.; Ashoori, R. C.; Jarillo-Herrero, P. Correlated insulator behavior at half-filling in magic-angle graphene superlattices. *Nature*, **2018**, *556*, 80–84.

(55) Chen, G.; Jiang, L.; Wu, S.; Lyu, B.; Li, H.; Chittari, B. L.; Watanabe, K.; Taniguchi, T.; Shi, Z.; Jung, J.; Zhang, Y.; Wang, F. Evidence of a gate-tunable Mott insulator in a trilayer graphene moiré superlattice. *Nature Physics*. **2019**, *15*, 237–241.

(56) Frindt, R. F. Single crystals of MoS_2 several molecular layers thick. *J. Appl. Phys*. **1966**, *37*, 1928-1929.

(57) Novoselov, K. S.; Castro Neto, A. H. Two-dimensional crystals-based heterostructures: materials with tailored properties. *Phys. Scr*. **2010**, *T146*, 014006.

(58) Blake, P.; Hill, E.; Neto, A. C.; Novoselov, K.; Jiang, D.; Yang, R.; Booth, T.; Geim, A. Making graphene visible. *Appl. Phys. Lett,* **2007**, *91*, 063124.

(59) Roddaro, S.; Pingue, P.; Piazza, V.; Pellegrini, V.; Beltram, F. The Optical Visibility of Graphene: Interference Colors of Ultrathin Graphite on SiO_2. *Nano Lett,* **2007**, *7*, 2707.

(60) Castellanos-Gomez, A.; Agraït, N.; Rubio-Bollinger, G. Optical identification of atomically thin dichalcogenide crystals. *Appl. Phys. Lett,* **2010**, *96*, 213116.

(61) Zomer, P. J.; Dash, S. P.; Tombros, N.; van Wees, B. J. A transfer technigue for high mobility graphene devices on commercially available hexagonal boron nitride. *Appl. Phys. Lett.* **2011**, *99*, 232104.

(62) Schneider, G. F.; Calado, V. E.; Zandbergen, H.; Vandersypen, L. M. K.; Dekker, C. Wedging Transfer of Nanostructures. *Nano Lett.* **2010**, *10*, 1912.

(63) Castellanos-Gomez, A.; Buscema, M.; Molenaar, R.; Singh, V.; Janssen, L.; van der Zant, H. S. J.; Steele, G. A. Deterministic transfer for two-dimensional materials by all-dry viscoelastic stamping. *2D Materials*, **2014**, *1*, 011002.

(64) Choi, A. Y.; Arthur, J. R. Molecular beam epitaxy. *Prog. Solid State Chem.* **1975**, *10*, 157-191.

(65) Zheleva, T.; Jagannadham, K.; Narayan, J. Epitaxial growth in large-lattice-mismatch systems. *J. Appl. Phys*. **1994**, *75*. 860

(66) Cheng, F.; Ding, Z.; Xu, H.; Tan, S. J. R.; Abdelwahab, I.; Su, J.; Zhou, P.; Martin, J.; Loh, K. P. Epitaxial growth of single-layer niobium selenides with controlled stoichiometric phases. *Adv. Mater. Interfaces.* **2018**, *5,* 1800429.

(67) Vishmanath, S. Sundar, A.; Liu, X.; Azcatl. A.; Lochocki, E.; Woll, A. R.; Rouvimov, S.; Hwang, W. S.; Lu, N.; Peng, X.; Lien, H.-H.; Weisenberger, J.; McDonnell, S.; Kim, M. J.; Dobrowolska, M.; Furdyna, J. K.; Shen, K.; Wallace, R. M.; Jena, D.; Xing, H. G. MBE growth of few-layer 2H-$MoTe_2$ on 3D substrates. *Journal of Crystal Growth.* **2018**, *482*, 61–69.

(68) Williams, J. R.; Smalley, A. L. E.; Sellinschegg, H.; Daniels-Hafer, C.; Harris, J.; Johnson, M. B.; Johnson, D. C. Synthesis of Crystalline Skutterudite Superlattices Using the Modulated Elemental Reactant Method. *J. Am. Chem. Soc.* **2003**, *125*, 10335-10341.

(69) Fister, L.; Johnson, D. C.; Controlling Solid-State Reaction Mechanisms Using Diffusion Length in Ultrathin-Film Superlattice Composites. *J. Am. Chem. Soc.* **1992**, *114*, 4639-4644.

(70) Mishra, S. K.; Satpathy, S.; Jepsen, O. Electronic structure and thermoelectric properties of bismuth telluride and bismuth selenide. *J. Phys.: Condens. Matter.* **1997**, *9,* 461.

(71) Yao, L. -Z.; Crisostomo, C. P.; Yeh, C. -C.; Lai, S. -M.; Huang, Z. -Q.; Hsu, C. -H.; Chuang, F.- C.; Lin, H.; Bansil, A. Predicted Growth of Two-Dimentionals Topological Insulator Thin Films of III-V Compounds on Si(111) Substrate. Sci. Rep. **2015**, 5, 15463.

(72) Zhang, H.; Liu, C. -X.; Qi, X. -L.; Dai, X.; Fang, Z.; Zhang, S. -C. Topological insulators in Bi_2Se_3, Bi_2Te_3, and Sb_2Te_3 with a single Dirac cone on the surface. *Nat. Physics.* **2009**, *5,* 438.

(73) Chen, Y. S.; Analytis, J. G.; Chu, J.-H.; Lui, Z. K.; Mo, S.-K.; Qi, X.-L.; Zhang, H. J.; Lu, D. H.; Dai, X.; Fang, Z.; Zhang, S.-C.; Fisher, I. R.; Hussain, Z.; Shen, Z. -X. Experimental Realization of a Three-Dimensional Topological Insulator, Bi_2Te_3. *Science*. **2009**, *325,* 178.

(74) Hsieh, D.; Xia, Y.; Qian, D.; Wray, L.; Dil, J. H.; Meirer, F.; Osterwalder, J.; Patthey, L.; Checkelsky, J.G.; Ong, N. P.; Fedorov, A. V.; Lin, H.; Bansil, A.; Grauer, D.; Hor, Y. S.; Cava, R. J.; Hasan, M. Z. A tunable topological insulator in the spin helical Dirac transport regime. *Nature.* **2009**, *460,* 1101.

(75) He, L.; Kou, X.; Wang, K. L. Review of 3D topological insulator thin-film growth by molecular beam epitaxy and potential applications. *Phys. Status Solidi RRL.* **2013**, *7*, 50-63.

(76) Wang, G.; Zhu, X.-G.; Sun, Y. -Y.; Li, Y.-Y.; Zhang, T.; Wen, J.; Chen, X.; He, K.; Wang, L. -L.; Ma, X. -C.; Jia, J.-F.; Zhang, S. B.; Xue, Q. -K. Topological Insulator Thin Films of Bi_2Te_3 Controlled Electronic Structure. *Adv. Mater.* **2011**, *23*, 2929.

(77) He, L.; Xiu, F.; Yu, X.; Teague, M.; Jiang, W.; Fan, Y.; Kou, X.; Lang, M.; Wang, Y.; Huang, G.; Yeh, N-.C.; Wang, K. L. Surface-dominated conduction in a 6 nm thick Bi_2Se_3 thin film. *Nano. Lett.* **2012**, *12*, 1486.

(78) Hadland, E. C.; Jang, H.; Wolff, N.; Fischer, R.; Lygo, A. C.; Mitchson, G.; Li, D.; Kienle, L.; Cahill, D. G.; Johnson, D. C. Ultralow thermal conductivity of turbostratically disordered $MoSe_2$ ultra-thin films and implications for heterostructures. *Nanotechnology.* **2019**, *30*, 285401.

(79) Wang, M-X.; Liu, C.; Xu, J-P.; Yang, F.; Miao, L.; Yao, M-Y.; Gao, C. L.; Shen, C.; Ma, X.; Chen, X.; Xu, Z. A.; Liu, Y.; Zhang, S-C.; Qian, D.; Jia, J-F.; Xue, Q-K. The coexistence of superconductivity and topological order in the Bi_2Se_3 thin films. *Science*. **2012**, *336*, 52.

(80) Matetskiy, A. V.; Kibirev, I. A.; Hirahara, T.; Hasegawa, S.; Zotov, A. V.; Saranin, A. A. Directo observation of a gap opening in topological interface states of $MnSe/Bi_2Se_3$ heterostructure. *Appl. Phys. Lett.* **2015**, *107*, 091604.

(81) Chen, K. H. M.; Lin, H. Y.; Yang, S. R.; Cheng, C. K.; Zhang, X. Q.; Cheng, C. M.; Lee, S. F.; Hsu, C. H.; Lee, Y. H.; Hong, M.; Kwo, J. Van der Waals epitaxy of topological insulator Bi_2Se_3 on single layer transition metal dichalcogenide MoS_2. *Appl. Phys. Lett.* **2017**, *111*, 083106.

(82) Xenogiannopoulou, E.; Tsipas, P.; Aretouli, K. E.; Tsoutsou, D.; Giamini, S. A.; Bazioti, C.; Dimitrakopulos, G. P.; Komninou, P.; Brems, S.; Huyghebaert, C.; Raduc, I. P.; Dimoulas, A. High-quality, large area $MoSe_2$ and $MoSe_2/Bi_2Se_3$ heterostructures on AIN(0001)/Si(111) substrates by molecular beam epitaxy. *Nanoscale*, **2015**, *7*, 7896.

(83) Vishwanatha, S.; Liu, X.; Rouvimov, S.; Basile. L.; Lu, N.; Azcatl, A.; Magno, K.; Wallace, R. M.; Kim, M.; Idrobo, J. -C.; Furdyna, J. K.; Jena, D.; Xingb, H. G. Controllable growth of layered selenides and telluride heterostructures and superlattices using molecular beam epitaxy. *J. Mater. Res.*, **2016**, *31,* 900.

(84) Wang, M-W.; Li, P.; Xu, J-P.; Liu, Z-L.; Ge, J-F.; Wang, G-Y.; Yang, X.; Xu, Z-A.; Ji, S-H.; Gao, C. L.; Qian, D.; Luo, W.; Liu, C.; Jia, J-F. Interface structure of a topological insulator/superconductor heterostructure. *New Journal of Physics*. **2014**, *16*, 123043.

(85) Esters, M.; Hennig, R. G.; Johnson, D. C. Insights into the Charge-Transfer Stabilization of Heterostructure Components with Unstable Bulk Analogs. Chem. Mater. **2018**, 30, 4738−4747.

(86) Falmbigl, M.; Alemayehu, M. B.; Merrill, D. R.; Beekman, M.; Johnson, D. C. In-Plane Structure of Ferecrystalline Compounds. *Cryst. Res. Technol.* **2015**, *50* (6), 464−472.

(87) Merrill, D. R.; Moore, D. B.; Coffey, M. N.; Jansons, A. W.; Falmbigl, M.; Johnson, D. C. Synthesis and Characterization of Turbostratically Disordered $(BiSe)_{1.15}TiSe_2$. *Semicond. Sci. Technol.* **2014**, *29* (6), 064004.

(88) Mitchson, G.; Falmbigl, M.; Ditto, J.; Johnson, D. C. Antiphase Boundaries in the Turbostratically Disordered Misfit Compound $(BiSe)_{1+\delta}NbSe_2$. *Inorg. Chem.* **2015**, *54* (21), 10309−10315.

(89) Zhou, W. Y.; Meetsma, A.; de Boer, J. L.; Wiegers, G. A. Characterization and Electrical Transport Properties of the Misfit Layer Compounds $(BiSe)_{1.10}NbSe_2$ and $(BiSe)_{1.09}TaSe_2$. *Mater. Res. Bull.* **1992**, *27*, 563−572.

(90) Petríček, V.; Cisarova, I.; de Boer, J. L.; Zhou, W.; Meetsma, A.; ˇ Wiegers, G. A.; van Smaalen, S. The Modulated Structure of the Commensurate Misfit-Layer Compound $(BiSe)_{1.09}TaSe_2$. *Acta Crystallogr., Sect. B: Struct. Sci.* **1993**, *49* (2), 258−266.

(91) Trump, B. A.; Livi, K. J. T.; McQueen, T. M. The New Misfit Compound $(BiSe)_{1.15}(TiSe_2)_2$ and the Role of Dimensionality in the Cux $(BiSe)_{1+\delta}(TiSe_2)_n$ Series. *J. Solid State Chem.* **2014**, *209*, 6−12.

(92) Clarke, S. M.; Freedman, D. E. (BiSe)1.23CrSe2 and $(BiSe)_{1.22}(Cr_{1.2}Se_2)_2$: Magnetic Anisotropy in the First Structurally Characterized Bi-Se-Cr Ternary Compounds. *Inorg. Chem.* **2015**, *54* (6), 2765−2771.

(93) Choffel, M. A.; Kam, T. M.; Johnson. D. C. Substituent Effects in the Synthesis of Heterostructures. *Inorg. Chem.* **2021**, *60*, 9598−9606.

(94) Hadland, E. C.; Gohler, F.; Mitchson, G.; Fender. S. S.; Schmidt, C.; Zahn, D. R. T.; Seyller, T.; Johnson, D. C. Synthesis and Properties of $(BiSe)_{0.97}MoSe_2$: A Heterostructure Containing Both 2H-$MoSe_2$ and 1T-$MoSe_2$. *Chem. Mater.* **2019**, *31*, 5824.

(95) Lygo, A. C.; Hamann, D. M.; Moore, D. B.; Merrill, D. R.; Ditto, J.; Esters, M.; Orlowicz, J.; Wood, S. R.; Johnson, D. C. Kinetically Controlled Formation and Decomposition of Metastable $[(BiSe)_{1+\delta}]_m[(TiSe_2)]_m$ Compounds. *J. Am. Chem. Soc.* **2018**, *140*, 3385−3393.

(96) Lygo, A. C.; Wood, S. R.; Ditto, J.; Johnson, D. C. Syntheis of $(BiSe)_{1+\delta}(Bi_2Se_3)_{1+\gamma}(BiSe)_{1+\delta}TiSe_2$ by Directed Self-Assembly of a Designed Precursor. *Chem. Mater.* **2019**, *31*, 216.

(97) Choffel, M. A.; Gannon, R. N.; Göhler, F.; Miller, A. M.; Medlin, D.; Seyller, T.; Johnson, D. C. Synthesis and Electrical Properties of a New Compound $(BiSe)_{0.97}(Bi_2Se_3)_{1.26}(BiSe)_{0.97}(MoSe_2)$ Containing Metallic 1T-$MoSe_2$. *Chem. Mater.* **2021**. 33, 16, 6403–6411

(98) Xia, Y.; Qian, D.; Hsieh, D.; Wray, L.; Pal, A.; Lin, H.; Bansil, A.; Grauer, D.; Hor, Y. S.; Cava, R. J.; Hasan, M. Z. Observation of a large-gap topological-insulator class with a single Dirac cone on the surface. *Nat. Phys.* **2009**, *5*, 398−402.

(99) Göhler, F.; Choffel, M. A.; Schmidt, C.; Zahn, D. R. T.; Johnson, D. C.; Seyller, T. Influence of Nanoarchitectures on Interlayer Interaction in Layered Bi-Mo-Se Heterostructures. *J. Phys. Chem. C.* **2021**, *125,* 9469-9478.

(100) Woods, S. R. Merrill, D. R.; Falmbigl, M.; Moore, D. B.; Ditto, J.; Esters, M.; Johnson. D. C. Tuning Electrical Properties through Control of $TiSe_2$ Thickness in $(BiSe)_{1+\delta}(TiSe_2)_n$ Compounds. *Chem. Mater.* **2015**, *27*, 6067−6076.

(101) Mitchson, G.; Falmigl, M.; Ditto, J.; Johnson, D. C. Antiphase Boundaries in the Turbostratically Disordered Misfit Compound $(BiSe)_{1+\delta}NbSe_2$. *Inorg. Chem.* **2015**, *54* (21) 10309–10315

(102) Mitchson, G.; Hadland, E.; Gohler, F.; Wanke, M.; Esters, M.; Ditto, J.; Bigwood, E.; Ta, K.; Henning, R. G.; Seyller, T.; Johnson, D. C. Structural Changes in 2D BiSe Bilayers as n Increases in $(BiSe)_{1+\delta}(NbSe_2)_n$ (n=1-4) Heterostructures. *ACS Nano.* **2016**, *10*, 9489−9499.

Chapter II

(1) Dumcenco, D. O.; Kobayashi, H.; Liu, Z.; Huang, Y. S.; Suenaga, K. Visualization and Quantification of Transition Metal Atomic Mixing in $Mo_{1-x}W_xS_2$ Single Layers. *Nat. Commun.* **2013**, *4*, 1351.

(2) Matetskiy, A. V.; Kibirev, I. A.; Hirahara, T.; Hasegawa, S.; Zotov, A. V.; Saranin, A. A. Direct Observation of a Gap Opening in Topological Interface States of MnSe/Bi_2Se_3 Heterostructure. *Appl. Phys. Lett.* **2015**, *107*, 091604.

(3) Hirahara, T.; Eremeev, S. V.; Shirasawa, T.; Okuyama, Y.; Kubo, T.; Nakanishi, R.; Akiyama, R.; Takayama, A.; Hajiri, T.; Ideta, S.; Matsunami, M.; Sumida, K.; Miyamoto, K.; Takagi, Y.; Tanaka, K.; Okuda, T.; Yokoyama, T.; Kimura, S.; Hasegawa, S.; Chulkov, E. V. Large-Gap Magnetic Topological Heterostructure Formed by Subsur- face Incorporation of a Ferromagnetic Layer. *Nano Lett.* **2017**, *17*, 3493−3500.

(4) Ohlhausen, J. A.; Zavadil, K. R. Time-of-Flight Secondary Ion Mass Spectrometry Measurements of a Fluorocarbon-Based Self-Assembled Monolayer on Si. *J. Vac. Sci. Technol., A* **2006**, *24*, 1172−1178.

(5) Hamann, D. M., Bardgett, D., Cordova, D. L. M., Maynard, L. A., Hadland, E. C, Lygo, A. C., Wood, S. R., Esters, M., and Johnson, D. C. Sub-Monolayer Accuracy in Determining the Number of Atoms per Unit Area in Ultrathin Films Using X-ray Fluorescence. *Chem. Mater.* **2018**, *30*, 6209.

(6) Stout, V. L.; Gibbons, M. D. Gettering of Gas by Titanium. *Journal of Applied Physics*. **1955**, *26*, 1488.

(7) Warren, B. E. *X-Ray Diffraction*, Reprinted; Dover Publications, **1990**.

(8) Huang, T. C.; Gilles, R.; Will, G. Thin-film thickness and density determination from X-ray reflectivity data using a conventional power diffractometer. *Thin Solid Films*, **1993**, *230*, 99-101.

(9) Nellist, P. D.; Pennycook, S. J. The Principles and Interpretation of Annular Dark-Field Z-Contrast Imaging. *Adv. Imaging Electron Phys.* **2000**, *113* (C), 147–203.

(10) D'Alfonso, A. J.; Freitag, B.; Klenov, D.; Allen, L. J. Atomic-Resolution Chemical Mapping Using Energy-Dispersive x-Ray Spectroscopy. *Phys. Rev. B - Condens. Matter Mater. Phys.* **2010**, *81* (10).

(11) Hollander, J. M.; Jolly, W. L. X-ray Photoelectron Spectroscopy. *Accounts of chemical research*. **1970**, *3*, 193-200.

(12) Sokolowski, E.; Nordling, C.; Siegbahn, K. Precision method for obtaining absolute values of atomic binding energies. *Phys. Rev.,* **1957**, *105*, 1676.

(13) van der Pauw, L. J. A Method of Measuring the Resistivity and Hall Coefficient on Lamellae of Arbitrary Shape. *Philips Res. Rept.*, **1958**, *13*, 1.

Chapter III

(1) Kraschinski, S.; Herzog, S.; Bensch, W. *Solid State Sci.* **2002**, *4* (10), 1237–1243.

(2) Herzog, S.; Kraschinski, S.; Bensch, W. *Zeitschrift für Anorg. und Allg. Chemie* **2003**, *629* (10), 1825–1832.

(3) Behrens, M.; Kiebach, R.; Bensch, W.; Haussler, D.; Jäger, W. *Inorg. Chem.,* **2006**, *45*, 2704-2712.

(4) Regus, M.; Kuhn, G.; Polesya, S.; Mankovsky, S.; Alemayehu, M.; Stolt, M.; Johnson, D. C.; Ebert, H.; Bensch, W. *Zeitschrift für Krist. - Cryst. Mater.* **2014**, *229* (7), 505–515.

(5) Fukuto, M.; Hornbostel, M. D.; Johnson, D. C. *J. Am. Chem. Soc.* **1994**, *116* (20), 9136–9140.

(6) Regus, M.; Mankovsky, S.; Polesya, S.; Kuhn, G.; Ditto, J.; Schürmann, U.; Jacquot, A.; Bartholomé, K.; Näther, C.; Winkler, M.; König, J. D.; Böttner, H.; Kienle, L.; Johnson, D. C.; Ebert, H.; Bensch, W. *J. Solid State Chem.* **2015**, *230*, 254–265.

(7) König, J. D.; Winkler, M.; Buller, S.; Bensch, W.; Schürmann, U.; Kienle, L.; Böttner, H. *J. Electron. Mater.* **2011**, *40* (5), 1266–1270.

(8) Novet, T.; Johnson, D. C. *J. Am. Chem. Soc.* **1991**, *113* (9), 3398–3403.

(9) Sun, W.; Dacek, S. T.; Ong, S. P.; Hautier, G.; Jain, A.; Richards, W. D.; Gamst, A. C.; Persson, K. A.; Ceder, G. *Sci. Adv.* **2016**, *2* (11), e1600225–e1600225.

(10) Oyelaran, O.; Novet, T.; Johnson, C. D.; Johnson, D. C. *J. Am. Chem. Soc.* **1996**, *118* (10), 2422–2426.

(11) Williams, J. R.; Johnson, M.; Johnson, D. C. *J. Am. Chem. Soc.* **2001**, *123,* 1645-1649.

(12) Williams, J. R.; Johnson, M.; Johnson, D. C. *J. Am. Chem. Soc.* **2003**, *125,* 3589-3592.

(13) Hornbostel, M. D.; Hyer, E. J.; Thiel, J.; Johnson, D. C. *Inorg. Chem.* **1997**, *36,* 4270-4274.

(14) Heimbrodt, W.; Goede, O.; Tschentscher, I.; Weinhold, V.; Klimakow, A.; Pohl, U.; Jacobs, K.; Hoffmann, N. *Phys. B Condens. Matter* **1993**, *185* (1–4), 357–361.

(15) Tomasini, P.; Haidoux, A.; Tédenac, J. C.; Maurin, M. *J. Cryst. Growth* **1998**, *193* (4), 572–576.

(16) Decker, D. L.; Wild, R. L. *Phys. Rev. B* **1971**, *4* (10), 3425–3437.

(17) Peng, Q; Dong, Y; Deng, Z.; Kou, H.; Gao, S.; Li, Y. *J. Phys. Chem. B.* **2002**, *106*, 9261-9265.

(18) Chun, H. J.; Lee, J. Y.; Kim, D. S.; Yoon, S. W.; Kang, J. H.; Park, J. *J. Phys. Chem. C.* **2006**, *111*, 519-525.

(19) Wang, L.; Chen, L.; Luo, T.; Bao, K.; Qian, Y. *Solid State Commun.* **2006**, *138* (2), 72–75.

(20) Wu, M.; Xiong, Y.; Jiang, N.; Ning, M.; Chen, Q. *J. Cryst. Growth* **2004**, *262* (1–4), 567–571.

(21) Qin, T.; Lu, J.; Wei, S.; Qi, P.; Peng, Y.; Yang, Z.; Qian, Y. *Inorg. Chem. Commun.* **2002**, *5* (5), 369–371.

(22) Norris, D. J.; Yao, N.; Charnock, F. T.; Kennedy, T. A. *Nano Letters.* **2000**, *1*, 3-7.

(23) Levy, L.; Feltin, N.; Ingert, D.; Pileni, M. P. *J. Phys. Chem. B.* **1997**, *101*, 9153-9160.

(24) Suyver, J. F.; van der Beek, T.; Wuister, S. F.; Kelly, J. J.; Meijerink, A. *Appl. Phys. Lett.* **2001**, *79,* 4222.

(25) Mehta, J. M.; Riewald, P. G.; Vlack, L. H. *J. Am. Ceram. Soc.* **1967**, *50* (3), 164–164.

(26) Elliott, N. *J. Am. Chem. Soc.* **1937**, *59* (10), 1958–1962.

(27) H. Schnaase. *Z. Phys. Chem. B* **1933**, *20*, 89.

(28) Baroni, A. *Z. Krist.* **1938**, No. A99, 336.

(29) Hamann, D. M.; Bardgett, D.; Cordova, D. L. M.; Maynard, L. A.; Hadland, E. C.; Lygo, A. C.; Wood, S. R.; Esters, M.; Johnson, D. C. *Chem. Mater.* **2018**, acs.chemmater.8b02591.

(30)Zeppenfeld, A. C.; Fiddler, S. L.; Ham, W. K.; Klopfenstein, B. J.; Page, C. J. *J. Am. Chem. Soc.* **1994**, *116* (20), 9158–9165.

(31) Vanyarkho, V.G.; Zlomanov, V.P; Novoselova, A.V.; Fokin, V. N. *Inorg. Mater.* **1969**, *5* (10), 1440–1443.

(32) Fister, L.; Johnson, D. C. *J. Am. Chem. Soc.* **1992**, *114* (12), 4639–4644.

Chapter IV

(1) Cao, Y.; Fatemi, V.; Fang, S.; Watanabe, K.; Taniguchi, T.; Kaxiras, E.; Jarillo-Herrero, P. Unconventional superconductivity in magic-angle graphene superlattices. *Nature*. **2018**, *556*, 43-50.

(2) Serlin, M.; Tschirhart, C. L.; Polshyn, H.; Zhang, Y.; Zhu, J.; Watanabe, K.; Taniguchi, T.; Balents, L.; Young, A. F. Intrinsic quantized anomalous Hall effect in a moiré heterostructure. *Science*, **2020**, *367*, 900–903.

(3) Sharpe, A. L.; Fox, E. J.; Barnard, A. W.; Finney, J.; Watanabe, K.; Taniguchi, T.; Kastner, M. A.; Goldhaber-Gordon, D. Emergent ferromagnetism near three-quarters filling in twisted bilayer graphene. *Science*, **2019**, 365, 605–608.

(4) Dean, C. R.; Wang, L.; Maher, P.; Forsythe, C.; Ghahari, F.; Gao, Y.; Katoch, J.; Ishigami, M.; moon, P.; Koshino, M.; Taniguchi, T.; Wantanabe, K.; Shepard, K. L.; Hone, J.; Kim, P. Hofstadter's butterfly and the fractal quantum Hall effect in moiré superlattices. *Nature*, **2013**, *497*, 598–602.

(5) Hunt, B.; Sanchez-Yamagishi, J. D.; Young, A. F.; Yankowitz, M.; LeRoy, B. J.; Watanabe, K.; Taniguchi, T.; Moon, P.; Koshino, M.; Jarillo-Herrero, P.; Ashoori, R. C. Massive Dirac Fermions and Hofstadter Butterfly in a van der Waals Heterostructure. *Science*, **2013**, *340*, 1427–1430.

(6) Jin, C.; Regan, E. C.; Yan, A.; Iqbal Bakti Utama, M.; Wang, D.; Zhao, S.; Qin, Y.; Yang, S.; Zheng, Z.; Shi, S.; Watanabe, K.; Taniguchi, T.; Tongay, S.; Zettl, A.; Wang, F. Observation of moiré excitons in WSe_2/WS_2 heterostructure superlattices. *Nature*, **2019**, *567*, 76–80.

(7) Tran, K.; Moody, G.; Wu, F.; Lu, X.; Choi, J.; Kim, K.; Rai, A.; Sanchez, D. A.; Quan, J.; Singh, A.; Embley, J.; Zepeda, A.; Campbell, M.; Autry, T.; Taniguchi, T.; Watanabe, K.; Lu, N.; Banerjee, S. K.; Silverman, K. L.; Kim, S.; Tutuc, E.; Yang, L.; MacDonald, A. H.; Li, X. Evidence for moire excitons in van der Waals heterostructures. *Nature*, **2019**, *567*, 71–75.

(8) Cao, Y.; Fatemi, V.; Demir, A.; Fang, S.; Tomarken, S. L.; Luo, J. Y.; Sanchez-Yamagishi, J. D.; Watanabe, K.; Taniguchi, T.; Kaxiras, E.; Ashoori, R. C.; Jarillo-Herrero, P. Correlated insulator behavior at half-filling in magic-angle graphene superlattices. *Nature*, **2018**, *556*, 80–84.

(9) Chen, G.; Jiang, L.; Wu, S.; Lyu, B.; Li, H.; Chittari, B. L.; Watanabe, K.; Taniguchi, T.; Shi, Z.; Jung, J.; Zhang, Y.; Wang, F. Evidence of a gate-tunable Mott insulator in a trilayer graphene moiré superlattice. *Nature Physics*. **2019**, *15*, 237–241.

(10) Liu, Y.; Rodrigues, J. N. B.; Luo, Y. Z.; Li, L.; Carvalho, A.; Yang, M.; Laksono, E.; Lu, J.; Bao, Y.; Xu, H.; Tan, S. J. R.; Qiu, Z.; Sow, C. H.; Feng, Y. P.; Neto, A. H. C.; Adam, S.; Lu, J.; Loh, K. P. Tailoring sample-wide pseudo-magnetic fields on a graphene-black phosphorus heterostructure. *Nature Nanotechnology*, **2018**, *13*, 828–834.

(11) Regan, E. C.; Wang, D.; Jin, C.; Bakti Utama, M. I.; Gao, B.; Wei, X.; Zhao, S.; Zhao, W.; Zhang, Z.; Yumigeta, K.; Blei, M.; Carlström, J. D.; Watanabe, K.; Taniguchi, T.; Tongay, S.; Crommie, M.; Zettl, A.; Wang, F. Mott and generalized Wigner crystal states in WSe_2/WS_2 moiré superlattices. *Nature*, **2020**, *579*, 359–363.

(12) Tang, Y.; Li, L.; Li, T.; Xu, Y.; Liu, S.; Barmak, K.; Watanabe, K.; Taniguchi, T.; MacDonald, A. H.; Shan, J.; Mak, K. F. Simulation of Hubbard model physics in WSe_2/WS_2 moiré superlattices. *Nature*, **2020**, *579*, 353–358.

(13) Xiao, Y.; Liu, J.; Fu, L. Moiré is More: Access to New Properties of Two-Dimensional Layered Materials. *Matter*, **2020**, *3*, 1142–1161.

(14) Novoselov, K. S.; Geim, A. K.; Morozov, S. V.; Jiang, D.; Zhange, Y.; Dubonos, S. V.; Grigorieva, I. V.; Firsov, A. A. Electronic Field Effect in Atomically Thin Carbon Films. *Science,* **2004**, *306,* 666-669.

(15) Cho, A. Y.; Arthur, J. R. Molecular beam epitaxy. *Prog. Solid State Chem.* **1975**, *10*, 157-191.

(16) Chen, Y.; Washburn, J. Structural Transition in Large-Lattice-Mismatch Heteroepitaxy. *Phys. Rev. Lett.,* **1996**, *77*, 4046.

(17) Zheleva, T.; Jagannadham, K.; Narayan, J. *Journal of Applied Physics*. **1994**, *75*, 860.

(18) Ingold, C. Structure and mechanism in organic chemistry. **1969**, ISBN 0801404991 9780801404993.

(19) Robinson, R. The Development of Electrochemical Theories of the Course of Reactions of Carbon Compounds. *J. Chem. Soc*. **1947**, 1288-1301.

(20) Xenogiannopoulou, E.; Tsipas, P.; Aretouli, K. E.; Tsoutsou, D.; Giamini, S. A.; Bazioti, C.; Dimitrakopulos, G. P.; Komninou, P.; Brems, S.; Huyghebaert, C.; Raduc, I. P.; Dimoulas, A. High-quality, large-area $MoSe_2$ and $MoSe_2/Bi_2Se_3$ heterostructures on AlN(0001)/Si(111) substrates by molecular beam epitaxy. *Nanoscale*, **2015**, *7*, 7896.

(21) Chen, K. H. M.; Lin, H. Y.; Yang, S. R.; Cheng, C. K.; Zhang, X. Q.; Cheng, C. M.; Lee, S. F.; Hsu, C. H.; Lee, Y. H.; Hong, M.; Kwo, J. Van der Waals epitaxy of topological insulator Bi_2Se_3 on single layer transition metal dichalcogenide MoS_2. *Appl. Phys. Lett.* **2017**, *111*, 083106.

(22) Vishwanatha, S.; Liu, X.; Rouvimov, S.; Basile. L.; Lu, N.; Azcatl, A.; Magno, K.; Wallace, R. M.; Kim, M.; Idrobo, J. -C.; Furdyna, J. K.; Jena, D.; Xingb, H. G. Controllable growth of layered selenides and telluride heterostructures and superlattices using molecular beam epitaxy. *J. Mater. Res.*, **2016**, *31,* 900.

(23) Wang, M-W.; Li, P.; Xu, J-P.; Liu, Z-L.; Ge, J-F.; Wang, G-Y.; Yang, X.; Xu, Z-A.; Ji, S-H.; Gao, C. L.; Qian, D.; Luo, W.; Liu, C.; Jia, J-F. Interface structure of a topological insulator/superconductor heterostructure. *New Journal of Physics*. **2014**, *16*, 123043.

(24) Hadland, E. C.; Gohler, F.; Mitchson, G.; Fender. S. S.; Schmidt, C.; Zahn, D. R. T.; Seyller, T.; Johnson, D. C. Synthesis and Properties of $(BiSe)_{0.97}MoSe_2$: A Heterostructure Containing Both 2H-$MoSe_2$ and 1T-$MoSe_2$. *Chem. Mater*. **2019**, *31*, 5824.

(25) Göhler, F.; Choffel, M. A.; Schmidt, C.; Zahn, D.R.T.; Johnson, D.C.; Seyller, T. Influence of Nanoarchitectures on Interlayer Interactions in Layered Bi−Mo−Se Heterostructures. *J. Phys. Chem. C,* **2021**, *125*, 17, 9469–9478.

(26) Hamann, D. M., Bardgett, D., Cordova, D. L. M., Maynard, L. A., Hadland, E. C, Lygo, A. C., Wood, S. R., Esters, M., and Johnson, D. C. Sub-Monolayer Accuracy in Determining the Number of Atoms per Unit Area in Ultrathin Films Using X-ray Fluorescence. *Chem. Mater.* **2018**, *30*, 6209.

(27) Novet, T.; Johnson, D. C. New Synthestiv Approach to Extened Solids: Selective Synthesis of Iron Silicides via the Amorphous State. *J. Am. Chem. Soc.* **1991**, *113*, 3398-3403.

(28) Fister, L.; Johnson, D. C.; Controlling Solid-State Reaction Mechanisms Using Diffusion Length in Ultrathin-Film Superlattice Composites. *J. Am. Chem. Soc.* **1992**, *114*, 4639-4644.

(29) Noh, M.; Johnson, C. D.; Hornbostel, M. D.; Thiel, J.; Johnson, D. J. Control of Reaction Pathway and the Nanostructure of Final Products through the Design of Modulated Elemental Reactants. Chem. Mater. **1996**, 8, 1625-1635.

(30) Kong, J. D.; Winkler, M.; Buller, S.; Bensch, W.; Schurmann, U.; Kienle, L.; Bottner, H. Bi_2Se_3-Sb_2Te_3 Superlattices Grown by Nanoalloying. *J. Electron. Mater.* **2011**, *40*(5), 1266.

(31) Cordova, D. L. M.; Johnson, D. C. Synthesis of Metastable Inorganic Solids with Extended Structures. *ChemPhysChem* **2020**, *21*, 1345– 1368.

(32) Perez, V. C.; Tirado, J. L.; Adouby, K.; Jumas, J.C.; Abba Toure, A.; Kra, G. X-ray Diffraction and ^{119}Sn Mossbauer Spectroscopy Study of a New Phase in the Bi_2Se_3-SnSe System: $SnBi_2Se_7$. *Inorganic Chemistry.* **1999**, *38,* 2131.

(33) Gardes, B.; Brun, G.; Tedenac, J. -C. Contribution to the study of the bismuth-selenium system. *European Journal of Solid State and Inorganic Chemistry.* **1989**, *26*, 221.

(34) Stasova, M. M. Crystal structure of bismuth selenides and bismuth and antimony tellurides. *Zhurnal Strukturnoi Khimii.* **1967**, *8*, 655.

(35) Imamov, P. M.; Semiletov, S. A. The Crystal Structure of the Phases in the Sustems Bi-Se, Bi-Te, and Sb-Te. *Kristallografiya.* **1970**, *15*, 972.

(36) Boechko, V.E.; Isarev, V.I. Crystalization Conditions and Properties of Single Crystals of p-Type Bi_2Se_3. *lzv. Akad. Nauk SSSR, Neorg. Mater,* **1975**, *11*, 1510.

(37) Sher, A.A.; Odin, I.E.; Novoselova, A.V. Investication of the Phases in the Bi-Se System. *Zh. Neorg. Khim.*, **1986**, *31*, 764.

(38) Wiese, J. R.; Muldawer, L. Lattice Constants of Bi_2Te_3-Bi_2Se_3 Solid Solution Alloys. *Phys. Chem. Solids*, **1960**, *15*, 13-16.

(39) Okamom, H. The Bi-Se (Bismuth-Selenium) System. *J. Phase Equilib*. **1994**, *15*, 195-201.

(40) Cordova, D. L. M.; Kam, T. K.; Fender, S. S.; Tsai, Y. H.; Johnson, D. C. Strong Non-Epitaxial Interactions: Crystallographically Aligned PbSe on VSe_2. *Phys. Status Solidi A*, **2019**, *216*, 1800896.

(41) Noda, Y.; Ohba, S.; Saito, Y. Charge distribution and atomic thermal vibration in lead chalcogenide crystals. *Acta Crystallographica, Section B: Structural Science.* **1983**, *39*, 312.

(42) Lygo, A. C.; Wood, S. R.; Ditto, J.; Johnson, D. C. Syntheis of $(BiSe)_{1+\delta}(Bi_2Se_3)_{1+\gamma}(BiSe)_{1+\delta}TiSe_2$ by Directed Self-Assembly of a Designed Precursor. *Chem. Mater.* **2019**, *31*, 216.

(43) Shelimova, L. E.; Karpinskii, O. G.; Konstantinov, P. P.; Avilov, E. S.; Kretova, M. A.; Lubman, G. U.; Nikhezina, I. Y.; Zemskov, V. S. Composition and properties of compounds in the PbSe-Bi_2Se_3 system. *Inorganic Materials*, **2010**, *46*, 120.

(44) Smeller, M. M.; Heideman, C. L.; Lin, Q.; Beekman, M. Anderson, M. D.; Zschack, P.; Anderson, I, M.; Johnson, D. C. Structure of Turbostratically Disordered Misfit Layer Compounds $[(PbSe)_{0.99}]_1[WSe_2]_1$, $[(PbSe)_{1.00}]_1[MoSe_2]_1$, and $[(SnSe)_{1.03}]_1[MoSe_2]_1$. *Z. Anorg. Allg. Chem.* **2012**, *638*, 2632.

(45) Moore, D. B.; Beekman, M.; Disch, S.; Zschack, P.; Hausler, I.; Neumann, W.; Johnson, D. C. Synthesis, Structure, and Properties of Turbostratically Disordered $(PbSe)_{1.18}(TiSe_2)_2$. *Chem. Mater.* **2013**, *25*, 2404.

(46) Grosse, C.; Alemayehu, M. B.; Falmbigl, M.; Mogilatenko, A.; Chiatti, O.; Johnson, D. C.; Fischer, S. F. Superconducting ferecrystals: turbostratically disordered atomic-scale layered $(PbSe)_{1.14}(NbSe_2)_n$ thin films. *Sci. Rep.* **2016**, *6*, 33457.

(47) Lygo, A. C.; Hamann, D. M.; Moore, D. B.; Merrill, D. R.; Ditto, J.; Esters, M.; Orlowicz, J.; Wood, S. R.; Johnson, D. C. Kinetically Controlled Formation and Decomposition of Metastable $[(BiSe)_{1+\delta}]_m[TiSe_2]_2$ Compounds. *J. Am. Chem. Soc.* **2018**, *140*, 3385.

(48) Zhang, W.; Yu, R.; Zhang, H.-J.; Dai, X.; Fang, Z. First-principles studies of the three-dimensional strong topological insulators Bi_2Te_3, Bi_2Se_3, and Sb_2Te_3. *New J. Phys.* **2010**, *12*, 065013.

(49) Hite, O. K.; Nellist, M.; Ditto, J.; Falmbigl, M.; Johnson, D. C. Transport properties of VSe_2 monolayers sperated by bilayers of BiSe. *J. Mater. Res.* **2016**, *31*, 886.

(50) Mitchson, G.; Falmbigl, M.; Ditto, J.; Johnson, D. C. Antiphase Boundaries in the Turbostratically Disordered Misfit Compound $(BiSe)_{1+\delta}NbSe_2$. *Inorg. Chem.* **2015**, *54*, 10309.

Chapter V

(1) Laursen, A. B.; Kegnas, S.; Dahl, S.; Chorkendorff, I. Molybdenum sulfides – efficient and viable materials for electro- and photoelectocatalytic hydrogen evolution. *Energy Environ. Sci.* **2012**, *5*, 5577-5591.

(2) Ambrosi, A.; Sofer, Z.; Pumera, M. 2H → 1T phase transition and hydrogen evolution activity of MoS_2, $MoSe_2$, WS_2 and WSe_2 strongly depends on the MX_2 composition. *Chem. Commun.* **2015**, *51*, 8450.

(3) Yin, Y.; Zhang, Y.; Gao, T.; Yao,, T.; Zhang, X.; Han, J.; Wang, X.; Zhang, Z.; Xu, P.; Zhang, P.; Cao, X.; Song, B.; Jin, S. Synergistic Phase and Disorder Engineering in 1T-$MoSe_2$ Nanosheets for Enhanced Hydrogen-Evolution Reaction. *Adv. Mater.* **2017**, *29*, 1700311.

(4) Puthussery, J.; Seefeld, S.; Berry, N.; Gibbs, M.; Law, M. Colloidal Iron Pyrite (FeS_2) Nanocrystal Inks for Thin-Film Photovoltaics. *J. Am. Chem. Soc.* **2011**, *133*, 716.

(5) Feng, J.; Sun, X.; Wu, C. Z.; Peng, L. L.; Lin, C. W.; Hu, S. L.; Yang, J. L.; Xie, Y. Metallic Few-Layered VS_2 Ultrathin Nanosheets: High Two-Dimensional Conductivity for In-Plane Supercapacitors. *J. Am. Chem. Soc.* **2011**, *133*, 17832.

(6) Ding, S. J.; Zhang, D. Y.; Chen, J. S.; Lou, X. W. Facile synthesis of hierarchical MoS_2 microspheres composed of few-layered nanosheets and their lithium storage properties. *Nanoscale* **2012**, *4*, 95.

(7) Wilson, J. A.; Yoffe, A. D. The transition metal dichalcogenides discussion and interpretation of the observed optical, electrical, and structural properties. *Adv. Phys.*, **1969**, *18*, 193–335.

(8) Chhowalla, M.; Shin, H. S.; Eda, G.; Li, L. -J.; Loh, K. P.; Zhang, H. The chemistry of two-dimensionbal layered transition metal dichalcogenide nanosheets. *Nature Chemistry*. **2013**, *5*, 263.

(9) Kobayashi, K.; Yamauchi, J. Electronic structure and scanning-tunneling-microscopy image of molybdenum dichalcogenide surfaces. *Phys. Rev. B.* **1995**, *51*, 17085.

(10) Ding, Y.; Wang, Y.; Ni, J.; Shi, L.; Shi, S.; Tang, W. First principles study of structural, vibrational, and electrica properties of graphene-like MX2 (M = Mo, Nb, W, Ta; X = S, Se, Te) monolayers. *Physica B* **2011**, *406*, 2254–2260.

(11) Tongay, S.; Zhou, J.; Ataca, C.; Lo, K.; Matthews, T. S.; Li, J.; Grossman, J. C.; Wu, J. Thermally driven crossover from indirect toward direct bandgap in 2D semiconductors: MoSe2 versus MoS2. *Nano Lett.* **2012**, *12*, 5576−5580.

(12) Splendiani, A.; Sun, L.; Zhang, Y.; Li, T.; Kim, T.; Chim, C.-Y.; Galli, G.; Wang, F. Emergin Photoluminescences in Monolayer MoS_2. *Nano Lett.* **2010**, *10*, 1271–1275.

(13) Yu, Z. G.; Yakosen, B. I.; Zhang, Y.-W. Realizing Indirect-to-Direct Band Gap Transition in Few-Layer Two-Dimensional MX_2 (M = Mo, W; X = S, Se). *ACS Appl. Energy Mater.* **2018**, *1*, 4115−4121.

(14) Steinhoff, A.; Kim, J. -H.; Jahnke, F.; Rosner, M.; Kim, D. -S.; Lee, C.; Han, G. H.; Jeong, M. S.; Wehling, T. O.; Gies, C. Efficient Excitonic Photoluminescence in Direct and Indirect Band Gap Monolayer MoS_2. *Nano Lett.* **2015**, *15*, 6841−6847.

(15) Zhao, W.; Ghorannevis, Z.; Chu, L.; Toh, M.; Kloc, C.; Tan, P. -H.; Eda, G. Evolution of electronic structure in atomically thin sheets of WS_2 and WSe_2. *ACS Nano.* **2013**, *7*, 791-797.

(16) McCreary, K. M.; Hanbicki, A. T.; Jernigan, G. G.; Culbertson, J. C.; Jonker, B. T. The effect of Preparation Conditions on Raman and Photoluminescence of Monolayer WS_2. *Sci. Rep.* **2016**, *6*, 19159.

(17) Hermann, A. M.; Somoano, R.; Hadek, V.; Rembaum, A. Electrical Resistivity of Intercalated Molybdenum Disulfide. *Solid State Communications*. **1973**, *13*, 1065.

(18) Py, M. A.; Haering, R. R. Structureal destabilization induced by lithium intercalation in MoS_2 and related compounds. *Can. J. Phys*. **1983**, *61*, 76.

(19) Kappera, R.; Voiry, D.; Yalcin, S. E.; Branch, B.; Gupta, G.; Mohite, A. D.; Chhowalla, M. Phase-engineered low-resistance constacts for ultrathin MoS_2 transistors. *Nat. Materials.* **2014**, *12*, 1128.

(20) Friedman, A. L.; Hanbicki, A. T.; Perkins, F. K.; Jernigan, G. G.; Culbertson, J. C.; Campbell, P. M. Evidence for Chemical Vapor Induced 2H to 1T Phase Transition in MoX_2 (X = Se, S) Transition Metal Dichalcogenide Films. *Scientific Reports*. **2017**, *7*, 3836.

(21) Rudorff, W. Alkali Metal Intercalation Compounds of Transition Metal Chalcogenides: TX_2, TX_3, and TX_4 Chalcogenides. *Chimia*, **1965**, 489.

(22) Schöllhorn, R.; Weiss, A. Cation exchange reactions and layer solvate complexes of ternary phases M_xMoS_2. *Journal of the Less-Common Metals,* **1974**, *36*, 229-236.

(23) Murphy, D.; Di Salvo, F.; Hull, G.; Waszczak, J. Convenient Preparation and Physical Properties of Lithium Intercalation Compounds of Group 4B and 5B Layered Transition Metal Dichalcogenides. *Inorg. Chem.* **1976**, *15*, 17.

(24) Schöllhorn, R.; Meyer, H. Cathodic reduction of layered transition metal chalcogenides. *Mat. Res. Bull.* **1974**, *9*, 1237.

(25) Haering, R. R.; Stiles, J. A. R.; Brandt, K. Lithium Molybdenum Disulphide Battery Cathode. US Patent 4, 224, 390, September 23, 1980.

(26) Radisavljevic, B.; Whitwick, M. B.; Kis, A. Integrated Circuits and Logic Operations Based on Single-Layer MoS_2. *ACS Nano* **2011**, *5*, 9934–9938.

(27) Cheng, X.B.; Zhang, R.; Zhao, C.Z.; Zhang Q. Toward Safe Lithium Metal Anode in Rechargeable Batteries: A Review. *Chem. Rev.,* **2017**, *117*, 10403-10473.

(28) Weigers, G. A. Misfit layer compounds: Structures and physical properties. *Prog. Solid. St. Chem.* **1996**, *24*, 1-139.

(29) Hadland, E. C.; Gohler, F.; Mitchson, G.; Fender. S. S.; Schmidt, C.; Zahn, D. R. T.; Seyller, T.; Johnson, D. C. Synthesis and Properties of $(BiSe)_{0.97}MoSe_2$: A Heterostructure Containing Both 2H-$MoSe_2$ and 1T-$MoSe_2$. *Chem. Mater.* **2019**, *31*, 5824.

(30) Lygo, A. C.; Hamann, D. M.; Moore, D. B.; Merrill, D. R.; Ditto, J.; Esters, M.; Orlowicz, J.; Wood, S. R.; Johnson, D. C. Kinetically Controlled Formation and Decomposition of Metastable $[(BiSe)_{1+\delta}]_m[(TiSe_2)]_m$ Compounds. *J. Am. Chem. Soc.* **2018**, *140*, 3385−3393.

(31) Lygo, A. C.; Wood, S. R.; Ditto, J.; Johnson, D. C. Syntheis of $(BiSe)_{1+\delta}(Bi_2Se_3)_{1+\gamma}(BiSe)_{1+\delta}TiSe_2$ by Directed Self-Assembly of a Designed Precursor. *Chem. Mater.* **2019**, *31*, 216.

(32) Hamann, D. M., Bardgett, D., Cordova, D. L. M., Maynard, L. A., Hadland, E. C, Lygo, A. C., Wood, S. R., Esters, M., and Johnson, D. C. Sub-Monolayer Accuracy in Determining the Number of Atoms per Unit Area in Ultrathin Films Using X-ray Fluorescence. *Chem. Mater.* **2018**, *30*, 6209.

(33) Schaffer, M.; Schaffer, B.; Ramasse, Q. Sample preparation for atomic-resolution STEM at low voltages by FIB. *Ultramicroscopy*, **2012**, *114*, 62-71.

(34) Miller, A. M.; Hamann, D. M.; Hadland, E. C.; Johnson, D. C. Investigating the Formation of $MoSe_2$ and $TiSe_2$ Films form Artificially Layered Precursors. I*norg. Chem.* **2020**, *59*, 12536–12544.

(35) Mitchson, G.; Falmbigl, M.; Ditto, J.; Johnson, D. C. Antiphase Boundaries in the Turbostratically Disordered Misfit Compound $(BiSe)_{1+\delta}NbSe_2$. *Inorg. Chem.* **2015**, *54*, 10309.

(36) Smeller, M. M.; Heideman, C. L.; Lin, Q.; Beekman, M. Anderson, M. D.; Zschack, P.; Anderson, I, M.; Johnson, D. C. Structure of Turbostratically Disordered Misfit Layer Compounds $[(PbSe)_{0.99}]_1[WSe_2]_1$, $[(PbSe)_{1.00}]_1[MoSe_2]_1$, and $[(SnSe)_{1.03}]_1[MoSe_2]_1$. *Z. Anorg. Allg. Chem.* **2012**, *638*, 2632.

(37) Moore, D. B.; Beekman, M.; Disch, S.; Zschack, P.; Hausler, I.; Neumann, W.; Johnson, D. C. Synthesis, Structure, and Properties of Turbostratically Disordered $(PbSe)_{1.18}(TiSe_2)_2$. *Chem. Mater.* **2013**, *25*, 2404.

(38) Grosse, C.; Alemayehu, M. B.; Falmbigl, M.; Mogilatenko, A.; Chiatti, O.; Johnson, D. C.; Fischer, S. F. Superconducting ferecrystals: turbostratically disordered atomic-scale layered $(PbSe)_{1.14}(NbSe_2)_n$ thin films. *Sci. Rep.* **2016**, *6*, 33457.

(39) Yu, Y.; Nam, G.-H.; He, Q.; Wu, X.-J.; Zhang, K.; Yang, Z.; Chen, J.; Ma, Q.; Zhao, M.; Liu, Z.; Ran, F.-R.; Wang, X.; Li, H.; Huang, X.; Li, B.; Xiong, Q.; Zhang, Q.; Liu, Z.; Gu, L.; Du, Y.; Huang, W.; Zhang, H. High phase-purity 1T'-MoS_2- and 1T'-$MoSe_2$-layered crystals. *Nat. Chem*, **2018**, *10*(6), 638.

(40) Esters, M.; Henning, R. G.; Johnson, D. C. Insights into the Charge-Transfer Stabilization of Heterostructure Components with Unstable Bulk Analogs. *Chem. Mater*. **2018**, *30*, 4738.

(41) Mitchson, G.; Hadland, E. C.; Gohler, F.; Wanke, M.; Esters, M.; Ditto, J.; Bigwood, E.; Ta, K.; Henning, R. G.; Seyller, T.; Johnson, D. C. Structure Changes in 2D BiSe Bilayers as n Increases in $(BiSe)_{1+\delta}(NbSe_2)_n$ (n = 1-4) Heterostructures. *ACS Nano* **2016**, *10*, 9489.

(42) Hadland, E. C.; Jang, H.; Wolff, N.; Fischer, R.; Lygo, A. C.; Mitchson, G.; Li, D.; Kienle, L.; Cahill, D. G.; Johnson, D. C. Ultralow thermal conductivity of turbostratically disordered $MoSe_2$ ultra-thin films and implications for heterostructures. *Nanotechnology.* **2019**, *30*, 285401.

Chapter VI

(1) Novoselov, K. S.; Geim, A. K.; Morozov, S. V.; Jiang, D.; Zhang, Y.; Dubonos, S. V.; Grigorieva, I. V.; Firsov, A. A. Electric Field Effect in Atomically Thin Carbon Films. *Science* **2004**, *306*, 666–669.

(2) Cao, Y.; Fatemi, V.; Fang, S.; Watanabe, K.; Taniguchi, T.; Kaxiras, E.; Jarillo-Herrero, P. Unconventional superconductivity in magic-angle graphene superlattices. *Nature*. **2018**, *556*, 43-50.

(3) Sharpe, A. L.; Fox, E. J.; Barnard, A. W.; Finney, J.; Watanabe, K.; Taniguchi, T.; Kastner, M. A.; Goldhaber-Gordon, D. Emergent ferromagnetism near three-quarters filling in twisted bilayer graphene. *Science*, **2019**, 365, 605–608.

(4) Gaim, A. K.; Grigorieva, I. V. Van der Waals heterostructures. *Nature*, **2013**, *499*, 419.

(5) Serlin, M.; Tschirhart, C. L.; Polshyn, H.; Zhang, Y.; Zhu, J.; Watanabe, K.; Taniguchi, T.; Balents, L.; Young, A. F. Intrinsic quantized anomalous Hall effect in a moiré heterostructure. *Science*, **2020**, *367*, 900–903.

(6) Tongay, S.; Zhou, J.; Ataca, C.; Lo, K.; Matthews, T. S.; Li, J.; Grossman, J. C.; Wu, J. Thermally driven crossover from indirect toward direct bandgap in 2D semiconductors: $MoSe_2$ versus MoS_2. *Nano Lett.* **2012**, *12*, 5576−5580.

(7) Wang, M.-W.; Li, P.; Xu, J.-P.; Liu, Z.-L.; Ge, J.-F.; Wang, G.-Y.; Yang, X.; Xu, Z.-A.; Ji, S.-H.; Gao, C. L.; Qian, D.; Luo, W.; Liu, C.; Jia, J.-F. Interface structure of a topological insulator/superconductor heterostructure. New J. Phys. **2014**, 16, 123043.

(8) Splendiani, A.; Sun, L.; Zhang, Y.; Li, T.; Kim, T.; Chim, C.-Y.; Galli, G.; Wang, F. Emerging Photoluminescence in Monolayer MoS_2. *Nano Lett.* **2010**, *10*, 1271–1275.

(9) Yu, Z. G.; Yakosen, B. I.; Zhang, Y.-W. Realizing Indirect-to-Direct Band Gap Transition in Few-Layer Two Dimensional MX_2 (M = Mo, W; S = S, Se). *ACS Appl. Energy Mater.* **2018**, *1*, 4115−4121.

(10) Py, M. A.; Haering, R. R. Structureal destabilization induced by lithium intercalation in MoS_2 and related compounds. *Can. J. Phys.* **1983**, *61*, 76.

(11) Rudorff, W. Alkali Metal Intercalation Compounds of Transition Metal Chalcogenides: TX_2, TX_3, and TX_4 Chalcogenides. *Chimia*, **1965**, 489.

(12) Schöllhorn, R.; Weiss, A. Cation exchange reactions and layer solvate complexes of ternary phases M_xMoS_2. *Journal of the Less-Common Metals,* **1974**, *36*, 229-236.

(13) Hadland, E. C.; Gohler, F.; Mitchson, G.; Fender. S. S.; Schmidt, C.; Zahn, D. R. T.; Seyller, T.; Johnson, D. C. Synthesis and Properties of $(BiSe)_{0.97}MoSe_2$: A Heterostructure Containing Both 2H-$MoSe_2$ and 1T-$MoSe_2$. *Chem. Mater.* **2019**, *31*, 5824.

(14) Esters, M.; Henning, R. G.; Johnson, D. C. Insights into the Charge-Transfer Stabilization of Heterostructure Components with Unstable Bulk Analogs. *Chem. Mater.* **2018**, *30*, 4738.

(15) Mishra, S. K.; Satpathy, S.; Jepsen, O. Electronic structure and thermoelectric properties of bismuth telluride and bismuth selenide. *J. Phys.: Condens. Matter.* **1997**, *9,* 461.

(16) Yao, L. -Z.; Crisostomo, C. P.; Yeh, C. -C.; Lai, S. -M.; Huang, Z. -Q.; Hsu, C. -H.; Chuang, F.- C.; Lin, H.; Bansil, A. Predicted Growth of Two-Dimentionals Topological Insulatore Thin Films of III-V Compounds on Si(111) Substrate. *Sci. Rep.* **2015**, *5*, 15463.

(17) Zhang, H.; Liu, C. -X.; Qi, X. -L.; Dai, X.; Fang, Z.; Zhang, S. -C. Topological insulators in Bi_2Se_3, Bi_2Te_3, and Sb_2Te_3 with a single Dirac cone on the surface. *Nat. Physics.* **2009**, *5,* 438.

(18) Choffel, M. A.; Gannon, R. N.; Göhler, F.; Miller, A. M.; Medlin, D.; Seyller, T.; Johnson, D. C. Synthesis and Electrical Properties of a New Compound $(BiSe)_{0.97}(Bi_2Se_3)_{1.26}(BiSe)_{0.97}(MoSe_2)$ Containing Metallic 1T-$MoSe_2$. *Chem. Mater.* **2021**. *33*, 16, 6403–6411

(19) Xenogiannopoulou, E.; Tsipas, P.; Aretouli, K. E.; Tsoutsou, D.; Giamini, S. A.; Bazioti, C.; Dimitrakopulos, G. P.; Komninou, P.; Brems, S.; Huyghebaert, C.; Raduc, I. P.; Dimoulas, A. High-quality, large-area $MoSe_2$ and $MoSe_2/Bi_2Se_3$ heterostructures on AlN(0001)/ Si(111) substrates by molecular beam epitaxy. *Nanoscale*. **2015**, *7*, 7896.

(20) Chen, K. H. M.; Lin, H. Y.; Yang, S. R.; Cheng, C. K.; Zhang, X. Q.; Cheng, C. M.; Lee, S. F.; Hsu, C. H.; Lee, Y. H.; Hong, M.; Kwo, J. Van der Waals epitaxy of topological insulator Bi_2Se_3 on single layer transition metal dichalcogenide MoS_2. *Appl. Phys. Lett.* **2017**, *111*, 083106.

(21) Vishwanatha, S.; Liu, X.; Rouvimov, S.; Basile, L.; Lu, N.; Azcatl, A.; Magno, K.; Wallace, R. M.; Kim, M.; Idrobo, J.-C.; Furdyna, J. K.; Jena, D.; Xingb, H. G. Controllable growth of layered selenides and telluride heterostructures and superlattices using molecular beam epitaxy. *J. Mater. Res.* **2016**, *31*, 900.

(22) Choffel, M. A.; Kam, T. M.; Johnson. D. C. Substituent Effects in the Synthesis of Heterostructures. *Inorg. Chem.* **2021**, *60*, 9598−9606.

(23) Lygo, A. C.; Hamann, D. M.; Moore, D. B.; Merrill, D. R.; Ditto, J.; Esters, M.; Orlowicz, J.; Wood, S. R.; Johnson, D. C. Kinetically Controlled Formation and Decomposition of Metastable $[(BiSe)_{1+\delta}]_m[(TiSe_2)]_m$ Compounds. *J. Am. Chem. Soc.* **2018**, *140*, 3385−3393.

(24) Fister, L.; Johnson, D. C.; Controlling Solid-State Reaction Mechanisms Using Diffusion Length in Ultrathin-Film Superlattice Composites. *J. Am. Chem. Soc.* **1992**, *114*, 4639-4644.

(25) Hamann, D. M.; Bardgett, D.; Cordova, D. L. M.; Maynard, L. A.; Hadland, E. C.; Lygo, A. C.; Wood, S. R.; Esters, M.; Johnson, D. C. Sub-Monolayer Accuracy in Determining the Number of Atoms per Unit Area in Ultrathin Films Using X-ray Fluorescence. *Chem. Mater.* **2018**, *30*, 6209−6216.

(26) Lygo, A. C.; Wood, S. R.; Ditto, J.; Johnson, D. C. Synthesis of $(BiSe)_{1+\delta}(Bi_2Se_3)_{1+\gamma}(BiSe)_{1+\delta}TiSe_2$ by Directed Self-Assembly of a Designed Precursor. *Chem. Mater.* **2019**, *31*, 216−223.

(27) Ambrosi, A.; Sofer, Z.; Pumera, M. 2H - 1T phase transition and hydrogen evolution activity of MoS_2, $MoSe_2$, WS_2 and WSe_2 strongly depends on the MX_2 composition. *Chem. Commun.* **2015**, *51*, 8450−8453.

(28) Yu, Y.; Nam, G.-H.; He, Q.; Wu, X.-J.; Zhang, K.; Yang, Z.; Chen, J.; Ma, Q.; Zhao, M.; Liu, Z.; Ran, F.-R.; Wang, X.; Li, H.; Huang, X.; Li, B.; Xiong, Q.; Zhang, Q.; Liu, Z.; Gu, L.; Du, Y.; Huang, W.; Zhang, H. *Nat. Chem*, **2018**, *10*(6), 638.

(29) Mitchson, G.; Falmbigl, M.; Ditto, J.; Johnson, D. C. *Inorg. Chem.* **2015**, *54*, 10309.

(30) Göhler, F.; Choffel, M. A.; Schmidt, C.; Zahn, D. R. T.; Johnson, D. C.; Seyller, T. Influence of Nanoarchitectures on Interlayer Interaction in Layered Bi-Mo-Se Heterostructures. *J. Phys. Chem. C*. **2021**, *125,* 9469-9478.

(31) Lind, H.; Lidin, S.; Häussermann, U. Structure and bonding properties of $(Bi_2Se_3)_m(Bi_2)_n$ stacks by first-principles density functional theory. *Phys. Rev. B* **2005**, *72*, No. 184101.

(32) He, L.; Xiu, F.; Wang, Y.; Fedorov, A. V.; Huang, G.; Kou, X.; Lang, M.; Beyermann, W. P.; Zou, J.; Wang, K. L. Epitaxial growth of Bi_2Se_3 topological insulator thin films on Si (111). *J. Appl. Phys*. **2011**, *109,* 103702.

(33) Kappera, R.; Voiry, D.; Yalcin, S. E.; Branch, B.; Gupta, G.; Mohite, A. D.; Chhowalla, M. Phase-engineered low-resistance contacts for ultrathin MoS_2 transistors. *Nat. Mater.* **2014**, *13*, 1128−1134.

(34) Friedman, A. L.; Hanbicki, A. T.; Perkins, F. K.; Jernigan, G. G.; Culbertson, J. C.; Campbell, P. M. Evidence for Chemical Vapor Induced 2H to 1T Phase Transition in MoX_2 (X = Se, S) Transition Metal Dichalcogenide Films. *Scientific Reports*. **2017**, *7*, 3836.

(35) Hadland, E. C.; Jang, H.; Wolff, N.; Fischer, R.; Lygo, A. C.; Mitchson, G.; Li, D.; Kienle, L.; Cahill, D. G.; Johnson, D. C. Ultralow thermal conductivity of turbostratically disordered $MoSe_2$ ultra-thin films and implications for heterostructures. *Nanotechnology* **2019**, *30*, 285401.

(36) Xia, Y.; Qian, D.; Hsieh, D.; Wray, L.; Pal, A.; Lin, H.; Bansil, A.; Grauer, D.; Hor, Y. S.; Cava, R. J. Observation of a large-gap topological-insulator class with a single Dirac cone on the surface. *Nat. Phys*. **2009**, *5*, 398−402.

Chapter VII

(1) Geim, A. K.; Grigorieva, I. V. Van der Waals heterostructures. *Nature* **2013**, *499*, 419−425.

(2) Robinson, J. A. Growing Vertical in the Flatland. *ACS Nano* **2016**, *10*, 42−45.

(3) Withers, F.; Pozo-Zamudio, O. D.; Mishchenko, A.; Rooney, A. P.; Gholinia, A.; Watanabe, K.; Taniguchi, T.; Haigh, S. J.; Geim, A. K.; Tartakovskii, A. I.; et al. Light-emitting diodes by band-structure engineering in van der Waals heterostructures. *Nat. Mater.* **2015**, *14*, 301−306.

(4) Novoselov, K. S.; Mishchenko, A.; Carvalho, A.; Neto, A. H. C. 2D materials and van der Waals heterostructures. *Science* **2016**, *353*, No. aac9439.

(5) Liu, Y.; Weiss, N. O.; Duan, X.; Cheng, H.-C.; Huang, Y.; Duan, X. Van der Waals heterostructures and devices. *Nat. Rev. Mater.* **2016**, *1*, No. 16042.

(6) Esters, M.; Alemayehu, M. B.; Jones, Z.; Nguyen, N. T.; Anderson, M. D.; Grosse, C.; Fischer, S. F.; Johnson, D. C. Synthesis of Inorganic Structural Isomers By Diffusion-Constrained Self-Assembly of Designed Precursors: A Novel Type of Isomerism. *Angew. Chem., Int. Ed.* **2015**, *54*, 1130−1134.

(7) Westover, R.; Atkins, R. A.; Falmbigl, M.; Ditto, J. J.; Johnson, D. C. Self-assembly of designed precursors: A route to crystallographically aligned new materials with controlled nanoarchitecture. *J. Solid State Chem.* **2016**, *236*, 173−185.

(8) Beekman, M.; Disch, S.; Gunning, N.; Johnson, D. C. Preparation, Formation, and Structure of $[(SnSe)_{1.04}]_m(MoSe_2)_n$ Intergrowth Compounds ($0 < m$ and $n < 32$) from Designed Precursors. *Inorg. Chem.* **2015**, *54*, 1091−1099.

(9) Alemayehu, M. B.; Falmbigl, M.; Ta, K.; Ditto, J.; Medlin, D. L.; Johnson, D. C. Designed Synthesis of van der Waals Heterostructures: The Power of Kinetic Control. *Angew. Chem.* **2015**, *127*, 15688− 15692.

(10) Wiegers, G. A. Misfit layer compounds: Structures and physical properties. *Prog. Solid State Chem.* **1996**, *24*, 1−139.

(11) Lygo, A. C.; Hamann, D. M.; Moore, D. B.; Merrill, D. R.; Ditto, J.; Esters, M.; Orlowicz, J.; Wood, S. R.; Johnson, D. C. Kinetically Controlled Formation and Decomposition of Metastable $[(BiSe)_{1+\delta}]_m[TiSe_2]_m$ Compounds. *J. Am. Chem. Soc.* **2018**, *140*, 3385−3393.

(12) Hadland, E. C.; Gӧhler, F.; Mitchson, G.; Fender, S. S.; Schmidt, C.; Zahn, D. R. T.; Seyller, T.; Johnson, D. C. Synthesis and Properties of $(BiSe)_{0.97}MoSe_2$: A Heterostructure Containing Both 2H-$MoSe_2$ and 1T-$MoSe_2$. *Chem. Mater.* **2019**, *31*, 5824−5831.

(13) Kappera, R.; Voiry, D.; Yalcin, S. E.; Branch, B.; Gupta, G.; Mohite, A. D.; Chhowalla, M. Phase-engineered low-resistance contacts for ultrathin MoS_2 transistors. *Nat. Mater.* **2014**, *13*, 1128−1134.

(14) Kappera, R.; Voiry, D.; Yalcin, S. E.; Jen, W.; Acerce, M.; Torrel, S.; Branch, B.; Lei, S.; Chen, W.; Najmaei, S.; et al. Metallic 1T phase source/drain electrodes for field effect transistors from chemical vapor deposited MoS_2. *APL Mater.* **2014**, *2*, 092516.

(15) Ambrosi, A.; Sofer, Z.; Pumera, M. 2H - 1T phase transition and hydrogen evolution activity of MoS_2, $MoSe_2$, WS_2 and WSe_2 strongly depends on the MX_2 composition. *Chem. Commun.* **2015**, *51*, 8450−8453.

(16) Yin, Y.; Zhang, Y.; Gao, T.; Yao, T.; Zhang, X.; Han, J.; Wang, X.; Zhang, Z.; Xu, P.; Zhang, P.; et al. Synergistic Phase and Disorder Engineerign in 1T-$MoSe_2$ Nanosheets for Enhances Hydrogen Evolution Reaction. *Adv. Mater.* **2017**, *29*, No, 1700311.

(17) Yu, Y.; Nam, G.-H.; He, Q.; Wu, X.-J.; Zhang, K.; Yang, Z.; Chen, J.; Ma, Q.; Zhao, M.; Liu, Z.; et al. High phase-purity 1T′- MoS_2- and 1T′-$MoSe_2$-layered crystals. *Nat. Chem.* **2018**, *10*, 638− 643.

(18) Ohno, Y. Electronic structure of the misfit-layer compounds $PbTiS_3$ and $SnNbS_3$. *Phys. Rev. B* **1991**, *44*, No. 1281.

(19) Ohno, Y. Interlayer interaction in misfit layer compounds MTS_3 (M = Sn, Pb, La; T = Ti, Nb). *Solid State Commun.* **1991**, *79*, 1081−1084.

(20) Eda, G.; Yamaguchi, H.; Voiry, D.; Fujita, T.; Chen, M.; Chhowalla, M. Photoluminescence from Chemically Exfoliated MoS_2. *Nano Lett.* **2011**, *11*, 5111−5116.

(21) Kallӓne, M.; Roßnagel, K.; Marczynski-Bühlow, M.; Kipp, L.; Starnberg, H. I.; Stoltz, S. E. Stabilization of the misfit layer compound $(PbS)_{1.13}TaS_2$ by metal cross substitution. *Phys. Rev. Lett.* **2008**, *100*, No. 065502.

(22) Hamann, D. M.; Bardgett, D.; Cordova, D. L. M.; Maynard, L. A.; Hadland, E. C.; Lygo, A. C.; Wood, S. R.; Esters, M.; Johnson, D. C. Sub-Monolayer Accuracy in Determining the Number of Atoms per Unit Area in Ultrathin Films Using X-ray Fluorescence. *Chem. Mater.* **2018**, *30*, 6209−6216.

(23) Hadland, E. C.; Jang, H.; Wolff, N.; Fischer, R.; Lygo, A. C.; Mitchson, G.; Li, D.; Kienle, L.; Cahill, D. G.; Johnson, D. C. Ultralow thermal conductivity of turbostratically disordered $MoSe_2$ ultra-thin films and implications for heterostructures. *Nanotechnology* **2019**, *30*, No. 285401.

(24) Boechko, V.; Isarev, V. Crystallization Conditions and Properties of Single Crystals of p-Type Bi_2Se_3. *Izv. Akad. Nauk SSSR, Neorg. Mater.* **1975**, *11*, 1510−1511.

(25) Sher, A. A.; Odin, I. E.; Novoselova, A. V. Investigation of the phases in the Bi-Se System. *Zh. Neorg. Khim.* **1986**, *31*, 764.

(26) Mitchson, G.; Hadland, E.; Göhler, F.; Wanke, M.; Esters, M.; Ditto, J.; Bigwood, E.; Ta, K.; Hennig, R. G.; Seyller, T.; et al. Structural Changes in 2D BiSe Bilayers as n Increases in $(BiSe)_{1+\delta}(NbSe_2)_n$ (n = 1−4) Heterostructures. *ACS Nano* **2016**, *10*, 9489−9499.

(27) Lygo, A. C.; Wood, S. R.; Ditto, J.; Johnson, D. C. Synthesis of $(BiSe)_{1+\delta}(Bi_2Se_3)_{1+\gamma}(BiSe)_{1+\delta}TiSe_2$ by Directed Self-Assembly of a Designed Precursor. *Chem. Mater.* **2019**, *31*, 216−223.

(28) Böker, Th.; Severin, R.; Müller, A.; Janowitz, C.; Manzke, R.; Voß, D.; Krüger, P.; Mazur, A.; Pollmann, J. Band structure of Mo_2, $MoSe_2$, and α-$MoTe_2$: Angle-resolved photoelectron spectroscopy and ab initio calculations. *Phys. Rev. B* **2001**, *64*, No. 235305.

(29) Kang, J.; Tongay, S.; Zhou, J.; Li, J.; Wu, J. Band offsets and heterostructures of two-dimensional semiconductors. *Appl. Phys. Lett.* **2013**, *102*, No. 012111.

(30) Johnson, D. C. Controlled synthesis of new compounds using modulated elemental reactants. Curr. Opin. *Solid State Mater. Sci.* **1998**, *3*, 159−167.

(31) Zhang, W.; Yu, R.; Zhang, H.-J.; Dai, X.; Fang, Z. First- principles studies of the three-dimensional strong topological insulators Bi_2Te_3, Bi_2Se_3 and Sb_2Te_3. *New J. Phys.* **2010**, *12*, No. 065013.

(32) Vyshnepolsky, M.; Klein, C.; Klasing, F.; Hanisch-Blicharski, A.; von Hoegen, M. H. Epitaxial growth of the topological insulator Bi_2Se_3 on Si(111): Growth mode, lattice parameter, and strain state. *Appl. Phys. Lett.* **2013**, *103*, No. 111909.

(33) Esters, M.; Hennig, R. G.; Johnson, D. C. Insights into the Charge-Transfer Stabilization of Heterostructure Components with Unstable Bulk Analogs. *Chem. Mater.* **2018**, *30*, 4738−4747.

(34) Mårtensson, N.; Nyholm, R. Electron spectroscopic determinations of M and N core-hole lifetimes for the elements Nb−Te (Z = 41−52). *Phys. Rev. B* **1981**, *24*, No. 7121.

(35) Xia, Y.; Qian, D.; Hsieh, D.; Wray, L.; Pal, A.; Lin, H.; Bansil, A.; Grauer, D.; Hor, Y. S.; Cava, R. J.; et al. Observation of a large-gap topological-insulator class with a single Dirac cone on the surface. *Nat. Phys.* **2009**, *5*, 398−402.

(36) Tonndorf, P.; Schmidt, R.; Böttger, P.; Zhang, X.; Börner, J.; Liebig, A.; Albrecht, M.; Kloc, C.; Gordan, O.; Zahn, D. R. T.; et al. Photoluminescence emission and Raman response of monolayer MoS_2, $MoSe_2$, and WSe_2. *Opt. Express* **2013**, *21*, 4908.

(37) Gupta, U.; Naidu, B. S.; Maitra, U.; Singh, A.; Shirodkar, S. N.; Waghmare, U. V.; Rao, C. N. R. Characterization of few-layer 1T-$MoSe_2$ and its superior performance in the visible-light induced hydrogen evolution reaction. *APL Mater.* **2014**, *2*, No. 092802.

(38) Zhang, J.; Peng, Z.; Soni, A.; Zhao, Y.; Xiong, Y.; Peng, B.; Wang, J.; Dresselhaus, M. S.; Xiong, Q. Raman Spectroscopy of Few-Quintuple Layer Topological Insulator Bi_2Se_3 Nanoplatelets. *Nano Lett.* **2011**, *11*, 2407−2414.

(39) Saito, R.; Tatsumi, Y.; Huang, S.; Ling, X.; Dresselhaus, M. S. Raman spectroscopy of transition metal dichalcogenides. J. Phys.: *Condens. Matter* **2016**, *28*, No. 353002.

(40) Lind, H.; Lidin, S.; Häussermann, U. Structure and bonding properties of $(Bi_2Se_3)_m(Bi_2)_n$ stacks by first-principles density functional theory. *Phys. Rev. B* **2005**, *72*, No. 184101.

(41) Göhler, F.; Mitchson, G.; Alemayehu, M. B.; Speck, F.; Wanke, M.; Johnson, D. C.; Seyller, T. Charge transfer in $(PbSe)_{1+\delta}(NbSe_2)_2$ and $(SnSe)_{1+\delta}(NbSe_2)_2$ ferecrystals investigated by photoelectron spectroscopy. *J. Phys.: Condens. Matter* **2018**, *30*, No. 055001.

(42) Chhowalla, M.; Shin, H. S.; Eda, G.; Li, L.-J.; Loh, K. P.; Zhang, H. The chemistry of two-dimensional layered transition metal dichalcogenide nanosheets. *Nat. Chem.* **2013**, *5*, 263−275.

(43) Zhang, Y.; Chang, T.-R.; Zhou, B.; Cui, Y.-T.; Yan, H.; Liu, Z.; Schmitt, F.; Lee, J.; Moore, R.; Chen, Y.; et al. Direct observation of the transition from indirect to direct bandgap in atomically thin epitaxial $MoSe_2$. *Nat. Nanotechnol.* **2014**, *9*, 111−115.

Chapter VIII

(1) Hamann, D. M., Bardgett, D., Cordova, D. L. M., Maynard, L. A., Hadland, E. C, Lygo, A. C., Wood, S. R., Esters, M., and Johnson, D. C. Sub-Monolayer Accuracy in Determining the Number of Atoms per Unit Area in Ultrathin Films Using X-ray Fluorescence. *Chem. Mater.* **2018**, *30*, 6209.

(2) Hadland, E. C.; Gohler, F.; Mitchson, G.; Fender. S. S.; Schmidt, C.; Zahn, D. R. T.; Seyller, T.; Johnson, D. C. Synthesis and Properties of $(BiSe)_{0.97}MoSe_2$: A Heterostructure Containing Both 2H-$MoSe_2$ and 1T-$MoSe_2$. *Chem. Mater.* **2019**, *31*, 5824.

(3) Miller, A. M.; Hamann, D. M.; Hadland, E. C.; Johnson, D. C. Investigating the Formation of $MoSe_2$ and $TiSe_2$ Films form Artificially Layered Precursors. I*norg. Chem.* **2020**, *59*, 12536–12544.

(4) Champion, J. A. Some Properties of (Mo, W)(Se, Te)2. *British Journal of Applied Physics.* **1965**, *16*, 1035.

(5) Mitchson, G.; Hadland, E. C.; Gohler, F.; Wanke, M.; Esters, M.; Ditto, J.; Bigwood, E.; Ta, K.; Henning, R. G.; Seyller, T.; Johnson, D. C. Structure Changes in 2D BiSe Bilayers as n Increases in $(BiSe)_{1+\delta}(NbSe_2)_n$ (n = 1-4) Heterostructures. *ACS Nano* **2016**, *10*, 9489.

(6) Woods, S. R. Merrill, D. R.; Falmbigl, M.; Moore, D. B.; Ditto, J.; Esters, M.; Johnson. D. C. Tuning Electrical Properties through Control of $TiSe_2$ Thickness in $(BiSe)_{1+\delta}(TiSe_2)_n$ Compounds. *Chem. Mater.* **2015**, *27*, 6067−6076.

(7) Mitchson, G.; Falmigl, M.; Ditto, J.; Johnson, D. C. Antiphase Boundaries in the Turbostratically Disordered Misfit Compound $(BiSe)_{1+\delta}NbSe_2$. *Inorg. Chem.* **2015**, *54* (21) 10309–10315

(8) Smeller, M. M.; Heideman, C. L.; Lin, Q.; Beekman, M. Anderson, M. D.; Zschack, P.; Anderson, I, M.; Johnson, D. C. Structure of Turbostratically Disordered Misfit Layer Compounds $[(PbSe)_{0.99}]_1[WSe_2]_1$, $[(PbSe)_{1.00}]_1[MoSe_2]_1$, and $[(SnSe)_{1.03}]_1[MoSe_2]_1$. *Z. Anorg. Allg. Chem.* **2012,** *638*, 2632.

(9) Moore, D. B.; Beekman, M.; Disch, S.; Zschack, P.; Hausler, I.; Neumann, W.; Johnson, D. C. Synthesis, Structure, and Properties of Turbostratically Disordered $(PbSe)_{1.18}(TiSe_2)_2$. *Chem. Mater.* **2013**, *25*, 2404.

(10) Grosse, C.; Alemayehu, M. B.; Falmbigl, M.; Mogilatenko, A.; Chiatti, O.; Johnson, D. C.; Fischer, S. F. Superconducting ferecrystals: turbostratically disordered atomic-scale layered $(PbSe)_{1.14}(NbSe_2)_n$ thin films. *Sci. Rep.* **2016**, *6*, 33457.

(11) Fister, L.; Johnson, D. C.; Controlling Solid-State Reaction Mechanisms Using Diffusion Length in Ultrathin-Film Superlattice Composites. *J. Am. Chem. Soc.* **1992**, *114*, 4639-4644.

Chapter IX

(1) Novoselov, K. S.; Geim, A. K.; Morozov, S. V.; Jiang, D.; Zhang, Y.; Dubonos, S. V.; Grigorieva, I. V.; Firsov, A. A. Electric Field Effect in Atomically Thin Carbon Films. *Science* **2004**, *306*, 666–669.

(2) Tongay, S.; Zhou, J.; Ataca, C.; Lo, K.; Matthews, T. S.; Li, J.; Grossman, J. C.; Wu, J. Thermally driven crossover from indirect toward direct bandgap in 2D semiconductors: MoSe2 versus MoS2. *Nano Lett.* **2012**, *12*, 5576−5580.

(3) Splendiani, A.; Sun, L.; Zhang, Y.; Li, T.; Kim, T.; Chim, C.-Y.; Galli, G.; Wang, F. Emergin Photoluminescences in Monolayer MoS_2. *Nano Lett.* **2010**, *10*, 1271–1275.

(4) Yu, Z. G.; Yakosen, B. I.; Zhang, Y.-W. Realizing Indirect-to-Direct Band Gap Transition in Few-Layer Two-Dimensional MX_2 (M = Mo, W; X = S, Se). *ACS Appl. Energy Mater.* **2018**, *1*, 4115−4121.

(5) Laursen, A. B.; Kegnas, S.; Dahl, S.; Chorkendorff, I. Molybdenum sulfides – efficient and viable materials for electro- and photoelectocatalytic hydrogen evolution. *Energy Environ. Sci.* **2012**, *5*, 5577-5591.

(6) Ambrosi, A.; Sofer, Z.; Pumera, M. 2H → 1T phase transition and hydrogen evolution activity of MoS_2, $MoSe_2$, WS_2 and WSe_2 strongly depends on the MX_2 composition. *Chem. Commun.* **2015**, *51*, 8450.

(7) Yin, Y.; Zhang, Y.; Gao, T.; Yao,, T.; Zhang, X.; Han, J.; Wang, X.; Zhang, Z.; Xu, P.; Zhang, P.; Cao, X.; Song, B.; Jin, S. Synergistic Phase and Disorder Engineering in 1T-$MoSe_2$ Nanosheets for Enhanced Hydrogen-Evolution Reaction. *Adv. Mater.* **2017**, *29*, 1700311.

(8) Puthussery, J.; Seefeld, S.; Berry, N.; Gibbs, M.; Law, M. Colloidal Iron Pyrite (FeS_2) Nanocrystal Inks for Thin-Film Photovoltaics. *J. Am. Chem. Soc.* **2011**, *133*, 716.

(9) Feng, J.; Sun, X.; Wu, C. Z.; Peng, L. L.; Lin, C. W.; Hu, S. L.; Yang, J. L.; Xie, Y. Metallic Few-Layered VS_2 Ultrathin Nanosheets: High Two-Dimensional Conductivity for In-Plane Supercapacitors. *J. Am. Chem. Soc.* **2011**, *133*, 17832.

(10) Kobayashi, K.; Yamauchi, J. Electronic structure and scanning-tunneling-microscopy image of molybdenum dichalcogenide surfaces. *Phys. Rev. B.* **1995**, *51*, 17085.

(11) Ding, Y.; Wang, Y.; Ni, J.; Shi, L.; Shi, S.; Tang, W. First principles study of structural, vibrational, and electrica properties of graphene-like MX2 (M = Mo, Nb, W, Ta; X = S, Se, Te) monolayers. *Physica B* **2011**, *406*, 2254–2260.

(12) Hermann, A. M.; Somoano, R.; Hadek, V.; Rembaum, A. Electrical Resistivity of Intercalated Molybdenum Disulfide. *Solid State Communications.* **1973**, *13*, 1065.

(13) Py, M. A.; Haering, R. R. Structureal destabilization induced by lithium intercalation in MoS_2 and related compounds. *Can. J. Phys.* **1983**, *61*, 76.

(14) Kappera, R.; Voiry, D.; Yalcin, S. E.; Branch, B.; Gupta, G.; Mohite, A. D.; Chhowalla, M. Phase-engineered low-resistance constacts for ultrathin MoS_2 transistors. *Nat. Materials.* **2014**, *12*, 1128.

(15) Friedman, A. L.; Hanbicki, A. T.; Perkins, F. K.; Jernigan, G. G.; Culbertson, J. C.; Campbell, P. M. Evidence for Chemical Vapor Induced 2H to 1T Phase Transition in MoX_2 (X = Se, S) Transition Metal Dichalcogenide Films. *Scientific Reports.* **2017**, *7*, 3836.

(16) Rudorff, W. Alkali Metal Intercalation Compounds of Transition Metal Chalcogenides: TX_2, TX_3, and TX_4 Chalcogenides. *Chimia*, **1965**, 489.

(17) Schöllhorn, R.; Weiss, A. Cation exchange reactions and layer solvate complexes of ternary phases M_xMoS_2. *Journal of the Less-Common Metals,* **1974**, *36*, 229-236.

(18) Haering, R. R.; Stiles, J. A. R.; Brandt, K. Lithium Molybdenum Disulphide Battery Cathode. US Patent 4, 224, 390, September 23, 1980.

(19) Radisavljevic, B.; Whitwick, M. B.; Kis, A. Integrated Circuits and Logic Operations Based on Single-Layer MoS_2. *ACS Nano* **2011**, *5*, 9934–9938.

(20) Hadland, E. C.; Gohler, F.; Mitchson, G.; Fender. S. S.; Schmidt, C.; Zahn, D. R. T.; Seyller, T.; Johnson, D. C. Synthesis and Properties of $(BiSe)_{0.97}MoSe_2$: A Heterostructure Containing Both 2H-$MoSe_2$ and 1T-$MoSe_2$. *Chem. Mater.* **2019**, *31*, 5824.

(21) Choffel, M. A.; Gannon, R. N.; Göhler, F.; Miller, A. M.; Medlin, D.; Seyller, T.; Johnson, D. C. Synthesis and Electrical Properties of a New Compound $(BiSe)_{0.97}(Bi_2Se_3)_{1.26}(BiSe)_{0.97}(MoSe_2)$ Containing Metallic 1T-$MoSe_2$. *Chem. Mater.* **2021.** 33, 16, 6403–6411

(22) Hamann, D. M., Bardgett, D., Cordova, D. L. M., Maynard, L. A., Hadland, E. C, Lygo, A. C., Wood, S. R., Esters, M., and Johnson, D. C. Sub-Monolayer Accuracy in Determining the Number of Atoms per Unit Area in Ultrathin Films Using X-ray Fluorescence. *Chem. Mater.* **2018**, *30*, 6209.

(23) Choffel, M. A.; Kam, T. M.; Johnson. D. C. Substituent Effects in the Synthesis of Heterostructures. *Inorg. Chem.* **2021**, *60*, 9598−9606.

(24) Miller, A. M.; Hamann, D. M.; Hadland, E. C.; Johnson, D. C. Investigating the Formation of $MoSe_2$ and $TiSe_2$ Films form Artificially Layered Precursors. I*norg. Chem.* **2020**, *59*, 12536–12544.

(25) Bronsema, K. D.; de Boer, J. L.; Jellinik, F. On the Structure of Molybdenum Diselenide and Disulfide. *Zeitschrift fur Anorg. und Allg. Chemie* **1986**, *540*, 15–17.

(26) Smeller, M. M.; Heideman, C. L.; Lin, Q.; Beekman, M. Anderson, M. D.; Zschack, P.; Anderson, I, M.; Johnson, D. C. Structure of Turbostratically Disordered Misfit Layer Compounds $[(PbSe)_{0.99}]_1[WSe_2]_1$, $[(PbSe)_{1.00}]_1[MoSe_2]_1$, and $[(SnSe)_{1.03}]_1[MoSe_2]_1$. *Z. Anorg. Allg. Chem.* **2012,** *638*, 2632.

(27) Moore, D. B.; Beekman, M.; Disch, S.; Zschack, P.; Hausler, I.; Neumann, W.; Johnson, D. C. Synthesis, Structure, and Properties of Turbostratically Disordered $(PbSe)_{1.18}(TiSe_2)_2$. *Chem. Mater.* **2013**, *25*, 2404.

(28) Grosse, C.; Alemayehu, M. B.; Falmbigl, M.; Mogilatenko, A.; Chiatti, O.; Johnson, D. C.; Fischer, S. F. Superconducting ferecrystals: turbostratically disordered atomic-scale layered $(PbSe)_{1.14}(NbSe_2)_n$ thin films. *Sci. Rep.* **2016**, *6*, 33457.

(29) Mann, J.; Ma, Q.; Odenthal, P. M.; Isarraraz, M.; Le, D.; Precisdo, E.; Barroso, D.; Yamaguchi, K.; von Son Palacio, G.; Nguyen, A.; Tran, T.; Wurch, M.; Nguyen, A.; Klee, V.; Bobek, S.; Sun, D.; Heinz, T. F.; Rahman, T. S.; Kawakami, R.; Bartels, L. *Adv. Mater.* **2014,** *26,* 1399-1404.

(30) Hadland, E. C.; Jang, H.; Wolff, N.; Fischer, R.; Lygo, A. C.; Mitchson, G.; Li, D.; Kienle, L.; Cahill, D. G.; Johnson, D. C. Ultralow thermal conductivity of turbostratically disordered $MoSe_2$ ultra-thin films and implications for heterostructures. *Nanotechnology.* **2019**, *30*, 285401.

Appendix C

(1) D. L. Duong, G. Ryu, A. Hoyer, C. Lin, M. Burghard, and K. Kern: Raman Characterization of the Charge Density Wave Phase of 1T-$TiSe_2$: From Bulk to Atomically Thin Layers. *ACS Nano 11*, 1034 (**2017**).

(2) Y. Wu, M. An, R. Xiong, J. Shi, and Q. M. Zhang: Raman scattering in the normal phase of 2H-$NbSe_2$. *J. Phys. D: Appl. Phys 41*, 175408 (**2008**).

(3) P. Tonndorf, R. Schmidt, P. Böttger, X. Zhang, J. Börner, A. Liebig, M. Albrecht, C. Kloc, O. Gordan, D. R. T. Zahn, S. M. de Vasconcellos, and R. Bratschitsch: Photoluminescence emission and Raman response of monolayer MoS_2, $MoSe_2$, and WSe_2. *Opt. Express 21*, 4908 (**2013**).

(4) U. Gupta, B. S. Naidu, U. Maitra, A. Singh, S. N. Shirodkar, U. V. Waghmare, and C. N. R. Rao: Characterization of few-layer 1T-$MoSe_2$ and its superior performance in the visible-light induced hydrogen evolution reaction. *APL Materials 2*, 092802 (**2014**).

(5) J. Zhang, Z. Peng, A. Soni, Y. Zhao, Y. Xiong, B. Peng, J. Wang, M. S. Dresselhaus, and Q. Xiong: Raman Spectroscopy of Few-Quintuple Layer Topological Insulator Bi_2Se_3 Nanoplatelets. *Nano Lett. 11*, 2407 (**2011**).